The Time Development of Hadronic Showers and the T3B Experiment

Christian Soldner

München 2013

The Time Development of Hadronic Showers and the T3B Experiment

Christian Soldner

Dissertation
an der Fakultät für Physik
der Ludwig–Maximilians–Universität
München

vorgelegt von
Christian Soldner
aus München

München, den 8. Mai 2013

Erstgutachter: Prof. Dr. Christian Kiesling
Zweitgutachter: Prof. Dr. Jochen Schieck
Tag der mündlichen Prüfung: 6. Juni 2013

Zusammenfassung

Der Compact Linear Collider (CLIC) ist ein zukünftiger e^+e^--Beschleuniger mit einer Kollisionsenergie von bis zu 3 TeV und einer Kollisionsrate der Teilchenbündel von 2 GHz. Damit stellt CLIC besondere Anforderungen an ein Gesamtdetektorsystem. Die Akkumulation von Hintergrundereignissen - wie zum Beispiel aus Beamstrahlung resultierende $\gamma\gamma \to Hadronen$ Interaktionen - soll durch eine zeitaufgelöste Teilchendetektion in allen Subdetektorsystemen minimiert werden. In der Ereignisrekonstruktion wird die präzise Zuordnung von Ereignissen zu einer kleinen Anzahl aufeinanderfolgender Teilchenbündelkollisionen insbesondere durch die Kalorimeter unterstützt indem man Energiedepositionen einen genauen Zeitstempel zuweist. Andererseits ist die Zeitentwicklung von hadronischen Schauern nicht instantan. Die Anforderungen an die Energieauflösung der Kalorimeter machen eine Integration über einen ausgedehnten Zeitraum unabdingbar. Wolfram ist eines der dichtesten Materialien und soll als Absorber verwendet werden um Teilchenschauer auf engstem Raum und innerhalb der Kalorimeter zu stoppen. Gegenwärtig ist die zeitaufgelöste Propagation hadronischer Schauer in Wolfram experimentell jedoch noch nicht hinreichend erforscht.
Das T3B Experiment (Tungsten Timing Test Beam) wurde im Rahmen dieser Arbeit entworfen und konstruiert. Es besteht aus einer Kette von 15 Szintillatorkacheln, deren Lichtsignal durch Photosensoren (SiPMs) detektiert und durch Oszilloskope mit einer Abtastrate von 1.25 GHz digitalisiert wird. Das Experiment wurde dafür entwickelt die Zeitstruktur hadronischer Schauer zu vermessen und herauszufinden wie stark verspätete Energiedepositionen innerhalb eines Schauers beitragen. Der T3B Kachelstreifen wurde hinter zwei Prototypen für Hadronenkalorimeter der CALICE Kollaboration montiert, die mit einer Stahl- bzw. Wolframabsorberstruktur ausgestattet waren.
Das T3B Experiment hat während der CALICE Teststrahlphase 2010/2011 am PS und SPS des CERN Hadronenschauer in einem Energiebereich von $2 - 300$ GeV zeitlich vermessen. Eine für den Teststrahlbetrieb optimierte Software zu Datennahme wurde neu konzipiert. Die Entwicklung eines neuartigen Softwarealgorithmus zur zeitlichen Dekomposition von SiPM-Signalen erlaubte es, den Detektionszeitpunkt einzelner Photonen und somit Schauer mit einer zeitlichen Präzision von ~ 1 ns zu studieren.
Das T3B Experiment konnte eine erhöhte späte Schaueraktivität in Wolfram relativ zu Stahl nachweisen. Hierzu wurde eine detaillierte Untersuchung der Zeitverteilung der Energiedepositionen bemüht. Außerdem wurde beobachtet, dass der relative Einfluss von späten Energiedepositionen radial mit der Distanz zur Schauerachse zunimmt. Diese Zunahme ist in Wolfram wesentlich stärker ausgeprägt als in Stahl. Es konnte nachgewiesen werden, dass das für Simulationen am LHC und für den Großteil der Physikstudien für CLIC standardmäßig verwendete hadronische Schauermodell QGSP_BERT späte Energiedepositionen systematisch überschätzt. Neu entwickelte Modelle mit speziellem Augenmerk auf niederenergetischen Neutronen reproduzieren die Daten besser. Im Bezug auf die Energie einfallender Teilchen in einem Bereich von $60 - 180$ GeV konnten keine signifikanten Unterschiede im Rahmen der Messunsicherheiten nachgewiesen werden.


Tungsten Timing
T3B
TestBeam

Abstract

The compact linear collider (CLIC) is a future linear e^+e^--collider operated at a center of mass energy of up to 3 TeV and with a collision rate of particle bunches of up to 2 GHz. This poses challenging requirements on the detector system. The accumulation of background events, such as $\gamma\gamma \rightarrow hadrons$ resulting from Beamstrahlung, must be minimized through a precise time stamping capability in all subdetector systems. In the event reconstruction, the energy depositions within the calorimeters will be used to assign events precisely to a small set of consecutive bunch crossings. The finite time evolution of hadronic showers, on the other hand, requires an extended integration time to achieve a satisfactory energy resolution in the calorimeter. The energy resolution is also deteriorated by the leakage of shower particles. Tungsten is foreseen as dense absorber material, but the time evolution of hadron showers within such a calorimeter is not sufficiently explored yet.

In the context of this thesis, the T3B experiment (short for Tungsten Timing Test Beam) was designed and constructed. It is optimized to measure the time development and the contribution of delayed energy depositions within hadronic cascades. The T3B experiment consists of 15 scintillator cells assembled in a strip. The scintillation light generated within the cells is detected by novel silicon photomultiplier whose signal is read out with fast oscilloscopes providing a sampling rate of 1.25 GHz. This strip was positioned behind two different calorimeter prototypes of the CALICE collaboration which use a tungsten and steel (for comparison) absorber structure.

T3B was part of the CALICE test beam campaign 2010/2011 carried out at the PS and SPS at CERN and acquired data on hadronic showers in an energy range of $2-300$ GeV. A test beam optimized data acquisition software was developed from scratch. With the development and application of a novel waveform decomposition algorithm, the time of arrival of photons on the light sensor could be determined with sub-nanosecond precision. Embedded in a custom calibration and analysis framework, this allows for a precise study of shower timing on the nanosecond level.

The T3B experiment could prove an increased contribution of the delayed shower component in tungsten with respect to steel via a detailed study of the time distribution of energy depositions. In addition, it is observed that the relative importance of late energy depositions increases with radial distance from the shower axis. This increase is substantially more pronounced in tungsten with respect to steel. It could be shown that the standard hadronic shower model QGSP_BERT, used for shower simulations at the LHC as well as for most CLIC physics studies, overestimates the delayed shower evolution systematically, while high precision extensions using precise neutron tracking models can reproduce the shower timing adequately. No significant difference in the delayed shower contribution was observed for different particle energies in a range between 60 GeV and 180 GeV.


Tungsten Timing
T3B
TestBeam

Contents

Chapter 1

Introduction

This thesis is devoted to something overarching, something that is indispensable for everyone and everything, although no one has ever seen it, felt it or tasted from it.
In his fantastic words, Tolkien describes it in its most negative and destructive form:

This thing all things devours:
Birds, beasts, trees, flowers;
Gnaws iron, bites steel;
Grinds hard stones to meal;
Slays king, ruins town,
And beats high mountain down.

J.R.R Tolkien

But it does not oppose mankind. It is everywhere with us, accompanies us and makes this thesis and the underlying work possible in multiple ways.
Therefore, I feel tempted to recover its reputation and reformulate this poem to live up to its scientific importance:

This thing all things permits:
Known laws of Physics, universal fits;
Lets young scientists grow and marvel;
Gives muse, ideas, helps riddles ungarble.
Their humble try reveals its beauty;
Builds machines large, satisfies their scrutiny.

The attentive reader might have already fathomed what we are talking about:
This thesis is all about **time** and the use of it to understand processes in particle physics detectors at a new level of precision.

Time is a term that is hard to grasp. It is not a substance or object but rather a special system of relations among events. The definition of time helps to categorize events from the past through the present to the future. So time can be understood as the order of successive events. In a philosophical view (defended by Gottfried Leibniz and

Immanuel Kant), one could state that time is irrelevant without events occurring in the universe and intelligence which attributes meaning to it. It depends on the human way of perception. In the realist view (defended by Newton), time is a fundamental dimension that would also exist in an entirely empty universe.
In any case, mankind tried for millennia to use phenomena of nature and to build devices that measure time through periodic processes. The more constant and exact the internal periodicity, the more precise is the achievable time measurement. As a consequence, the duration or intervals between observed events can be exactly quantified. The first devices exploiting the rotation of earth and specifying the time of the day through the celestial position of the sun through sundials were later replaced by more precise watches which use the optimized oscillation of balance wheels as periodic cycle. Since 1967, the atomic clock is the de facto standard for the definition of time intervals. By the International System of Units (SI) one second is defined as the duration of 9.192.631.770 cycles of radiation corresponding to the transition of a shell electron between the two hyperfine structure energy levels of the ground state of the ^{133}Cs atom. Within this system, we describe all processes of nature as multiples (or fractions) of this most stable period. The second is one of the seven fundamental physical quantities together with the meter (length), the kilogram (mass), the ampere (electric current), the kelvin (temperature), the mole (amount of substance) and the candela (luminous intensity). All other physical quantities are derived from them (e.g. velocity is defined by the second and the meter).

In the theory of special relativity formulated by Albert Einstein, time is combined with the three space coordinates to a four-dimensional space time. While time is the order of successive events, space is the order of co-existing objects. An event has to be specified by both. Through the absolute finite value of the speed of light, distances can also be quantified in terms of time (e.g. a light year). But there is no absolute location in either space or time. In the Christian calendar, the supposed year of the birth of Christ was taken as an arbitrary starting point of modern common time. Any other point in time - like the Big Bang which set off the creation of the known universe - would have been possible, but enough people agreed on this reference early on. In fact, not even space and time are absolute but relative meaning that they depend - according to special relativity - on the reference frame of the observer. As a consequence, time passes slower for moving objects (time dilatation) and moving objects are contracted in length.

Apart from theoretical considerations, special relativity has also important implications for experimental particle physics. For example, an unstable particle that decays with a lifetime τ in its proper time lives significantly longer when accelerated close to of the speed of light relative to the laboratory rest frame ($\tau' = \gamma \cdot \tau$). Such a particle might be directly measurable by a particle detector, although at rest one could only reconstruct its decay products. A particle detector, on the other hand, that is capable of measuring and reconstructing collisions of high energetic particles in four dimensions could profit from the additionally accessible time dimension in many ways. Among others, it is e.g. a powerful tool to disentangle successive collision events and reject the background caused by the acceleration scheme.

In this thesis, we will show how the time evolution of physical events in general and of hadronic particle cascades in particular can be determined and exploited experimentally to obtain a more precise understanding of observable phenomena. In Chapter 2, we will first elaborate on the well established theoretical background of particle physics, namely the Standard Model, and on hypothetical models beyond. We will then explain how microscopic particles are accelerated and brought to collision in modern particle accelerators. In the context of a future electron-positron collider, we will show how the time development of the particles created in such collisions could be exploited with future particle detectors to achieve a more reliable event reconstruction to support e.g. the discovery of new particles sorts. Calorimetric subdetectors determine the energy of final state collision particles by measuring particle showers generated in dense absorbers such as iron or tungsten. They are a crucial component on the way to a four dimensional investigation of particle events. In Chapter 3, we discuss the basic concepts of calorimetry and study the theoretical and empirical background of the time development of hadronic showers in detail. The T3B experiment was designed in the context of this thesis for a direct and experimental investigation of the time evolution of hadron showers with a so far unprecedented precision. Its general outline and design concept is elaborated in Chapter 4. The T3B experiment took data on hadronic showers at different test beam accelerators in the year 2010/2011. The application of a set calibration methods on the collected data is explained in Chapter 5. Finally, a detailed presentation of the developed analysis framework and its results are given in Chapter 6.

Chapter 2

Prospects for a Future Linear e^+e^--Collider at the Terascale

In the year 2012, particle physics stands on the verge of new discoveries that could tighten or change our fundamental understanding of nature. In July, the European center of particle physics, CERN [1], announced the discovery of a new heavy particle [2] [3] with a mass of around 125 GeV by both multi-purpose particle detectors CMS [4] and ATLAS [5] at the Large Hadron Collider (LHC). While this new particle is compatible with the predicted Higgs boson, which is part of the well established Standard Model of particle physics, the LHC offers the opportunity for the search and exploration of new physical phenomena at the energy scale of TeV within the next years of operation. It is, for example, hoped that the LHC will find evidence of Supersymmetry (SUSY) and thus open the door to a new set of heavy particles, that can be studied at the LHC and at future collider experiments. A future e^+e^--collider could perform precision measurements of the newly discovered boson and other potential discoveries at the LHC, complement the physics programme of the LHC and possibly discover new physics beyond the Standard Model through measurements that are not easily accessible to the detectors of a hadron machine.

In this chapter, we provide a short overview over the fundamental physics of the Standard Model and the idea of supersymmetric theories beyond. We will then discuss the benefit of a possible future linear e^+e^--collider operating at the terascale and the precision physics that could be performed with such a machine. We will show how the realization of a linear collider could be achieved following current design concepts and discuss characteristics intrinsic to the used technology. Finally, we explain the requirements a detector system needs to fulfill to address the physics goals and cope with the environmental conditions of the collider and present the outline of such a detector concept.

2.1 Physics Introduction - The Standard Model of Particle Physics and Beyond

The formulation of the Standard Model of particle physics is one of the greatest achievements of the 20$^{\text{th}}$ century. It is a self-consistent theory which defines the elementary particles of Nature and describes the interactions between them incorporating three of the four fundamental forces of nature: the strong, the weak and the electromagnetic force [6]. Its current theoretical formulation was finalized in the 70's. At that time, many of the included elementary particles were only postulated out of logical considerations such as symmetries. The success of the Standard Model manifests itself in the accuracy of theoretical predictions that proved to be very robust against experimental probing (e.g. in collider experiments) and the successive discovery of all of the postulated particles such as the bottom quark in 1977 [7], the top quark in 1995 [8] [9], the tau neutrino in 2000 [10] and the potential discovery of the last missing link, the Higgs particle in 2012 [2] [3]. In this sense, all key foundations of the Standard Model have been experimentally verified.

But the Standard Model is certainly not the end of the story. It relies on about 20 input parameters [11] such as the values of the elementary particle masses, the Weinberg angle or the CKM parameters, which it cannot predict and which had to be determined experimentally. It does not consider the fourth fundamental force, the gravitation, at all. Moreover, it predicts the existence of three different neutrinos, but cannot incorporate neutrino masses, although it has been observed that at least two of them are massive [12] [13]. The Standard Model cannot explain the full extent of the baryon asymmetry in the universe for which our existence and the apparent non-existence of galaxies that consist out of antimatter is the most plausible proof. Measurements on the rotational speed of galaxies and gravitational lensing prove the existence of Dark Matter while all known particle sorts represent only about 5 % of the total mass of the universe. The Standard Model gives no hint on the nature of the remaining 95 %. This is only a small compendium of unresolved, but proven phenomena that have to be addressed by new more powerful theories. Without experimental proof such theories remain speculative assumptions. The successful operation of the LHC at the energy frontier of high energy physics raises the hope for the discovery of new particles or new interactions. In this sense, particle physics stays as exciting as ever.

In the following, we will describe the Standard Model in its current form (similar to [14]), explain the Higgs mechanism and introduce Supersymmetry as an example of physics beyond the Standard Model (BSM).

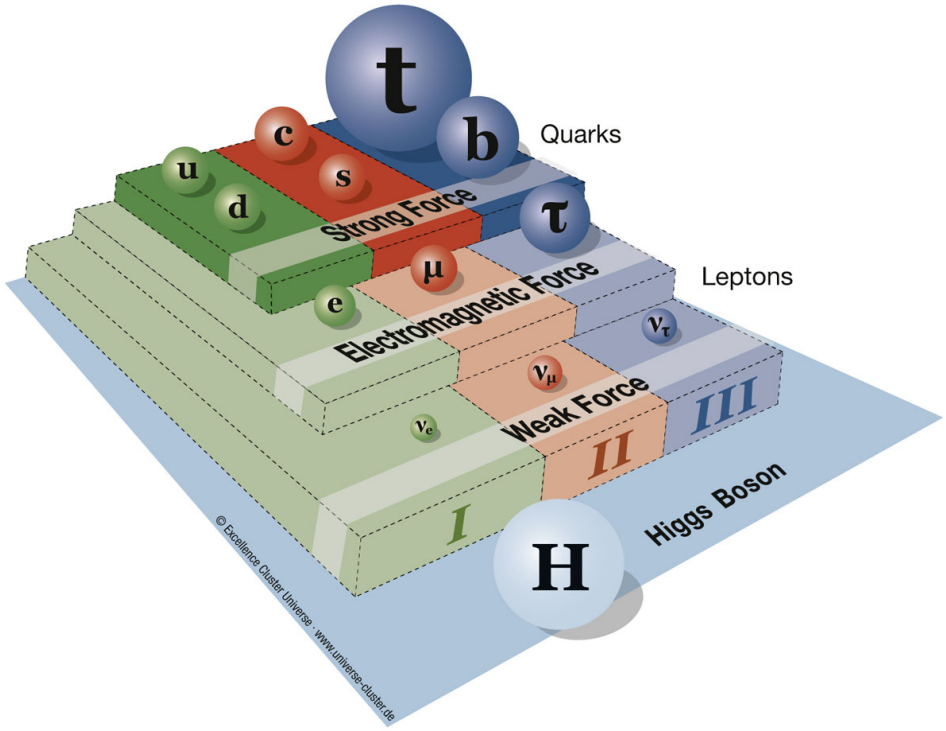

Figure 2.1: The pyramid of the Standard Model showing all fermions it comprises and the Higgs boson. The fundamental forces and the Higgs boson interact with all particle sorts which are at the same level of the pyramid or higher. The masses of the particles are indicated by their respective sizes in the sketch. The three generations of particles are indicated by roman letters.

2.1.1 The Standard Model

The Fundamental Forces of Nature

Until the year 1900, the only known interactions were the classical electromagnetism as derived by Maxwell (1831-1879) and Newton's (1643-1727) laws of gravitation. At that time Max Planck (1858-1947) introduced the revolutionary concept of the quantization of the electromagnetic field and opened the door to the theory of quantum mechanics [15]. The idea evolved that the fundamental forces of nature are mediated by the exchange of so-called messenger particles [6]. Initially only conceived for electromagnetism, mediated by the photon, the idea was later also transferred to the other forces. The $W^{\pm}$ and Z^0 were attributed as the force carriers to the weak force, gluons to the strong force and the graviton to gravitation, although the latter is only hypothetical until today.

All charged particles are subject to electromagnetic interactions (see Figure 2.1), although the photon itself remains uncharged. The quantum theory of electromagnetism is called quantum electrodynamics (QED). In this context, the mathematical symmetry group U(1) is assigned to the electromagnetic interaction by the principle of local gauge

invariance giving rise to a massless boson of spin 1, the photon. At small energies, the coupling strength of electromagnetism is given by the Sommerfeld fine-structure constant $\alpha \approx 1/137$ whose smallness allows for a perturbative description of electromagnetic interaction cross sections.
The strong force affects only particles with a so-called color charge. It is a quantum number that can take the values red, green and blue and three respective anticolors with the interesting feature that the combination of all three colors or a color and an anti-color cancels to zero. Until today six different quark flavours have been discovered each of which carries color. Ordered by their mass and consequently by their chronological order of discovery these quarks are called the up and the down, the strange, the charm, the bottom and top quark. All known hadrons consist of three quarks (baryons) or a quark-antiquark pair (mesons) and have to be in total colorless by the laws of the quantum theory of the strong force which is called very fittingly Quantum Chromo Dynamics (QCD). The strength of the strong force is described by the coupling constant α_S which increases with the separation distance of e.g. two quarks. This phenomenon is called color confinement and is the underlying reason why individual quarks (carrying only one color) may not exist freely. They are rather bound by the strong force to compound hadrons. Note that the strong force can not be described by perturbative theories (in the low energy regime) due to its long range behaviour ($\alpha_S \approx 1$). As there are three different colors, the underlying symmetry group of QCD is $\mathrm{SU}(3)_C$. The strong force is mediated by a set of gluons which carry two colors, a color and an anti-color, and are therefore self-interacting. The existence of eight different gluons originates from the eight allowed combinations of three colors and their anti-colors.
The first experimental manifestation of the weak force was investigated in the context of the nuclear beta decay in 1930 [16]. In contrast to the expectations, the emitted electron exhibited a continuous energy spectrum which would be impossible in the two body decay into an electron and a recoiling nucleus only. A new invisible particle was postulated, the neutrino ($\bar{\nu}_e$ in this case), which is closely connected to weak interactions in the lepton sector. The weak force affects all known fermions (i.e. quarks and leptons). It is mediated by the heavy gauge bosons $\mathrm{W}^\pm$ and Z^0 which have a mass of 80.4 GeV and 91.2 GeV [17], respectively. Due to this large mass, weak interactions are suppressed and the weak force is so weak (i.e. at low energies the propagator of the Z^0 or $\mathrm{W}^\pm$ bosons is proportional to $1/M_Z^2$ or $1/M_W^2$ which suppresses the cross section for weak processes). It has the unique property of changing the quark flavour (e.g. $u \to d + W^+$) which is also allowed cross-generational ($s \to u + W^-$). Thus, a model was developed by Cabibbo, Kobayashi and Maskawa in which the weak force acts upon so-called weak quark eigenstates which are composed of an admixture of the mass eigenstates of different quarks [18]. This is represented by the CKM-matrix. This matrix does also contain a phase which accounts for the CP-symmetry breaking nature of the weak force. Similar to electricity and magnetism, the weak force could be unified with the electromagnetic force in a mathematical way using again the concept of gauge invariance. The underlying symmetry group of the electroweak force is the $\mathrm{SU}(2)_L \times \mathrm{U}(1)_Y$ which results in four force carriers out of which three ($\mathrm{W}^\pm$, Z^0) acquire mass through the Higgs mechanism (explained below) whereas one (the photon) remains massless.

Formulation of the Standard Model

The fundamental forces (with the exception of gravity) and all known manifestations of matter are described comprehensively by the Standard Model: All matter consists of two kinds of elementary particles: leptons and quarks. The forces between the particles are mediated by the exchange of their respective field quanta, namely eight gluons, one photon and three weak gauge bosons ($W^{\pm}$ and Z^0). There are six different quarks classified by their charge (+2/3 for u,c,t or -1/3 for d,s,b) and flavour. Similarly, there are six leptons: the electron, the muon, the tau and their respective neutrinos. The leptons are categorized by their charge (-1 for e, μ, τ and 0 for the neutrinos ν_e, ν_μ, ν_τ) and by their generation conserving lepton number (L_e, L_μ and L_τ, not conserved by the weak force). An antiparticle exists for each of the 12 fermions. Furthermore, each of the six quarks (and six antiquarks) can come in three different colors. So altogether, the Standard Model comprises 48 elementary fermions, 12 leptons and 36 quarks. With the addition of 12 bosonic force carriers (eight gluons, $W^{\pm}$ and Z^0, and the photon) the Standard Model is nearly complete. Using the overarching concept of local gauge invariance, each of the three forces is described by its respective renormalizable symmetry group. With respect to QCD and the theory of electroweak unification, the conclusive symmetry group of all three interactions is $SU(3)_C \times SU(2)_L \times U(1)_Y$. All this makes up the Standard Model [19]. The only missing piece is the Higgs particle which has a somewhat special role.

The Higgs Particle

In contrast to the force mediating vector bosons, the Higgs boson is the only scalar (spin 0) particle within the Standard Model. In this sense, the Higgs has a unique role. It carries neither a charge nor a color charge and is its own antiparticle. The Higgs mechanism gives rise to the mass of the Standard Model Higgs particle, which has presumably a value of around 125 GeV, and to a mass term for other elementary particles (except for the photon and gluons) [20]. In the view of this mechanism, one can in particular explain why the photon remains massless while $W^{\pm}$ and the Z^0 are massive.
The principle of local gauge invariance works perfectly for strong and electromagnetic interactions. Similarly to these interactions, its application to weak interactions leads inevitably to massless gauge fields contradicting observations of the $W^{\pm}$ and the Z^0 masses. This problem can only be solved by a more subtle approach including the Higgs potential. In a perturbative field theory, such as the Feynman Calculus commonly used to describe particle interactions, one identifies the vacuum ground state of minimal energy and treats the fields as fluctuations around that state [6]. One now introduces the Higgs field as a new complex scalar $SU(2)_L$ doublet with hypercharge 1 into the theory of electroweak interactions. It consists of four components (with four degrees of freedom), two neutral and two charged component fields, and comes with a new (Higgs) potential. This potential is energy dependent. At very high energies or in a very early universe the vacuum ground state was at the center of the potential and all particles

were massless. Towards lower energies, e.g. in today's universe, the potential develops a "Mexican hat" shape which has the remarkable property of a non-zero amplitude in the ground state or, in other words, a non-zero VEV (short for vacuum expectation value). As a consequence, the weak isospin symmetry is spontaneously broken. It is this feature of electroweak symmetry breaking which explains consistently how the electroweak interaction divides at low energies into electromagnetism and the weak force. At the same time, all fermions and the weak gauge bosons become massive through this potential. Within the mathematical details of Goldstone's theorem it could be shown that a symmetry can, under certain conditions, be broken withouth disrupting gauge invariance and without having to postulate new unphysical particles or forces. Applying the concept of gauge invariance to the Lagrangian of the scalar Higgs field and its potential and expanding around a particular ground state of the Higgs potential (which is displaced from the center) gives rise to the Higgs boson and its self-couplings. With the choice of an explicit gauge, one can eliminate the contribution of unphysical massless particles (Goldstone bosons) and establish mass terms for the vector bosons in a comprehensive form [6]. So instead of simply introducing a mass term, which would be incompatible with a preservation of gauge invariance in the theory, mass can be understood as a manifestation of potential energy transferred to the particle during interactions ("coupling") with the Higgs field.
Analyzing the degrees of freedom, one finds that three of the four Higgs field components were absorbed by the initially massless $SU(2)_L \times U(1)_Y$ gauge bosons. This results eventually in the massive $W^{\pm}$ and the Z^0. No mass term arises for the photon. The Higgs particle can be understood as a quantum excitation of the fourth (neutral) field component. This field component couples separately to the fermions via Yukawa couplings which are free parameters to the Standard Model (one for each massive fermion). Nevertheless, the values of these free parameters are accessible through a measurement of the respective fermion masses. Although the Higgs mass can be narrowed down, the Higgs self-coupling parameter and therefore the value of its mass remains a free parameter to the theory (the Higgs potential comprises two parameters only one of which can be determined) and has to be measured experimentally.

2.1.2 Beyond the Standard Model - Supersymmetry

From detailed measurements of the properties of the weak interaction a Standard Model Higgs mass of the order of 100 GeV was favoured already years ago [21]. The recent discovery of a boson at 125 GeV at the LHC would prove this, provided it is the long sought-after Higgs boson. But it raises a theoretical challenge also known as the hierarchy problem or the naturalness problem of the Higgs. In simple words the problem can be reformulated as: Why is gravitation so much weaker than the weak force?

The Hierarchy Problem

In quantum field theory, loop corrections contribute to fundamental parameters such as the mass of a particle or the coupling constants. One usually distinguishes between the effective, measurable mass (or coupling constant) that includes corrections from quantum loops and the "bare" mass (or coupling constant). Arising divergences can be avoided by a so-called renormalization scheme [6]. Now, a hierarchy problem arises if such quantum corrections exceed the measurable mass by orders of magnitude. This is the case for the Higgs mass. In contrast to fermions (spin 1/2) or vector gauge bosons (spin 1), a particularity of the scalar Higgs (spin 0) is that the quantum corrections of fermion loops scale with the ultraviolet momentum cutoff Λ_{UV}. Λ_{UV} can be understood as the energy scale up to which the Standard Model is valid and new physics phenomena influence the high-energy behaviour of the theory. One can be sure that Λ_{UV} is at maximum equivalent to the Planck Scale $M_P \sim 10^{19}\,\mathrm{GeV}$ at which quantum gravitational effects become relevant. If we assume that $\Lambda_{UV} \approx M_P$, then the quantum corrections turn out to be about 30 orders of magnitude larger than the expected (quadratic) value of the Higgs mass [22]. In other words, arguing simply with the contribution from quantum corrections the natural value of the Higgs mass should be close to the Planck Scale which is presumably not the case. Since the energy scale of the electroweak interaction is determined by the masses of the weak gauge bosons (which are generated through the Higgs mechanism), also the weak scale should be close to the Planck scale. But it is of the order $10^2\,\mathrm{GeV}$ instead of $10^{19}\,\mathrm{GeV}$, and the Higgs mechanism requires a Higgs mass close to the electroweak scale instead of its natural scale (naturalness problem). Additionally, finite higher order corrections to the Higgs mass depend on the mass of the interacting loop particle and become very large if new heavy particles beyond the Standard Model exist. In this sense the Higgs mass is very sensitive to new physics. So if the Higgs is a fundamental particle and physics beyond the Standard Model exists this has two precarious implications: It would be possible to renormalize the quadratic divergence of quantum loop corrections away, assuming e.g. an incredible fine-tuning cancellation between the "bare" Higgs mass and the radiative corrections. Such a step appears very artificial and prevents a deeper understanding of the origin of the Higgs mass. Moreover, one would have to make the assumptions that no high-mass particles or effects that couple to the Higgs exist within the 16 orders of magnitude between the electroweak and the Planck scale which is also a very unfavourable option bearing the rich particle content in mind that was discovered at the lower energies of the Standard Model so far.

Supersymmetry

It is more natural to introduce a new symmetry for which a cancellation of the disruptive effect of radiative corrections is not only possible, but practically unavoidable. This is the motivation for the introduction of Supersymmtery (SUSY). SUSY is a symmetry that relates fermions and bosons with each other via a new gauge transformation, i.e. each fermion in the Standard Model is accompanied by a corresponding boson which

differs by spin 1/2 and vice versa (find technical details in [22]). As a consequence, the amount of elementary particles is doubled in one step. SUSY is motivated by the fact that fermions and bosons contribute with opposite sign to the quantum corrections. In the case of an exact symmetry the divergent terms cancel automatically. A fine tuning as discussed above is not necessary. But this implies that the superpartners must have exactly the same electric charge, weak isospin and color degrees of freedom and the same mass as their respective Standard Model partners. If this was true in today's universe, manifestations of these superpartners would have been already observed. So Supersymmetry must be spontaneously broken in its ground state to render the superpartners very heavy (to a mass of about $\mathcal{O}(1\,\mathrm{TeV})$).
Furthermore, not all supersymmetric renormalizable couplings conserve baryon and lepton number. Nevertheless, this is an observational necessity since a violation would imply the rapid decay of the proton whose lifetime was determined to be larger than $10^{33} - 10^{34}$ years [23]. To not conflict with experimental data these respective couplings are set to zero by the introduction of the so-called R-parity. It is a multiplicative quantum number which is +1 for particles and -1 for their supersymmetric partners. An implication of R-Parity is that supersymmetric particles can only be created in pairs and that a stable lightest supersymmetric particle (LSP) exists into which all other SUSY particles will eventually decay. The LSP needs to be neutral, weakly interacting and very massive (also called WIMP). Otherwise such a stable particle would have already been observed. With these properties, LSPs could be a largely abundant remnant from the Big Bang and therefore explain the existence of dark matter to a certain extent [24].
In grand unified theories (GUTs), the three fundamental interactions - the strong, the weak and the electromagnetic force - are low energy manifestations of one single interaction which becomes relevant at the GUT energy scale. This means that the three running (= energy dependent) gauge coupling constants have to merge at one high energy scale. Investigating this energy dependence within the Standard Model, it turns out that this is not the case for all three couplings. Nevertheless, the evolution of the coupling constants is sensitive to the particle content present within the theory. With the addition of supersymmetric particles at the TeV scale, a joint convergence of all three couplings becomes possible at an energy scale of about $10^{16}\,\mathrm{GeV}$ [17].
Until today, no manifestations for SUSY particles have been observed. The entire motivation is based on its capability of providing attractive solutions to prominent theoretical problems. The LHC experiments are undertaking extensive searches for supersymmetric particles and increase the exclusion limits continuously. If manifestations of SUSY exist at the energy scale of $\sim 1\,\mathrm{TeV}$, the LHC is well prepared to reach out for it, in particular when the center of mass energy is eventually increased to the design value of 14 TeV in the next years.

2.2 Motivation and Physics Prospects of a Future e^+e^--Collider

In this section, we will motivate the case of a future e^+e^--collider in comparison to the LHC and discuss accessible precision measurements of such a machine explicitly in the following.

2.2.1 Motivation for a future e^+e^--Collider

As hadron collider, the LHC is well suited for the discovery of new heavy particles in a wide energy range. The center of mass energy (CME) of the colliding protons amounted to 7 TeV in 2011, 8 TeV in 2012 and will be increased up to the design energy of 14 TeV in the future. Protons are composite particles consisting of three valence quarks, gluons and sea quarks, that can carry a variable fraction of the total proton energy (see e.g. [25]). Interesting physics processes originate from the interaction of two partons whose initial states are not precisely known while the remainder of the colliding protons hadronizes to secondary particles that are emitted into the detector system built around the interaction point. This is called underlying event and may disguise the signal of the interesting physics process. The extraction of relevant signatures is additionally complicated by pile-up events: At the LHC, packets of protons, so-called bunches, intersect in the interaction region of a detector. Within one bunch crossing dozens of individual proton-proton collisions can occur. These events can only be unambiguously distinguished if the geometrical distance is high and the vertexing resolution of the detector is good enough. At a proton-proton collider the total cross section for an interaction is with approximately 10^{14} fb very high [26]. The cross section for interesting physics events is, on the other hand, at least 10^{-6} to 10^{-10} times smaller (depending on the studied physics channel). Therefore, a hadron collider requires a dedicated trigger system which preselects and restricts the events that are recorded to disk, possibly rejecting signals of new physics in regions where no interesting phenomena were expected. Due to the high interaction probability with the dominant role of QCD jet production and the large variety of possible processes in proton-proton collisions, the irreducible standard model background makes the analysis of many interesting physics channels challenging or even impossible. At the least a stringent event selection is required when trying to investigate fully-hadronic decay modes. Small signal-to-background ratios are to be expected here.

A e^+e^--collider is advantageous in many of the discussed aspects. Once the energy scale and the base properties of new particles is known, a future e^+e^--collider can perform complementary precision measurements for a deeper understanding of the discovered physics phenomena. In contrast to protons, electrons and positrons are - to our current knowledge - elementary particles. This implies that the collision energy corresponds ideally directly to the center of mass energy of the collider and that no underlying background events occur. In this sense, a e^+e^--collider offers a very clean environment

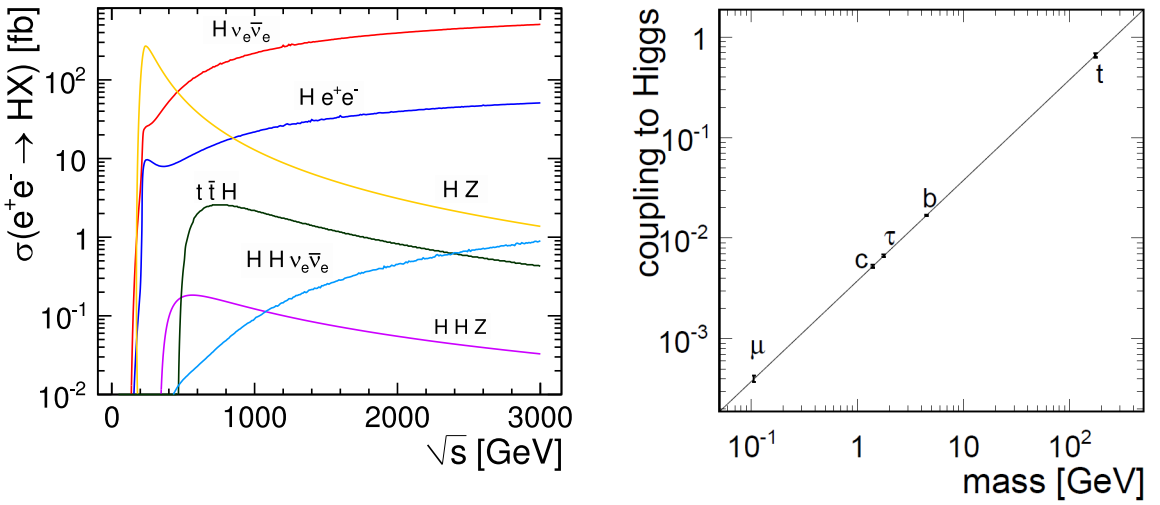

Figure 2.2: Dependence of the Higgs production cross section in different channels in dependence of the center of mass energy of a e^+e^--collider (left). Strength of the Yukawa coupling of the Higgs particle to fermions of the Standard Model in dependence of their mass (right). The precision achieved for the individual couplings is the result of a full simulation study carried out in the context of a future linear collider operating at different center of mass energies. Figures from [27] (left) and [28] (right).

in which the initial state of the interacting particles is well defined. Note however, that at a e^+e^--collider different forms of background, like the pile-up of consecutive bunch crossings or events that may arise related to beamstrahlung (see Section 2.3), complicate the reconstruction of interesting physics events. The cross section of interesting events, such as the production of a Higgs boson with a mass of $\sim 125\,\text{GeV}$, is comparable to the cross section of the backgrounds [26] within a factor of approximately 100. In addition, these backgrounds are to a large extent reducible. Due to this cleaner environment, the signal-to-background ratios are much more favourable for a e^+e^--collider which allows for more precise measurements of e.g. the properties of the Higgs particle. In addition, the cross section for several processes such as the double Higgs production can be boosted through the usage of polarized electron and positron beams. At a e^+e^--collider no specialized restrictive trigger conditions are necessary. The majority of the physics events can be recorded which allows for a model-independent search also for unexpected new physics. While the LHC has good prospects of discovering strongly interacting new particles, a e^+e^--collider is suited for the production and discovery of color neutral and electroweakly charged heavy particles.

2.2.2 Physics Potential at a future e^+e^--Collider

The exploration of the sector of electroweak symmetry breaking does not end with the discovery of the Higgs particle. A e^+e^--collider could measure fundamental properties

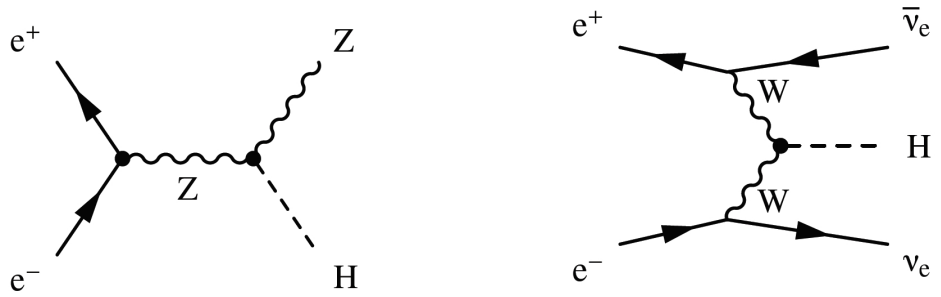

Figure 2.3: Feynman diagrams of the dominant Higgs production channels: Higgsstrahlung (left) at low ($< 450\,\text{GeV}$) and vector boson fusion (right) at high ($> 450\,\text{GeV}$) e^+e^- collision energies.

of the Higgs particle such as its mass and total decay width, its couplings to fermions, bosons and to itself and its spin-parity quantum numbers. The question if it is a fundamental scalar particle or part of a more extended Higgs sector has far-reaching consequences for theories beyond the Standard Model such as Supersymmetry. Many of the measurements necessary to address these open questions are difficult or even impossible for a hadron machine. A future e^+e^--collider operated at several different center of mass energies in a range from 250 GeV up to 1 TeV or 3 TeV has the best prospects to deliver decisive answers.

Figure 2.2 (left) shows the production cross sections of various Higgs processes in dependence of the center of mass energy of an electron-positron collision. The associated production of a Higgs together with a Z boson (Higgsstrahlung, see Figure 2.3, left) dominates at energies below 450 GeV. As s-channel process, its cross section falls off rapidly as $1/s$ towards higher energies. It provides the unique opportunity for a precise measurement of the cross section of the Higgsstrahlungs process and consequently of the HZZ coupling in a model independent way. Instead of directly reconstructing the Higgs, one can reconstruct the Z boson (most precisely through its leptonic decay into two muons) and investigate the recoil mass spectrum which peaks at the mass of the Higgs particle. The Higgs mass can be determined with a precision of better than 40 MeV [28]. Such a measurement does not imply any model specific assumptions and is made possible through a precise knowledge of the collision energy at a e^+e^- machine and a good momentum resolution of the detectors. In addition, possible invisible decays of the Higgs boson could be constrained. If the Higgs boson is also reconstructed explicitly, a determination of the branching fractions of the decays into b and c quarks, τ leptons, WW^* and gluons is possible. Measuring the cross section behaviour close to the production threshold one can draw conclusions on the spin and CP properties of the Higgs boson.

The t-channel W boson fusion process results in a Higgs and two neutrinos (see Figure 2.3, right). Its cross section increases logarithmically with the center of mass energy and dominates above $\sim 500\,\text{GeV}$ (see Figure 2.2, left). This process provides, for example, the possibility to measure the total width of the Higgs boson with a precision of $4-5\,\%$ [28].

At energies above 500 GeV also more rare Higgs production processes such as $e^+e^- \rightarrow$

$t\bar{t}H$, $e^+e^- \to ZHH$ or $e^+e^- \to HH\nu\bar{\nu}$ become accessible provided the integrated luminosity achieved by the e^+e^- machine is high enough. Despite the smaller production rates, these mechanisms become relevant when studying the Yukawa couplings of the Higgs to the top quark and the Higgs self-coupling. Such measurements are a challenge, also for a future e^+e^--collider. With enhanced knowledge on the Higgs trilinear self-coupling one can directly reconstruct the scalar potential that is responsible of electroweak symmetry breaking.
If the Higgs field is responsible for the masses of all particles, the strength of its coupling should be proportional to the mass of the individual particles. This situation is demonstrated in Figure 2.2 (right). Deviations from this linear behaviour could be a hint towards the existence of additional heavy Higgs particles and therefore towards physics beyond the Standard Model.
Although an extended Higgs sector may exist in different models beyond the Standard Model, it is most justified within Supersymmetry. Here, the Higgs sector is enlarged to five scalar particles. Supersymmetry provides not only a comprehensive solution to the naturalness problem of the Higgs particle (see Section 2.1.2), but also postulates the existence of a new set of heavy particles. At the LHC, heavy sleptons, neutralinos and charginos can only be produced through decay chains of strongly interacting supersymmetric particles [27]. A e^+e^--collider could thoroughly investigate the existence of supersymmetric particles with electroweak charges at the TeV scale. Precise measurements of the masses and couplings could e.g. reveal details about the mechanism of supersymmetry breaking, about the viability of the lightest supersymmetric particle as a candidate for dark matter and about a possible unification of the three gauge couplings. The exact requirements and the energy regime a future e^+e^--collider needs to access to study supersymmetric particles depends on the revelations of the LHC experiments in the years to come.

2.3 Design of a Future Linear e^+e^--Collider

Two concepts for a future e^+e^--collider are currently under development whose key difference is the maximal reachable center of mass energy: The International Linear Collider (ILC) is supposed to operate with a maximal CME of 1 TeV while the Compact Linear Collider (CLIC) aims to achieve a CME of up to 3 TeV. As discussed in the last section, the physics potential of a linear e^+e^--collider can be maximized when running at different collision energies. But the electron or positron beam of a fully constructed CLIC machine, for example, cannot be steered to arbitrarily low center of mass energies of e.g. $250 - 350\,\text{GeV}$ without reducing the luminosity significantly. A staged construction, on the other hand, with an initially low CME and later extensions of the accelerator complex bears many advantages. For one, the initial costs are reduced and the total costs are spread over a longer period of time. First physics results are to be expected faster through a shorter initial construction phase. Furthermore, these results and possible technological advancements can be taken into account for later upgrades. For CLIC, three different stages with a maximal CME of 500 GeV, $1.4 - 1.5\,\text{TeV}$ and

3 TeV in the final upgrade, are planned. The ILC is supposed to start off with a CME of 250 GeV or 350 GeV, should be upgraded to 500 GeV later on and reach 1 TeV in the final extension stage.
Both concepts are based on a linear acceleration scheme. If a high energetic charged particle is forced to a circular path by an external magnetic field, it looses energy through synchrotron radiation. Assuming relativistic particle velocities (i.e. $v \approx c$), the energy such a particle looses per revolution in a circular accelerator, a so-called synchrotron, due to synchrotron radiation can be quantified by the following formula:

$$\Delta E = \frac{(Ze)^2}{3\varepsilon_0} \cdot \frac{E^4}{R \cdot (m_0 c^2)^4}, \tag{2.1}$$

where (Ze) is the charge of the accelerated particle, ε_0 the vacuum permittivity, E and m_0 the energy and the rest mass of the particle and R the radius of the circle. The rest mass of an electron is approximately 2000 times smaller than the rest mass of a proton, so the energy loss due to synchrotron radiation is emphasized by a factor of the order 10^{13} in the case of an electron. Since acceleration power would have to compensate for this loss, cost considerations set an upper limit to the maximal energy that is feasible for a circular e^+e^- accelerator. From 1989 to the year 2000 the LEP collider was located in the same tunnel as the LHC today and accelerated electrons and positrons circularly to a maximal energy of about 100 GeV. For a future e^+e^--collider operated at the terascale ΔE would be at least $10^4 = 10.000$ times higher. Since the radius of the collider contributes only as 1/R, an increase of the dimensions of the accelerator is no viable option. In the case of protons, a circular acceleration scheme is feasible and the maximum energy is primarily limited by the cost and performance of the dipole magnets that keep the protons on their circular track. If a e^+e^--collider is supposed to reach TeV energies, it has to be designed with a linear outline.
This implies challenging requirements on the machine performance. In the case of a synchrotron, a large amount of particles can be injected and gradually accelerated in many revolutions to their final energy. Since only few particles interact when the particle bunches intersect within the experiments, they can be stored within the ring and be reused in subsequent bunch crossings. The situation is very different for a linear collider. Here, the particle bunches are guided in "single shots" to the interaction point and the expended acceleration power is in principle lost after the bunch crossing. To be still able to deliver the high luminosity necessary to study rare physics processes, a high beam current, bunch repetition rate and beam focussing has to be realized. The planned collision energy and the maximal length of the collider, which should not exceed 50 km out of cost considerations, dictate the acceleration gradient that needs to be achieved. Thus, the acceleration gradient of CLIC ($E_{max} = 3$ TeV) needs to be about three times higher than for the ILC ($E_{max} = 1$ TeV) (see Table 2.1). The acceleration technology for the ILC has been studied and tested for many years. It is well established and the construction of the ILC could in principle commence once the energy scale of new physics is known. If a CME of 3 TeV is required, a realization of CLIC is the favoured option. But the acceleration gradient necessary for CLIC cannot be reached with ILC technology. An independent R&D programme has been started and a new acceleration

Parameter	ILC	CLIC	CLIC
Center of Mass Energy	0.5 TeV	0.5 TeV	3 TeV
Total Luminosity ($10^{34}\,\mathrm{cm^{-2}s^{-1}}$)	2.05	2.3	5.9
Peak 1 % Luminosity ($10^{34}\,\mathrm{cm^{-2}s^{-1}}$)	~ 1.25	1.4	2.0
Total Tunnel Length (km)	31	13.2	48.3
Acceleration Gradient (MV/m)	31.5	80	100
Bunch Separation (ns)	~ 700	0.5	0.5
# Bunches per Bunch Train	1312	354	312
Bunch Train Length (μs)	~ 1000	0.177	0.156
Bunch Train Repetition Rate (Hz)	5	50	50
Bunch Charge (10^9 e)	20	6.8	3.7
Total Power Consumption (MW)	n.A.	240	560

Table 2.1: Key parameters of the ILC and CLIC. The values of the ILC are based on the ILC Reference Design Report published in 2007 [29] and the update of several design parameters given in [30] in 2011. The numbers of CLIC are based on the CLIC Conceptual Design Report published in 2012 [31].

approach has been worked out to meet the requirements. It will be presented in section 2.3.2. CLIC is an alternative concept for which several issues concerning the power consumption, cost and stability have to be studied in detail within the next years.
Apart from this, the linear outline of the ILC or CLIC implies that there will be only one interaction point for particle collisions. To allow for complementary measurements, two different detectors have to share the same interaction point. A push-pull scenario was developed in which the detectors can be exchanged and share the beam time in regular intervals.

2.3.1 The International Linear Collider (ILC)

Figure 2.4 shows the preliminary outline of the International Linear Collider complex which has a total length of 31 km in the expansion stage of 500 GeV delivering an instantaneous luminosity of $2.05 \cdot 10^{34}\,\mathrm{cm^{-2}s^{-1}}$ [29] (see Table 2.1). Initially, a polarized electron beam is created with a drive laser which detaches electrons from a photokathode. The generated electrons are collected and accelerated in a linear pre-acceleration structure to an energy of 5 GeV. Then, the electron beam is injected into a 3.2 km long damping and storage ring which reduces the beam emittance and accelerates the electrons up to an energy of 15 GeV. The acceleration to the final beam energy of 250 GeV is done by the main linac which is the key acceleration component. It consists of superconducting radio-frequency accelerating cavities, which are operated at a frequency of 1.3 GHz and with an acceleration gradient of 31.5 MV/m. At an energy of 150 GeV, the electron beam is used to produce the positron beam. It traverses a so-called undulator which contains a magnetic dipole field with alternating poles at very short periodic distances. The electrons undergo a transverse oscillation and emit

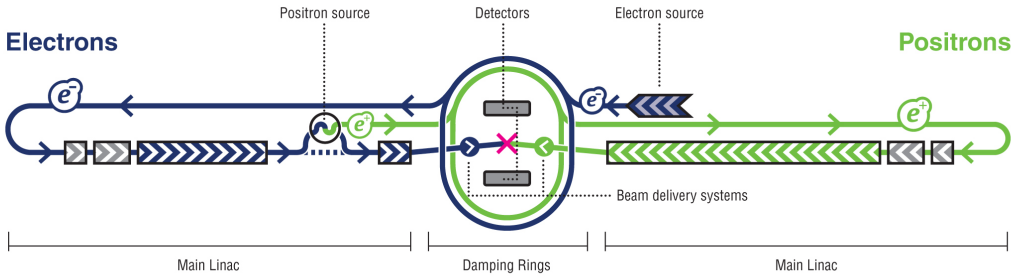

Figure 2.4: Preliminary outline of the International Linear Collider according to [29] at the 500 GeV construction stage.

polarized electromagnetic radiation with an energy of ~ 10 MeV which hits a titanium-alloy target. The photons are converted into an electron-positron pair. The positrons are collected, steered to a second damping ring and finally accelerated to 250 GeV in a second main linac. After reaching the final energy both the electron and the positron beam are focussed by the beam delivery system and steered to the interaction point which is located in the center of the detector system. At the interaction point the beams collide with a crossing angle of 14 mrad to reduce beam induced backgrounds. For an upgrade to a center of mass energy of 1 TeV, the linacs and the beam transport lines would need to be extended significantly.
A polarization of larger than 80 % is planned for the electron beam and of ~ 22 % for the positron beam. In the discussed collider design, a bunch crossing would occur every ~ 700 ns (see Table 2.1). A bunch train consists of 1312 bunches and would collide every 200 ms. Each bunch would consist of approximately 20 billion individual charges.

2.3.2 The Compact Linear Collider (CLIC)

The Compact Linear Collider will achieve a collision energy of 3 TeV in its final stage and deliver a total luminosity of $5.9 \cdot 10^{34}\,\mathrm{cm}^{-2}\mathrm{s}^{-1}$. This can be realized with the acceleration complex shown in Figure 2.5 with a length of 48.3 km. An acceleration gradient of about 100 MV/m must be achieved in the main linacs [31].
At CLIC, the colliding (main) beams are produced with conventional electron and positron sources. Their emittances are reduced in a predamping ring followed by a second damping ring. Before their delivery to the main linacs they are pre-accelerated to an energy of 9 GeV and then accelerated in one pass up to the final energy of 1.5 TeV. Each beam is collimated, compressed and lead to the interaction point by the 2.75 km long beam delivery system. Similarly to the ILC, a beam polarization is foreseen in the CLIC concept.
The challenge at CLIC is to achieve the high acceleration gradient while maintaining a good beam quality. Therefore, a second beam complex creates a so-called drive beam

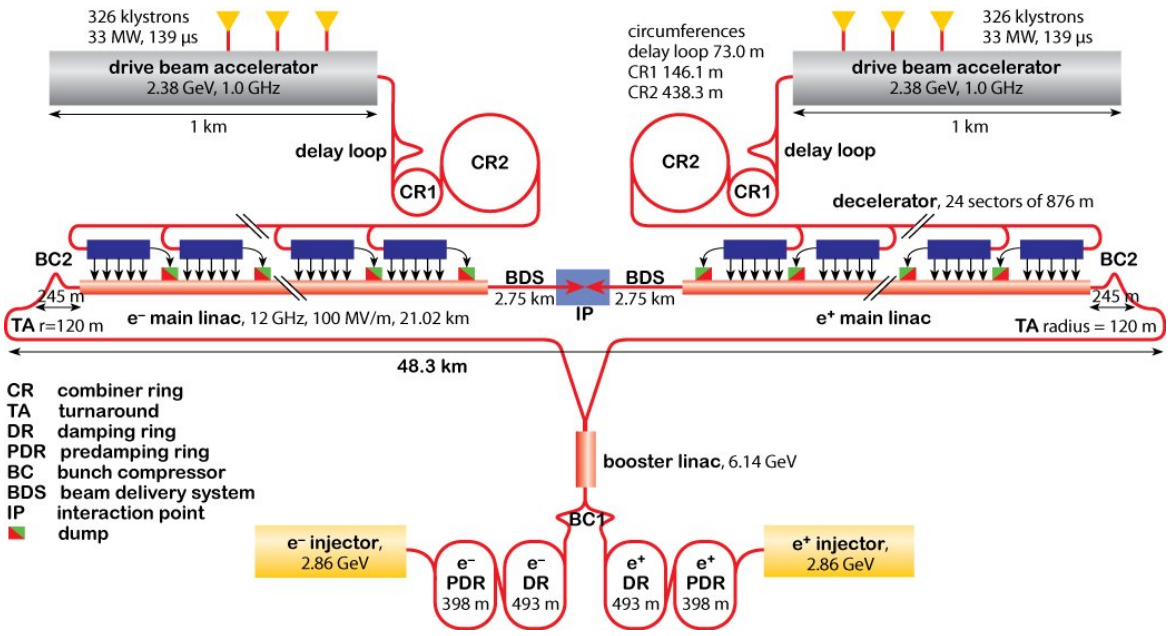

Figure 2.5: Outline of the Compact Linear Collider at the 3 TeV construction stage. Figure from [31].

which runs at a relatively low energy of only 2.37 GeV but with a very high peak current of about 100 A. The main and the drive beam run in parallel within the same tunnel. The acceleration power is transferred from the drive to the main beam by so-called PETS (power extraction and transfer system). Within the PETS, radio frequency (RF) power with a frequency of about 12 GHz is generated and transferred to the main beam via waveguides operating at room temperature. Superconducting accelerating cavities as used for the ILC are not applicable, due to intrinsic limitations of the maximum field strength. This radio frequency acceleration technique favours very short particle bunches. On the other hand, a bunch separation of only 500 ps (see Table 2.1) is very challenging for the detector design and the reconstruction of events (see Section 2.4). At CLIC, 312 particle bunches collide within only 156 ns. Such a bunch train collision occurs every 20 ms. Another challenge originates from the ultra-small bunch size which is necessary to meet the high luminosity requirements. At the interaction point a lateral beam size of only 40×1 nm is envisaged. This increases the effect of beamstrahlung drastically compared to the ILC for which a beam size of 474×3.8 nm at 500 GeV CME is planned. Beamstrahlung is a strong electromagnetic radiation created by the electron and positron bunches in the high field of the opposite beam. The emission of beamstrahlung reduces the energy of individual electrons or positrons. The consequence is a effective luminosity spectrum which peaks at CLIC at the nominal center of mass energy of 3 TeV and has a long tail towards lower collision energies. Table 2.1 shows that, at a CME of 3 TeV, the luminosity in the most energetic 1 % fraction of the spectrum is about three times smaller than the total luminosity (compare: for the ILC at 500 GeV the 1 % fraction is reduced by only about 40 %). Thus, the collision energy of the elementary electrons and positrons is not as clearly defined as initially

assumed. The luminosity spectrum is measurable in-situ through wide angle Bhabha scattering. Furthermore, beamstrahlung generates a large background contribution from two photon interactions into hadrons ($\gamma\gamma \rightarrow$ hadrons) which can have high transverse momentum (p_T) and would influence the event reconstruction significantly without advanced hardware and software supported background rejection techniques. This is a challenge particularly at CLIC due to the very small inter-bunch spacing and the corresponding pile-up of events. While only a small fraction of the bunch trains result in a e^+e^--interaction with an interesting physics signature, 3.2 $\gamma\gamma \rightarrow$ hadrons interactions occur, on average, per bunch crossing in the case of 3 TeV operation. Integrated over one whole bunch train, a background energy of 19 TeV is emitted into the detector system, out of which 90 % is deposited in the forward (endcap) region and 10 % in the region of high p_T (barrel). The presence of the $\gamma\gamma \rightarrow$ hadrons background is one of the main challenges for a detector system at CLIC.

2.4 Design of a Detector System for a Future Linear Collider

In this section, we will first present options for the overall design of a detector for a future linear e^+e^--collider. We will then elaborate the requirements such a detector needs to fulfill to handle the background environment and enable the physics programme of the ILC and CLIC, respectively.

2.4.1 The Detector Concept of ILC and CLIC

The concept of two large scale detector systems, namely the International Large Detector (ILD) and the Silicon Detector (SiD) have been worked out in the context of the ILC. Their respective Letters of Intent [32] [33] were validated by an international review committee in 2009. The ILD and the SiD are designed as multi-purpose detectors with a cylindrical outline that is governed by the overall concept of Particle Flow (details in Section 2.4.2). Therefore, the tracking system and a novel highly granular calorimeter system are located inside the superconducting solenoid. The detectors are subdivided into a barrel and an endcap region. The ILD and SiD concepts form also the basis for the CLIC detectors [27]. The ideas have been extended to be suited for the higher center of mass energy and the short bunch spacing of only 0.5 ns and its implications. The adapted concepts are called CLIC_ILD and CLIC_SiD and shown in Figure 2.6. At first, we will give an exemplary overview on the (barrel) design of the CLIC_ILD and explain its components from the interaction point outwards.

The center of the CLIC_ILD consists of a tracking system that measures the direction and the momentum of charged particles through a determination of the radius of their track bent by a surrounding the magnetic field. Furthermore, the tracking system supports the identification of primary and secondary interaction vertices. It comprises three

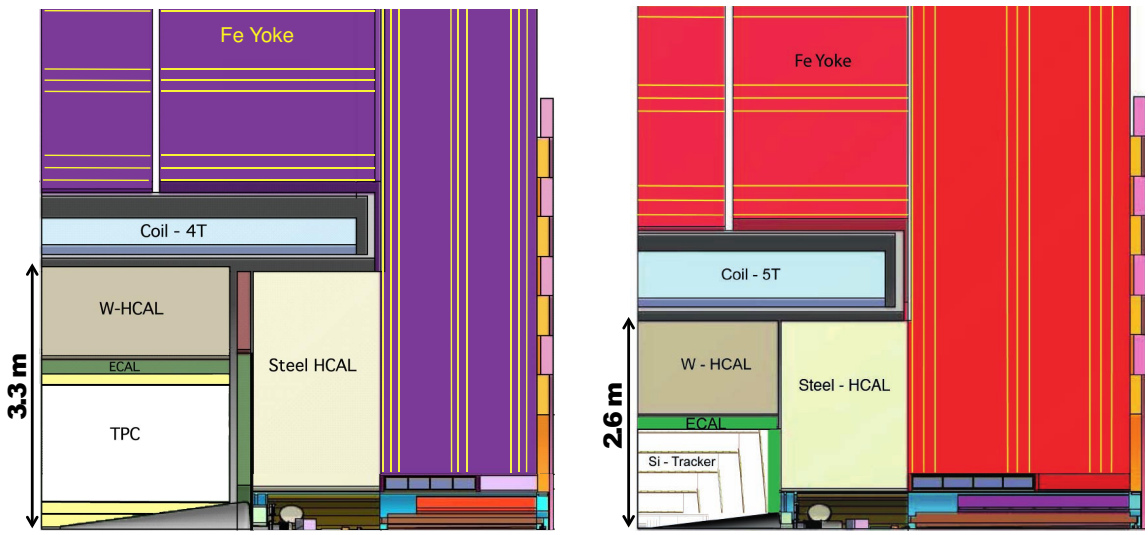

Figure 2.6: Longitudinal cross section of the top quadrant of the CLIC_ILD (left) and the CLIC_SiD (right). Figure from [27].

double layers of a silicon pixel vertex detector (VTX) starting in a distance of 3.1 cm from the interaction point. The VTX is surrounded by a Time Projection Chamber (TPC). As gaseous detector, the TPC has a low material budget and delivers many space points for a precise reconstruction of particle tracks. It allows for a redundant and continuous tracking. The TPC has a large outer radius of 1.8 m which increases the separation of calorimeter energy deposits supporting Particle Flow (see Section 2.4.2). To optimize the achievable momentum resolution, the tracking system is completed by a supplementary silicon detector layer outside of the TPC.

A calorimetric system adjoins the trackers directly. Impinging high-energetic particles, such as e^+, e^- and photons or hadrons, generate particle showers whose energy depositions are measured to reconstruct the energy of the impinging particle. The calorimeters are highly-granular meaning that they are longitudinally and laterally finely segmented such that the calorimetric system comprises in total of the order 10^8 readout channels. The emphasis of the calorimeter design lies on the separation of close-by particle showers. The calorimetric system is subdivided into an inner electromagnetic calorimeter (ECAL) and an outer hadron calorimeter (HCAL). Both calorimeters will be realized as sampling calorimeters (see Section 3.2.4) with alternating layers of active detection and passive tungsten absorber plates. Compared to the HCAL, the ECAL has a higher lateral and longitudinal segmentation to account for the smaller extension of electromagnetic showers. In the current concept, the active layers consist of silicon readout pads with a lateral size of $5.1 \times 5.1\,\mathrm{mm}^2$. The active layers of the HCAL, on the other hand, comprise scintillator cells with a lateral size of $30 \times 30\,\mathrm{mm}^2$. The calorimetric system extends to a radius of approximately 3.3 m. The basics and details of calorimetry are explained in detail in Chapter 3.

The outer part of the detector is occupied by the solenoid generating a homogeneous magnetic field of 4 T and an iron yoke which returns the magnetic flux. For an enhanced

identification capability of high-energetic muons which escape the inner detectors, the return yoke is instrumented with track-sensitive chambers using either the technology of resistive plate chambers (see Section 3.3.1) or scintillator plates (see Section 3.3.3). The total radius of the CLIC_ILD amounts to about 7 m.

The main difference between the detection concept of the CLIC_ILD and CLIC_SiD is the philosophy of the tracking system. In contrast to the CLIC_ILD an all-silicon tracker is planned for the CLIC_SiD which consists of five single silicon pixel layers surrounded by five layers of silicon strips (see Figure 2.6, right). This increases the material budget of the tracking system, but allows for an improved single-hit resolution and a reduction of the overall size of the inner detector. The outer radius of the tracking system of the CLIC_SiD is only 1.3 m. To compensate for the smaller size and keep the momentum resolution comparable, the magnetic field strength amounts to 5 T in the case of the SiD. Unlike the TPC, whose readout is relatively slow such that it needs to integrate all particle tracks over a whole bunch train, an all-silicon tracker can provide a fast charge collection. It can therefore deliver a timestamp for a particle track.

Major changes from the detector design for the ILC compared to CLIC concern the hadron calorimeter and the inner tracking system. The calorimetric system must be hermetic, meaning that a hadronic shower is maximally contained, to guarantee a precise energy measurement of impinging hadrons. The depth of the calorimeter is mostly expressed in terms of its nuclear interaction length λ_I (see Section 3.1.3 for details). Due to the higher center of mass energy at CLIC, the depth of the HCAL is increased from $5.5\,\lambda_I$ to $7.5\,\lambda_I$ in the case of the ILD and CLIC_ILD, respectively. A higher nuclear depth can be either achieved by increasing the total size of the calorimeter or by choosing a more compact calorimeter design. Since the radius of the solenoid is one of the major cost drivers of the whole detector, the second option is favoured and the more dense tungsten is chosen (for the barrel of the CLIC_ILD) over steel (planned for the ILD) as passive absorber material of the HCAL.
At CLIC, the high background contribution from $\gamma\gamma \rightarrow$ hadrons interactions has to be mitigated by a timestamping of particle clusters (identified showers) on the level of 1 ns (see next Section 2.4.2 for details). This is made possible through the fast timing capabilities of scintillation-based particle detection in the HCAL. The silicon-based tracking detectors are somewhat slower, but with further R&D a timestamping precision of approximately 10 ns will be achievable. At the ILC the background conditions are more relaxed and time stamping plays only an minor role due to the higher bunch spacing of $\sim$ 700 ns (see Table 2.1) and the larger dimensions of the beams at the interaction point (474×3.8 nm).
Apart from this, the innermost layer of the pixel vertex detector has to be moved further outwards by 15 mm (from 16 mm for the ILD to 31 mm for the CLIC_ILD) due to the harsher background conditions at CLIC compared to the ILC.

2.4.2 Detector Requirements

The requirements of a detector system for a future e^+e^--collider are driven by the precision physics aims. The Standard Model Higgs mass, for example, can be precisely reconstructed from the Higgsstrahlungs process ($e^+e^- \to ZH$) in the decay of the Z boson into two muons ($Z \to \mu^+\mu^-$). This process defines the track momentum resolution that has to be achieved by the detector. Studies showed that for CLIC, operating at a CME of 500 GeV, it has to be better than $\sigma_{p_T}/p_T^2 \sim 2 \cdot 10^{-5}\text{GeV}^{-1}$ [27]. Many precision measurements at the ILC or CLIC are characterized by multi-jet final states. Jets are sets of particles which are created through the hadronization of e.g. a quark created in the collision which must not exist freely. The jet particles are boosted from the interaction point into an initially common direction. The overall detector design of both ILD and SiD detector versions is governed by the requirement of an excellent jet energy resolution (JER). One goal is that the JER is precise enough to discriminate between the hadronic decays of the W ($W \to qq'$) and the Z boson ($Z \to qq'$) through a reconstruction of the invariant di-jet mass. Figure 2.7 (left) shows the mass distribution of reconstructed W and Z bosons for different assumed mass resolutions. It turns out, that a good separation can be obtained if the mass resolution is better than 2.5 %. This corresponds to a required jet energy resolution of 3.5 % for the entire range of accessible jet energies from 50 GeV to 1 TeV in the case of CLIC at 3 TeV. For example, a distinction between the production channels of heavy supersymmetric neutralinos ($e^+e^- \to \tilde{\chi}_2^0\tilde{\chi}_2^0$) and charginos ($e^+e^- \to \tilde{\chi}_1^+\tilde{\chi}_1^-$), in which the final state corresponds to four jets (hh and hZ in the former, W^+W^- in the latter case) and missing energy ($\tilde{\chi}_1^0\tilde{\chi}_1^0$), would profit significantly from such a good mass resolution and W/Z separation capability (see [27] for details). The necessary performance can be achieved by applying the concept of Particle Flow in the event reconstruction (see next Subsection).
Furthermore, a determination of the coupling of the Higgs to the b- and c-quark depends on the ability to efficiently tag these quarks. Hadrons containing bottom quarks have a lifetime sufficient to travel a certain distance before decaying. With a good impact parameter resolution it is possible to identify particles which originate from a different place than the interaction point indicating the presence of a heavy quark jet. The impact parameter resolution depends on the amount of material used for the inner trackers. Thus, a low material budget is favourable (see [27] for details).
Apart from this, many of the potential channels with physics beyond the Standard Model require a lepton identification efficiency of $> 95\,\%$ and a detector coverage for electrons down to very low angles.

Particle Flow

The currently most promising approach to achieve the highly precise reconstruction of jet energies required at the ILC and CLIC is by an application of the concept of Particle Flow. It is based on the idea to determine the four vectors of individual particles within a jet in the subdetector system that can deliver the best resolution. The reconstructed

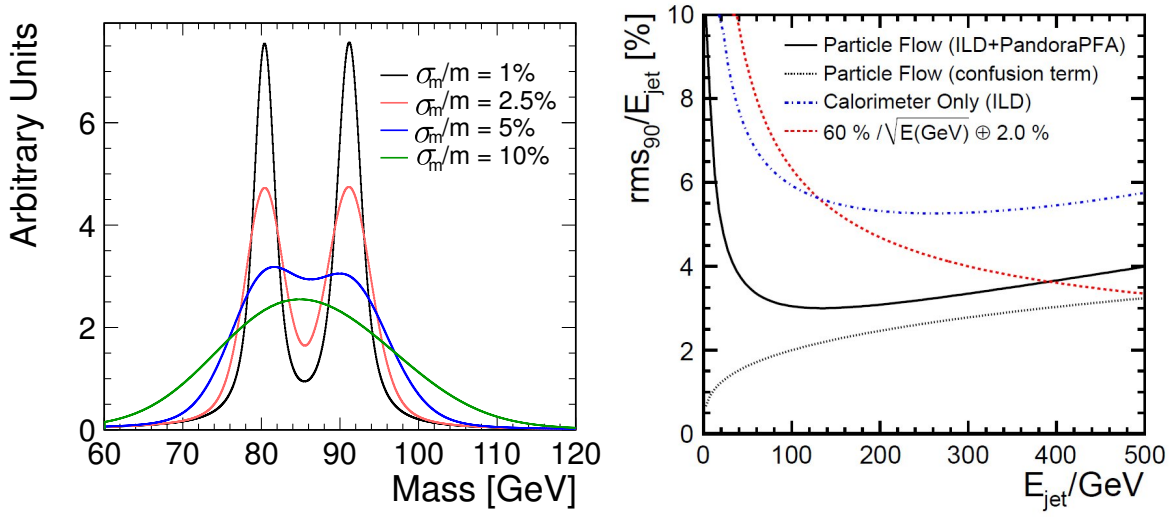

Figure 2.7: Ideal W/Z separation in dependence of the jet mass resolution (left, Figure from [27]). Jet energy resolution in dependence of the jet energy for the ILD (right, Figure from [34]). The Figure shows explicitly the JER of the ILD (solid black line) and the influence of the confusion term (black dotted line) compared to using the total calorimetric energy depositions only (blue dot-dashed line) and to the resolution achievable using a traditional jet energy reconstruction approach (red dashed line).

jet energy is the sum of the energies of the individual jet particles.
Measurements of jet fragmentation at LEP could provide detailed information on the average particle composition of jets [35] [36]. In a typical jet, approximately 62 % of the total energy is carried by charged particles (mainly hadrons), 27 % by photons (originating predominantly from π^0 decays), 10 % by neutral long-lived hadrons and 1.5 % by invisible neutrinos. While these are averages, the jet to jet fluctuations of these values can be substantial. In the traditional approach, the total jet energy is inferred from the energy depositions in the ECAL and the HCAL. The energy resolution of the HCAL is typically rather poor, but it would measure nevertheless about 72 % of the jet particles. The performance goal for the JER would be missed (see Figure 2.7, right). In the Particle Flow approach, the charged jet particles are reconstructed in the tracking system, the photons in the ECAL and only the neutral hadrons (10 % of the jet energy) rely exclusively on the HCAL. Focussing on the tracking system reduces the dependence on hadronic calorimetry and results in the required jet energy resolution over the whole range of accessible jet energies (see Figure 2.7, right, in the case of the ILD).
The Particle Flow approach poses some demands on the overall design of a detector. First of all, the calorimetric system has to be positioned entirely inside the solenoid to minimize the dead material in front of the calorimeters and to be able to detect the whole set of jet particles and associate them correctly with the corresponding jet. The calorimetric energy depositions need to be separated and categorized as belonging to a specific impinging jet particle. For this, the ECAL and the HCAL have to be highly granular. Detailed simulation studies showed that a lateral cell size of $1 \times 1\,\mathrm{cm}^2$ in the ECAL [27] and $3 \times 3\,\mathrm{cm}^2$ in the HCAL [34] are a good compromise between technical

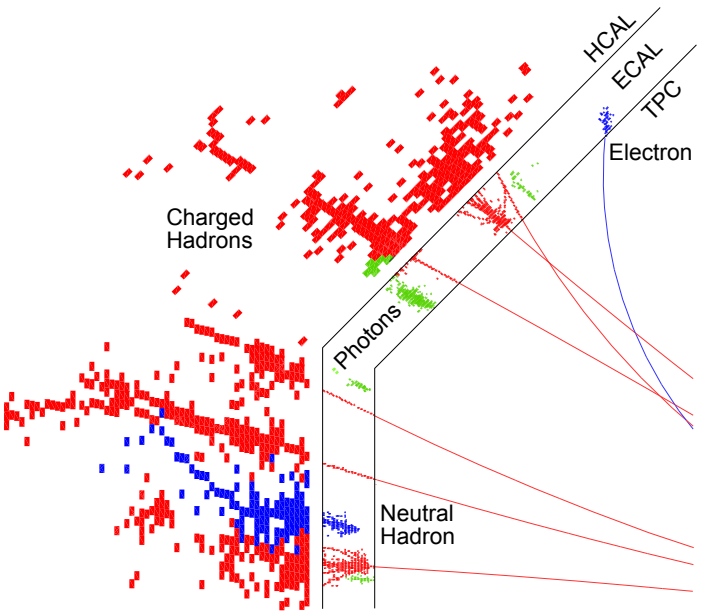

Figure 2.8: Visible energy depositions in a typical jet with an energy of 250 GeV in the CLIC_ILD detector using highly granular calorimeters. The particle types are depicted by the respective labels. Figure from [37].

feasibility and optimal JER. In the case of the HCAL, one would not profit significantly from a smaller cell size if analog energy information for each cell is available. Figure 2.8 shows the visible energy depositions of a typical jet in a detector system optimized for Particle Flow. Sophisticated software algorithms (PandoraPFA) were developed to define calorimetric clusters and assign them to incoming particles. The challenge is to distinguish the energy depositions of hadronic showers induced by neutral or charged hadrons within the HCAL which might overlap for highly boosted jets. The contribution from charged hadrons is to be rejected to measure only neutral hadrons within the HCAL. At jet energies above approximately 100 GeV, the JER is dominated by mistakes in the assignment of energy depositions, also called confusion, rather than the intrinsic resolution of the calorimeters (see Figure 2.7, right).

Timing Requirements

At CLIC, a principal factor for the design of the detector is the need to efficiently identify and reject energy depositions in the calorimeter that originate from beam-induced background. For 3 TeV operation, the integration of the background from $\gamma\gamma \to$ hadrons interactions over a whole bunch train disguises the signatures from interesting physics events significantly and results, on average, in the deposition of 19 TeV of energy in the calorimeters. Figure 2.9 (left) shows an event of the type $e^+e^- \to H^+H^- \to t\bar{b}\bar{t}b$ overlayed with the background from 60 BXs. The fact that the majority of the induced background particles is emitted with low transverse momentum p_T (only 10 % of the total energy is deposited in the barrel calorimeters) and that their

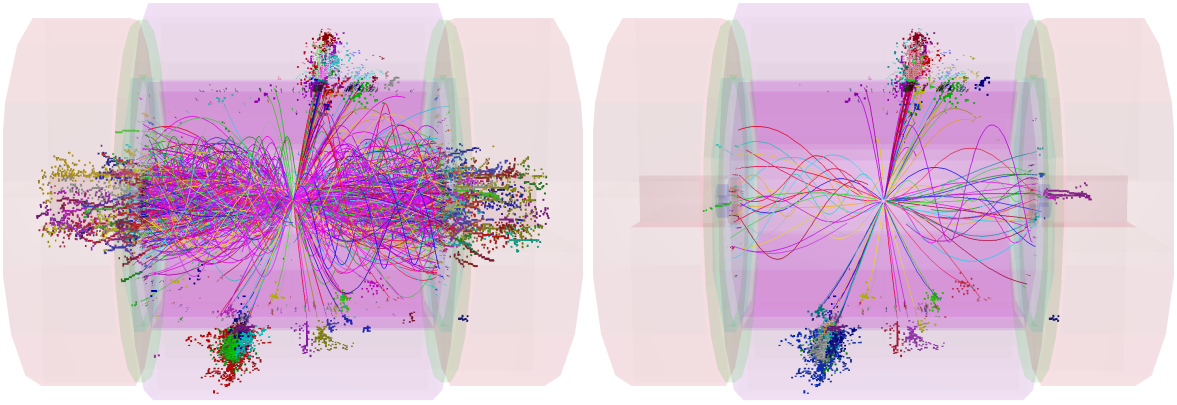

Figure 2.9: Event display of a simulated $e^+e^- \to H^+H^- \to t\bar{b}\bar{t}b$ event overlayed with the background from $\gamma\gamma \to$ hadrons interactions of 60 bunch crossings (left) and the effect of applying tight (p_T and time) selection cuts on the reconstructed Particle Flow objects (right). The Figures show the CLIC_ILD at a collision energy of 3 TeV. All particles are reconstructed for a time window of 10 ns (100 ns in the HCAL barrel). Figures from [27].

occurrence spreads evenly over the whole bunch train and is proportional to the number of superimposed BXs allows for the application of sophisticated reduction methods. Two competing effects have to be taken into account here: The desire for a maximal background rejection suggesting an event integration over a very small time window and tight p_T cuts on the one hand, and the finite time evolution of hadronic showers and the time of flight of lower momentum particles suggesting a very long time window and looser p_T cuts on the other hand. We will elaborate this in the following.
The most obvious way to reduce the background that overlays a physics event is to use the time stamps of the detector hits and associate them to a small range of BXs within a bunch train. A generator level study of the W boson mass resolution in the decay $W \to q\bar{q}$ superimposed by a various number of BXs suggests that the acceptable level of background corresponds to 5-10 BXs or an integration time of < 5 ns [27]. But this neglects the contribution of delayed shower particles within hadronic cascades which originate from nuclear processes that occur on a timescale significantly longer than 5 ns. Thus, the application of a too stringent time cut can deteriorate the HCAL energy resolution and eventually the jet energy resolution.
A two-stage approach has been adopted. If the signature of an interesting physics event is identified within a bunch train, initially a window of 10 ns for the tracking systems and 100 ns for the barrel calorimeters is defined around this time. The data is passed to the offline event reconstruction. The most precise time stamping on the level of 1 ns can be achieved for calorimeter hits. All cell hits belonging to an identified calorimeter cluster are weighted with the deposited energy. The truncated mean of the energy weighted hit time distribution is then defined as the cluster time. If the particle was charged, the cluster is associated with the corresponding track from the TPC (which integrates over a whole bunch train) and (or) the silicon-based detectors (with a time stamping

resolution of $\sim 10\,\text{ns}$). The tightness of the applied timing cut depends on the p_T of the reconstructed particles. The effectiveness of this cluster timing based background rejection is shown in Figure 2.9 (right). The energy deposited by $\gamma\gamma \rightarrow$ hadrons background is reduced from 1.2 TeV to approximately 100 GeV with negligible impact on the underlying physics event. Apart from this time stamping supported event reconstruction, the integration time window for the energy reconstruction of hadrons in the barrel calorimeters is driven by the intrinsic shower development time and could be extended up to 100 ns. The time development of hadronic showers in tungsten is subject to further R&D studies and will be discussed and analyzed in detail in the next chapters of this thesis.

Chapter 3

Calorimetry in High Energy Physics

The word calorimeter originates from the Latin word "calor" meaning heat. Historically, calorimeters were used to study exothermal chemical reactions by measuring the increase in temperature of a water bath surrounding the interacting substances with precise thermometers. Although the denotation stayed the same, it is not the heat that is measured within the calorimeters used in high energy physics. In modern particle calorimeters, the energy of an impinging charged or neutral particle is measured through its absorption by the surrounding calorimeter material. But it is the sum of photons or ionization charges generated by the multiple interactions in this absorption process which is actually detected. Ideally, this total signal sum is then proportional to the initial energy of the impinging high energetic particle.
In this chapter, we will develop an in depth view of calorimetry in particle physics. First, we will study the physics of particle showers, the various interactions contributing for the different particle sorts within different materials and the consequences for the detection of the respective particles. We will then present some approaches for the design of modern particle calorimeters and the instrumentation and technology needed for the detection of signals. Finally, we discuss the requirements of a calorimeter specifically designed for a future linear collider experiment and present details on some of the existing prototypes. In all sections, we refer to aspects important for the time resolved measurement of particle showers in calorimetry.

3.1 The Physics of Particle Showers

When highly energetic particles encounter a dense material they are subject to a multitude of different interactions governed by the electromagnetic, strong and sometimes also the weak force. Which interaction is relevant for the impinging particle and the mechanism of how its energy is distributed and eventually absorbed depends on the nature of the particle and the encountered material. A fundamental difference in the behaviour can be observed for purely electromagnetically interacting particles (such as

electrons, positrons or photons) and hadronic particles (such as protons, neutrons etc.). The latter are subject to nuclear interactions with the constituents of the absorbing material which has far-reaching consequences for the design of a calorimeter. In this section, we discuss the characteristics of the shower development of the different particle sorts together with their implications for the design of a calorimeter in high energy physics.

3.1.1 The Passage of Charged Particles through Matter

All charged particles are subject to electromagnetic energy losses on their passage through an absorber material. The two most important mechanisms are ionization losses and losses through the emission of bremsstrahlung. The former is predominant for the majority of muons and hadrons created at accelerator based experiments, while radiative losses are most relevant for impinging electrons or positrons.

Ionization Losses

When a charged particle traverses an absorber, energy losses are induced by the excitation and ionization of hull electrons bound to atoms of the absorber material. The Bethe-Bloch equation describes the mean energy loss dE per unit length dx that a particle of charge ze deposits in an absorber of atomic number Z and atomic mass A by these processes (elaborations of the Bethe-Bloch formula follow [14] closely):

$$-\left\langle \frac{\mathrm{d}E}{\mathrm{d}x} \right\rangle = Kz^2 \frac{Z}{A} \frac{1}{\beta^2} \left(\frac{1}{2} \cdot \ln \left(\frac{2m_e c^2 \beta^2 \gamma^2 T_{\max}}{I^2} \right) - \beta^2 - \frac{\delta(\beta\gamma)}{2} \right), \tag{3.1}$$

Here:

K	$= 4\pi N_A r_e^2 m_e c^2$ with the classical electron radius $r_e = e^2/4\pi\epsilon_0 m_e c^2$
ze	charge of incoming particle
A	atomic mass of absorber
Z	atomic number of absorber
m_e	electron mass
β	$= \frac{v}{c}$
γ	$= \frac{1}{\sqrt{1-\beta^2}}$
$T_{\max}$	maximum kinetic energy transferred to a free electron in a single collision
I	mean excitation energy
δ	density correction factor

Figure 3.1 shows the energy loss distribution of muons traversing copper as absorber material. The range between $0.1 \lesssim \beta\gamma \lesssim 1000$, the so-called Bethe range, is described by the Bethe-Bloch equation with an accuracy of a few percent. The energy loss $\frac{dE}{dx}$ is high for low particle energies. It decreases to a broad minimum around $\beta\gamma \approx 3 - 4$. Particles with an energy in this range are called minimum ionizing particles (MIPs).

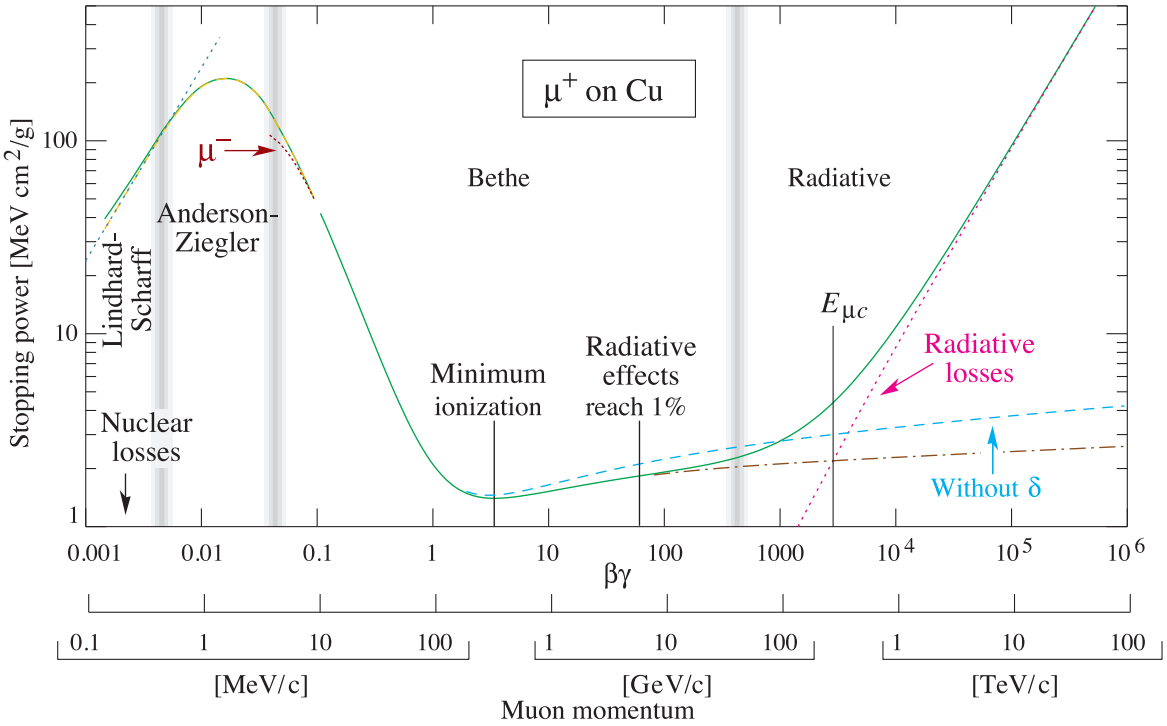

Figure 3.1: The energy loss of muons in copper is described by the Bethe-Bloch formula [17]. The point of minimum ionization is at $3 - 4\,\beta\gamma$. At this energy the muon looses about $1 - 2\,\frac{\text{MeV cm}^2}{g}$.

Due to this well-defined energy deposition, MIPs are often used for detector calibration. After this minimum the energy loss increases slightly which is called relativistic rise. An additional high energy correction originates from a polarisation of the absorber medium that shields the electric field of a charged particle which traverses at relativistic energies. This is accounted for by the Sternheimer correction function $\delta(\beta\gamma)$.
The Bethe-Bloch equation describes only the mean energy loss of a charged particle per path length. But the energy loss is a stochastic process: A charged particle crossing matter is subject to many individual interactions with the electrons of the absorbing material. The energy transfer per interaction varies substantially from event to event, a property referred to as energy straggling. If the absorber material is thick the energy deposition will follow a Gaussian distribution. This is due to the Central Limit Theorem which states that the sum of a sufficiently large number of independent random variables (in our case the many interactions with the absorber atoms) is normally distributed.
If the absorbing material is thin (i.e. if the number of collisions is too small for the Central Limit Theorem to hold), which is usually the case for the sensitive detector layers of a sampling calorimeter (explained in Section 3.2), the situation is more complicated. The energy loss probability of a traversing particle follows approximately a Landau-Vavilov distribution (the improved Bichsel distribution does also respect the density correction $\delta(\beta\gamma)$, see Figure 3.2) [17]. The region around the peak of the distribution is nearly Gaussian distributed. But it has a long tail which corresponds to an increased

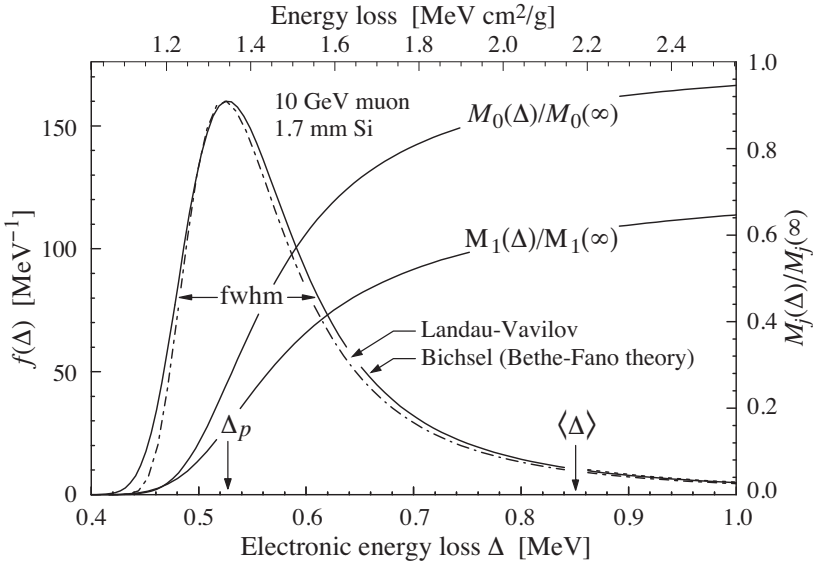

Figure 3.2: Electronic energy deposit distribution for a 10 GeV muon traversing 1.7 mm of silicon, the stopping power equivalent of about 3 mm of PVC scintillator [17].

probability of high energy transfers. In distinct collisions, atomic electrons can acquire so much energy that they leave a long ionizing trace, depositing energy high above average (so-called δ-electrons). Furthermore, there is a finite probability for a very high "one-shot" energy loss which makes the tail of the distribution even longer. Due to these fluctuations the most probable value (MPV) and the mean value of the distribution do not coincide.

Radiative Losses and the Special Role of Muons

Bremsstrahlung occurs when a charged particle is deflected by the electric field of the atomic nuclei of the absorber. In this process, the particle looses a fraction of its energy which is radiated away through the emission of a photon. The energy spectrum of the emitted photons falls of as $1/E$ [38]. In principle, a particle could loose almost all of its kinetic energy through the emission of one bremsstrahlung photon, but for the majority of interactions the fractional energy loss is small.
The radiative energy loss per unit length dE/dx through bremsstrahlung increases linearly with the particle energy, whereas ionization losses increase only logarithmically [39]. For muons, radiative losses become dominant at very high energies above $\beta\gamma \approx 1000$ or above muon momenta of a few hundred GeV (see Figure 3.1). The transition between the two competing effects is characterized by the critical energy E_c. This is the particle energy at which the average ionization losses equal the energy losses from radiative processes. Since the emission probability for bremsstrahlung is proportional to the inverse square of the particle mass, the critical energy is $(m_\mu/m_e)^2 \approx 40.000$ times smaller for electrons and bremsstrahlung becomes already dominant at particle energies above ~ 100 MeV (depending on the absorber type). Thus, electrons can easily trigger

electromagnetic cascades and loose most of their initial energy within a short distance travelled in an absorber (see next Section 3.1.2).
This underlines the special role of muons. For most muons created at particle accelerator experiments, energy losses through bremsstrahlung can be neglected due to their relatively large mass. Due to their leptonic nature, muons are not affected by the strong force and do not induce nuclear interactions with the absorber nuclei. So the only relevant energy loss mechanism is ionization which amounts to only $1 - 2\,\mathrm{MeV} \cdot \mathrm{cm}^2/\mathrm{g}$ (e.g. 1.1 GeV/m in iron). High energetic muons have an extremely large penetration depth and a relatively long lifetime of $2.2\,\mu$s [17]. Since the calorimeters used in large scale detectors have a thickness of usually only a few meters, muons have a high probability to escape without decaying. The calorimetric signals induced by muons follow a well-defined distribution of energy deposit and occur quasi-instantaneous (apart from their time of flight). They therefore represent a good reference for the response of active detector components and are usually used for calibration purposes. The measured signals of e.g. hadronic showers can be studied relative to the standard signal of muons for a given detector technology.

3.1.2 Electromagnetic Showers

The energy loss mechanisms governed by the electromagnetic force are well-described by the theory of Quantum Electro-Dynamics and can be calculated with high precision. It is therefore possible to make relatively accurate predictions and develop reliable electromagnetic shower models. Such models (electromagnetic and hadronic, see Section 3.1.3) are used in Monte-Carlo simulations to parametrize how showers evolve within different absorber materials.
Electromagnetic cascades are initiated by electrons (positrons) or photons, but the nature of the first electromagnetic interaction is intrinsically different. For high energetic electrons, the most probable process is the creation of a photon through bremsstrahlung, whereas for high energetic photons, the relevant process is the production of an electron-positron pair. Below a photon energy of $\sim 1\,\mathrm{MeV}$, which is equivalent to the rest mass energy of an electron-positron pair, the dominant processes are Compton scattering and the Photo Effect. The cross sections of the respective processes depend, among others, on the electron density (and therefore on the atomic number Z) of the traversed absorber.

Pair Production: For energies of $> 1\,\mathrm{MeV}$, a photon may produce an electron-positron pair in the electromagnetic field of an absorber nucleus. It becomes the dominant process above $5 - 10\,\mathrm{MeV}$ in the most common absorbers. The cross section for Pair Production σ_{pair} rises with energy and reaches a plateau at photon energies of the order of 1 GeV.

Compton Scattering: Compton scattering plays a role in an intermediate energy range between $\sim 100\,\mathrm{keV} - 5\,\mathrm{MeV}$. The cross section $\sigma_{compton}$ scales with the energy as $1/E$. The fact that more than 1/2 of the total energy of a high energetic

Absorber	ρ [g/cm^3]	X_0 [cm]	R_M [cm]	λ_I [cm]	λ_I/X_0	$\Delta E_{ioniz.}/\lambda_I$ [MeV/cm]
Fe	7.87	1.76	1.69	16.8	9.55	90.9
W	19.3	0.35	0.93	9.6	27.43	162
Pb	11.3	0.56	1.6	17	30.36	173

Table 3.1: Key properties of different absorber materials relevant for calorimetry [38]. The average energy loss of minimum ionizing hadrons is shown by the rightmost column. See text for more details.

($\mathcal{O}(1\,\text{GeV})$) impinging photon or electron is absorbed within the electromagnetic cascade by Compton scattering underlines its importance [38]. In the process, a photon scatters with one atomic shell electron passing a fraction of its energy to it. In the following, the electron is unbound and continues the passage - like the scattered photon - through the absorber. In electromagnetic cascades, the photon energy is reduced in a sequence of Compton scatterings until it can be absorbed by the Photo Effect.

Photoelectric Effect: The Photo Effect is dominant at low photon energies. Within the most common absorbers, the cross section σ_{photo} for the Photo Effect exceeds all other effects at photon energies below $0.1 - 1\,\text{MeV}$ (e.g. for $< 0.7\,\text{MeV}$ in Uranium and for $< 0.1\,\text{MeV}$ in Iron) [38]. Note that σ_{photo} decreases rapidly with increasing energy as E^{-3}. In the process, the photon is absorbed by the atomic shell of an absorber atom which gets excited and releases this excess by the emission of an electron.

Scaling Variables of Electromagnetic Showers

The dimensions of an electromagnetic shower within a certain absorber material are characterized by the radiation length X_0 and the Molière Radius R_M. X_0 is defined as the average distance z over which the energy of a high energetic electron or positron ($> 1\,\text{GeV}$) is reduced to $1/e = 36.8\,\%$ due to bremsstrahlung:

$$E = E_0 \cdot exp(\frac{-z}{X_0}) \tag{3.2}$$

In the case of photons, it is $^7/_9$th of the mean free path before another pair production process occurs [38]. The radiation length X_0 depends on the atomic number Z of the traversed absorber. In iron it amounts to 1.76 cm, while it is only 0.56 cm in lead (see Table 3.1).
The Molière Radius R_M describes the transverse extension of electromagnetic showers. In an empirical parametrization it can be estimated as:

$$R_M = 21.2\,\text{MeV} \cdot \frac{X_0}{E_c}, \tag{3.3}$$

where E_c is the critical energy. On average, 90 % of the total energy of an electromagnetic shower is contained within a cylinder with radius R_M around the lateral impact position of the impinging particle. Note that R_M scales differently in different absorber materials relative to X_0. While the radiation length is more than 3 times longer for iron compared to lead, the Molière Radius is approximately equal.

The Development of Electromagnetic Showers

When a highly energetic electron (or positron) enters a dense absorber it may radiate thousands of photons through bremsstrahlung. While the majority of those photons is low-energetic and gets absorbed, a small fraction carries a substantial amount of energy. Such photons create further electrons and positrons through pair production, which in turn generate more photons through bremsstrahlung. This multiplication process initiates the electromagnetic cascade. The shower energy is deposited through the ionization of the traversed medium.
At a certain depth after the starting point of the electromagnetic cascade, the number of shower particles created per unit length and consequently the amount of deposited energy reaches a maximum and decreases afterwards. At lower energies, photons are more likely to produce one instead of two particles through Compton scattering or the Photo Effect. Electrons (or positrons) tend to deposit their energy through the ionization of the surrounding medium instead of generating new photons. Low energetic positrons annihilate with electrons of the absorber atoms and generate two photons ($E_\gamma = 511\,\mathrm{keV}$) which loose their energy through a series of Compton scatterings ending with the photoelectric absorption. Eventually, the remaining low energetic electrons get absorbed by the traversed medium and the electromagnetic cascade ceases. Figure 3.3 (left) shows a simplified schematic of the development of an electromagnetic shower.
Note that a high fraction of the total shower energy is deposited through relatively low energetic electrons and positrons (e.g. $\sim 40\,\%$ for energies of $< 1\,\mathrm{MeV}$ and $\sim 65\,\%$ for $< 4\,\mathrm{MeV}$ in uranium). Furthermore, one finds that approximately one quarter of the total energy is deposited by shower positrons and three quarters by electrons [38]. Together, this corroborates the assumption that most of the shower energy is deposited through electrons created through Compton scattering and the Photo Effect and that these are the most abundant processes in electromagnetic cascades.

3.1.3 Hadronic Showers

In contrast to electromagnetic showers, hadronic showers are dominated by nuclear interactions of the hadronic projectiles with the absorber nuclei and therefore largely influenced by the strong force. The multitude of processes that contribute to the hadronic cascade and the variety of different particle types that can be created, most of which behave very differently within the absorber material, complicate the fundamental understanding hadron showers significantly (see Figure 3.3). Within the hadronic cascade, some of the initial energy is deposited through hadrons, some electromagnetically

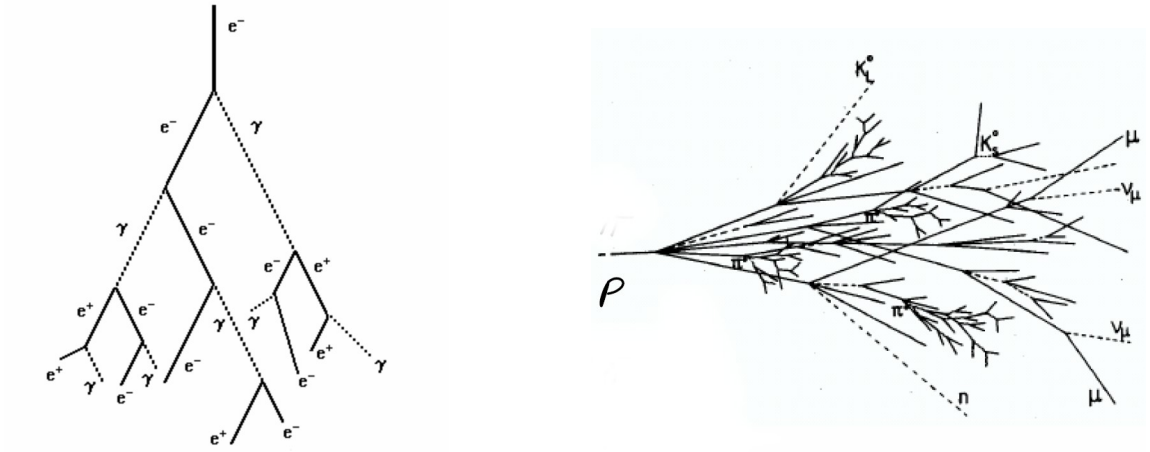

Figure 3.3: Schematic example of a particle shower in case of an electromagnetic (left) or hadronic (right) cascade [40].

and some of it is completely lost for calorimetric detection. The event-to-event fluctuations of the respective fractions are large and pose an intrinsic limit to the achievable performance of hadronic calorimeters. In the following, we investigate the key processes within hadronic cascades and their respective contributions.

Ionization Loss of Charged Hadrons

Figure 3.4 shows a simplified sketch of relevant aspects for the development of hadronic showers. At first, a e.g. high energetic proton that encounters an absorber material looses energy through ionization. The average distance the proton travels before it undergoes a nuclear interaction is defined by the nuclear interaction length λ_I which depends on the type of the absorber material (see Table 3.1) and amounts to e.g. 16.8 cm in iron or 9.6 cm in tungsten. In other words, the probability that the proton travels a distance of z within the absorber without causing a nuclear interaction can be expressed as:

$$P = exp(\frac{-z}{\lambda_I}) \tag{3.4}$$

Note that the hadronic shower start can be defined as the longitudinal position of the first nuclear interaction. The amount of energy the impinging proton looses until this point does also depend on the absorber type and increases with its atomic number. It is e.g. 90.9 MeV/λ_I for Iron and $\sim$ 1.8 times higher for tungsten (see Table 3.1). The situation is slightly different for high-energetic impinging pions for which the cross section for nuclear interactions is reduced. This is related to the reduced size of a pion whose charge radius is significantly smaller than for the proton [41] [42]. It travels typically a $25 - 50\,\%$ longer distance within the absorber before it undergoes a nuclear interaction [38]. This is the reason why the nuclear interaction probability of a pion has to be defined through the pion interaction length λ_π instead of λ_I.

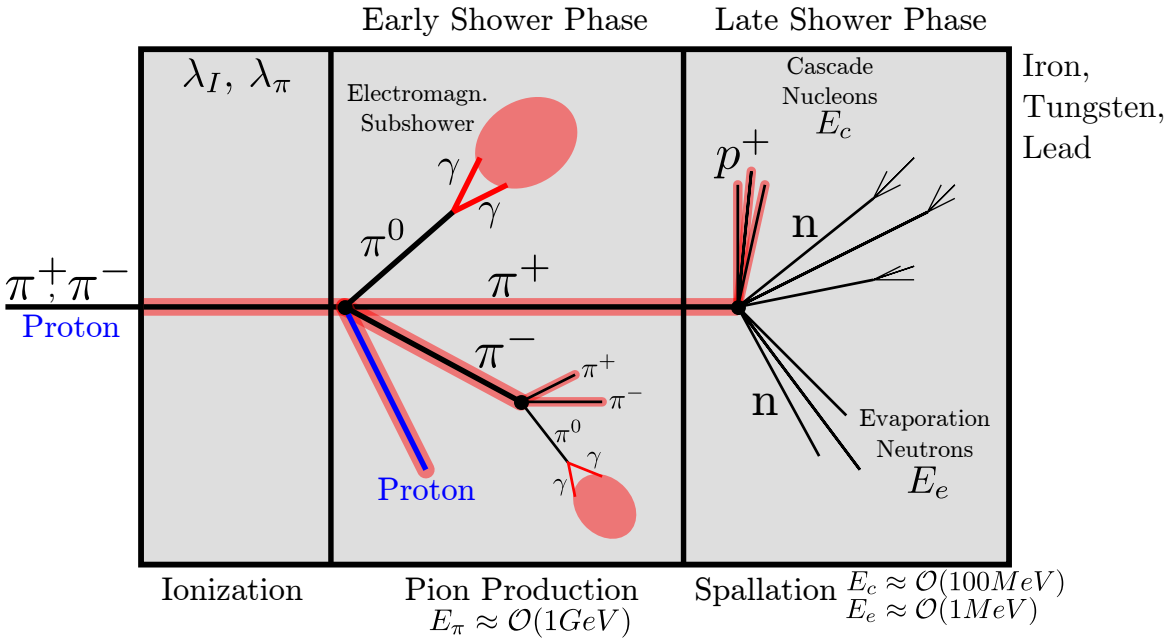

Figure 3.4: Simplified sketch of interactions within hadron cascades. After a charged hadron entered the absorber it looses energy through ionization of the surrounding medium (red), creates pions through partonic interactions in the early shower phase and releases nucleons in the late shower phase. If the impinging particle is a proton, a baryon has to emerge from the partonic interaction (blue). The depicted sequence of interaction phases is to be understood chronologically in the shower development, not spatially.

General Hadronic Shower Development

The hadronic shower starts after the first nuclear interaction occurred. The particles produced by this initial interaction (mesons, nucleons, γs) can in turn loose their energy through ionization processes and undergo further nuclear reactions. As the hadronic cascade develops, the number of generated particles is multiplied and the amount of energy the shower deposits increases. At a certain depth within the absorber, a maximum is reached and the multiplication is balanced by the absorption of shower particles within the absorber material. The particle absorption takes gradually over until the hadronic cascade eventually ceases. In a calorimeter this manifests in the longitudinal shower profile which is characterized through a steep rise in the detected energy deposition followed by a less steep decay.

The Electromagnetic Fraction of Hadronic Showers

In the early phase of the shower development, when the hadronic shower particles have still energies of $> \mathcal{O}(1\,\mathrm{GeV})$ (dependent on the absorber material), interactions between a hadronic shower particle and an absorber nucleon are energetically possible

on a partonic level and result primarily in the production of pions [38]. On average, approximately one-third of the mesons produced in these partonic interactions are π^0s which decay with an extremely short lifetime of 8.4×10^{-17} s into two photons [17]. These photons form an electromagnetic subshower within the cascade and are irrevocably lost to the hadronic fraction of the cascade. The electromagnetic energy fraction f_{em} of hadronic showers is subject to large fluctuations and depends predominantly on the nature of the first few interactions. Furthermore, f_{em} is dependent on the energy of the impinging particle. This can be understood by a somewhat oversimplified view: If one-third of the initial energy is converted to f_{em} in the initial nuclear interaction and one-third of the remaining two-thirds of energy is converted to f_{em} in the second generation of nuclear interactions and so on, then the total electromagnetic energy fraction scales with the number of generations n of nuclear interactions above the pion production threshold E_0 (remember $> \mathcal{O}(1\,\mathrm{GeV})$) that are accessible with the energy E of the impinging particle. Extensive simulation studies showed that with a more realistic scenario f_{em} can be parametrized in the following way [43]:

$$f_{em} = 1 - (\frac{E}{E_0})^{k-1} = 1 - < m >^{n \cdot (k-1)}, \tag{3.5}$$

where the exponent k depends on the average number of mesons $< m >$ and the average fraction of π^0s produced per interaction (the latter was chosen to be one-third in the oversimplified model). Note that k is always < 1. With this formula and sufficient knowledge on the properties of an absorber, one can calculate that the electromagnetic shower fraction increases from 0.54 (0.48) at 50 GeV to 0.64 (0.60) at 200 GeV within a copper (lead) absorber environment.
Furthermore, it turns out that f_{em} depends on the atomic number Z of the absorber material. For example, f_{em} decreases from 61 % in aluminium down to 52 % for lead for hadron showers induced by 100 GeV pions [43]. This can be explained by the increased ionization losses in high-Z materials (see Table 3.1, right). If a larger fraction of the incident energy is lost through ionization, the number of accessible generations above the pion production threshold decreases and so does f_{em}.
With Equation 3.5, it can also be understood that the electromagnetic fraction is smaller for protons than for pions impinging with the same energy. If a proton undergoes a partonic interaction in the early shower development, a baryon has to emerge in the final state due to baryon number conservation. This is true for the first and all consecutive generations of partonic interactions. Consequently, less energy is transferred to the mesonic part of the shower and since the electromagnetic fraction of hadron showers is primarily generated by the decay of π_0s, f_{em} is in total reduced. In general, f_{em} is of the order of 15 % smaller for protons than for pions and there are no indications of an energy dependence of this effect [43].

Nuclear Spallation within Hadronic Showers

To get a rough estimate of the distribution of the initial particle energy onto the different sectors we learned so far, we will have a closer look at 100 GeV pions showering in copper

(details can be found in [38]). Here, f_{em} amounts to 60 %, so 60 GeV are deposited through electromagnetic subshowers. In copper, E_0 is 0.7 GeV, so approximately $40/0.7 \approx 58$ hadrons (which are not π_0s) can be created in the early shower phase, each of which looses on average 150 MeV through ionization. This amounts to ≈ 9 GeV deposited through ionization losses. The remaining $\approx$ 31 GeV of available shower energy are used to excite and dissociate the nuclei of the absorber material. As shown above, these quantities are dependent on the incident particle type, its energy and the absorber type (i.e. its atomic number). We will now have an in-depth look into the non-electromagnetic shower fraction.

When a high energetic hadron interacts with a nucleus of the absorber material, it will most likely dissociate it. This process is called spallation and can be subdivided into a fast intranuclear cascade occurring within the first few nanoseconds and a slow nuclear evaporation phase.
At first, the incident hadron undergoes a number of quasi-free collisions within the nucleus in which it passes a fraction of its energy to the nucleons which in turn distribute their energy to further nucleons and so on. In this initial phase, a cascade of fast nucleons develops, which can escape the struck absorber nucleus. Apart from the early shower phase, in which partonic interactions occur inducing the creation of unstable mesons (see above), the intranuclear cascade results predominantly in the creation of protons and neutrons. The ratio of released protons to neutrons reflects their numerical presence within the absorber nucleus. So e.g. for tungsten, 1.49 times more cascade neutrons than protons are released, while for iron, the ratio is only 1.15. If we assume (somewhat simplified) that the pion production threshold E_0 - which is of the order of 1 GeV - is the energy scale for the average hadron produced in the non-em component of the initial shower development phase, then the released cascade protons and neutrons carry at maximum a kinetic energy of $\mathcal{O}(100\,\text{MeV})$ (in lead, see [38]). At this energy, the penetration depth of protons within dense absorbers (such as iron or lead) is significantly lower than λ_I, so they are unlikely to carry the nuclear cascade further, but become stopped and incorporated into the absorber structure. The released cascade neutrons, on the other hand, are not subject to ionization losses and initiate further spallation reactions which become in each following generation less energetic.
In the second slow phase of the spallation, the evaporation phase, the nucleus de-excites its remaining energy releasing a number of low energetic evaporation nucleons. This is energetically allowed until the excitation energy is less than the binding energy per nucleon. Protons are less likely to be created within this phase than neutrons, because unlike neutrons the charge carrying protons have to overcome the nuclear coulomb barrier in addition. The extent of this proton neutron asymmetry depends sensitively on the height of the coulomb barrier of different absorbers. After a few nanoseconds, when the initial cascade phase has ceased, almost all neutrons present within the hadron shower are soft evaporation neutrons. The kinetic energy spectrum of these thermal neutrons follows a Maxwell-Boltzmann distribution with an average kinetic energy of 3 MeV [38]. Unlike the other particles a hadron shower consists of (such as pions, protons etc.), these soft evaporation neutrons behave very differently within a dense material. Their interactions can be significantly delayed up to several hundreds of nanoseconds,

and they can carry a significant portion of the total energy contained within the non-em fraction of the hadron shower.
Investigating the fractional energy deposit of the non-em part of the shower for the several mechanisms discussed above, one finds that about 50 % of the energy is deposited through ionization (primarily by cascade protons) while around 35 % is lost for calorimetric detection [38]. This invisible energy is largely emphasized for absorbers with high atomic number (see next Section). The total kinetic energy carried by evaporation neutrons ranges between $5-15$ % and depends sensitively on the absorber material. For example, it is about 50 % higher in lead compared to iron and also the neutron abundance is very different. In lead, the number of created evaporation neutrons is ~ 6 times higher than in iron [38]. The neutron content can have detrimental consequences for the performance of a calorimeter equipped with high-Z absorber material if e.g. the sensitive detector material is not suited for the detection of neutrons or the products created in their absorption or if the time window over which a hadron shower is integrated has to be chosen very short. The drastically increased abundance of evaporation neutrons within a hadronic shower developing in high-Z absorbers can be explained by three considerations:

The nuclear binding energy: For high-Z material, the nuclear binding energy per nucleon is lower. In lead, for example, it is 7.9 MeV (for Z=82) and 8 MeV in tungsten (for Z=74) while it amounts to 8.8 MeV (for Z=26) for iron [44]. Therefore, it takes less energy to release a nucleon and in total, a larger number of nucleons can be released in higher-Z material to de-excite the same amount of energy contained within the nucleus.

The proton/neutron asymmetry: High-Z materials exhibit a strong asymmetry between the evaporative emission of neutrons and protons. This effect can be attributed to differences in the height of the coulomb barrier which protons have to overcome when leaving a nucleus. The height of the coulomb barrier is proportional to $Z/A^{1/3}$ (where A is the mass number) [19] and therefore 1.9 (2) times larger for tungsten (lead) compared to iron. As a result, the probability for evaporating a proton or a neutron is not very different for iron, but for lead or tungsten it is. So the neutron/proton ratio of nucleons emitted by a nucleus with a certain excitation energy is drastically increased for high-Z materials. The asymmetry is even more emphasized by the fact that emitted neutrons can induce further spallation reactions which create even more neutrons while protons are usually absorbed very quickly.

Re-interaction within the nucleus: In the intranuclear cascade evolving in a nuclear interaction, the energy of struck nucleons is distributed to other nucleons. If the nucleus is larger (i.e. has a higher mass number), a higher fraction of the deposited energy is distributed within the nucleus. This contained energy is released in form of evaporation nucleons instead of fast cascade nucleons. So for high-Z materials ($\rightarrow$ high A) a higher fraction of nucleons is emitted in the evaporation than in the cascade phase.

Unlike cascade nucleons which are boosted in the direction of the impinging particle, evaporation neutrons are emitted isotropically by an excited nucleus. In addition, the mean free path of e.g. 1 MeV neutrons is orders of magnitudes higher than that of charged particles. In lead, for example, it is ~ 6 cm for neutrons, < 1 mm for electrons and $< 10\,\mu$m for protons [38]. So evaporation neutrons can in principle create energy depositions in distant areas of the calorimeter which the charged part of the hadron shower did not even access. Thus, they dominate the tails of the longitudinal and lateral profile of hadronic showers.

Energy Lost for Detection

The total amount of invisible energy is primarily correlated with the total number of released nucleons since the nuclear binding energy that has to be spent is to a large extent lost for calorimetric detection. This, together with the lower binding energy per nucleon, results in a by about 20 % higher fraction of invisible energy for lead compared to iron [38]. A part of this lost energy can be gained back if the sensitive detector material is capable of measuring the particles emitted after the neutrons were captured by the absorber (see next Section).
Due to momentum conservation, the forward boost of the emitted cascade nucleons induces a recoil of the struck nucleus. This form of energy deposition is irrevocably lost for detection. It only "heats up" the absorber material.
Minor contributions arise from particles that can escape the calorimeter and carry away their share of the shower energy. Examples are muons created within the cascade or neutrinos that arise from the decay of instable mesons. Note that in hadronic showers, all discussed mechanisms are subject to large event-to-event fluctuations and that the given hierarchy is just valid on average.

Absorption Mechanisms for Evaporation Neutrons

The kinetic energy of evaporation neutrons is Maxwell-Boltzmann distributed with a high-energy tail and an average energy of 3 MeV. When the neutron energy is significantly higher than the binding energy per nucleon (in the order of 8 MeV for most absorbers), spallation reactions are energetically allowed. However, the majority of evaporation neutrons carries an energy that is significantly smaller than this. The dominant processes before the final absorption of the neutrons depend on their kinetic energy (see Figure 3.5).
At kinetic energies above $\sim$ 1 MeV **inelastic neutron scattering** is the relevant process. A neutron collides with an absorber nucleus and spends a part of its kinetic energy to excite it. In the following, the nucleus emits the transferred energy in the form of one or more photons that are detectable by a calorimeter. Another contributing inelastic scattering process is the emission of α-particles which can be released from the nucleus by neutrons impinging with an energy in the range of $3 - 20$ MeV [38]. The cross section for this process is maximal for carbon-rich materials, like polystyrene

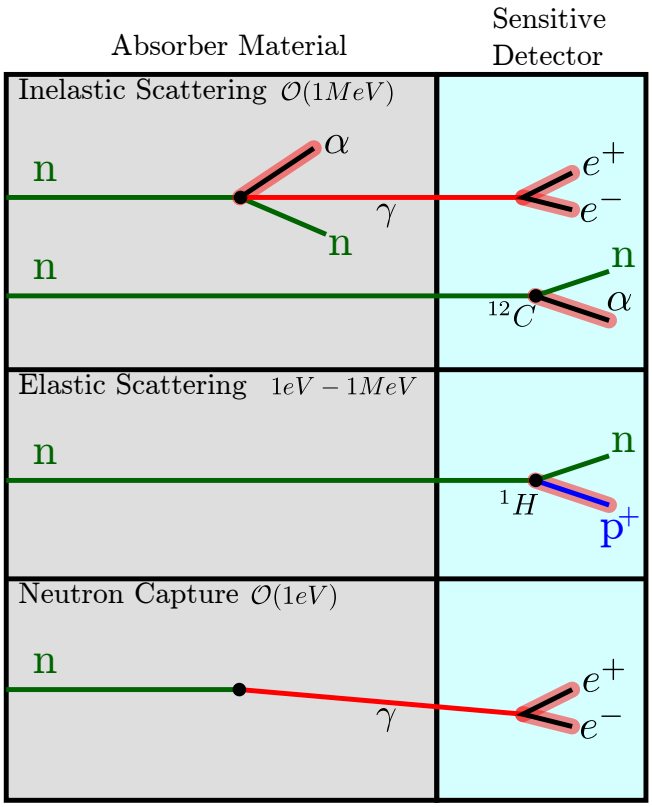

Figure 3.5: Simplified sketch of the interaction of evaporation neutrons with the absorber and the sensitive detector material before their final absorption. Particles which are subject to ionization losses are highlighted in red.

with the chemical composition $(C_8H_8)_n$ which is often used as base material for plastic scintillators. For high-Z material like iron or tungsten α-emission plays only a minor role. As a result, evaporation neutrons can be sampled very differently (in a sampling calorimeter, see Section 3.2) than the charged part of a hadronic shower.
At energies between $\sim 1\,\text{eV}$ and $\sim 1\,\text{MeV}$, the predominant energy loss mechanism of evaporation neutrons is **elastic scattering**. The mechanism emphasizes the very different sampling of neutrons also in this lower energy range. Here, the hydrogen content of the absorbing material is important because the maximal energy transfer to the nucleus is proportional to $4A/(A+1)^2$. For hydrogen, the average transferred energy fraction is ~ 52 (~ 14) times higher than for lead (iron) [38]. So a neutron in this energy range that traverses a hydrogen-rich scintillator has an increased probability to knock out a proton from the molecular structure and create a detectable signal.
After an evaporation neutron has lost nearly all of its kinetic energy through elastic scattering, it can be captured by an absorber nucleus (**neutron capture**). This represents one of the only mechanisms in which the nuclear binding energy that had to be expended to release the neutron is gained back. In this aspect, neutrons behave very different than protons which simply become part of the absorber structure. The neutrons, on the other hand, become captured and transform an absorber nucleus into another. The nucleus becomes excited by the gained binding energy and radiates this

excess away by the emission of photons.

Implications for the Time Development of Hadronic Showers

The timing of calorimetric energy depositions is very different for the various particle types created during the development of the hadronic cascade and their respective interaction mechanisms. While the energy of the majority of particles a hadron shower consists of (such as charged hadrons or e^+, e^- and photons in the electromagnetic shower fraction) is deposited within a few nanoseconds, the energy depositions of low energetic, non-relativistic neutrons can occur significantly delayed. This is due to the different timescale of the different neutron interaction processes. Within an Uranium-scintillator calorimeter for example, the timescale of the energy depositions induced by elastic neutron scattering was found to be of the order of 10 ns whereas only 20 % of the neutrons are captured within 100 ns and the timing of neutron capture induced energy depositions extends up to $100 - 1000$ ns [45][46]. Delayed neutrons carry $\mathcal{O}(10\,\%)$ of the energy contained within the non-em fraction of a hadron shower [38] and additional energy can be gained back through the release of nuclear binding energy. The timescales and the relative contributions differ for different absorber materials and are still to be determined for many. The timing characteristics of hadron showers within a tungsten absorber structure and the comparison relative to steel are the major subject of this thesis.
The performance of a hadron calorimeter can be tuned and improved when respecting delayed contributions present within hadronic showers. In the following, we present some features caused by the time development of hadronic showers and prospects how they can be put to a beneficial use in calorimetry.

Since the electromagnetic fraction f_{em} of a hadron shower is deposited quasi-instantaneously, it is expected that the delayed shower component contributes, in total, less if f_{em} is large and, consequently, that less late energy depositions can be detected in a given calorimeter. Several external factors influence f_{em} and therefore the shower timing. For one, f_{em} increases for higher particle energies due to the increased number of π_0s that can be created within the cascade (see above). Furthermore, the impinging particle sort is of relevance. Since the average number of mesons produced per nuclear interaction is reduced for impinging protons compared to pions due to baryon number conservation, proton induced showers exhibit a reduced electromagnetic fraction and the delayed component is expected to be increased.
π_0s are produced within the first few generations of nuclear interactions in the shower development. This is where electromagnetic subshowers start. Since the radiation length is a factor of ~ 10 lower than the nuclear interaction length for iron absorbers, and even a factor of ~ 30 for tungsten [38], a hadronic shower can be geometrically subdivided into a shower core with a high energy density given mainly by the electromagnetic fraction, and a low energetic halo, which is dominated by the hadronic component. The tails of hadron showers are largely influenced by the neutron component since the mean free path is significantly higher for low energetic neutrons than for charged hadrons.

It could even be shown for the example of an uranium absorber that the tails of the shower development are dominated by neutron capture, while the activity of spallation neutrons concentrates in the intermediate region between the core and the shower tails [47]. One therefore expects that the fraction of delayed energy depositions rises, on average, steeply with increasing distance from the shower core which can be made visible by studying the longitudinal and lateral profile of the calorimetric response in a time resolved manner.
Large differences in the shower timing are to be expected for high-Z (lead, tungsten) absorber materials compared to absorbers with relatively low atomic number (iron). The total number of emitted spallation nucleons and the ratio of emitted neutrons to protons is significantly higher for high-Z materials (e.g. by a factor 6 higher in lead compared to iron). Thus, calorimeters equipped with high-Z absorbers should exhibit a drastic increase in the number of observed delayed energy depositions.

A fraction of the energy contained in the hadronic part of the shower is invisible for calorimetric detection, but through the increased detection of neutrons a part of it can be gained back. In an ideal calorimeter, the response to the electromagnetic and hadronic shower fraction is identical (e/h-ratio equals 1), because then event-by-event fluctuations in the creation of π_0s become irrelevant. Such a hadron calorimeter is called self-compensating. This has beneficial effects on the overall detector performance (e.g. the energy resolution, see Section 3.2). By choosing a long enough time window until which the calorimetric response is integrated and therefore taking more energy depositions of delayed neutron interactions into account, the e/h ratio can be tuned and brought closer to unity [46].
Furthermore, the timing properties of hadronic showers can be used as a complementary mean to obtain a calorimetric particle identification. By comparing the fraction of energy deposited before, and after a certain time cut, an efficient calorimetric distinction between e.g. pions and electrons can be made [46].

3.2 The Detection of Particle Showers

After the details on the underlying physics of shower development, we will now discuss possible approaches for the design of a calorimeter in particle physics. There is a variety of different concepts: Calorimeter systems are usually subdivided in an electromagnetic (ECAL) and into a hadronic (HCAL) part. They can be homogeneous (usually only realized for ECALs) meaning that the absorber is the sensitive detector or of a sampling structure in which dense absorber material is alternated with sensitive detector material. The latter can be segmented longitudinally or laterally. Which type of calorimeter suits best is decided by the requirements of the large-scale detector concept. In this section, we will give an overview over different calorimetric concepts, but focus on properties of the detector type which is under investigation for a future linear collider, namely a longitudinally segmented sampling calorimeter subdivided into an ECAL and a HCAL.

3.2.1 Calorimetric Measurements and Leakage

In general, the main purpose of a calorimeter is to reconstruct the energy of a highly energetic particle. The particle enters the dense material of the calorimeter structure and undergoes a series of interactions in which a multitude of secondary particles is generated. Each of these shower particles can deposit energy within the calorimeter. Ideally, the sum of the detected energy is then proportional to the initial energy of the impinging particle (linearity). A requirement is that the particle shower is completely contained within the calorimeter. The calorimeter has to be thick enough in terms of the radiation length or the nuclear interaction length respectively that no substantial fraction of the total shower energy leaks out. Otherwise the energy resolution and the linearity would be deteriorated. The longitudinal depth of a calorimeter necessary to contain a particle shower varies weakly with the energy of the impinging particle as ln(E) [40]. On the other hand, the depth of the calorimeter that can be realized depends on factors such as the physical size and the stability of the support structure, cost considerations et cetera. Calorimeters are often subdivided into a part specialized for the detection of electromagnetic showers and a part well suited to contain and measure hadronic showers (see next Section 3.2.2). ECALs are typically of a longitudinal size of $15 - 30\,X_0$, while hadronic calorimeters are mostly designed with a depth of $5 - 8\,\lambda_I$ [17].
Another important aspect of calorimetric measurements is the achievable position and angular resolution. The exact position of a particle shower plays an important role in the event reconstruction of large-scale collider detectors. This position is often approximated as the center of gravity (COG) of the energy deposited in all calorimeter cells that detected a signal in response to a particle shower. The position resolution depends sensitively on the shower radius (the Molière Radius for electromagnetic showers) within the used absorber material and the lateral segmentation of the calorimeter design [17]. For most calorimetric concepts, its depth within the calorimeter is not as important as its lateral position relative to the interaction point of colliding particle beams. A reconstruction of the angle of incidence, meaning the direction from which a high energetic particle entered the calorimeter and in which the shower consequently develops, is of relevance for neutral particles, for which the tracking system cannot detect any space points. It also plays a role if e.g. a high energetic photon does not originate from the interaction point, but represents machine background from the collider. For a determination of the angle of incidence, the calorimeter has to be longitudinally segmented since several calorimetric space points are required to reconstruct the orientation of the particle shower.
In the case of a calorimeter suited for the purposes of Particle Flow (see Section 2.4.2) the calorimeter has to be finely segmented (longitudinally and laterally). Here, the priority is to resolve the individual shower particles so precisely that they can be attributed clearly to the high energetic particles impinging the calorimeter. The mistakes in such assignments are most relevant for the achievable jet energy resolution of a detector system optimized for Particle Flow. Also the positional and angular resolution improve significantly due to this high granularity.

The calorimetric information is also used for an efficient discrimination of different impinging particle types. The very different longitudinal and lateral dimensions (λ_I/X_0-ratio) or the fraction of the energy deposited in the tails relative to the shower core (for highly granular calorimeters) can be used to distinguish between e.g. electrons and pions. Further calorimetric particle identification concepts can be found in [38].
For calorimeters which are capable of recording information on the timing of particle showers, this information can be used to obtain a timestamp for individual calorimetric energy depositions of a particle shower and assign them to an impinging particle belonging to a distinct collider event. This can help to avoid the pile-up of consecutive collider events (see Chapter 2) provided the used detection technology is fast enough to collect and process the induced signals. Furthermore, the timing information can be used to tune the e/h-ratio of the calorimeter and distinguish electron from pion showers as elaborated above (see Section 3.1.3).

3.2.2 The Classification into ECAL and HCAL

The subdivision into ECAL and HCAL can be explained by the fundamentally different dimensions of electromagnetic and hadronic showers. Electromagnetic cascades are very small and condensed. They develop longitudinally and laterally on a scale of the radiation length and the Molière Radius, respectively, which is for common absorber materials (such as iron or tungsten, see Table 3.1) at maximum few centimeters. If one is to measure the substructure within electromagnetic cascades and detect shower particles individually, the active cells within an ECAL should have an extent which is comparable to this length scale or smaller. The ECAL has to be longitudinally and laterally subdivided accordingly. For hadronic showers the situation is different. Here, the relevant length scale is the nuclear interaction length, which is for the common absorber materials of the order of few decimeter. This length scale and the required geometrical resolution of electromagnetic subshowers defines the size of the active cells within a HCAL. Usually the cells of a HCAL are chosen somewhat larger (also due to cost considerations). Since the penetration depth of hadronic showers is much higher, calorimeters are often designed such that high energetic particles encounter first a finely segmented ECAL in which predominantly e^+, e^- and photon induced showers are measured and a coarser HCAL in which hadron showers are characterized and that is positioned behind.

3.2.3 Homogeneous Calorimeters

In homogeneous calorimeters the entire volume consists of active detection material. Nevertheless, such calorimeters have to be very dense and contain heavy absorber atoms (with high Z) to stop particle showers at a reasonable distance. When an electromagnetic shower evolves within a dense material it deposits all of its energy eventually by excitation or ionization of the absorbing atoms or molecules. Homogeneous

calorimeters use inorganic scintillating crystals such as Caesium Iodide (CsI) or Lead Tungstate ($PbWO_4$, e.g. used in the ECAL of the CMS experiment at the LHC [4]) in which a part of this excitation energy is converted into scintillation light that can be detected. Since the whole detector volume is sensitive, the response of an ideal homogeneous ECAL is linear meaning that an electron or photon impinging with twice the energy will generate a twice as high calorimeter response (in reality e.g. detector saturation effects can deteriorate this intrinsic linearity). And as practically no energy is lost for detection, the homogeneous ECALs built could deliver the best energy resolution achieved so far. The stochastic term amounts to only $\sim 3\,\%/\sqrt{E}$ for the ECAL of the CMS detector [48] (see next Section for details on the energy resolution of a calorimeter). The situation would be very different for a homogeneous HCAL. A part of the hadronic shower fraction is invisible for detection. Thus, homogeneous HCALs are intrinsically non-compensating meaning that the response to the hadronic shower fraction is lower than to the electromagnetic one. So fluctuations in the electromagnetic shower fraction cause a deterioration of the energy resolution and a homogeneous HCAL would be intrinsically non-linear. Due to these reasons and because the required inorganic crystals are too expensive to be used for the larger volume of a HCAL, homogeneous calorimeters were exclusively realized as ECALs.

3.2.4 Sampling Calorimeters

Sampling calorimeters are subdivided into a passive and an active medium which alternate with a certain sampling frequency. Note that this division is not necessarily arranged perpendicular to the direction of the impinging particle. The sampling can also be realized in this direction because a substantial part of the particles created within a particle shower are emitted isotropically. An example is the accordion structure of the ECAL of the ATLAS detector at the LHC [5][49]. The passive material consists usually of a dense material with high atomic number such as iron, lead or tungsten. For the active material, on the other hand, one can choose rather freely. Popular choices are, for example, scintillating plastic or liquid argon for the generation of a measurable light or charge signal in response to the traversing particle shower. So in sampling calorimeters, the purpose of particle absorption and signal generation is geometrically separated.

The Opportunity for Compensation in Hadronic Sampling Calorimeters

An important peculiarity of hadronic sampling calorimeters is that they can be designed in a way that their response to the electromagnetic shower fraction e is the same as to the hadronic shower part h ($e/h = 1$). This compensation can be achieved by a specific choice of the absorber and the active material and the right adjustment of the sampling fraction. The sampling fraction is the amount of energy deposited by a minimum ionizing particle (MIP) and measured within the active material relative to the total energy deposited by a MIP within the whole calorimeter. Note that the sampling fraction is approximately proportional to the ratio of the thickness of the active layers

relative to the thickness of the passive layers for a given calorimeter. To understand these interconnections one can look at the factors that influence the e/h-ratio:

$$\frac{e}{h} = \frac{e/\text{MIP}}{f_{rel} \cdot rel/\text{MIP} + f_p \cdot p/\text{MIP} + f_n \cdot n/\text{MIP}} \tag{3.6}$$

Here, f_{rel}, f_p and f_n are the average fractions of the energy in the non-electromagnetic part of the hadron shower that are carried by relativistic charged particles, spallation protons and evaporation neutrons, respectively. rel, p and n are the calorimetric response to the respective particle sorts normalized to the response of MIPs. f_{rel}, f_p and f_n are fixed through the choice of the active and passive calorimeter material and rel/Mip is approximately 1. The best possibility to modify e/h and to achieve compensation is to decrease the response to the electromagnetic shower fraction and/or to increase the calorimetric response to evaporation neutrons.
The electromagnetic response can be reduced by choosing an absorber with very high atomic number Z. This can be understood as follows: In Section 3.1.2 we showed that most of the energy of an electromagnetic shower is deposited through electrons created in Compton scattering and Photo Effect processes. It can also be shown that the cross section for the Photo Effect increases as Z^4 to Z^5 for photons with an energy of 100 keV and 1 MeV, respectively [38]. Thus, photons with an energy below 1 MeV interact almost exclusively with the passive absorber in calorimeters with high-Z absorber material. The created electrons have a range which is orders of magnitude smaller than the thickness of the absorber plates in a hadron calorimeter (e.g. 0.67 mm for 1 MeV electrons in lead [38]). Thus, the signal response within the active layers is significantly reduced (e/Mip is only 0.6-0.7 for lead absorbers [38]). This reduction of the electromagnetic response causes a relative enhancement of the response to the hadronic shower fraction (see Equation 3.6) and in turn an e/h-ratio that is closer to unity.
The response to evaporation neutrons can be increased by choosing a material for the active layers which has a high hydrogen content (like scintillating plastic consisting of $(C_8H_8)_n$ chains or the gas Isobutane consisting of C_4H_{10} molecules) and by choosing a small sampling fraction. This can be explained by the properties of elastic neutron scattering which is the dominant energy loss mechanism for neutrons in an energy range between 1 MeV and 1 eV. If present, soft neutrons loose their energy predominantly in collisions with protons by this process (see Section 3.1.3). The recoiling protons are densely ionizing and contribute considerably to the calorimetric signal. So for active materials with high proton content the neutron part of the hadronic shower fraction is sampled very differently than for proton free materials and the contribution of neutrons to the energy measured is in total increased. Furthermore, the average energy deposited by MIPs increases approximately linearly with the thickness of an active layer. Soft neutrons, on the other hand, deposit most of their energy within the hydrogen-rich active layers. Consequently, the response to neutrons is increased relative to the response to MIPs (increased n/MIP in Equation 3.6) for a calorimeter with a small sampling fraction or, in other words, thin active layers relative to the thickness of the absorber. With the right choice of the sampling fraction and with the right hydrogen content within the active layers, e/h can in principle be tuned towards

a value of 1, although in practice many other factors, such as cost, space or stability constraints play a role in the final design of a calorimeter.
It is important to note that calorimetric signals from the interactions of soft neutrons can be significantly delayed relative to the signals from relativistic charged shower particles (especially for the case of neutron capture processes in which a photon is emitted). Therefore, the time window over which a calorimetric signal is integrated has to be long enough to measure a large fraction of the neutron activity or, in other words, the n/MIP ratio can be fine-tuned by the choice of the time cut. A deeper understanding of the time structure of neutron interactions within the used calorimeter materials (a major subject of this thesis) is indispensable for the success of such a fine tuning.

The Energy Resolution of Sampling Calorimeters

As discussed above, the most important purpose of a calorimeter is to reconstruct the energy of an impinging particle. For this, the total signal sum that is measured in response to a particle shower needs to be related to the energy of the incoming particle. This calibration can be obtained from test beam experiments where the incident particle energy is precisely known. The precision with which the energy can be reconstructed by a certain calorimeter is given by its energy resolution. It is defined as the uncertainty of the measured energy sum σ_E divided by the actual energy of the particle E. The energy resolution is characterized by the stochastic term $\frac{a}{\sqrt{E}}$, the noise term $\frac{b}{E}$ and the constant term c. If the sources of these three fluctuation terms are uncorrelated, one can express the energy resolution as a quadratic addition of the terms:

$$\frac{\sigma_E}{E} = \frac{a}{\sqrt{E}} \oplus \frac{b}{E} \oplus c \tag{3.7}$$

The stochastic term is primarily influenced by sampling and quantum fluctuations. The response of a sampling calorimeter is the sum of the signals created by ionizing shower particles that traverse the active layers of the calorimeter. Therefore, statistical fluctuations in the number of shower particles N_p that contribute to the calorimetric signal influence the energy resolution. The general development of the stochastic term with increasing energy can be understood though the Poissonian nature of the statistical fluctuations:

$$\sigma(E) \propto \sigma(N_p) \propto \sqrt{N_p} \propto \sqrt{E} \tag{3.8}$$

If event-to-event fluctuations correspond to Poissonian fluctuations in N_p, then the statistical uncertainty on N_p can be expressed as $\sqrt{N_p}$. If the measured shower energy E is furthermore proportional to the number of ionizing shower particles N_p, then uncertainties on the measured energy are proportional to $\sqrt{E}$ and the stochastic term can be given as $\sigma_E/E \propto a/\sqrt{E}$. Concerning the stochastic term, the energy resolution improves with increasing particle energy, since, on average, more shower particles are created that contribute to the signal. The same is true if the sampling fraction f_{samp} is increased. One can show that the factor a is proportional to $\sqrt{d/f_{samp}}$, where d is the

thickness of an active layer [38].
In addition to these sampling fluctuations, fluctuations in the number of created signal quanta (e.g. photo electrons that make up the calorimetric signal if photosensors measure scintillation photons) influence the energy resolution in a Poissonian way (quantum fluctuations). Such fluctuations can be e.g. reduced for an increased light output (LO) per GeV of deposited shower energy. In this context, the factor a is proportional to $\sqrt{1/LO}$. Now it becomes clear that the energy resolution of homogeneous electromagnetic calorimeters (see Section 3.2.3), in which the light output per GeV of deposited energy is large due to the usage of large continuous scintillating crystals and in which sampling fluctuations are not present, is so exceptionally good. For sampling calorimeters, also Landau fluctuations, i.e. statistical fluctuations in the number of collisions and deposited energy of traversing shower particles within thin calorimeter layers, play a role.
In general, the energy resolution is worse for high energetic hadrons (nuclear shower processes) than for electrons or photons (all involved processes purely electromagnetic). In hadron showers, a sizeable fraction of the energy is invisible for calorimetric detection. This invisible energy is expended within the hadronic cascade for the nuclear binding energy needed to release nucleons from the absorber nuclei and deposited in the form of nuclear recoil energy. The event-to-event fluctuations of the invisible energy deteriorate the energy resolution of hadron calorimeters considerably.

For non-compensating hadron calorimeters a significant deterioration of the energy resolution originates from fluctuations in the electromagnetic fraction f_{em} of the hadron shower. Note that in contrast to all other fluctuations treated so far, fluctuations in f_{em} are not purely governed by Poissonian statistics. In the standard parametrization given in Equation 3.7 its contribution influences the stochastic as well as the constant term c. This is due to the fact that the underlying distribution of f_{em} is asymmetric towards higher values (explained by the leading particle phenomenon in the production of π^0s, see [38] for details). In some cases, fluctuations in f_{em} may dominate the energy resolution of a non-compensating hadron calorimeter at high energies. Furthermore, systematic uncertainties in the detector calibration and cell signal non-uniformities contribute in a constant way. Such non-uniformities can depend on the detector life time if e.g. radiation damages influence the performance of the active detector elements of the calorimeter.
Apart from this, the energy resolution is influenced by the leakage of shower particles which plays a role if the calorimeter is not sufficiently large to contain the particle shower. A shower can leak laterally out of the sides, longitudinally out of the back and even in opposite direction of the impinging particle out of the front of the calorimeter (also known as Albedo Effect). The shower leakage depends also on the particle type, since impinging mesons (e.g. pions) have a larger penetration depth than baryons (e.g. protons) (see Section 3.1), which complicates its influence further. In general, the energy dependence of longitudinal shower leakage is weak (often $\propto ln(E)$), but the uncertainties σ_{leak} increase with the energy E. Its influence on the energy resolution σ_E/E is therefore often assigned to the constant term c.

A special role is attributed to electronic noise of the active calorimeter cells (e.g. the photon sensors used for the detection of scintillation light) which affects the overall energy resolution as b/E. Due to the steeper rise towards lower energies relative to Poissonian fluctuations ($\propto 1/\sqrt{E}$), noise fluctuations tend to dominate in the low energy regime. Electronic noise, which is present even in the absence of a shower, contributes on average a fixed amount of fake energy to the measured energy sum (usually corrected for by a pedestal subtraction procedure) and uncertainties on this noise value σ_{noise} are intrinsically independent of the particle energy. Noise fluctuations become less relevant at higher particle energies.

The quality of the calorimetric reconstruction of the energy of impinging particles plays a major role for the 4π-detectors used at collider experiments. It is particularly important for collider events in which missing energy is involved and should be determined with high accuracy. For many detectors (which are not optimized for Particle Flow) the calorimetric energy resolution limits the separation capability between particles with similar masses (like in the fully hadronic decay of the W and Z boson) and the precision with which the mass of heavy particles (like the top quark) can be determined.

3.3 Instrumentation for Calorimeters

There is a large variety of different technologies that can be used for the detection of shower particles within calorimeters, each of which has their own characteristics and advantages. Most of them are based on the collection of ionization charges or scintillation (or even Cerenkov) light. Popular choices are cryogenic liquid Argon equipped with charge detecting electrodes, silicon based semiconductor layers counting the charge of generated electron-hole pairs, gas-filled chambers exposed to electric fields in which the created space charges drift to the electrodes or tiles of scintillating plastic or crystals in which generated photons are detected through photo multiplier tubes or semiconductor based photon sensors. In this section, we will focus on the operation principle and characteristics of the active elements used within the T3B experiment and the analog CALICE calorimeter prototype (AHCAL, see Section 3.4.2), namely plastic scintillator tiles mechanically coupled to and read out by novel silicon photomultipliers (SiPMs). Note that the elaborations on SiPMs and scintillation detectors follow reference [14] closely. Furthermore, we will briefly introduce the technology of resistive plate chambers (RPCs) as used within the semi-digital CALICE calorimeter prototype (SDHCAL, see Section 3.4.1) with which the T3B experiment took data in one of its test beam phases.

3.3.1 Gaseous Detectors - Resistive Plate Chambers

A resistive plate chamber is a detector that measures ionization charges that are generated when a charged particle traverses a special gas.
Figure 3.6 shows the systematic sketch of a glass RPC. It consists of a thin gap (here

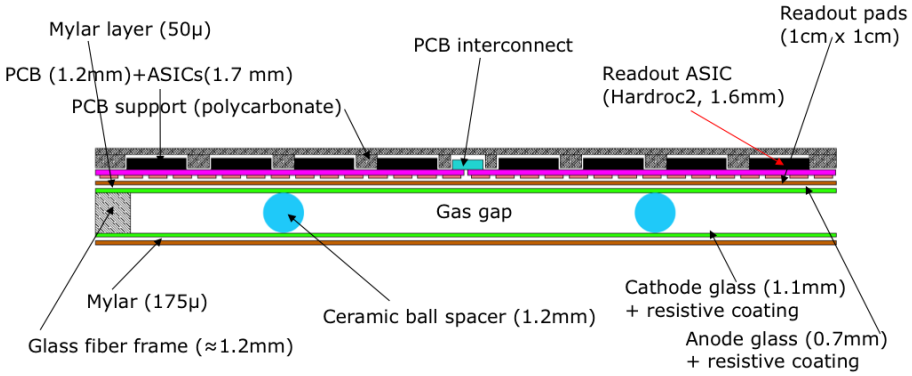

Figure 3.6: Cross section through a glass resistive plate chamber as used within the CALICE semi-digital hadron calorimeter prototype.

1.2 mm) that is filled with gas under atmospheric pressure and surrounded by two parallel glass plates with high resistivity. The glass plates are coated on the outer sides with a lower resistive material and a high potential of usually around 7 kV is maintained between those electrodes.
A common RPC works as follows: A charged particle, that traverses the thin RPC gas gap ionizes several gas molecules along its path. The ionized electrons drift within the high homogeneous electric field maintained within the gas gap towards the anode and are continuously accelerated along their path. If their kinetic energy grows large enough, they interact themselves with the gas molecules and create secondary ionization charges which are accelerated to the electrodes as well and can initiate further ionizations. Eventually, a charge avalanche develops and the signal of the RPC-traversing particle is amplified (find details in [17]). Without the highly resistive glass plates, a potential of $\sim 7\,\mathrm{kV}$ in a distance of only 1.2 mm would cause an immediate electrical breakdown between the electrodes and damage the detector. The glass plates serve as insulator, but prevent a direct detection of the generated charge avalanchne. Instead, readout pads of small size ($1 \times 1\,\mathrm{cm}^2$ in Figure 3.6) are positioned behind the anode on the other side of the glass plate and capacitively coupled. Here, a charge is influenced by the avalanche created within the gas and this is the signal measured by the readout pads. The readout pads are protected from the high voltage through a thin layer of insulating Mylar. The rear detector face (behind the pads, see Figure 3.6) is taken up by the electronics which digitizes and transfers the collected data.
The size and the duration of a charge avalanche needs to be limited to avoid a discharge of the whole gas volume and allow for a simultaneous detection of multiple particles traversing the RPC. On the one hand, the current of the avalanche itself reduces the potential locally to below that needed to maintain the discharge [17]. Furthermore, this is supported by the right choice of the gas mixture. A so-called quenching gas is used to absorb UV-photons emitted within the avalanche which could otherwise enlarge the size of the discharge significantly. A second gas constituent exhibits a high specific ionization which is necessary to initiate the charge avalanche. Popular choices are e.g.

Isobutane (for the quenching) and Argon (for the ionization), respectively. For the RPC shown in Figure 3.6 a mixture of TetraFluoroEthane, CO_2 and SF_6 was used (details on the SDHCAL in Section 3.4.1).

RPCs are well suited for particle detection in high energy physics and a viable option for a hadron calorimeter optimized for Particle Flow. They exhibit in general a very low noise rate of $< 1\,\mathrm{Hz/cm^2}$ [32] and can offer a signal timing capability of the order of 1 ns. Furthermore, they can be produced very thin (only $\sim 6\,\mathrm{mm}$ in the example of Figure 3.6), with a fine lateral pad segmentation and are very cost-efficient. On the downside, RPCs are intrinsically limited in the rate with which they can detect particles since the time that is needed for the recovery of the electric field after the discharge is proportional to the (intrinsically high) plate resistance and the chamber capacitance. Therefore, the particle detection efficiency decreases for high event rates. Apart from this, the noise rises with the ambient temperature which makes active cooling systems necessary. The small extent of the active gas gap results in a very small sampling fraction which is why RPCs are not used within electromagnetic calorimeters where the energy deposition needs to be quantified due to the high energy density and small dimensions of electromagnetic showers. Nevertheless, RPCs can provide a good resolution of individual hadron shower particles and are considered as the active elements within future hadron calorimeters, especially in the context of Particle Flow. In this case, RPCs count the number of shower particles in a digital way (find details in Section 3.4.1).

3.3.2 The Silicon Photomultiplier

Silicon photomultiplier are novel semiconductor devices applied for photon detection. They were invented in the 1990's [50] and have been continuously improved since then. Over the years, new photo lithographic and etching procedures - developed in the semiconductor industry - made a refined manufacturing process possible. SiPMs allow for a single photon detection. They are insensitive to magnetic fields and very small. Common dimensions of the sensitive area of the device are $1 \times 1\,\mathrm{mm^2}$ (used within the T3B experiment and the CALICE AHCAL), but SiPMs with larger or smaller active areas are available. SiPMs can be easily integrated into tiles of scintillating plastic to form an efficient detector for charged particles (SiPM-tile assembly). Furthermore, they are exceptionally fast with a pulse duration of a few nanoseconds in case of the detection of a single photon. All those properties make it the perfect photosensor for the application in high energy physics. In the following, we will explain the working principle and some important properties that emerge during the operation of a SiPM.

The General Concept

A silicon photomultiplier is an array of avalanche photo diodes (APDs). Figure 3.7 (right) shows a SiPM produced at the Moscow Engineering Physics Institute (MEPhI,

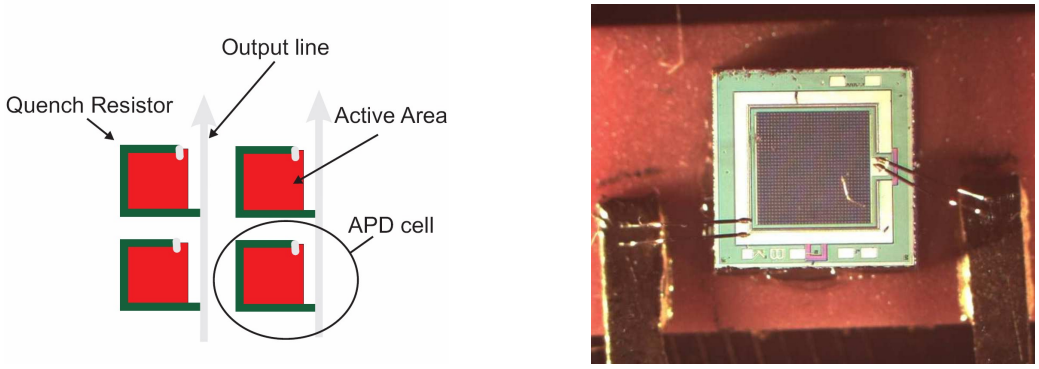

Figure 3.7: Schematic of the SiPM pixel design (left) [50] and picture of a SiPM produced at MEPhI (right).

[51]). It has a sensitive area of $1.1 \times 1.1\,\mathrm{mm}^2$ which is subdivided into 34×34 pixels. Each of these pixels is an independent semiconducting photo diode and sensitive to single photons. The SiPM has two terminals, one for the applied voltage (the bias voltage U_{Bias}) and another one for the output signal. The pixels are connected in series and thus the output is the added up signal of all pixels that "fire" simultaneously.

The Working Principle

A photo diode is a pn-junction typically implemented in silicon. The application of a bias voltage creates a depletion region within the junction. If a photon is absorbed in this region, it can create an electron-hole pair which is separated by the high electric field in the junction. The negatively charged electron and the positively charged hole are accelerated in opposite directions.
A photo diode has a characteristic break down voltage U_{break}. SiPMs are operated above this voltage in the so-called Geiger mode in which the electron and the hole create a charge avalanche on their way to the electrodes (see Figure 3.8, right): After a short distance the initial electron has acquired enough kinetic energy to create another electron hole pair through impact ionization of an atom. Now, two electrons get accelerated and ionize further atoms. The avalanche evolves. The same multiplication process happens for the initially created hole which sets off an avalanche in opposite direction. Each SiPM pixel is operated this way individually.

In Geiger mode, the avalanche of an APD is able to sustain itself. If not suppressed quickly, the discharge could damage the diode. Therefore, the APD is connected in series to a large quenching resistor ($\mathcal{O}(1\,\mathrm{M}\Omega)$). When the diode fires, the resulting current causes a voltage drop over the diode. If the resistor is chosen properly, the bias voltage falls below the breakdown voltage and the avalanche dies out. As seen in Figure 3.7 (left), an integrated quenching resistor is added to every SiPM pixel. The bias voltage is typically restored after the recovery time τ ($\sim 10 - 100\,\mathrm{ns}$ depending on the type of SiPM and the manufacturer) and the pixel is ready for the next avalanche.

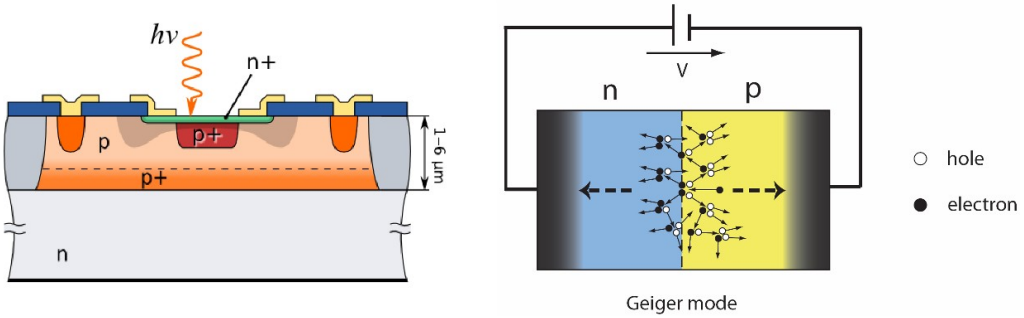

Figure 3.8: Schematic of the Geiger APD working principle. Cross section through the sensitive area of a SiPM pixel [52] (left) and systematic sketch of a charge avalanche in the depletion region (right).

The charge of the initial electron-hole pair is multiplied by a factor of the order 10^6 for one fired SiPM pixel. This is the gain G of the SiPM. The gain is proportional to the difference between the bias and the breakdown voltage (called overvoltage U_o):

$$Q_{pix} = G \cdot e = C_{pix} \cdot (U_{bias} - U_{break}) = C_{pix} \cdot U_o \tag{3.9}$$

C_{pix} is the capacitance of a single pixel. It is determined by the dimensions of a pixel and the doping of the semiconductor material. Q_{pix} is the charge of an avalanche.
The avalanche charge is not proportional to the number of initially created electron-hole pairs and thus to the number of incident photons on a single pixel. As seen in Equation 3.9, the avalanche charge depends only on the pixel capacitance and the overvoltage which is approximately the same for each pixel. So strictly speaking, every pixel is operated in binary mode. The response of the whole APD array, on the other hand, is proportional to the number of incident photons, provided the pixels are small and the light source is weak enough that no pixel is hit by more than one photon simultaneously. So SiPMs achieve a high dynamic range through a fine segmentation of the photosensitive area. The dynamic range is the difference between the largest and the smallest (1 photon per definition) light signal a SiPM can detect. The pixel dimensions of the SiPMs used within the T3B experiment are $50 \times 50\,\mu\text{m}^2$.
As mentioned above, the charge avalanche of a pixel stays the same if it is hit by many photons within the recovery time. Hence, the SiPM is subject to a saturation effect meaning that its response to strong light signals drops below linearity.

The Photon Detection Efficiency

The photon detection efficiency ϵ_{PDE} (also referred to as PDE) describes the sensitivity of a SiPM and is defined as the probability that a photon, hitting the photo detector operated in Geiger mode, generates a Geiger discharge. It is the product of the quantum efficiency (QE), the breakdown efficiency (BE) and a geometrical fill-factor (GF):

$$\epsilon_{\text{PDE}} = \text{QE} \cdot \text{BE} \cdot \text{GF} \tag{3.10}$$

The quantum efficiency QE is the probability that a photon, traversing an avalanche photo diode, creates an electron-hole pair in the high-field region. It is dependent on the photon energy since electron excitation is only possible for energies above the band gap. Additionally, most SiPMs have a very low QE for photons with a wavelength shorter than $\sim 400\,\text{nm}$. Blue and UV light will mostly be absorbed just beneath the silicon surface within less than 100 nm [50]. If it does not reach the depletion region, the created electron-hole pairs will most probably be lost due to very short recombination times. Figure 3.8 (left) shows the schematic of a vertical cut through a SiPM pixel. The top layer of the pixel has to be extremely thin to reach a high QE for short wavelengths. Until several years ago, the fabrication of blue and UV sensitive SiPMs was a challenge. Today, blue sensitive SiPMs are available from Hamamatsu and several other manufacturers.
The breakdown efficiency BE corresponds to the probability that an electron-hole pair, created in the depletion region of a SiPM pixel, triggers a Geiger discharge. It depends mainly on the electrical field strength in the pn-junction of a pixel.
Finally, the geometrical fill-factor GF is the ratio between the photosensitive area and the total area of a pixel. It is less than unity since the physical separation of the SiPM pixels and the integrated quenching resistors represent dead space. In most SiPM designs, GF has the biggest impact on the achieved PDE.

SiPM Noise Effects

The small dimensions of the SiPM pixels are not only useful, they are a requirement. Electron-hole pairs are permanently generated by thermal excitation and their occurrence increases with the temperature of the silicon and the amount of material the sensitive pixel volume contains (i.e. the pixel size). Such thermal pairs can cause a Geiger discharge as well. Since **Thermal Pulses** occur without illumination, they contribute to the so-called darkrate. Darkrate is the rate of pixels firing in a perfectly dark box. In general, a dark pulse is identical to a photon pulse and it is very difficult to distinguish darkrate contributions from the real light signal. Hence, one measures the SiPM signal only in photon equivalents (p.e.). The darkrate is different for every individual SiPM device.
Dark pulses can have a signal height above one pixel avalanche. During a Geiger discharge electron-hole pairs can recombine and emit photons. These luminescence photons propagate within the device. If such a photon is absorbed within the sensitive area of another pixel, it can trigger a second discharge almost simultaneously. The signal cannot be distinguished from a real two photon event. The effect is called **Optical Crosstalk** (CT) and can occur for every pixel avalanche. It increases the height of real photon signals as well as the height of thermal or afterpulses.
Afterpulses (AP) are another SiPM characteristic. Some of the electrons of an avalanche can be trapped in crystal lattice defects of the silicon. After a certain time, they can be released and trigger another Geiger discharge, provided the bias voltage of this pixel has recovered above the breakdown voltage in the meantime. Another source of afterpulses are electron-hole pairs that are created e.g. by recombination photons of

a preceding avalanche on the outside of the high field region. The holes can drift slowly into the high field region and cause a delayed SiPM avalanche.

Temperature Dependence of the SiPM Response and Gain

Silicon photomultiplier are sensitive to temperature variations. More precisely, the device-specific breakdown voltage increases linearly with the temperature. For example, dU_{break}/dT is 56 mV/K for SiPMs of the type MPPC from Hamamatsu with 25 μm pitch and 1600 pixels [53]. The applied bias voltage, on the other hand, is usually kept constant. Therefore, the overvoltage decreases linearly with increasing temperature. Since the gain is directly proportional to the overvoltage (see Equation 3.9), this leads to a linear temperature dependence of the gain with negative slope.

$$\frac{dG}{dT} = -\frac{C_{pix}}{e} \cdot \frac{dU_{break}}{dT} \tag{3.11}$$

To be independent of device specific parameters like C_{pix} we determine the relative gain temperature dependence,

$$\frac{1}{G}\frac{dG}{dT} = -\frac{1}{U_o} \cdot \frac{dU_{break}}{dT}. \tag{3.12}$$

The total response signal A of a SiPM to a weak light pulse is proportional to the number of incoming photons N_γ, the gain G and the photon detection efficiency ϵ_{PDE}:

$$A = N_\gamma \cdot \epsilon_{\mathrm{PDE}} \cdot (1 + \kappa) \cdot G \tag{3.13}$$

κ increases the response due to optical interpixel crosstalk. The equation holds only true for weak light pulses. High photon signals require a correction function which takes the saturation of the SiPM response into account.
We intend to derive the temperature dependence of the SiPM response A. Note that the gain and also the breakdown efficiency BE depend on the overvoltage. A high overvoltage increases the strength of the electric field in the pn-junction. Therefore, the probability increases that an excited electron-hole pair triggers a Geiger discharge. The BE and thus the PDE (see Equation 3.10) increases linearly with U_o in the voltage range of operation and saturates for very high overvoltages since the efficiency cannot rise above 100 %. Following the same argumentation as for the gain, we also obtain a linear temperature dependence with negative slope for the BE.
Differentiating Equation 3.13, the relative temperature dependence of the SiPM response is determined as:

$$\frac{1}{A}\frac{dA}{dT} = \frac{1}{G}\frac{dG}{dT} + \frac{1}{(\mathrm{BE})}\frac{d(\mathrm{BE})}{dT} \tag{3.14}$$

As dG/dT and $d(\mathrm{BE})/dT$ have the same sign, the relative temperature dependence of the response A is always higher than the dependence of the SiPM gain G. In the case of the T3B experiment, a specialized calibration procedure made an elimination of the gain temperature dependence (see Section 5.1.1) and of the remaining amplitude temperature dependence originating from $d(\mathrm{BE})/dT$ (see Section 5.1.2 for the calibration procedure of dA/dG due to ambient temperature changes) possible.

Parameter	MPPC-50 P-type
Effective Active Area:	$1 \times 1\,\mathrm{mm}^2$
Number of Pixels:	400
Pixel Size:	$50 \times 50\,\mu\mathrm{m}^2$
Geometrical Fill-Factor:	61.5 %
Quantum Efficiency:	$\geq 70\,\%$
PDE (incl. AP and CT):	50 %
Darkrate (incl. AP):	$\mathcal{O}(10^5 - 10^6\,\mathrm{Hz})$
Gain:	$\mathcal{O}(10^6)$

Figure 3.9: Specifications of the SiPM type used within the T3B experiment as quoted by Hamamatsu [54]. The abbreviations AP and CT stand for SiPM afterpulsing and cross talk, respectively (see text for details).

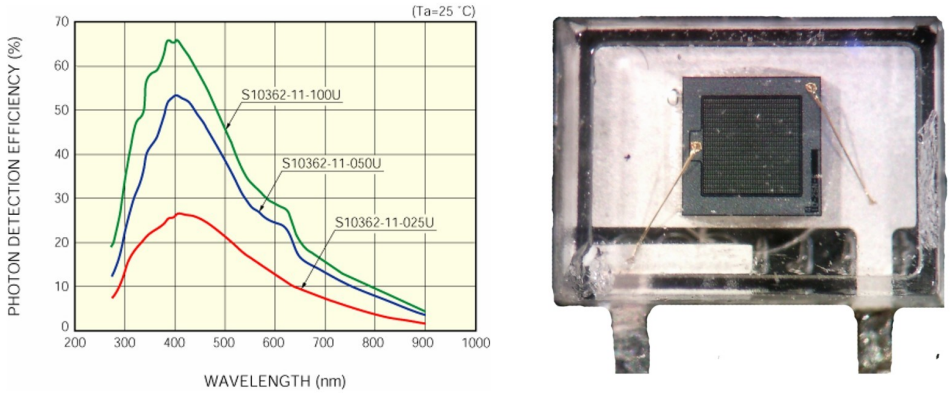

Figure 3.10: Left: PDE of SiPMs of different types [54]. The blue line corresponds to the used SiPMs with $50 \times 50\,\mu\mathrm{m}^2$ pixel size. The red and the green curve correspond to $25 \times 25\,\mu\mathrm{m}^2$ and $100 \times 100\,\mu\mathrm{m}^2$ pixel size, respectively. Right: Photograph of a MPPC with an active area of $1 \times 1\,\mathrm{mm}^2$ and translucent plastic casing as used within the T3B experiment.

T3B SiPM Devices

For the T3B experiment we used SiPM devices from Hamamatsu. Table 3.9 shows the specifications of the multi-pixel photon counter MPPC-50 as quoted by Hamamatsu. It has a pixel size of $50 \times 50\,\mu\mathrm{m}^2$ and a translucent plastic casing around the sensitive pixel area (see Figure 3.10, (right)). The firm casing makes the sensitive area more robust against direct contact which might, for example, occur if one couples the SiPM tightly to a scintillator tile. This plastic casing is not commercially available and we refer to it as P-Type SiPM (for Prototype) in the following.
The applied SiPMs reach their maximum photon detection efficiency at a wavelength of 400 nm. As seen in Figure 3.10 (left), the PDE increases with the pixel size as one would expect. A large pixel size corresponds to a high geometrical fill-factor, but a lower dynamic range for the same dimensions of the sensitive area.

3.3.3 Scintillation Detectors

Scintillation detectors are commonly used in particle physics. Such detectors make use of the fact that certain materials emit photons in the visible range of light when traversed by ionizing particles. We focus on the working principle of plastic scintillator material, as used for the T3B experiment and in the CALICE AHCAL.
Not every scintillation material is suitable for particle detection. For the application in a particle detector, as needed in high energy physics, it should fulfill the following requirements:

1. High efficiency for the conversion of the energy deposition of particles to fluorescent light.
2. Transparency to its own emission wavelength.
3. Emission in a spectral range that matches the spectral response of the used photon sensor.
4. Short signal rise time for an accurate time stamping capability of energy depositions.
5. In the case of the T3B experiment and its signal processing methods (see Chapter 5) a short decay time of the generated light pulse is favourable.

General Specifications

Plastic scintillators are solutions of organic molecules, cast into solid plastic forms. Their chemical base material is usually polystyrene which consists of long chains of C_8H_8 sub-molecules and has therefore a high hydrogen content which is of special importance for shower timing applications (see Section 3.1.3). They can be easily machined and in principle every kind of geometry is possible. The chemical compound used for T3B is called BC-420 (a Polyvinyltoluene based plastic scintillator) and distributed by Saint-Gobain [55]. The CALICE AHCAL tiles are made of Vladimir BASF-143 [56] (a polystyrene based solvent). It generates about 50 % less light, but it is five times cheaper than BC-420. Table 3.2 shows the basic properties of BC-420 as quoted by the vendor [57]. These properties will be discussed in the following.

Conversion of Deposited Energy

Charged particles, that cross the scintillator, deposit energy in the material by an excitation of molecules. The subsequent relaxation process produces scintillation light a part of which is detected when a SiPM is coupled to a tile of scintillation material.
We present a rough estimation of the number of photons produced within 5 mm scintillator material. The scintillator tiles used within the T3B experiment have a thickness of 5 mm (and a lateral size of $30 \times 30\,\mathrm{mm}^2$). Figure 3.11 shows the penetration depth

Parameter	BC-420
Wavelength of max. Emission:	391 nm
Light Attenuation Length:	140 cm
Pulse Rise Time:	0.5 ns
Pulse Decay Time:	1.5 ns
Pulse Width (FWHM):	1.3 ns
Density:	1.032 g/cm^3
Ratio (H:C) Atoms:	1.1

Table 3.2: Specifications of the scintillator material used within the T3B experiment as quoted by Saint-Gobain [57].

of different particles in BC-420. An electron of approximately 1 MeV, for example deposits all its energy within those 5 mm. The average energy loss required for the creation of one photon is around 100 eV [39]. Consequently, the amount of created scintillation photons is of the order 10000. The number of photons that arrive at the SiPM coupled to a T3B scintillator tile is significantly smaller due to the small light collection efficiency of the SiPM within the tile. The largest part of the photons is lost due to an imperfect reflection at the side faces of the tile. The number of photons that is actually detected by the SiPM is further reduced by the PDE and amounts to only $\sim 20 - 30$, on average. See Section 4.2 for details on the properties of the SiPM-tile assembly used within the T3B experiment.
The light yield of a SiPM-tile assembly is the number of SiPM pixels firing when a single minimum ionizing particle deposits energy in the tile the SiPM is connected to. In other words, it is the ratio between the MIP response and the gain of a SiPM.

$$LY[\frac{pix}{MIP}] = \frac{A^{MIP}}{G_{SiPM}} \tag{3.15}$$

This light yield is a measure for the detector performance.

Self Emission Transparency

The emitted scintillation light must traverse the scintillator nearly unaffected from absorption to achieve a reasonable light yield of the SiPM-tile assembly. This is guaranteed by the working principle of the scintillating material. Each possible energy state of the valence electrons has a fine structure, which corresponds to vibrational modes of a molecule. An excited electron relaxes first under photon emission to the high energetic and subsequently to the lowest vibrational modes of the ground state. As a result, the energy required to produce an excited state exceeds that of the emitted photons. The probability for reabsorption is small. So the scintillator is transparent to the light that it generates.

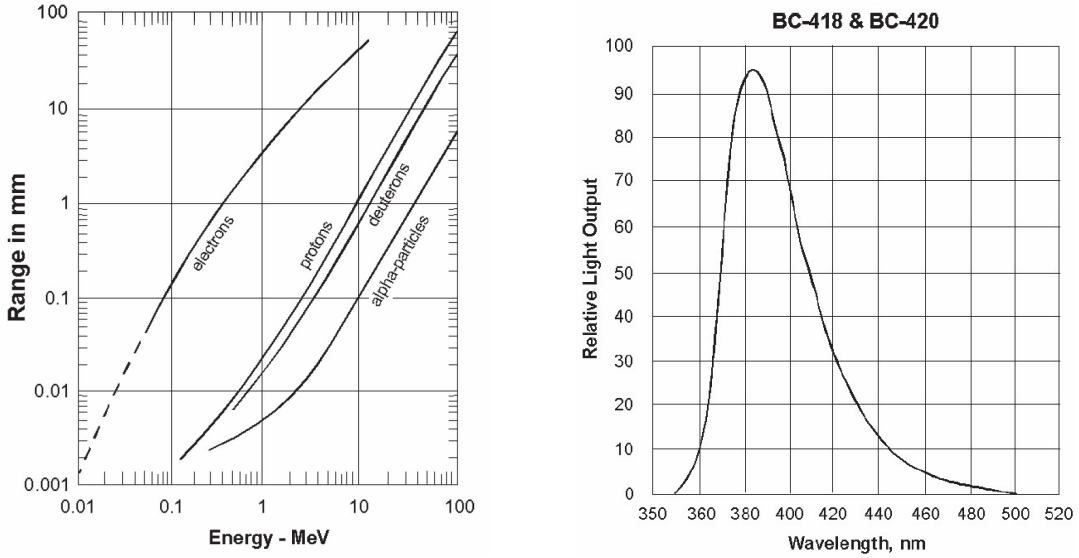

Figure 3.11: Range of different particles in Bicron BC-420 from Saint-Gobain (left) [57] and emission spectrum of BC-420 (right).

Emission Spectrum

Figure 3.11 (right) shows the emission spectrum of BC-420. The material emits light in the range between 350 nm and 500 nm. The wavelength of maximum emission is at 391 nm and the FWHM is about 50 nm. Recalling Figure 3.10 (left), we notice that this emission maximum matches the maximum of the photon detection efficiency for the Hamamatsu MPPCs approximately. Therefore, an optimal light detection can be achieved without the application of a wavelength shifting fiber (WLS). Most organic plastic scintillators emit photons in the blue and UV part of the electromagnetic spectrum. Since blue sensitive SiPMs became available only several years ago, the WLS option was the best solution before. Within the T3B experiment, the SiPMs were directly coupled to the scintillator tiles (see Section 4.2).

The Timing of Scintillation Pulses

Plastic scintillators offer an extremely fast signal. The light pulse of BC-420, when crossed by a particle, has a decay time of only 1.5 ns (to $1/e$ of the initial signal height). The pulse width (FWHM) is 1.3 ns. This allows for the distinction of particle signals occurring with a high rate. The pulse width of a SiPM-tile assembly is further influenced by the response time of the SiPM, the reflectivity of the tile faces and the light attenuation length of the scintillator material, which is 140 cm for Bicron 420. The short rise time of only 0.5 ns is advantageous for the precision with which a time stamp can be attributed to the energy deposition of a traversing particle.

The Distribution of the Signal of a SiPM-tile Assembly

In Section 3.1.1, we derived that the energy deposition of charged particles, traversing a thin absorber, is Landau-Vavilov distributed. Histogramming the signal of minimum ionizing particles, as experimentally detected by a calorimeter cell consisting of a scintillator tile equipped with one SiPM, one finds that the obtained distribution is a convolution of a Landau-Vavilov and a Gaussian distribution. For simplicity, we here refer to this distribution as "Langau". As a result, the width of this Langau distribution is increased and the most probable value is shifted to a higher value relative to a Landau-Vavilov distribution. The occurrence of the Gaussian part can be understood as follows: If we assume a number of MIPs that generate the identical number of scintillation photons on their passage through the tile, the fraction of photons that propagate to the sensitive surface of the SiPM varies because the produced photons are emitted into random directions in the atomic relaxation process. This statistical fluctuation is Poissonian distributed. If the mean number of detected photons is large (i.e. >10), the Poissonian distribution can be approximated well by a Gaussian distribution. Thus, the Landau-Vavilov distributed energy deposition is smeared by a Gauss and the detected signal distribution follows a Langau. Usually electronic noise causes an additional, although smaller, Gaussian broadening.

3.4 Design of a Calorimeter for a Future Linear Collider

CALICE stands for **CA**lorimeter for the **LI**near **C**ollider **E**xperiment. The CALICE collaboration was founded to investigate new design options and approaches for the calorimetric system of the detector at a future high-energy linear e^+e^- collider. Several prototypes for the electromagnetic calorimeter, the hadron calorimeter and the tail catching system (a tail catcher measures the longitudinal leakage of a shower), have been built and their performance and properties have been or are still extensively studied by test beam programs at various facilities (CERN [1], Fermilab [58] and DESY [59]). The prototypes follow different technological approaches ranging from gaseous or silicon based detection principles to plastic scintillator and photon collection systems. All prototypes have in common that they are optimized for the requirements of Particle Flow (see Section 2.4.2). They are longitudinally and laterally very finely segmented (also referred to as highly granular) sampling calorimeters and can deliver an in-depth picture of hadronic or electromagnetic showers.
In this section, we focus on the two prototypes of hadron calorimeters the T3B experiment performed test beam measurements with, namely the CALICE semi-digital hadron calorimeter (SDHCAL) and the CALICE analog hadron calorimeter (AHCAL). While a steel absorber structure is an adequate choice for the calorimeter of an ILC detector (see Section 2.3.1), the quest for higher collider energies makes the exploration of maximally dense absorber materials and its applicability for the hadron calorimeter

system of a CLIC detector (see Section 2.3.2) necessary. The CALICE AHCAL was the first CALICE hadron calorimeter to be tested within a tungsten stack, while the CALICE SDHCAL measured hadron showers within a steel absorber stack. In this section, we explain the two calorimeter prototypes in their configuration at the SPS test beam programme at CERN in 2011. More precisely, we refer to the AHCAL as it was assembled in June, July and September 2011 and to the SDHCAL as assembled in October 2011.
All CALICE calorimeter prototypes designed so far have no capability to timestamp calorimetric energy depositions with nanosecond precision, although this is a requirement for a calorimeter suited for the CLIC collider concept. A highly integrated second generation AHCAL prototype is currently designed and tested to satisfy this need. It is furthermore optimized for the large scale application within a CLIC detector. The T3B experiment, which is the primary topic of this thesis, started its test beam campaign about two years earlier in November 2010 and delivers in an independent and more fundamentally oriented approach first results on the properties of the time development of hadron showers in tungsten. At the end of this section, we discuss some challenges the shower timing requirement imposes on a calorimeter.

3.4.1 The Semi-Digital Hadron Calorimeter Physics Prototype

The CALICE SDHCAL consists of 48 active layers with a thickness of 11 mm interleaved by steel absorber plates with a thickness of 15 mm. The lateral size of the active and the passive elements is $1 \times 1\,\mathrm{m}^2$. Each of the active layers comprises a glass resistive plate chamber (GRPC, 3 mm thick, described in Section 3.3.1) and an electronics board mounted on the front face of the GRPC (3 mm thick) for the signal processing. These elements are surrounded by two thin stainless steel plates with a thickness of 2.5 mm each, which confine them into a cassette structure. The cassettes provide mechanical stability and can be inserted modularly into the absorber structure. Their steel plates constitute a part of the calorimeter absorber. The GRPC signal of one active layer is read out by 9216 pads with a lateral size of $1 \times 1\,\mathrm{cm}^2$. Each of these pads can respond independently to the signal of traversing particles. The waste heat of the in total more than 440.000 readout channels of the calorimeter prototype is carried away through an active water cooling system.
The gas mixture used to run the GRPC consisted of 93 % TetraFluoroEthane ($C_2H_2F_4$), 5 % CO_2 and 2 % SF_6 at the test beam. Note the low fractional hydrogen content of the gas mixture which is of major importance for the elastic scattering cross section of evaporation neutrons (see Section 3.1.3) and therefore the sensitivity to delayed energy depositions within a hadron shower. An admixture of the hydrogen-rich Isobutane (C_4H_{10}) is often avoided because of its flammability and its therefore more difficult handling. On the other hand, an admixture of hydrogen-rich gas would allow a tuning of the delayed component of the measured shower energy.

Within the Particle Flow paradigm (see Section 2.4.2), the main purpose of the calori-

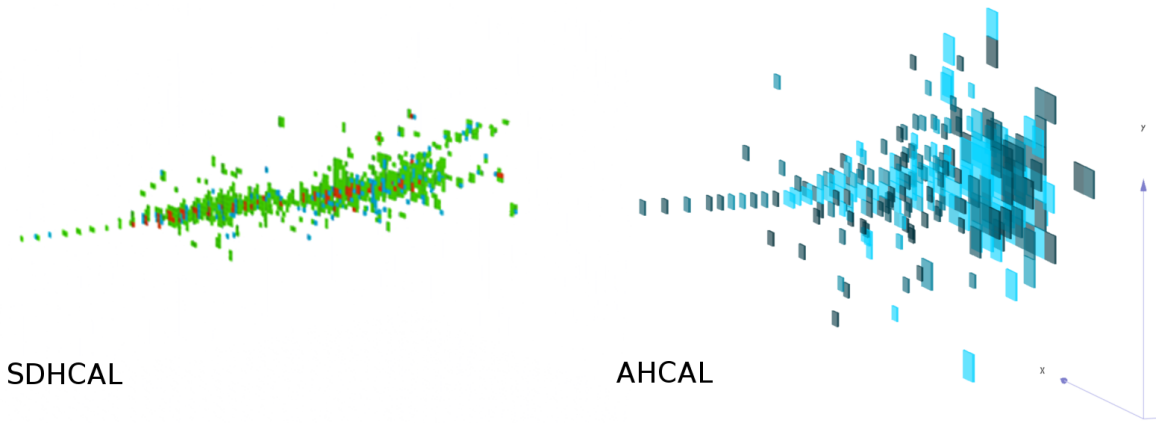

Figure 3.12: Event displays of pion showers in the CALICE calorimeters. The SDHCAL (left) characterizes the number of traversing particles per cell through three thresholds (blue, green, red), whereas the CALICE AHCAL (right) quantifies the amount of deposited energy in an analog way.

metric system is to distinguish neutral from charged particles and reconstruct the energy of the neutral particles with high precision. The SDHCAL emphasizes the former and reaches with its very small pad size an ultra-high granularity which is well suited for particle separation algorithms. A disadvantage of such a fine segmentation is that the readout has to be performed in a (semi-)digital way since the number of readout channels is extremely high and cost, data handling and storage related issues do not allow for an analog readout in which the cell response is proportional to the deposited energy (see AHCAL in Section 3.4.2). In a digital calorimeter, one counts the number of hit pads instead. Ideally, the reconstructed particle energy is proportional to the number of pad hits. The SDHCAL is called semi-digital, since the electronics does not only register if a readout pad observed a signal or not, it additionally provides three thresholds which classify the detected signal of the pad roughly into few, many or very many traversing charged shower particles (see Figure 3.12, left).
In the past years, the RPC technology was used within many experiments in particle physics (e.g. Belle, BaBar [17]) due to its high particle detection efficiency, ease of construction and low cost at covering large detector areas. GRPCs are about to prove as a reliable and stable detector technology suitable for hadron calorimetry within an extended test beam campaign executed by the CALICE collaboration.

3.4.2 The Analog Hadron Calorimeter Physics Prototype

The CALICE analog hadron calorimeter prototype consists of a sandwich structure of 38 active layers and 38 absorber plates. While the first version of the AHCAL was equipped with steel as absorber material, we refer here only to the second version in which a tungsten alloy was chosen as absorber material. The active layers were the same in both versions. The tungsten absorber plates have a lateral dimension of

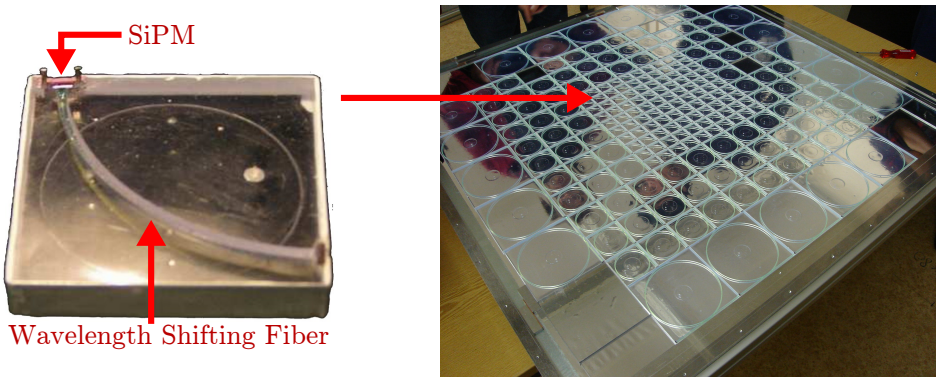

Figure 3.13: Picture of a scintillator cell of the CALICE AHCAL with embedded wavelength shifting fiber and SiPM (left) and of a complete sensitive HCAL layer equipped with cell of this kind pointing out its high granularity (right).

$1 \times 1\,\mathrm{m}^2$ and a thickness of 1 cm. Each active layer has a finely segmented pattern of individual calorimeter cells (see Figure 3.13, right). The heart of the AHCAL prototype are scintillator tiles with a lateral size of $3 \times 3\,\mathrm{cm}^2$ and a thickness of 5 mm (see Figure 3.13, left). A wavelength shifting fiber is embedded into each tile. A reflective mirror is coupled to one end of the fiber and a silicon photomultiplier to the other. The used SiPMs were produced at MEPhI and provide 1156 photon sensitive pixels (see Figure 3.7). 216 scintillator cells were assembled to the particle sensitive area of an active calorimeter layer (see Figure 3.13, right). The cell size increases towards the outside to $6 \times 6\,\mathrm{cm}^2$ and $12 \times 12\,\mathrm{cm}^2$. This represents a balance between shower sampling and cost [60]. In the current design plans of the International Large Detector (see Chapter 2) - the large scale ILC or CLIC detector with a scintillator based HCAL - all cells will have a size of $3 \times 3\,\mathrm{cm}^2$. Detailed studies showed that for an analog scintillator tile calorimeter the Particle Flow performance and therefore the jet energy resolution is not significantly improved by a further reduction of the cell size [34]. The cells are covered with reflective mirror foil and the whole scintillator plane is placed inside a cassette structure consisting of two steel plates with a thickness of 2 mm each. The prototype has a total of 7608 readout channels.

In the AHCAL prototype, 38 boards for calibration and monitoring and for the readout electronics are located on the outside of the calorimeter, but the space restrictions of a full collider detector require a highly integrated and more compact design of the active layers. In the past years, extensive R&D work has been done and a second generation AHCAL design for the active layers has been developed. Several prototype modules have been constructed and their performance under test beam conditions is about to be evaluated within the CALICE test beam campaign 2012. In this new design, the active layer has a thickness of only 5.3 mm (see Figure 3.14, top) [61]. The electronics is accommodated on one side of a thin PCB, while the scintillator cells are assembled on the other side (see Figure 3.14, bottom). The thickness of the cells is reduced to 3 mm to meet the space constraints, but the light yield of the SiPM-tile entity is approximately the same as for the 1^{st} generation prototype because of the usage of a new type of

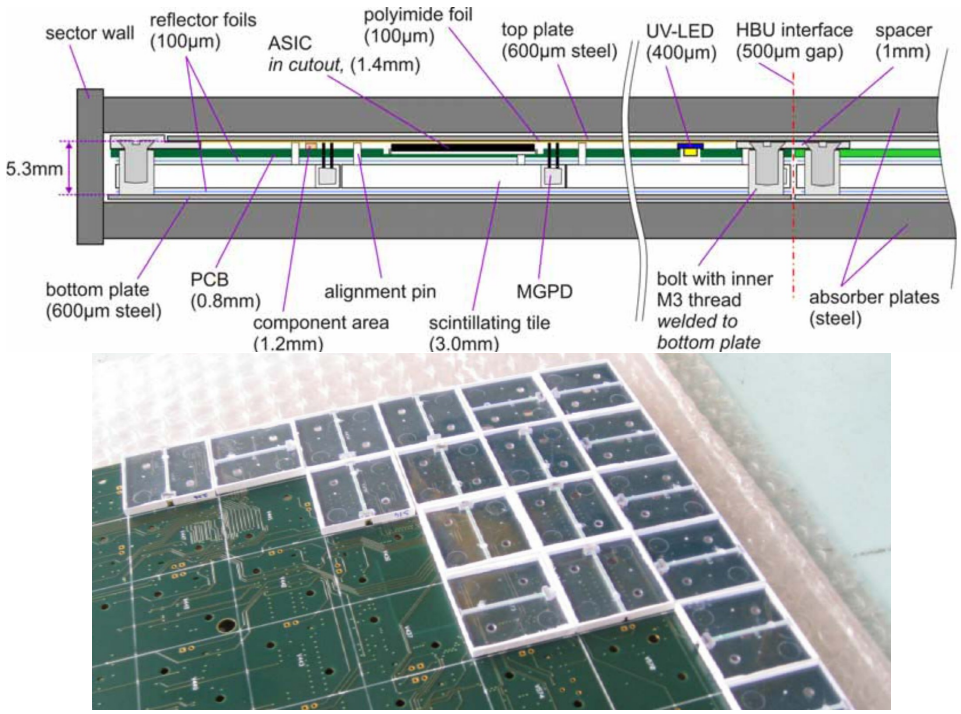

Figure 3.14: New integrated design of the active layers for the second generation CALICE AHCAL prototype [61]. See text for details.

SiPMs. Furthermore, the cell architecture was subject to optimizations. In the current version, the cells do still comprise a wavelength shifting fiber (see Figure 3.14, bottom), but it is under discussion to equip the next batch of produced active layers with cells with a fiberless scintillator tile design similar to the one used within the T3B experiment (explained in Section 4.2). This promises an easier and more time and cost efficient machining and production of the active cells.
The design of the 2^{nd} generation AHCAL prototype modules allows for an automated assembly and should be capable of fulfilling the requirements in terms of stability and rigidness, modularity and operational reliability in the future. It is therefore well suited for mass production and scalable to a calorimetric system used within a full collider detector. Furthermore - in contrast to the 1^{st} generation prototype - the capability to timestamp energy depositions is an inherent part of the design of the 2^{nd} generation AHCAL prototype [62] [63]. This is further elaborated in Section 3.4.3.

With a scintillator cell size of $3 \times 3\,\mathrm{cm}^2$, an analog quantification of energy depositions is feasible in terms of costs, data processing and storage considering the number of readout channels of a full collider detector ($\mathcal{O}(10^7)$ channels in the HCAL of the ILD). The analog information can be exploited to improve the energy resolution for neutral hadrons which is a key performance parameter of a HCAL system optimized for Particle Flow.
The precision of the energy reconstruction of neutral hadrons dominates the Particle Flow performance for jet energies up to approximately 100 GeV [34] (see Section

2.4.2). The application of an offline software compensation algorithm aims to equalize the calorimetric response to electromagnetic sub-showers and purely hadronic shower depositions based on their different spacial characteristics. This reduces the sensitivity to event-to-event fluctuations in the electromagnetic shower fraction and consequently improves the overall energy resolution. Note that the e/h ratio cannot be measured directly. Instead, one quantifies the ratio of the calorimetric response to electrons relative to the response to pions of the same energy - the e/π-ratio. Despite the intrinsically high hydrogen content of the scintillator material which increases the calorimetric response to the hadronic shower fraction, studies showed that the AHCAL prototype - in this study located within a steel absorber structure with a thickness of on average 17.4 mm per layer - features an e/π-ratio of around 1.2 (in an energy range between 10 GeV and 80 GeV) and is therefore non-compensating [64]. This undercompensation can be corrected on an event-by-event basis by an intelligent weighting of the detected energy depositions based on their height. While a high electromagnetic shower fraction and therefore a high energy density is expected within the core of a hadron shower, the surrounding halo and the tails are dominated by the hadronic shower component and exhibit a lower particle density. Thus, the software compensation algorithm reduces the e/h-ratio by weighting high energy depositions down and low energy depositions up (details in [64]). Utilizing the analog nature of the recorded cell signals of the AHCAL prototype (see Figure 3.12, right), the hadronic energy resolution could be improved by up to 20 % [64].

3.4.3 The Challenge of Shower Timing

As shown in Section 2.4, calorimetric energy depositions need to be timestamped with a precision on the nanosecond level for a good event separation and pile-up rejection in the context of a CLIC detector. Apart from this, the energy depositions within hadron showers need to be detected over a sufficiently large time window to obtain an adequate jet energy resolution. This requirement originates from the tendency of hadron showers to deposit a significant part of their energy through a delayed shower component (see Section 3.1.3), which is emphasized in particular in an absorber environment that consists of material with a high atomic number, such as tungsten. It would be advantageous if the length of the time window was adjustable depending on the actual background environment the calorimetric system is exposed to by the collider and possibly also for fine-tuning considerations of the level of compensation.
These requirements could be met best if the signal waveform of energy depositions was sampled in time with sub-nanosecond precision. A realization of this is unrealistic on a larger scale (like for a CLIC calorimeter which comprises millions of calorimeter cells) since the acquired data volume would be impossible to handle. Instead, the electronics of the 2^{nd} generation AHCAL prototype modules contains an integrated time to digital converter which measures the time of the analog signal rise of cells with high precision. This allows for a time resolution of individual hits of better than 1 ns [62]. The deposited energy is quantified within a certain time window around this timestamp. The 2^{nd}

generation AHCAL prototype modules are capable of delivering the timing performance required within a CLIC detector and provide a scalable solution at the same time.
For a first fundamental study of the time development of hadronic showers, a small number of cells is sufficient and a time sampling of energy depositions is possible. This is the approach of the T3B experiment which will be explained in detail in the next chapters.

Chapter 4

The T3B Experiment - General

T3B stands for **T**ungsten **T**iming **T**est **B**eam. It is a test beam experiment that was running at the CERN [1] Proton Synchrotron (PS) and Super Proton Synchrotron (SPS) in the years 2010/2011 as part of the CALICE test beam campaign. The campaign was started to evaluate tungsten as absorber material for the calorimetric system of the next linear collider experiment and to study its properties and its effect on hadronic showers. For its measurements, the T3B experiment was positioned behind the CALICE tungsten hadron calorimeter prototype for most of the beam time and behind CALICE steel SDHCAL to provide a comparison of the different absorber properties. The T3B experiment is designed to acquire additional information on the time development of hadronic showers with a so far unprecedented time resolution. Shower timing is a property relevant for the operation of a detector for the International Linear Collider concept and crucial for the operation of calorimeters in the harsh background environment intrinsic to the concept of the Compact Linear Collider.

A motivation for the T3B experiment will be given in the first section of this chapter. We will then describe the releveant technological concepts and the hardware used for the assembly of the T3B detector. The general outline and the hard- and software necessary for the commissioning of the detector is explained in the following section. Finally, we provide details on the installation of the T3B detector, the run conditions and the data sets acquired at the various test beam phases. We will also describe the data acquisition sequence of the detector in standard operation under test beam conditions.

4.1 Motivation for the T3B Experiment

The T3B experiment was created to study the development of hadronic showers in a time resolved manner. While the existing prototypes of the CALICE Collaboration can provide excellent information on the achievable energy resolution and the response of the calorimeter, the longitudinal and lateral shape of hadronic showers and more (see

Section 3.4), none of them (in the 1^{st} generation) is capable of measuring the timing of the hadronic cascade on the time scale intrinsic to the shower evolution.

The calorimeter prototypes were originally designed for the background environment of the ILC at which the particle bunches cross only every $\sim 700\,\text{ns}$ within a bunch train [30]. This leaves enough time for the particle showers to decay before the next bunch crossing and for the detector electronics to assign the energy depositions to the respective bunch crossing correctly. This is the basis for a reliable event reconstruction. At CLIC the bunches collide every 0.5 ns within a bunch train due to the machine design [27]. This is significantly shorter than the time scale at which hadron showers evolve and the detector needs to provide an excellent time stamping accuracy to avoid the pile up of physics and underlying background events. One needs to decide on how long to integrate the energy depositions of an hadronic shower to maintain an acceptable energy resolution on the one hand and to minimize the confusion in assigning the energy depositions to the bunch crossing of the respective event on the other hand (see Section 2.4). But to evaluate this, one needs to know the time development of hadron showers exactly. This is where the T3B experiment comes in. T3B is supposed to measure the decay time of the hadronic cascade. It might be very different for the technology used in the different calorimeter prototypes. T3B uses a scintillation detector technology very similar to the one of the CALICE AHCAL whereas the follow up experiment of T3B - the FastRPC experiment (see [65] for details) - uses RPC technology for the same purpose.

The timing properties of hadron showers differ significantly for different absorber materials. Tungsten is expected to have an increased delayed component relative to steel due to a higher contribution of evaporation neutrons for materials with high atomic number (details in 3.1.3). Absorber nuclei excited by inelastic interactions within the hadron shower release neutrons with a certain decay time. When interacting within the calorimeter, these neutrons initiate delayed energy depositions a fraction of which is visible to the active detector material. Scintillating plastic has a high probability to interact directly with delayed neutrons (via elastic scattering processes) due to its high hydrogen content, so it was chosen to be the right detector material for T3B to measure the delayed shower part. Since tungsten as well as steel will be used as absorber material within the calorimetric system of CLIC (in the barrel and endcaps, respectively) [27], a detailed comparison of its shower timing properties is desirable. The T3B experiment is able to deliver this.

When trying to optimize a detector system before construction one has to rely on the accuracy of Monte Carlo (MC) simulations to reproduce the physics correctly and study computer generated MC data sets. MC simulation frameworks - the most prominent of which is called Geant4 [66] - use so-called physics lists. These lists are often based on physical models of particle interactions at various energies, with parameters tuned to available experimental data (see Section 5.2). One of the most reliable and best tested lists is called QGSP_BERT. It is chosen to be the default physics list for the LHC experiments [67] and was used for the physics benchmark tests for the CLIC Conceptual Design Report [27] which studies the physics potential of a CLIC detector.

But QGSP_BERT and most other physics list do not respect the timing properties of hadron showers in detail. High precision extensions of the well proven physics lists that treat neutron interactions with high accuracy are available in the newer versions of Geant4. In the context of a CLIC detector it is desirable to design an experiment that measures particle showers in a time resolved manner and to optimize the new physics lists with the data acquired. This is the major motivation of the T3B experiment.

4.2 Design of the T3B Experiment

The design of the T3B experiment is governed by three major aspects:

Fast Timing Capability: Hadronic showers evolve at a timescale in the range of nanoseconds (see Section 3.1.3). The hardware components detecting the energy depositions within such showers have to be capable of creating a signal response at a timescale comparable or smaller. Furthermore, the data acquisition hardware must be able to digitize that signal with a minimal loss of timing accuracy.

Similarity to the CALICE AHCAL: The T3B experiment should not only measure the timing of hadronic showers, but also evaluate the timing capability of the existing and well-proven detector technology used for the CALICE AHCAL prototype. Staying as close as possible to the particle detection components of the AHCAL, namely the scintillator cells, optimizing them for fast timing measurements and proving their operational stability under test beam conditions gives rise to the possibility of upgrading the next calorimeter prototype.

Fulfill Test Beam Requirements: All components used for T3B must be fit to cope with the test beam environment. At test beam facilities particles arrive in short bunches of particles - so-called spills - of a certain length and with a certain periodicity that depends on the accelerator. The workflow of the data acquisition hardware and software has to be optimized to handle this spill structure. It must record as many particle spills as possible to maximize the statistics and store the data to disk before the next spill arrives at the experiment.

The different hardware components, their properties and their fitness to meet these requirements will be elaborated in the following.

4.2.1 Detector Components of T3B

The scintillator cells used for the T3B experiment are similar to the ones used in the CALICE AHCAL. Nevertheless, there are differences due to the optimization of T3B for timing measurements and due to technological advances since the AHCAL was assembled in 2005/2006. Figure 4.1 shows how the different components were assembled into the final T3B cell module.

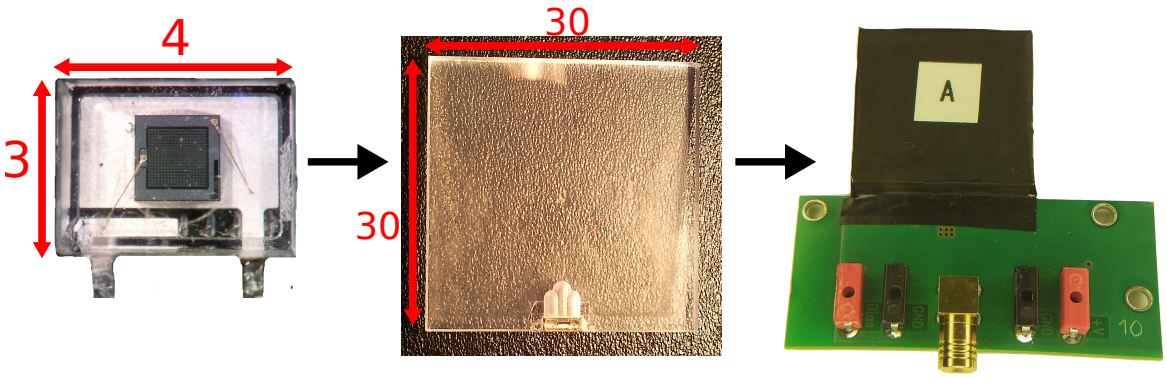

Figure 4.1: Assembly process and components of a T3B scintillator cell. Left: Hamamatsu SiPM of the type MPPC-50 P-Type. Center: Scintillator tile with attached SiPM and inserted dimple. Right: Completely assembled T3B cell attached to a preamplifier board. All dimensions are given in millimeter.

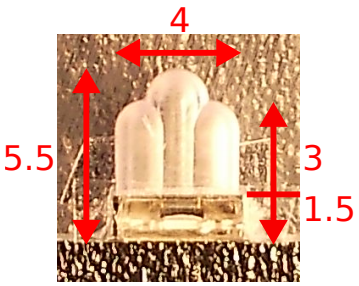

Figure 4.2: Picture of the dimple drilled into the T3B tiles and of the SiPM coupled to it. All dimensions are in millimeter.

In the production procedure, a silicon photomultiplier of the type MPPC-50 P-type [54] with translucent casing is coupled directly via air gap to one side of a plain scintillator tile of the type Bicron-420 [57] (see Section 3.3.3). The SiPM is inserted into a gap that matches the dimensions of its casing. That way the SiPM is aligned to the center of the side face of the tile. The SiPM-tile entity is then enclosed on all tile faces by a highly reflective mirror foil [68] and a low reflective and low transmissive black absorber foil [69]. In the final step, the packaged tile is soldered to a custom preamplifier board designed and produced at the Max-Planck-Institute for Physics in Munich (MPI) [70]. The board needs a supply voltage of 5V to power the amplifier and a bias voltage of $\sim 70\,\mathrm{V}$ that is supplied and device specific to the powered SiPM. The SiPM signal is amplified by a factor of 8.9 and read out by a SMB connector (for details on the board design see [52]). Table 4.1 shows a summary of the individual components and their specifications.

In contrast to the scintillator tiles used for the CALICE AHCAL, the T3B tiles are designed without embedded wavelength shifting fiber (WLS). This is made possible by the advent of blue-sensitive silicon photomultiplier in the last years (e.g. the MPPCs from Hamamatsu). It simplifies the production procedure significantly, but comes for the price of a non-uniform signal response meaning that number of photons collected by the SiPM varies largely depending on where a particle traverses the tile. To regain the uniformity a dimple of optimized shape is drilled into the tile at the SiPM coupling position (see Figure 4.2). More details on tile uniformity optimization studies can be found in [71] or [14]. Avoiding the WLS also improves the timing performance of the T3B cells. The absorption and re-emission of light by the wavelength shifter introduces a decay time constant of the order of a few nanoseconds that delays the time of arrival

Detector Component	Manufacturer	Dimensions	Specifications
MPPC-50 P-Type	Hamamatsu	Case: $4 \times 3\,\mathrm{mm}^2$, Sens area: $1 \times 1\,\mathrm{mm}^2$	50 micrometer pixel pitch
BC-420 Scintillator Tile	Saint Gobain	$30 \times 30 \times 5\,\mathrm{mm}^3$	SiPM insertion gap, uniformity dimple
Radiant Mirror Foil	3M	encloses all tile faces	$> 90\,\%$ reflectivity for $> 400\,\mathrm{nm}$
Black Al Foil BKF24	Thorlabs	encloses all tile faces	$< 20\,\%$ reflectivity for $380 - 850\,\mathrm{nm}$, small transmission
Preamplifier Board	custom prod.	$\approx 6 \times 6\,\mathrm{cm}^2$ minus cut outs	Amplification factor of 8.9 in relevant bandwidth

Table 4.1: Main specifications of the components used within the T3B cell modules.

of photons on the SiPM. That way the rise time of the detected signal is stretched which reduces the accuracy to time stamp the energy deposition of tile traversing particles (see Figure 4.3, left). Furthermore, the total signal width and therefore the time necessary to integrate over a large fraction of the signal is increased significantly. A large scale calorimeter assembled with tiles with embedded WLS would need to integrate longer to achieve the same energy resolution compared to a calorimeter that uses directly coupled tiles (see Figure 4.3, right).

For T3B, MPPCs with a pixel pitch of $50\,\mu\mathrm{m}$ were used. This guarantees a relatively high photon detection efficiency (PDE) of above $20\,\%$ for an overbias of $\approx 1.5\,\mathrm{V}$. At the same time the afterpulsing probability is with less than $25\,\%$ moderately small [72] and the darkrate with $\approx 500\,\mathrm{kHz}$ at an acceptable level [54] as we will see in Chapter 5 (compared to the other available MPPC devices with $25\,\mu\mathrm{m}$ and $100\,\mu\mathrm{m}$ pitch, respectively). These three parameters are most relevant for the timing performance of the T3B cells. A high PDE allows for the detection of even small energy depositions within the T3B cell. A high afterpulsing probability and dark rate, on the other hand, can fake late energy depositions and therefore increase the systematic errors on the timing measurements.

Bicron-420 is with a light emission rise time of $0.5\,\mathrm{ns}$ and pulse width of $1.3\,\mathrm{ns}$ (FWHM) one of the faster scintillator materials on the market. These time constants make the scintillator one of the factors limiting the signal time stamping accuracy and the width of the detected light signal. Another factor is the unwanted but existing self scintillation of the mirror foil which might have a long time constant and cause the late emission of photons. Furthermore, timing effects of the SiPM contribute some of which will be eliminated during the calibration procedure discussed in Chapter 5. A minor contribution originates from the photon travelling time within the scintillator which is prolonged by the high reflectivity of $> 90\,\%$ of the attached mirror foil.
The black absorber foil that encloses the tile has a very low and lab proven light

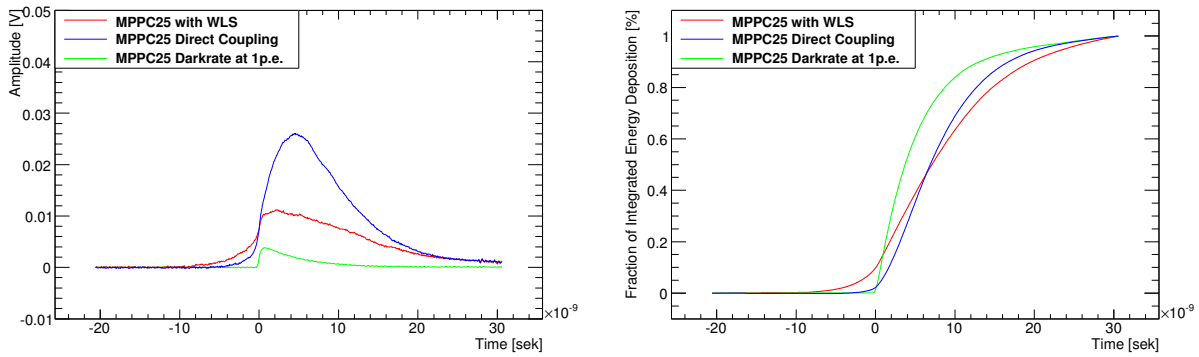

Figure 4.3: Photon signal delay introduced by a wavelength shifting fiber. Left: The averaged signal of traversing electrons originating from a Sr-90 source for a tile of the CALICE AHCAL with WLS (red) and a directly coupled tile with BC-420 scintillator and applied dimple (blue). The signal of a single photon equivalent is shown for comparison (green). Right: Fraction of the total signal detected at a certain point in time. In the case of direct coupling, it takes 15.1 ns for the signal fraction to increase from 10 % to 90 %. With embedded WLS it takes 19.5 ns.

transmission that minimizes the probability for ambient light to reach the SiPM. Otherwise, ambient light would represent an additional source of error on the timing measurements.

4.2.2 T3B Layer Setup

15 T3B scintillator cells were assembled on an aluminium base plate with a size of $1 \times 1\,\mathrm{m}^2$ (see Figure 4.4, left) matching the lateral size of the CALICE AHCAL prototype. The cells were positioned in a strip that extends by 449 mm from the center to one side (see Figure 4.4, right). The tiles have a width of 30 mm and a tolerance of 1 mm in between for the enclosing mirror and absorber foil. The strip is positioned on the base plate such that the lateral location of the central T3B tile matches the lateral location of the central tile of the CALICE AHCAL the particle beam is usually focussed on at the test beam (tile 46/46 in the CALICE numbering scheme meaning 46 cm from the bottom and side of the active area of an AHCAL cassette). Due to the temperature sensitivity of the SiPM (see Section 3.3.2) each cell is equipped with a 4-wire temperature sensor of the type PT-1000 - a platinum based resistance thermometer (PRT) which changes its resistance according to the ambient temperature. The PRT is attached closely to the position of the SiPM of the cell. To protect the electronics from physical damage, ambient light and electronic pick up noise, an aluminium cover is mounted on the base plate and the resulting T3B cassette is sealed by black masking tape. The cell strip is by design automatically aligned to the cells of the AHCAL cassettes when the T3B cassette is inserted into one of the slots of the tungsten or steel absorber stack.

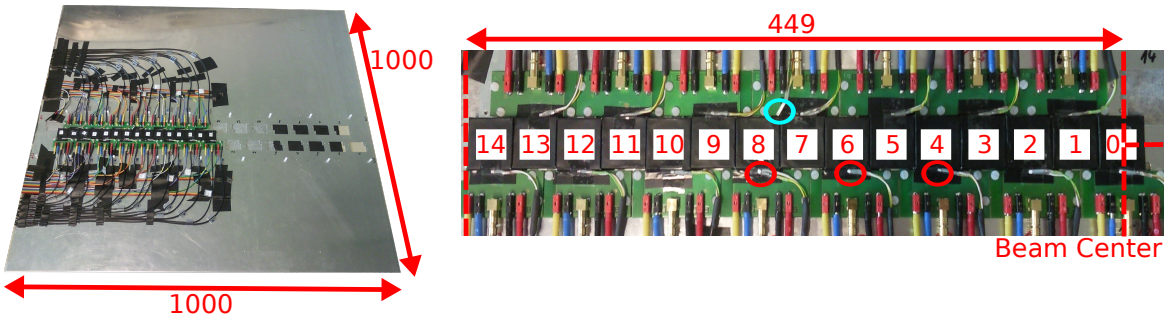

Figure 4.4: Picture of the whole T3B layer (left) and zoomed view on the assembly of the strip of scintillator cells (right). Each cell has its own temperature sensor that is attached close to the SiPM (shown by red circles). Additionally one independent layer sensor was attached (blue circle). All dimensions are given in millimeter.

4.2.3 Operational Hardware Components

After finishing the assembly of the T3B cassette, the preamplifier and the photosensor need to be supplied with the correct voltage, the resistance of the temperature sensor needs to be monitored and the signals of the 15 SiPMs need to be recorded. We will highlight some key aspects of the operational hardware used for the T3B experiment in the following.

Picoscopes

Up to five USB-Oscilloscopes of the type PS6403 [73] (see Figure 4.5, right) were used to acquire the data of the experiment. They record the SiPM signals of the T3B cells, digitize them, buffer the data and transfer it via USB to a PC which stores it to the hard drive. The PS6403 series has a couple of specifications that make it the ideal choice for a test beam experiment that focuses on the time resolved recording of fast signals. For one, the oscilloscope can sample four signals with a rate of 1.25 GSamples/sec simultaneously. The delivered driver can handle oscilloscope requests and callbacks in a multithreaded way such that multiple units can be operated from the same PC at the same time. In contrast to most regular oscilloscopes, the PS6403 have a very large internal buffer of 1 GB and a so-called rapid block mode. This means that the user can specify the number of signals he wants to acquire, store them in the buffer and transfer all of them to the PC only afterwards. By this, the PS6403 can achieve a signal acquisition rate of up to 1 MHz until the buffer is filled. The data transfer takes then up to 40 seconds provided the whole buffer was filled. Additionally, it can check the number of signals that are in the buffer and trigger the transfer to the PC upon request. This is extremely useful for test beam experiments in which the particles arrive in short spills. During the spill there is no time for the data transfer of individual signals as it takes orders of magnitude longer than the time available till the next spill particle arrives at the calorimeter (details on the spill structure at the different accelerators will

Figure 4.5: Picture of the Picoscope PS2203 (left) and PS6403 (right).

be explained later in Section 4.3.1). Using the rapid block mode, the user can record all events within a spill, trigger the data transfer once the spill is finished and be ready for the next spill on time. This guarantees a maximal efficiency in recording the particle events the accelerator can deliver.
Concerning its functionality, the PS6403 is a normal oscilloscope. One can configure the vertical range and analog offset of the recorded waveform, adjust the sampling rate and configure various trigger options. For the test beam operation the external trigger option is of major relevance. An external trigger signal can be fed to the back plane of the oscilloscope and the trigger threshold can be adjusted correspondingly. This way all five oscilloscopes can be triggered simultaneously provided one splits a trigger signal and chooses an identical trigger cable length.

The PS2203 oscilloscope series (see Figure 4.5, left) has a low maximum sampling rate of 40 MSamples (when operating one of the two channels) and a buffer depth of only 8000 samples [73]. This suffices to record the spill signal that is delivered by the accelerator to indicate when the particle spill starts and stops. The PS2203 can trigger the initialisation of the rapid block mode of the five PS6403 oscilloscopes via the data acquisition software (see Section 4.2.4) after the start of the spill signal, and their data transfer to the PC after the spill has finished. A PS2203 oscilloscope is therefore vital for the successful test beam operation of T3B. One PS2203 device was used for that purpose.

Power Distribution System

Two power distribution boxes (PDB) have been assembled to supply the signal preamplifier and the SiPMs with their respective voltages. They consist of a breadboard which hosts the circuitry and a plastic box for protection. The preamplifier needs an operating voltage of 5 V. An external power supply feeds this voltage into the first PDB which simply parallelizes it 15 times so that it can be wired to the T3B cells.

The second PDB is somewhat more complicated. The device specific operating voltages

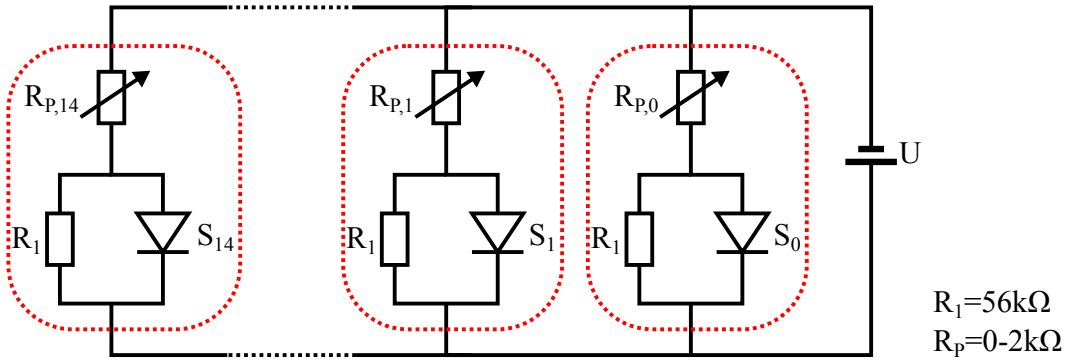

Figure 4.6: Electronic circuit of the power distribution box for the SiPM bias voltage. Each SiPM has its own circuitry to adjust to its device specific bias voltage (shown by red circles) consisting of a resistor in parallel to the SiPM and an adjustable potentiometer positioned in series to those two components.

of the used SiPMs vary in a range from 70.9 V to 72 V. The supply voltage U (see Figure 4.6) is fed into the PDB by an external power supply and has a value of e.g. 73 V (this varies depending on the test beam phase). Each SiPM has its own circuitry which reduces this voltage to its individual bias voltage. The resistance of the potentiometer $R_{P,i}$ can be manually adjusted in a range of $0 - 2\,\mathrm{k\Omega}$ and the ratio of the resistance R_1 (fixed to $56\,\mathrm{k\Omega}$) to the total resistance R_{tot} determines the voltage $U_{S,i}$ that is applied to the respective SiPM:

$$U_{S,i} \approx \frac{R_1}{R_{tot}} \times U = \frac{R_1}{R_1 + R_{P,i}} \times U \tag{4.1}$$

where i is the index of the SiPM S_i ranging from 0 to 14.
Note that the resistance of R_1 and $R_{P,i}$ have been chosen low enough that the resistance of the SiPM can be assumed as infinite and high enough that the overall power consumption is small. The applied voltage can be adjusted in a range of $70.5\,\mathrm{V} - 73\,\mathrm{V}$ which covers the needed range with a convenient tolerance. This PDB represents a very simple and easy realizable way to power multiple SiPM with their specific bias voltages.

Temperature Monitoring System

15 PT-1000 sensors attached to the T3B cells and up to 6 PT-1000 sensors positioned in the test beam area are read out by a temperature board designed and constructed at the MPI. It measures the temperature values periodically and transfers them via USB to the PC which stores them to disk. It is beyond this thesis to explain every detail of the board design. We will only highlight some key aspects relevant for its operation. The heart of the board is an integrated circuit (IC) from Texas Instruments of the type ADS1248IPW [74] which is a 24-bit analog to digital converter specifically designed to measure the resistance values of temperature sensors with high precision. One chip can read out three PT-1000 sensors and takes ~ 2 seconds for it. Up to 21

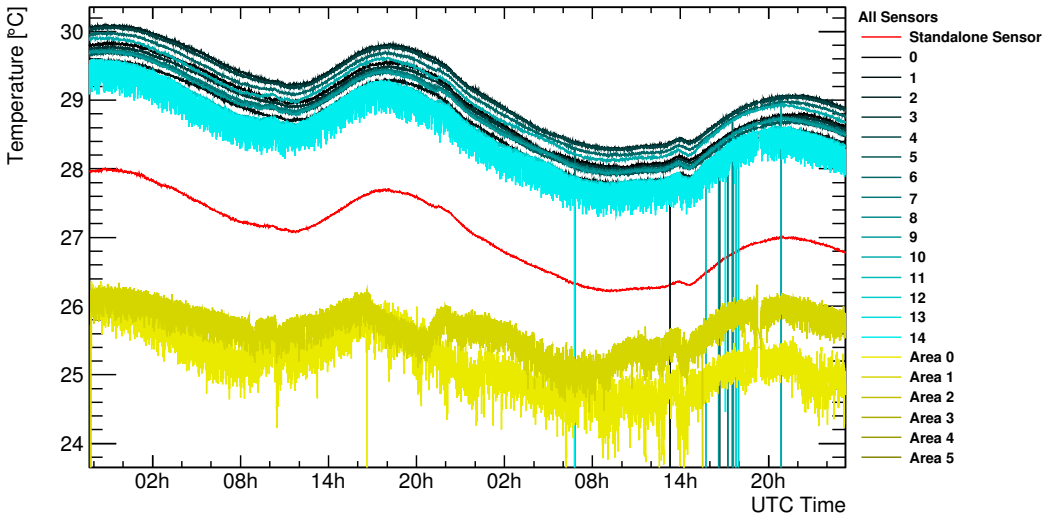

Figure 4.7: Temperature development of the T3B cells as measured by the temperature monitoring system for two days at the test beam. 15 PT-1000 (black to turquoise, labeled 0-14) and one standalone PT-100 sensor (red) were attached to the T3B cells. 2 PT-1000 sensors (yellow) were monitoring the temperature of the test beam area. Up to 6 area sensors can be connected (labeled Area 0 to Area 5). The day-night cycle can be clearly identified.

temperature sensors can be wired to the board. They are read out one after another, so one whole measurement sequence takes up to ~ 15 seconds. This is fast enough because temperature changes occur at the test beam on a timescale of hours. The day-night cycle is the main source of variations (see Figure 4.7). Due to systematics in the board design every third channel shows a higher measurement error. A relative precision of $\pm 0.015\,°\mathrm{C}$ could be achieved for the 14 good channels and a precision of $\pm 0.25\,°\mathrm{C}$ for the other 7 channels. These channels were used to monitor the temperature of the test beam area and for the outermost T3B cell. Measurement outliers that occur from time to time can be easily rejected in the analysis.

Additionally, one independent layer sensor of the type PT-100 was read out by a digital multimeter of the type Agilent 34411A [75]. Its measured temperatures are about $2\,°\mathrm{C}$ lower than for the cell sensors since the main source of waste heat is the used preamplifier located underneath the center of the cell board and the standalone sensor was positioned between T3B cell number 7 and 8 (see Figure 4.4). The standalone sensor achieves a relative precision of $\pm 0.01\,°\mathrm{C}$. Due to the large number of sensors and the high measurement precision, the T3B temperature monitoring system allows for a good cross check of the stability of the SiPM performance over time and for an accurate determination of the temperature sensitivity of every SiPM individually.

4.2.4 T3B Software Development

Having the T3B layer assembled, the T3B cells powered and connected to the Picoscopes, one needs to configure the oscilloscopes, operate them in a test beam optimized way and control and validate the recorded data. A new data acquisition software and an online monitor suiting the requirements for a successful T3B operation have been designed and developed from scratch.

Data Acquisition Software

Unlike the data acquisition software (DAQ) provided by Picotech [73], the T3B DAQ can control multiple Picoscopes at the same time, it provides a repetitive acquisition loop that can be started and interrupted by an external trigger source and it can switch dynamically between predefined sets of oscilloscope configuration settings. The T3B DAQ is a C++ based, object oriented framework built around the oscilloscope driver delivered by the manufacturer and accessed by the user via a graphical user interface based on Qt [76]. A picture of the main window of the T3B DAQ is shown in Figure 4.8. It is subdivided into a section for run steering that can be handled by every member of the crew working at the test beam, a section that is meant to be only modified by T3B experts and a section that notifies the user of the progress of the run. In the steering section the user can select a set of preconfigured oscilloscopes settings and start and stop the acquisition loop by clicking the corresponding button. In the expert section the user can enforce an interruption of the acquisition in case of an error and modify the run number and the location the data is saved to. Here, the user can furthermore switch to the configuration window (not shown) which allows a modification of the oscilloscope settings such as the vertical range, the time base, the trigger option and more. The notification section indicates the current status of the five PS6403, the PS2203 oscilloscope and the DAQ and displays additional information on the data acquired so far, the disk space used and the duration of the ongoing run. Under run notes the user can document any kind of information related to the run he is acquiring.

The underlying workflow of the DAQ software under test beam conditions, hidden underneath the graphical interface, is shown in Figure 4.9. After the start-up of the DAQ and the connected oscilloscopes, the control is passed to the user who needs to configure or just select the settings suitable for the next run and eventually start the data taking. Then the DAQ software enters the fully automated acquisition loop. The settings are uploaded to the oscilloscopes and the DAQ waits for the particle spill to arrive in the following. During this time, the PS2203 is in capturing mode and notifies the DAQ of the spill start, meaning that it detected the rising edge of the spill signal delivered by the accelerator. When this happens, the capturing mode (rapid block) of the PS6403 is activated and the five oscilloscopes are triggered synchronously by an external source indicating the arrival of individual spill particles (see Section 4.3 for details on the trigger setup specific for the different test beam phases). When the PS2203 detects the end of the spill the rapid block mode of the PS6403 is interrupted

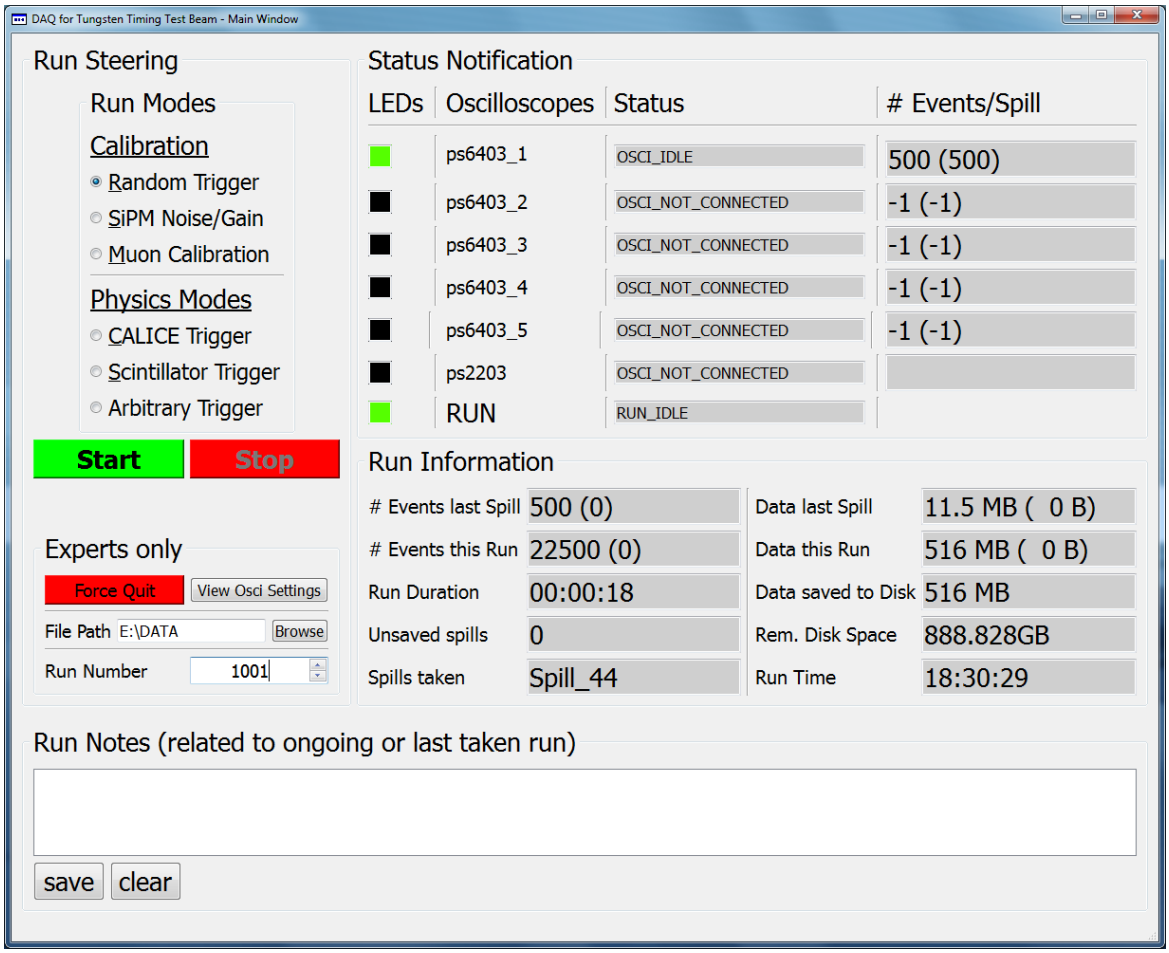

Figure 4.8: Picture of the main window of the data acquisition software.

and they transfer the acquired data to the DAQ PC. Afterwards the settings of the so-called intermediate run mode (IRM) are uploaded to the PS6403. This mode is usually used to record random thermal darkrate from the SiPMs. It allows for a live determination of the SiPM gain which is crucial for the calibration procedure of the T3B data (see Chapter 5). In the IRM the PS6403 capture a predefined number of events in self triggered mode provided this does not take longer than a specified maximum time T_{max}. Otherwise the capturing will be interrupted. When the IRM data is transferred to the DAQ PC, the physics mode settings are uploaded to the oscilloscopes and the whole acquisition sequence starts over. The run can be ended at any time by the user, but this does not cause the DAQ to interrupt the sequence, but it waits till the physics and the intermediate run mode are finished and drops out of the sequence in a controlled way then. For a successful test beam operation the DAQ sequence and the settings needed to be optimized in terms of speed and timing so that the oscilloscopes finish all activity before the arrival of the next spill. The remaining limiting factor is the data transfer speed achievable with the USB 2.0 standard. It restricts the amount of events that can be captured per spill and that the T3B experiment can process on time. More details on the data acquisition software can be found in [77].

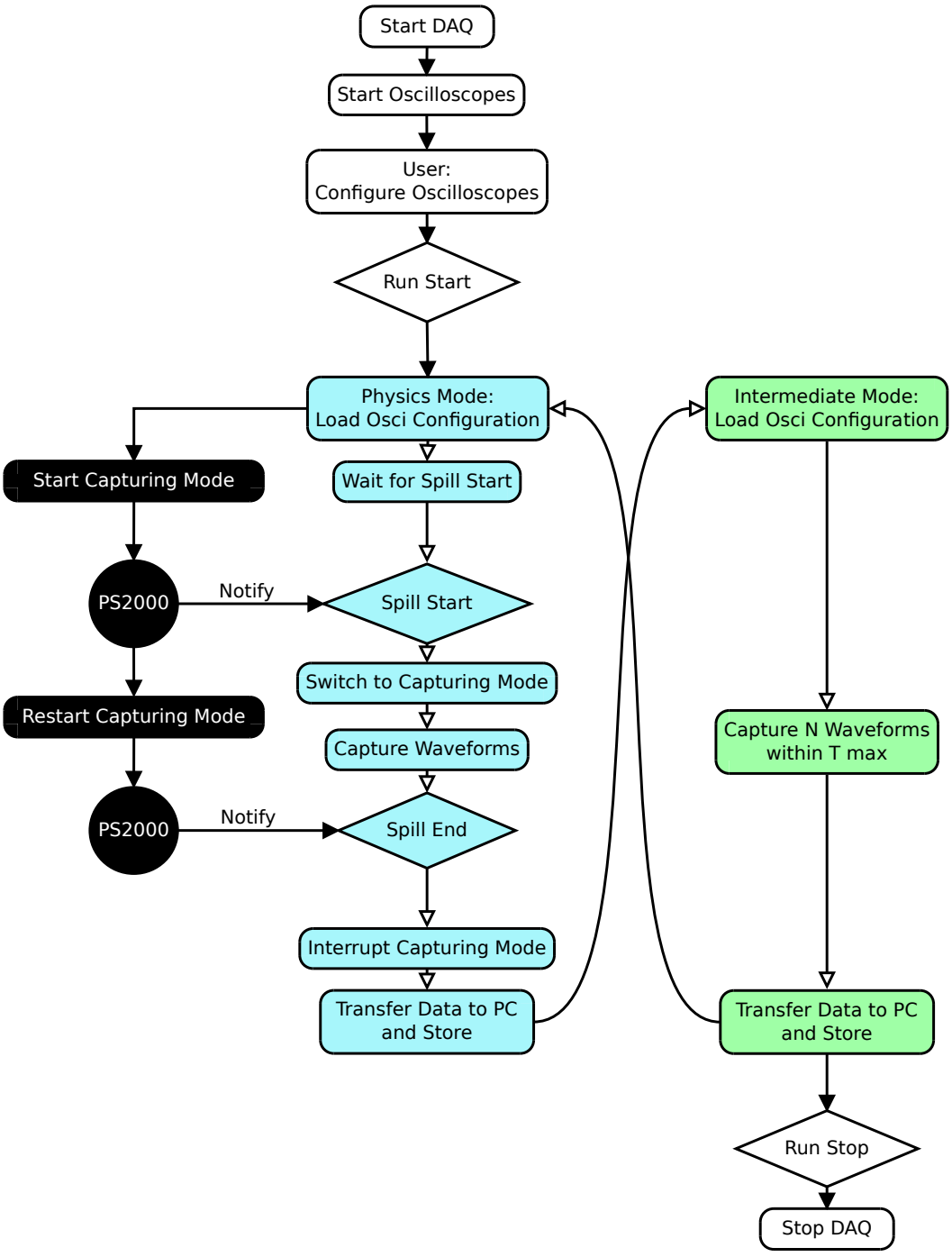

Figure 4.9: Workflow of the data acquisition software under test beam conditions. After the initialisation and configuration of the oscilloscopes (top), the acquisition loop can be started. The physics run mode recording the particle events (blue for the PS6403, black for the spill triggering of the PS2203) is alternated by the intermediate run mode recording a set of calibration events (green) until the user stops the acquisition (bottom).

Online Monitor

A C++ based online monitor (OM) using the data analysis framework ROOT [78] has been designed as a complement to the T3B DAQ software. The OM allows the user to verify the successful operation of the T3B hardware components and the quality of the data while the acquisition of a run is still ongoing. It displays the captured waveforms of all activated oscilloscope channels, their integral and the integral of the waveforms captured in the IRM. Furthermore, the OM can show if all PS6403 oscilloscopes are running synchronously, meaning that they triggered the same number of events for a given spill. It can display a time distribution of the so far acquired statistics per spill and in total, and it can show a preliminary lateral hit profile in which the number of hits per T3B cell are histogrammed.

Pedestal shifts and instabilities in the SiPM operation such as a changing gain can be identified through the waveform integrals. Pick up noise through imperfect shielding manifests itself through spikes or interference signals in the waveforms. Problems with the beam quality such as an insufficient focussing manifest themselves in the hit profile. Lost spills manifest themselves in the statistics plots and general errors in the setup manifest themselves potentially in all plots. This is just a small selection of the potential problems at the test beam that can be noticed quickly by monitoring the data with the OM.

4.3 Test Beam Campaign

T3B undertook a rich test beam programme consisting of one phase at the PS (three weeks, November 2010), three phases at the SPS (three times one week, June, July, September 2011) together with the CALICE analog tungsten HCAL and one phase at the SPS (one week, October 2011) together with the CALICE steel SDHCAL observing particle showers in a wide energy range between 2 and 300 GeV. Table 4.2 shows the acquired statistics for the various test beam periods and for the particle energies relevant for the analysis in Chapter 6. In this section, we will give details on the operation of the respective accelerators, explain the trigger and signal distribution system the T3B experiment was connected to and show under which premises the T3B detector was commissioned. We will finally point out the differences of the setups and run conditions for the various test beam phases.

4.3.1 Accelerator and Beam Line Characteristics

With a maximum proton energy of 28 GeV and a circumference of 628 m, the Proton Synchrotron was the world leading accelerator machine by the time it was commissioned at CERN in 1959. 17 years later from 1976 on, the Super Proton Synchrotron with a circumference of 7 km could deliver a proton energy of up to 400 GeV (later 450 GeV) to

Hadron Data			
Test Beam / Energy	PS	SPS AHCAL	SPS SDHCAL
10 GeV	5.3 M Events	-	-
60 GeV	-	4.6 M Events	1.6 M Events
80 GeV	-	5.1 M Events	2.0 M Events
180 GeV	-	1.6 M Events	1.2 M Events

Muon Data			
Test Beam / Energy	PS	SPS AHCAL	SPS SDHCAL
6 GeV	0.02 M Events	-	-
180 GeV	-	2.3 M Events	13.4 M Events

Table 4.2: Acquired statistics of the T3B experiment at the various test beam phases for hadronic particle shower events and for muon data.

the experiments using the PS as a preaccelerator. Today the SPS acts as an injector to the Large Hadron Collider which will eventually be capable to accelerate the protons to the design energy of 7 TeV. Additionally, the PS and SPS deliver protons to fixed target experiments such as the CALICE calorimeter prototypes and the T3B experiment. The test beam experiments are located at different beam lines within experimental halls (East Area for the PS, North Area for the SPS). Each beam line is consecutively served by the accelerator following a certain periodicity that is called supercycle and that is decided on by the PS and SPS committees before the respective run periods.

The monoenergetic proton beam stored within the accelerators is not delivered to the respective beam lines directly. Instead the protons are steered on a target creating secondary particles of various momenta and masses. A magnetic deflection system steers particles of the desired momentum through a collimator. This is also called wobbling. One can easily choose between a positive or negative particle beam by changing the polarity of the magnets. A positive particle beam as arriving at the experiment consists primarily of protons, π^+ and μ^+, whereas a negative beam comprises mainly π^-, e^- and μ^-. The exact composition depends on the target type, the selected beam momentum and various other factors.

In many beam lines a set of two Cerenkov counters allows for an event-by-event identification of the different particle types. Here, a Cerenkov counter is realized as an airtight tube positioned along the beam line and filled with a gas (e.g. CO_2, Nitrogen or Helium) at a certain pressure. If a beam particle traverses the tube with a velocity faster than the speed of light within the medium, a flash of light caused by the localized polarization of the gas is emitted in forward direction. The inside of the tube is covered with reflective mirror foil and a photomultiplier tube (PMT) attached to one side of the Cerenkov counter detects the light signal. Increasing the gas pressure results in a

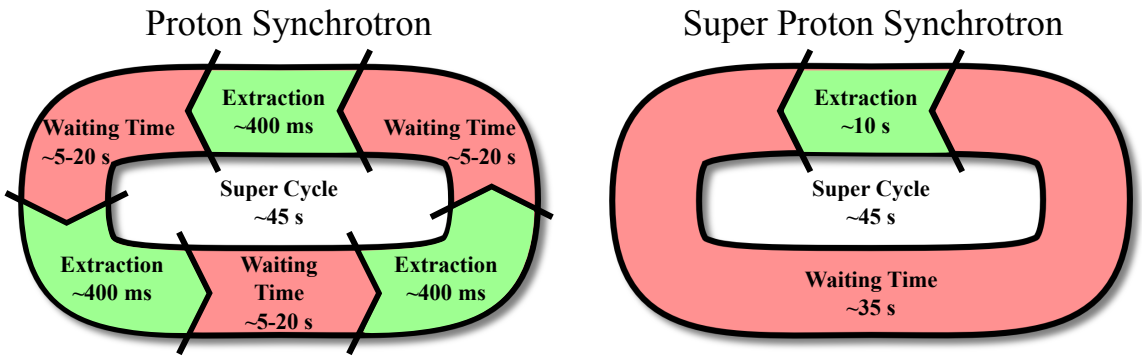

Figure 4.10: Sketch of the spill delivery sequence to the CALICE/T3B experimental area for one supercycle of the PS and SPS at CERN. During the extraction (green) the machine delivers particles to the experiments followed by a waiting time (red) in which other experimental areas are served.

decrease of the speed of light within the medium. Since all particles within the beam have the same momentum after the wobbling, heavier particles have a lower velocity and vice versa. Now the pressure of the gas can be adjusted such that the speed of light is slightly higher than the velocity of e.g. the protons within the beam. Therefore, the protons cannot induce Cerenkov radiation whereas all lighter particles can. If one adjusts the pressure of a second Cerenkov counter such that all particles lighter than pions create light, one can efficiently identify pions. The pion identification signature would be: Cerenkov A: On, Cherenkov B Off. Note that the gas pressures necessary to identify e.g. pions varies with the beam momentum. If the required pressures are out of the operation range of the used Cerenkov counter, the particle ID can only be determined with low efficiency or not at all.

In case the Cerenkov counters cannot provide a reliable particle ID, the CALICE calorimeters have further options. In the offline analysis, one can cut all events that do not start a shower before the last active layer of the calorimeter. This removes all non-interacting hadrons - so-called punch-throughs - but also all muons from the analyzed data set. The radiation length of electrons or positrons is significantly smaller than the nuclear interaction length of hadrons (see Section 3.1). Therefore, one can cut events that deposit a large fraction of their energy within the first few layers of the calorimeter to efficiently reject pure electromagnetic showers.

Very long and dense shutters are located along the beam line to stop the beam if access to the test beam area is required. The only measurable particles that traverse all obstacles with high probability are muons. By closing all shutters and defocussing the beam one can irradiate the calorimeter almost exclusively with minimum ionizing particles. Such muon runs are very valuable for the calibration procedure of the T3B and CALICE AHCAL cells and have been carried out at all test beam phases (see Chapter 5).

Figure 4.10 (left) shows the supercycle of the PS and SPS as experienced by the T3B experiment during its test beam phases. The PS delivered up to three spills of particles

within a supercycle of 45 s to the T9 beam line in which CALICE/T3B was located. The particle energy could be adjusted in a range of $1 - 10$ GeV. Each spill had a length of ~ 400 ms in which T3B recorded on average ~ 600 particle events synchronously to the CALICE AHCAL. The variable waiting time of $5 - 20$ s was a challenge for the T3B DAQ. The operation mode of T3B had to be optimized to be capable of processing the acquired events and the consecutive intermediate run mode in less than 5 s to avoid the loss of spills. During the SPS phases (see Figure 4.10, right), the supercycle was more constant. After a waiting time of ~ 35 s, a spill with a length of ~ 10 s was extracted by the machine and delivered to the H8 beam line. In H8, the particle energy could be steered in the range of $10 - 300$ GeV. When triggering particle events synchronously to the CALICE AHCAL, the T3B experiment could record up to ~ 2500 events per spill. The number of collected events per spill was limited by the finite event buffer size of the AHCAL electronics. Triggering standalone, the T3B DAQ is capable of processing up to 6500 events per spill and finishing the readout before the next supercycle starts (find more details on the trigger system in the next Section). In this mode, up to ~ 500.000 events can be accumulated per hour under stable beam conditions.

4.3.2 T3B Trigger System

The T3B experiment can acquire events in two different trigger modes: CALICE sync mode and standalone mode. Figure 4.11 shows a simplified sketch of the most relevant beam line instrumentation during the T3B test beam phases and essential parts of the trigger system. A more detailed elaboration can be found in [79]. Peculiarities of the various test beam phases will be discussed in Section 4.3.3. In the sketch, the T3B experiment is triggered in CALICE sync mode. First, the particle beam traversed two Cerenkov counters. Their signals were discriminated and then recorded by the CALICE and the T3B DAQ. This allows for an offline determination of the incoming particle type corresponding to the event.
Downstream of the Cerenkov counters was a veto scintillator positioned. This is a large scintillator of $30 \times 30\,\mathrm{cm}^2$ with a circular hole of 8 cm in diameter in the center and an attached PMT. If a beam particle propagates far from the beam axis, it will traverse the veto scintillator and trigger a veto signal that is recorded. Rejecting such events in the offline analysis can improve the beam collimation of the analyzed data set.

For hadron runs, the triggering of an event is performed by two $10 \times 10\,\mathrm{cm}^2$ scintillators located in the beam center and in front of the calorimeter. If both trigger scintillators detect light simultaneously, the coincidence signal is fed into the CALICE trigger electronics and induces the readout of all calorimeter cells. For muon runs two large $80 \times 80\,\mathrm{cm}^2$ scintillators located in front and behind the calorimeter were used to trigger the events. This assured nearly full coverage of the lateral area of the HCAL and the total penetration of minimum ionizing muons which is relevant for the calibration of all calorimeter cells. For a timing experiment like T3B, the size of the trigger scintillators is a crucial parameter. Usually a PMT is attached to one side of the scintillator. So the trigger signal of a particle that traverses in maximal distance of the PMT has a delay

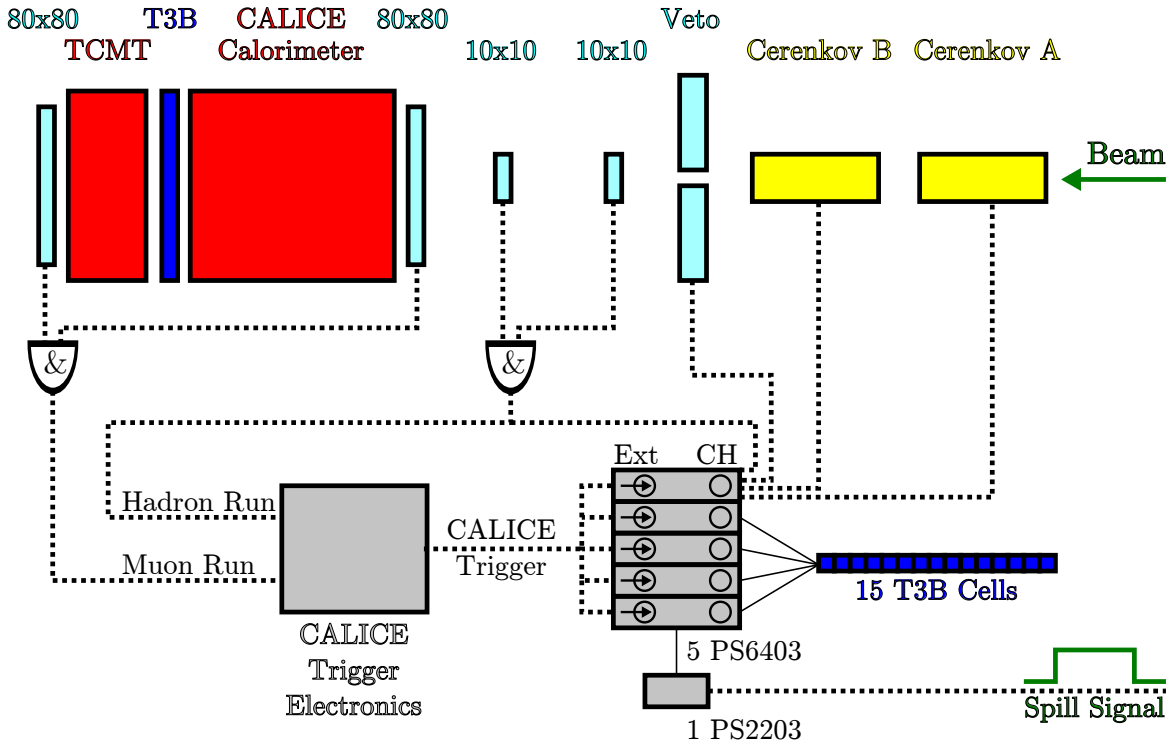

Figure 4.11: Systematic sketch of the beam line and the trigger setup of T3B together with the CALICE AHCAL (not to scale). TCMT stands for Tail Catcher and Muon Tracker. Not all elements were available for all run periods.

of $> 2\,\text{ns}$ with respect to a particle traversing close to it for a scintillator of 80 cm edge length. Furthermore, the time jitter increases since scintillation photons are emitted in random directions. For T3B, this results in a trade off between the coverage of a large cross section of the beam for larger scintillators and the capability of small scintillators for fast timing. For muons runs, good coverage is favoured whereas the CALICE team chose the smaller trigger scintillators for the triggering of the usually highly collimated hadron beam.

The CALICE electronics exhibits a certain dead time for the processing of an event ($\mathcal{O}(1\,\text{ms})$) and has a limited event buffer size. Therefore, the number of coincidence signals is significantly larger than the number of events acquired by the CALICE DAQ (see Figure 4.12). The T3B DAQ is not capable of assigning an individual timestamp to each of the recorded events. Thus, one needs to assure that the T3B DAQ records exactly the same events as the CALICE DAQ for a successful offline matching. Fortunately, the CALICE DAQ has a live trigger output. In the CALICE sync mode this output was multiplied and used to trigger the oscilloscopes of the T3B experiment simultaneously. So a successful synchronization relies on a spill-by-spill matching of the event count of T3B and CALICE. This is further complicated by the output of timeout triggers by the CALICE DAQ. In test beam operation, the T3B DAQ switches to capturing mode when the spill start is detected and stops it with the end of the spill signal. In this process, the capturing mode of the five PS6403 oscilloscopes is finished consecutively

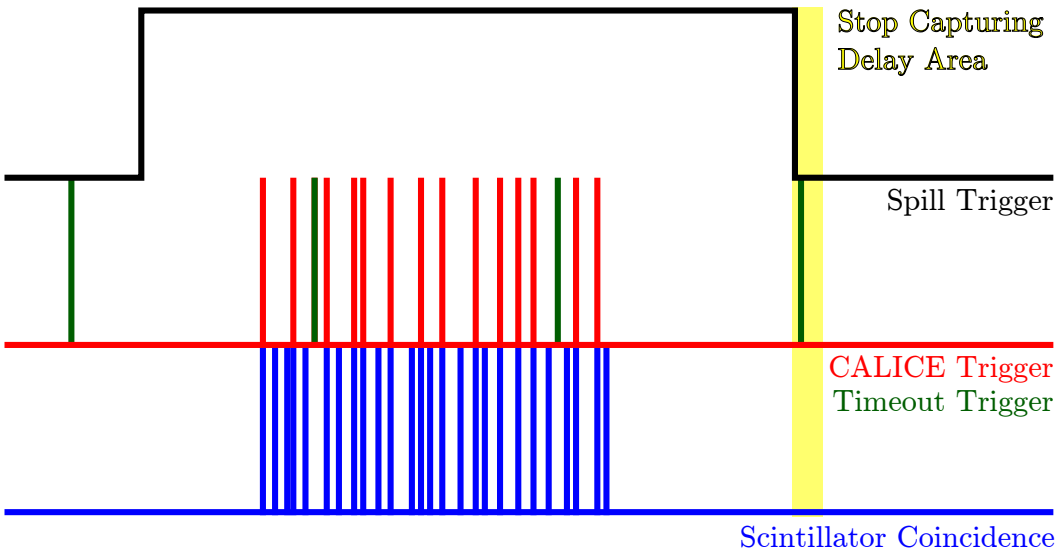

Figure 4.12: Sketch of the trigger signals needed for the test beam operation of the T3B experiment. A scintillator coincidence signal is created when a particle traverses two trigger scintillators simultaneously (blue). A fraction of these signals triggers the CALICE DAQ. The trigger output of CALICE is characterized by particle triggers (red) and timeout triggers (green) which can be distinguished since T3B records the scintillator coincidence signal of particle events explicitly. The event triggers occur within the spill. The spill start and the spill stop are indicated by a spill signal (black) supplied by the accelerator.

which takes a few milliseconds. If a trigger signal arrives within this time (see Figure 4.12), the number of captured events differs among the oscilloscopes. In addition to the beam trigger, the CALICE DAQ has a so-called timeout trigger which probes if the spill signal is still HIGH, meaning within the spill. The timeout trigger releases a trigger signal with a periodicity usually set in the order of 1 s. This can occur exactly when the oscilloscopes stop capturing consecutively and are the most probable reason for event mismatches. But since this case cannot be distinguished from a true mismatching of particle triggers, such spills have to be rejected completely. This effect reduces the statistics of T3B by approximately $5 - 10\,\%$.

When T3B is in standalone mode the oscilloscopes are triggered directly by the coincidence signal of the trigger scintillators. This increases the acquisition rate of T3B significantly, but excludes the possibility to combine the data of CALICE and T3B in the later analysis.

4.3.3 The T3B Test Beam Phases

The T3B experiment was part of the CALICE test beam campaign 2010/2011. It measured muon and hadron shower events being located behind the tungsten absorber stack equipped with the active layers of the CALICE analog HCAL and behind the

Figure 4.13: Pictures of the test beam setup of the T3B experiment together with the CALICE tungsten AHCAL (left) and the CALICE steel SDHCAL (right). The position of the scintillator cells of T3B is indicated by a blue strip.

steel absorber stack of the CALICE SDHCAL (see Figure 4.13). Table 4.3 gives an overview over the characteristics and differences of the five phases of the T3B test beam programme. This will be relevant for the calibration and analysis of the T3B data. At its first test beam phase, the AHCAL consisted of 30 layers and was extended to its full length of 38 layers later for the SPS periods. The SDHCAL consisted of 50 steel absorber and 40 active layers. Expressing this in terms of the nuclear interaction length of the respective calorimeter which determines the penetration depth of hadronic showers, one obtains $4.0\,\lambda_I$ and $5.1\,\lambda_I$ respectively for the AHCAL and $6.5\,\lambda_I$ for the SDHCAL. Since T3B was positioned behind the respective calorimeters, it was located at different depths, both geometrically and in terms of λ_I. We will investigate the effects of this in detail in Section 6.2.2.

Silicon photomultiplier have the disadvantage of being very sensitive to changes in the ambient temperature and the bias voltage applied (see Section 3.3). Due to technical reasons and seasonal changes both parameters changed significantly during the five test beam phases (see Table 4.3). The calibration procedure applied to the T3B data has to take these test beam specific conditions into account to minimize the effect of detector systematics on the analysis results.

The majority of the T3B data that was acquired together with the CALICE AHCAL was taken in CALICE sync mode. This allows for an offline combination of the two otherwise independent data sets and the usage of otherwise inaccessible trigger information. Table 4.3 shows the signal channels recorded by the T3B DAQ for the various test beam phases. 15 channels were occupied by the 15 T3B cells whereas one channel always recorded the scintillator coincidence to enable the distinction between true particle triggers and fake trigger events. Due to the lack of a fifth PS6403 oscilloscope for the early T3B test beam phases, the signal of the Cerenkov counters could not be recorded, which prevents T3B a priori from identifying particles of different types. Via data synchronization, T3B can access this information event-by-event from the CALICE

Test Beam Characteristics		AHCAL				SDHCAL
		PS 11/2010	SPS 06/2011	SPS 07/2011	SPS 09/2011	SPS 10/2011
Calorimeter	Absorber	Tungsten				Steel
	Abs. Layers	30	38			50
	Abs. Thickness	1 cm				2 cm
	Cal. Layers	30	38			40
	Cal. depth	4.0 λ_I	5.1 λ_I			6.5 λ_I
	Micromegas	✓	✗	✗	✗	✓
	TCMT	✗	✗	✓	✓	✗
T3B general	global ΔV_{bias}	0			+0.3 V	+0.1 V
	T sensors	1 PT100	1 PT100 + 15 PT1000			
	Average T	∼ 22 C°	∼ 29 C°	∼ 30 C°	∼ 28 C°	∼ 26 C°
T3B Trigger	Mode	CALICE sync				Standal.
	Scint. Overlap	10 × 10 cm^2				6×8cm^2
T3B Signal	T3B Cells	15				
	Cher A,B	✗ v.C.	✗ v.C.	✗ v.C.	✓	✓
	Scint. Coinc.	✓	✓	✓	✓	✓
	Veto	✗	✗	✗ v. C.	✓	✗

Table 4.3: Differences of the test beam setup for all run periods. The bias voltage applied to the SiPMs was not always identical. For some test beam phases, the overall bias voltage was increased by a certain value which is indicated by ΔV_{bias}. The abbreviation v.C. stands for via CALICE meaning that T3B is cannot retrieve this information, but the CALICE calorimeter did acquire it and it can be accessed when recording data in CALICE sync mode. Micromegas is a dedicated detector prototype module positioned in front of T3B at two test beam phases.

calorimeter, which was always logging all trigger signals. In the run period together with the SDHCAL, T3B was triggering exclusively in standalone mode to increase the statistics. Due to considerations related to the saturation of the gaseous detector layers of the SDHCAL, the rate of impinging particles was restricted to $\mathcal{O}(100)$ per spill whereas T3B can handle up to $\sim$ 6500 events per spill in standalone mode.

4.4 Potential and Challenges of T3B

Being located behind the calorimeter, the measurements of T3B rely on the fact that a fraction of the secondary particles of an hadronic shower traverses the calorimeter and leaks out of the back. This is the part of the shower that T3B can detect provided a T3B cell is hit. The T3B strip of cells covers only a small lateral area of 30 × 450 cm^2 compared to the 1 × 1 m^2 of the calorimeter. So the fraction of events in which T3B was hit is small. Figure 4.14 shows the lateral hit fraction of the 15 T3B cells. Whereas

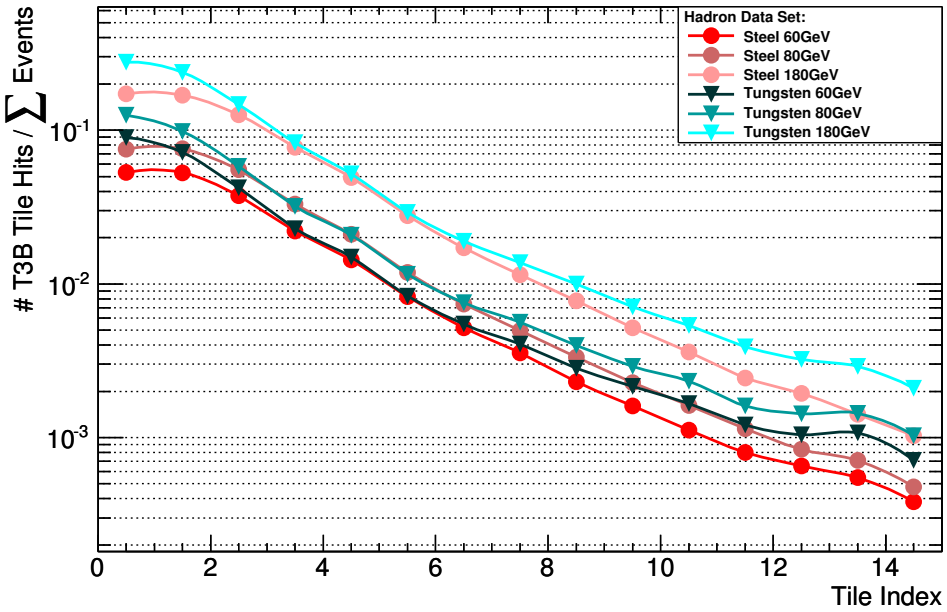

Figure 4.14: Fraction of events in which the T3B cells were hit by a particle (in which >15 photon equivalents were detected within the total acquisition window of 2.4 μs) for data sets with steel and tungsten absorber at three different particle energy points.

the central cell is hit in 28 % of all events for very high energetic showers of 180 GeV, the outermost cell in a distance of 43.4 cm from the beam center is only hit in 0.2 % of the cases. The hit probability drops further for lower shower energies. This means that a large number of events needs to be collected to draw reliable conclusions. T3B is a high statistics experiment. It is not designed to measure hadronic showers on an event-by-event basis. For most shower events, the T3B cells are not hit at all and if a part of the shower leaks out of the calorimeter usually only few T3B cells are hit. But on average showers are radially symmetric. With millions of events the average lateral timing profile of hadronic showers is measurable with the T3B detector.

Furthermore, the first hadronic interaction can happen in various depths within the calorimeter. By the definition of the nuclear interaction length λ_I (pion interaction length λ_π), the probability of a proton (pion) to undergo a nuclear interaction within a distance of $1\,\lambda_I$ ($1\,\lambda_\pi$) is 63 %. After $5\,\lambda_I$ the probability that the particle did not interact is 0.7 %. So even if the T3B strip is at a fixed position behind the calorimeter, its longitudinal position relative to the shower start varies. For a characterization of the development of hadron showers one is interested in the properties at different shower depths not at different calorimeter depths. By a combination of T3B and CALICE data, the shower start can be determined from the calorimeter information. The T3B events can be categorized according to their position within the shower and used to study the longitudinal shower profile.

Two key parameters allow for a good characterization of the timing properties of hadronic showers: The time of the first hit (TofH) and the time of hit (ToH). The TofH is the moment when the analysis algorithm detects the signature of an energy deposition in a T3B cell. Note that the first hit of a T3B cell can also originate from a delayed shower particle. The TofH is a very clean parameter meaning that it is least influenced by detector effects. Furthermore, the energy deposition of the first hit can be quantified reliably (details in Section 6.2). The TofH is also a good measure for the intrinsic time stamping capabilities of a calorimeter. This is most relevant if the TofH of a calorimeter cell should be used to assign its energy deposition to the respective bunch crossing of a collider like CLIC (see Chapter 2).
The time of hit on the other hand follows a different approach. It takes every photon equivalent into account that was ever detected and therefore exploits the full information of the time window recorded by T3B. This parameter is harder to calibrate - mainly because of the afterpulsing of silicon photomultiplier - and the energy deposition of individual particle hits is difficult to quantify. But it can be used to determine which fraction of the total shower signal is deposited after which time. As shown in Chapter 2, the jet energy resolution of a large scale detector depends on the time over which a shower is integrated. So the ToH information is valuable in the context of a collider detector for CLIC. Here, the integration time has to be limited due to a high bunch crossing rate and the related background.

Acquiring ultra-high statistics gives T3B the opportunity to observe the lateral and longitudinal timing profile of hadronic showers with sub-nanosecond precision. The challenge was to record enough statistics - at least in the order of a few million events - under stable test beam conditions. Remaining differences at the test beam (see Table 4.3) need to be identified and calibrated. The calibration procedure undertaken for the T3B data is subject of the following chapter.

Chapter 5

The T3B Experiment - Calibration, Data Reconstruction and Simulation

Under test beam conditions, many factors influence the performance of a detector. The T3B experiment carried out test beam measurements at five different run periods distributed over one entire year. During this time, the T3B detector was reallocated two times, subject to systematic changes in the test beam configuration, subject to seasonal temperature changes and more (see Chapter 4). An extensive calibration procedure was performed on the T3B data to disentangle the resulting detector effects from shower properties. The goal is to be able to compare data sets with different particle energies, different absorber materials and from different run periods on an equal footing and to be able to compare this data to Monte Carlo simulated data sets.

In the first section of this chapter we will have a closer look at the oscilloscope waveforms the T3B data consists of. We will apply a set of calibration routines to clean the waveforms from its raw appearance dominated by properties of the oscilloscopes and the photosensor to extract the underlying timing of the energy depositions of shower particles. We will furthermore show methods that help to equalize the data taken at different run periods. In the second section, we will explain details on the generation of simulated Monte Carlo data sets and how we can introduce detector properties into the otherwise too idealistic simulation (also called digitization process) for a better comparability to the T3B data. Finally, we will give a short overview over the combination of T3B and CALICE data and over the advantages of this synchronization procedure.

5.1 T3B Data

The calibration of the T3B data is separated into two different stages. For the first level calibration (L1) a novel waveform processing technique was developed that is capable of determining the arrival time of photons on the light sensor with sub-nanosecond precision. The L1 calibration is not specific to T3B test beam data. It can in principle

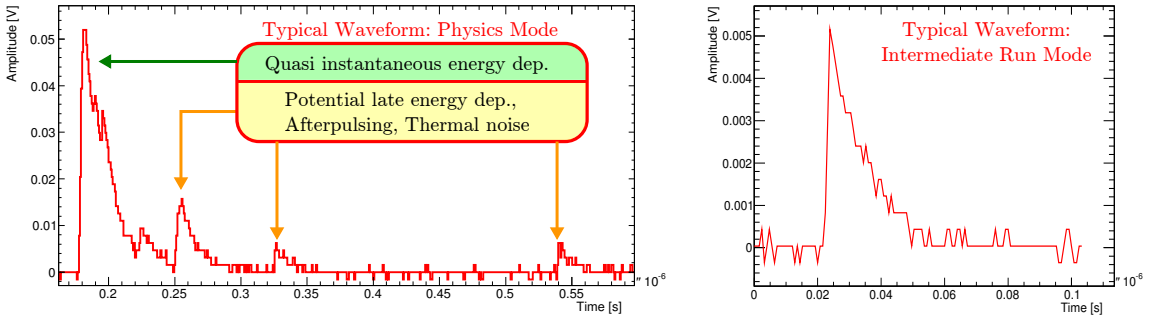

Figure 5.1: Raw waveform of a typical hadron event at 60 GeV on one oscilloscope channel in physics mode (left) and the corresponding representative waveform of one photon equivalent (≙ one firing SiPM pixel) in intermediate run mode (right). Note the different vertical ranges of the respective waveforms.

be applied to any oscilloscope waveform that represents a SiPM signal. The second level calibration (L2) uses the data of dedicated measurements performed in the laboratory and muon data sets from the test beam to determine key parameters of the detector response. These parameters are crucial for the correction of SiPM afterpulsing and for the calibration of energy depositions to the energy scale of minimum ionizing particles (MIP). The L2 calibration data will be used in the analysis to correct for dynamic detector effects that are specific to a certain test beam phase.

5.1.1 First Level Calibration and Data Reconstruction Procedure (L1)

T3B Signal Shape

Figure 5.1 (left) shows the waveform of a typical hadron event as acquired at the test beam by the T3B DAQ. One can clearly identify the signature of a high, fast energy deposition that occurred shortly after the minimal particle travelling time T_{min}. This is the minimal time a particle flying with the speed of light takes to reach the T3B layer. The instantaneous component of the hadronic shower arrives $\mathcal{O}(1\,\text{ns})$ after T_{min}. It is followed by a delayed shower component. The potential late energy depositions highlighted in the figure are at this stage indistinguishable from SiPM afterpulsing or random thermal noise. The thermal darkrate plays only a minor role. It occurs with a rate of $\sim 500\,\text{kHz}$ for the used SiPMs. The acquisition time window of the T3B DAQ is fixed to $2.4\,\mu\text{s}$ for all test beam data sets, so on average one pixel fires due to thermal excitation within an acquired waveform. The afterpulsing behaviour of the SiPMs on the other hand plays an important role, as it occurs with a much higher probability and by definition after the true photon signal of a shower particle. It will be investigated in detail in Section 5.1.2. Both contributions can mimic delayed energy depositions and will be corrected for in the analysis (see Chapter 6).

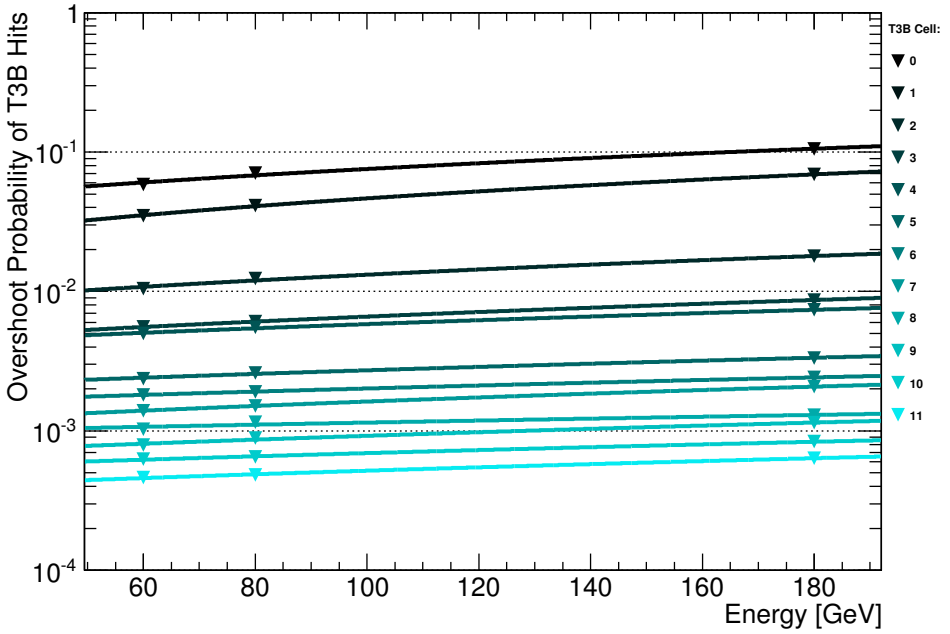

Figure 5.2: Quantification of the probability that a waveform overshoots the dynamic range of the T3B DAQ for the innermost 12 T3B cells and three representative particle energies. The values are normalized to the number of events in which at least one T3B cell was hit by a shower particle (i.e. > 15 p.e. within the acquisition window of 2.4 μs).

The vertical range of the waveforms recorded in physics mode was chosen to be 400 mV. This is the optimal compromise between a maximal dynamic range and a sufficiently high vertical precision. For a reliable recognition of the signal of one firing pixel (1 p.e.), which is the smallest possible signal of a SiPM, we demand to have at least three vertically accessible oscilloscope values within 5 mV. During the commissioning of the T3B layer, the bias voltage of every cell was adjusted such that a 1 p.e. waveform has a peak amplitude of 5 mV (see Figure 5.1, right). This procedure results in a cell-by-cell gain equalization. Acquiring data with an 8-bit oscilloscope (vertical range split into 256 slices) limits the vertical range consequently to 400 mV. This means that ~ 80 (or $\sim 20\,\%$) of the SiPM pixels can fire at the same time without cutting the waveform. This corresponds, on average, to the signal of five minimum ionizing particles traversing a T3B cell at once. Compared to the number of acquired events, the probability that the signal of a particle shower overshoots the vertical range of T3B is very low. But the influence becomes significant when normalizing to the fraction of events in which T3B was hit (see Figure 5.2). This influence cannot be neglected an will be discussed further in Chapter 6. For the intermediate run mode in which only waveforms with few fired pixels are of relevance the vertical precision was increased by choosing a vertical range of 100 mV.

The waveform acquired in physics mode is an additive combination of multiple 1-pixel waveforms occurring at different times. This is a property intrinsic to the working

principle of the SiPM (see Section 3.3.2 for details). The corresponding signal of one single SiPM pixel firing as recorded by the intermediate run mode (see Figure 5.1, right) is characterized by a fast signal rise originating from the charge avalanche that develops in the pixel followed by an exponential signal decay with a time constant of $\sim 12\,\mathrm{ns}$ (for the used SiPMs of the type MPPC-50) that is caused by the quenching of the avalanche (see Section 3.3.2). The goal of the L1 calibration is to find out the exact time values at which the individual SiPM pixels within the physics waveform fired. This can be achieved by an iterative subtraction of the representative 1-pixel waveform or, in other words, by a decomposition of the physics waveform. These pixel hit times contain the full information of the recorded waveform, but reduce the data volume of a waveform by a factor of ~ 100 and eliminate any dependence on variations in the SiPM gain. The SiPM gain is highly temperature dependent ($dG/dT \approx -3\,\%/K$, see following Section) and one of the main sources of variations in the raw data, since the temperature changed by $> 8°\mathrm{C}$ over the different test beam periods of T3B.
A signal within the analog physics waveform extends over dozens of nanoseconds while the contributions of the individually firing pixels overlap. This makes it difficult to determine the deposited energy of a shower particle within a distinct time window in a reliable way. Performing a waveform decomposition allows for a much higher timing precision and makes it even possible to study the substructure of energy depositions i.e. the arrival time distribution of photons during the energy deposition. The calibration sequence necessary for a successful waveform decomposition will be explained in the following.

Outline of the Calibration

Figure 5.3 shows the workflow of the L1 Calibration. As mentioned above, the T3B data consists of waveforms acquired in physics mode, which represent the T3B response to shower events, and a set of calibration waveforms (intermediate run mode or IRM) which are triggered by the thermal darkrate of the T3B cells and are recorded directly after the end of a particle spill at the test beam. Both data sets are calibrated independently until the final step in which the information from the IRM is fed in for a successful decomposition of the physics waveforms. The L2 calibration and the analysis is exclusively performed on the decomposed waveforms. Each calibration step results in a binary file that can be loaded in the following steps or even in the analysis and in a Root [78] file that contains control plots to verify the success of the respective step.

T3B Synchronization Information: The first L1 calibration step is called T3B synchronization information. It scans quickly over the T3B data and extracts the number of events recorded by each oscilloscope and the number of scintillator coincidences on a spill-by-spill basis. Mismatches in the event count of the different oscilloscopes (see Section 4.3.2) are identified and such spills will be rejected in the subsequent calibration steps. The T3B synchronization step is applied to the physics data and for cross checking purposes also to the IRM.

Pedestal Subtraction: A pedestal subtraction is performed on a spill-by-spill basis

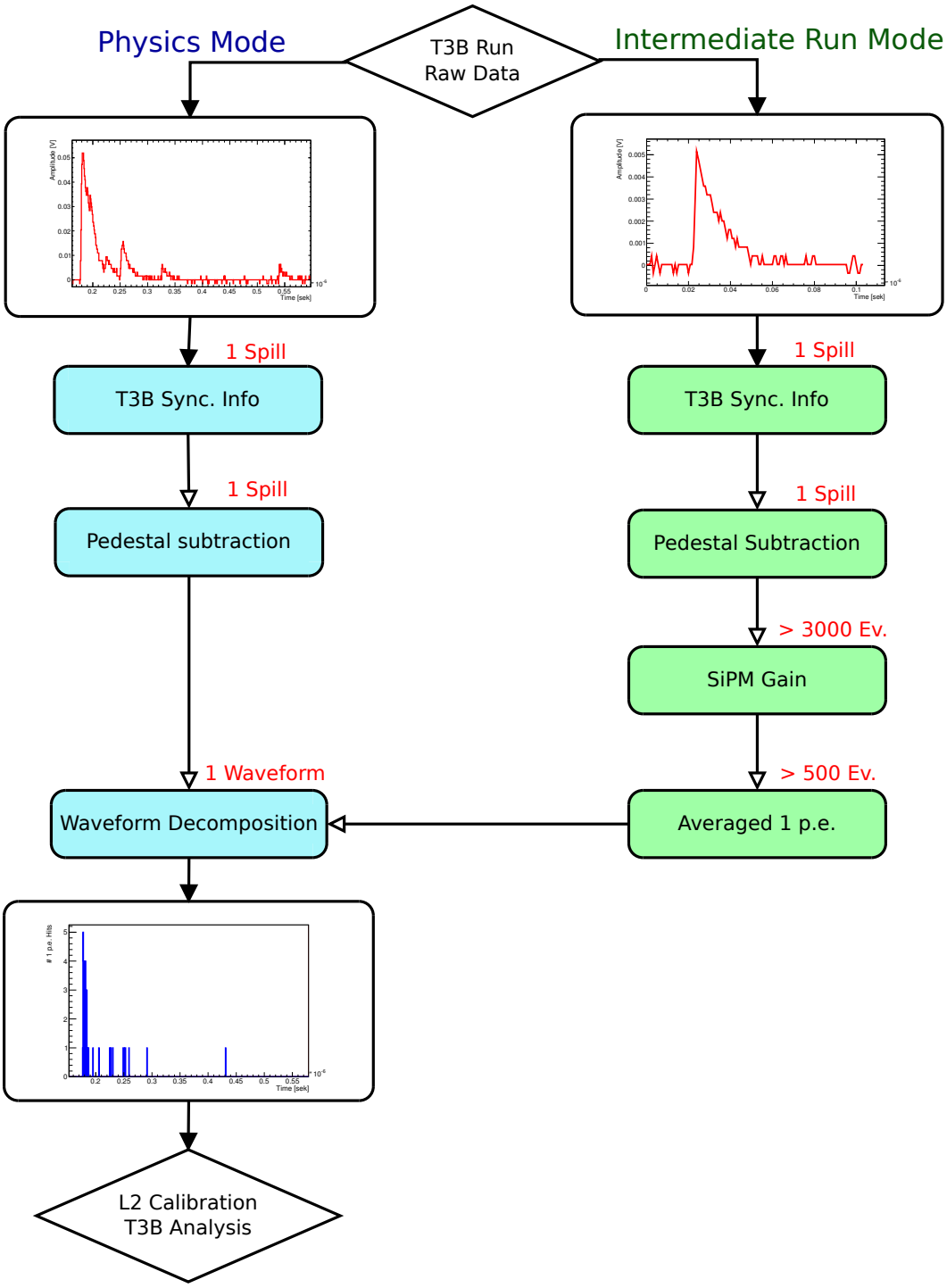

Figure 5.3: Workflow of the L1 calibration sequence. The raw waveforms from the intermediate run mode (green) and the physics mode (blue) undergo a set of calibration steps to enable a decomposition of the physics waveform into its 1-pixel components. The statistics required for the respective calibration step is shown in red.

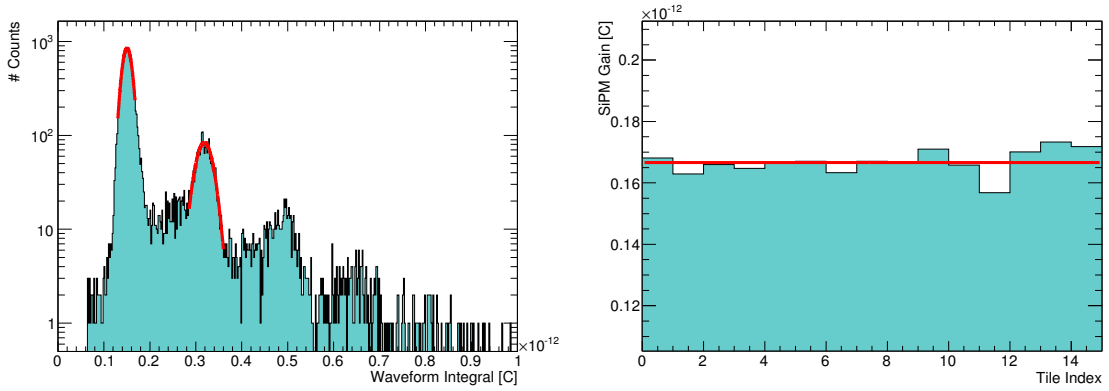

Figure 5.4: Control plots of the SiPM gain calibration step. The gain value is extracted by fitting the 1- and 2-pixel peaks of the waveform integral distribution and extracting the difference of the maxima (left). The gain value of the 15 T3B cells spreads around an average of 0.166 pC or 1.0×10^6 e^- in this measurement (right). Note that the gain value is already divided by the amplification factor of 8.9 which was introduced by the preamplifier.

and for each T3B cell individually. Possible shifts in the pedestal during data taking can be eliminated. A software algorithm removes all SiPM signals from the waveform for this step. It identifies all vertical oscilloscope values above a threshold of a few millivolts, defines a tolerance time window around these values and rejects all values in the respective windows. The remaining vertical oscilloscope values are filled into a histogram. The mean of the bins in this histogram that contain more than 5 % of the entries is then stored as pedestal value and will be subtracted in the following calibration. The procedure uses the maximal information available and can identify a highly accurate pedestal value even with a small number of waveforms.

SiPM Gain Calibration: A gain calibration is performed using the waveforms of the IRM. The waveform integral is determined and histogrammed cell-by-cell (see Figure 5.4, left). The IRM contains primarily 1-pixel waveforms, but due to e.g. optical cross talk it can happen that two or more pixels fire at the same time. This leads to a multi-gaussian distribution of the waveform integral which can be exploited in the gain calibration. Each gaussian peak can be attributed to a number of fired pixels because the avalanche of every SiPM pixel carries approximately the same charge. This charge is also called SiPM gain. A software algorithm identifies the maximum of the 1- and 2-pixel peak and performs a gaussian fit. The difference of the two fit maxima is the extracted gain value. Figure 5.4 (right) shows the determined gain value of all 15 T3B cells. The required statistics for a gain extraction is > 3000 waveforms which corresponds to a gain determination every ~ 15 minutes for the SPS and ~ 12 minutes for the PS test beam phases. The gain calibration is highly reliable and worked for all run periods with 100 % efficiency.

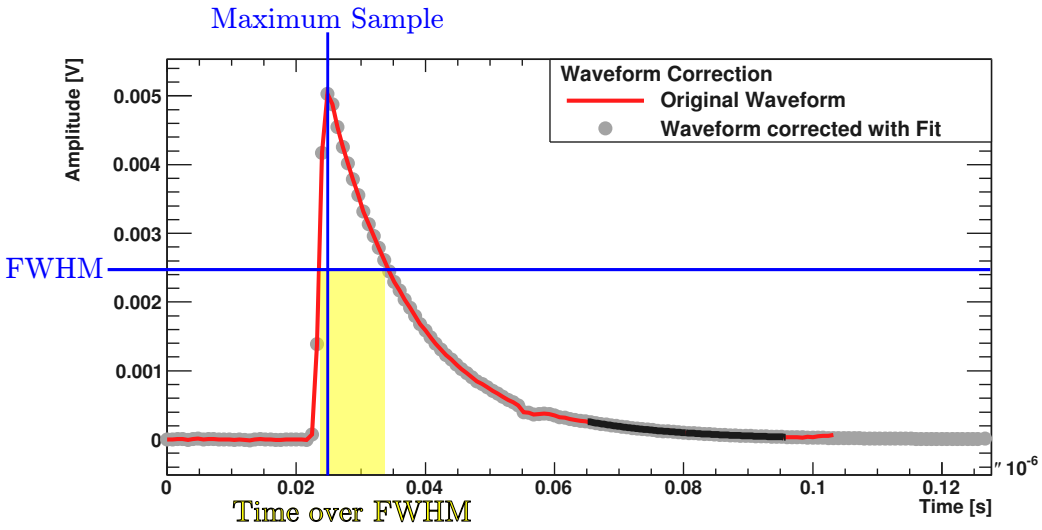

Figure 5.5: Control plot of the averaged 1 p.e. calibration step. The averaged 1-pixel waveform (red) is extended by an exponential fit (black) to correct for the sudden cut at the end of the acquisition window of the intermediate run mode waveforms. The resulting waveform that is propagated to the waveform decomposition is shown in grey. The sample with the maximum voltage value and the full width at half maximum are highlighted in blue, the time the waveform exceeds the FWHM value in yellow.

Averaged 1 p.e. Calibration: In the next step, the average signal of a 1-pixel waveform is determined cell-by-cell. Using the information obtained by the gain calibration step, a cut is applied on the waveform integral to select exclusively 1-pixel waveforms. Only waveforms with an integral of the respective gain value $\pm 25\,\%$ are accepted for averaging. The selected waveforms are then averaged sample by sample (see Figure 5.5). The averaged 1 p.e. waveform has a characteristic dip at 55 ns and a sudden cut at 104 ns due to the limited acquisition window. The dip is caused by a systematic reflection in the cabling of the T3B cells and needs to stay as it is also present in the physics waveforms. The sudden cut in the waveform on the other hand requires correction so that it cannot cause artifacts in the waveform decomposition. An exponential fit is applied to the late part of the 1-pixel waveform and extended until it drops below a voltage value of $5\,\mu$V. This cut value is chosen such that the waveform decomposition cannot leave a remainder (caused by this waveform cut) that is misinterpreted as 1-pixel signal, even if all 400 SiPM pixels were firing at once. The required statistics for this calibration step amounts to > 500 waveforms. The averaged 1 p.e. information is crucial for the waveform decomposition which is performed as the final L1 calibration step.

Waveform Decomposition: Every physics waveform acquired at the test beam that contains at least one sample with a value of $> 12.5\,$mV - this means that at least three SiPM pixels fired simultaneously somewhere within the acquisition time window - will be decomposed into its 1-pixel components. The other waveforms are

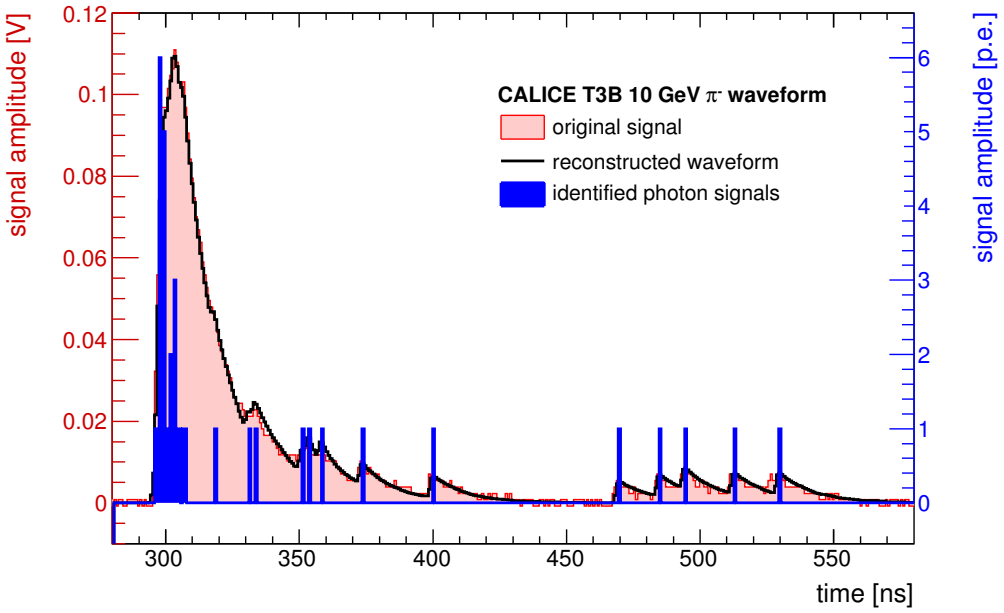

Figure 5.6: Control plot of the waveform decomposition calibration step. The averaged waveform of a 1-pixel signal is subtracted iteratively from the analog physics waveform (red) resulting in a 1 p.e. hit histogram (blue) depicting the time of arrival of photons on the light sensor. From this histogram, the original waveform can be reconstructed for cross checking purposes.

classified as random SiPM noise and skipped. The initial step of the decomposition is to identify the global maximum sample within the physics waveform. The time of the maximum of the representative averaged 1 p.e. waveform is matched with the time of this global maximum. Having the relative timing determined, the voltage values of the averaged waveform are subtracted from the physics waveform. The time of this global maximum will be assigned to the waveform as the time when a SiPM pixel fired. Then, the global maximum of the resulting physics waveform is determined and the subtraction procedure starts over. The decomposition continues iteratively until stopped by a terminating condition. The challenge is to define a condition that ensures the identification and subtraction of the signal of all fired SiPM pixels without being sensitive to artifacts that might be created during the decomposition and therefore subtracting too much or at wrong points in time. Two terminating conditions have been used for the decomposition of the T3B signals. They become relevant when only few 1-pixel signals are left. As a first condition, the found maximum has to be larger than 2.5 mV. Note that the maximum of a 1-pixel signal is definitely larger. It amounts to approximately 5 mV (dependent on the ambient temperature). For the second condition a sample rejection list is introduced. During the decomposition it can happen that an isolated sample with a value > 2.5 mV is left over. Such artifacts must not initiate a 1 p.e. subtraction. To avoid this, the full width at half maximum (FWHM) of the averaged 1 p.e. waveform is determined and the time span relative to the

maximum in which the waveform is above this FWHM value (see Figure 5.5). In the physics waveform, a global maximum sample is accepted for subtraction if all samples within this FWHM time span are larger than 30 % of the known voltage value of the 1 p.e. maximum. Otherwise, this sample is rejected and added to the sample rejection list. Then, the algorithm searches for the next global maximum. The decomposition stops if no samples $> 2.5\,\mathrm{mV}$ can be found that are not on the sample rejection list.
The waveform decomposition proved to be very stable in the determination of the time of arrival of photons on the light sensor. Using these 1 p.e. hit times and the averaged 1 p.e. waveform, one can reconstruct the analog waveform and compare it to the original oscilloscope waveform to control and verify that the decomposition procedure worked (see Figure 5.6). The χ^2 can be computed and used as a quality factor. Due to the overall good performance and stability of the waveform decomposition, no waveform rejection was applied in dependence of this quality factor. The result of the waveform decomposition is a 1 p.e. histogram which replaces the analog waveform of the T3B data and is now available for further analysis.

Calibration and Data Quality Check

The results of the respective calibration steps can be used to check the stability and performance of the T3B cells and the calibration itself on a run-by-run basis or even for an entire test beam period. We will present a small selection out of a big pool of calibration control plots that help in the categorization into bad and good runs. Only runs classified as good will be used for the analysis of the T3B data. Figure 5.7 gives an overview of the spill synchronization of the T3B data for one test beam run. The plot shows in a boolean way if a spill contains data at all, if the T3B oscilloscopes were in sync in that spill and if waveforms were decomposed. It is further quantified how many scintillator coincidences occurred and for how many of these events a waveform decomposition was performed. At one glance one can identify possible problems during data taking (e.g. if too many spills are out of sync) or reasons why no calibrated data exists for a certain spill. Another quality check is the monitoring of the time development (see Figure 5.8) and the distribution (not shown) of the pedestal subtraction value. Instabilities at the test beam could manifest in a unsteadiness of this value and be identified quickly. The same information is available for the SiPM gain values determined for all T3B cells throughout the calibration. Figure 5.9 shows the gain dependence on the ambient temperature using the information from the PT1000 sensors attached to each cell for an entire test beam period. Fitting this dependence results in a temperature dependence of $1/G \times dG/dT = 3.2\,\%/K$ averaged over all cells. This is a reasonable value for the used SiPMs of the type MPPC-50 and matches laboratory tests performed before the commissioning of the T3B detector. Many further control plots exist to verify the success of the calibration and the data selection, but explaining each of them is beyond the scope of this thesis.

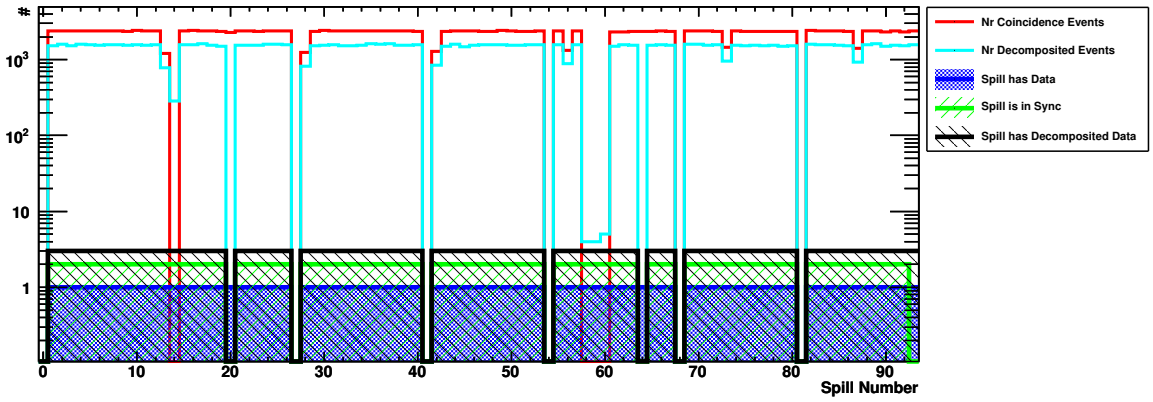

Figure 5.7: Quality check of the T3B synchronization for one test beam run. Seven spills do not contain decomposed data. For five of these spills no particle events occurred, while T3B and CALICE were out of sync for two of these spills.

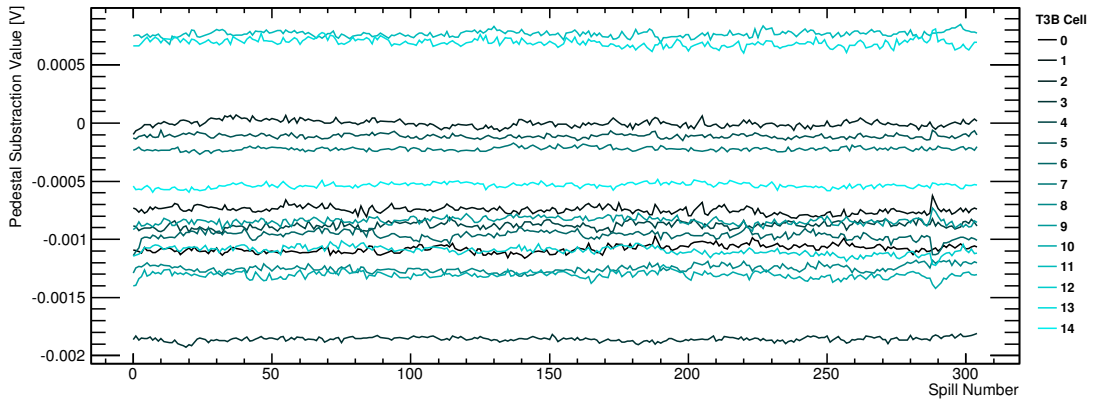

Figure 5.8: Evolution of the pedestal subtraction value for all T3B cells during one test beam run.

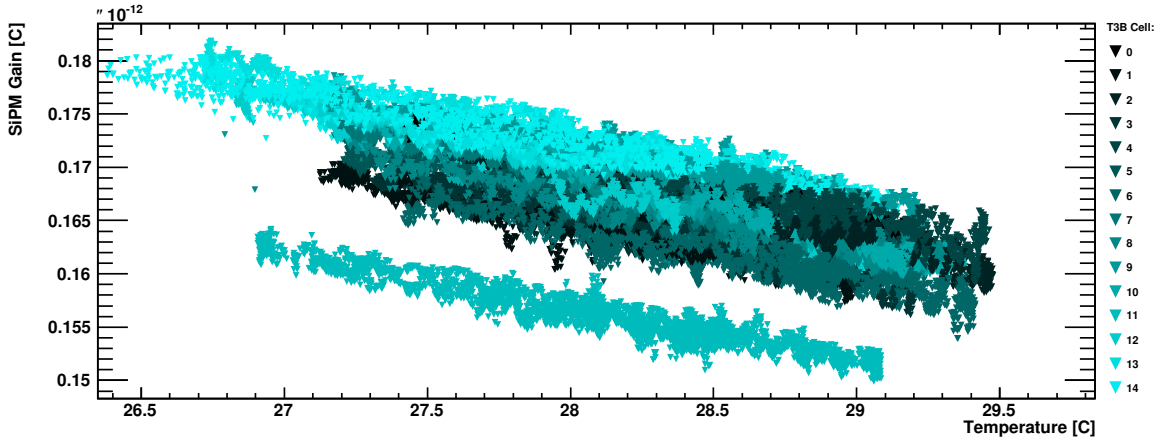

Figure 5.9: Dependence of the gain of the T3B cells on the ambient temperature conditions for the September 2011 test beam period.

5.1.2 Second Level Calibration Procedure (L2)

The L2 calibration as well as the T3B analysis (see Chapter 6) is performed exclusively on decomposed waveforms resulting from the L1 calibration and data reconstruction sequence. But while the test beam data on hadron shower physics is used for the T3B analysis, the L2 calibration determines key parameters of the T3B cells through dedicated measurements performed in the laboratory. We investigate parameters that changed dynamically at the test beam such as the afterpulsing of SiPM pixels and the most probable light yield detected in response of a minimum ionizing particle (MIP). Information on these parameters is made accessible to the T3B analysis through a plug-in system. The information is used to equalize different test beam phases and to express shower properties in terms of shower parameters rather than in terms of detector parameters. With the L2 calibration detector effects that obscure the underlying shower development can be stripped from the T3B data.

Afterpulsing Correction

Lattice defects in the silicon of a SiPM pixel and slow drifting holes created outside of the high field region of a SiPM pixel can initiate a second delayed avalanche in the same pixel of the original avalanche (see Section 3.3.2 for details). This delayed signal is called afterpulse (AP). Dozens of SiPM pixels fire in response to the energy deposition of a shower particle, each of which has a certain probability to afterpulse. These SiPM afterpulses cannot be distinguished from real energy depositions of e.g. delayed shower components. But their contribution can be determined statistically and corrected for accordingly. The goal of this L2 calibration step is to quantify the occurrence and time distribution of SiPM afterpulses. An average AP contribution can then be subtracted for every SiPM pixel that fired in the test beam data.

Like most SiPM properties, the afterpulsing probability of a SiPM is very dependent on the ambient temperature and on the applied bias voltage (see [80] for further details on SiPM AP). As discussed in Section 4.3.3, these parameters changed significantly throughout the T3B test beam programme. The bias voltage was varied for different test beam phases in a range of 300 mV and the operating SiPM temperature changed from an average of $\sim 22°C$ in November 2010 up to $\sim 30°C$ in July 2011. It would be the best approach to correct for SiPM AP on a spill-by-spill basis using the current temperature and voltage setting of each T3B cell individually as done for the SiPM gain calibration. Unfortunately, not enough data exists on the afterpulsing behaviour at the test beam. The data taken in intermediate run mode does contain information on the AP of the SiPM, but the statistics is too low for a reliable AP quantification and the acquisition time window is too short. Therefore, we followed a different approach to correct for AP. The exact conditions of the T3B test beam phases in terms of temperature and SiPM voltage were recreated in the laboratory and the average SiPM afterpulsing was measured using the T3B hardware and DAQ system. Since the test beam phases were short relative to seasonal changes, the SiPM temperature variations

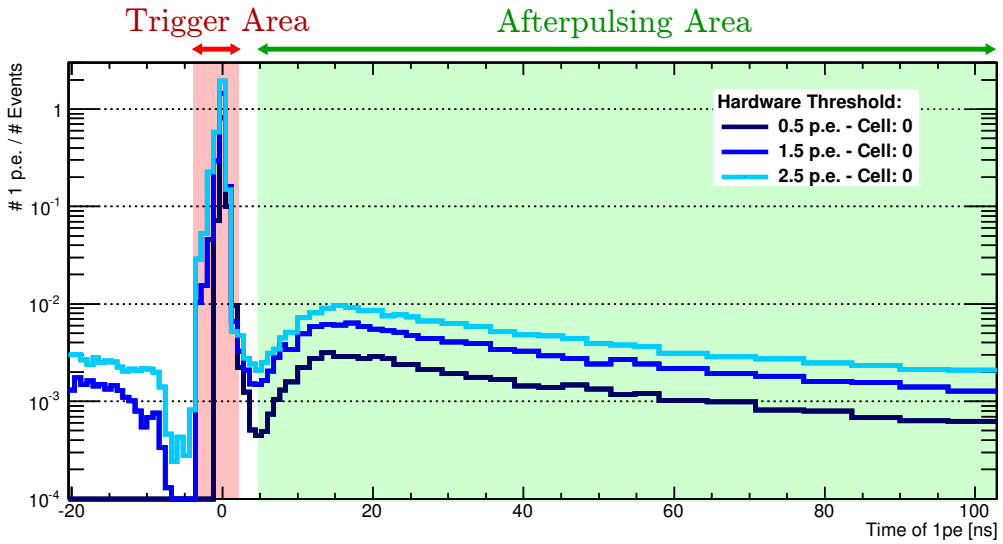

Figure 5.10: Average time distribution of the afterpulsing of T3B cell 0. The conditions of the September 2011 test beam phase were recreated in the laboratory. While the number of pixels firing in the trigger area (red) is fixed, the distribution of the pixels firing in the delayed afterpulsing area (green) is measured. The height of the AP distribution scales linearly with the number pixels contained in the trigger area.

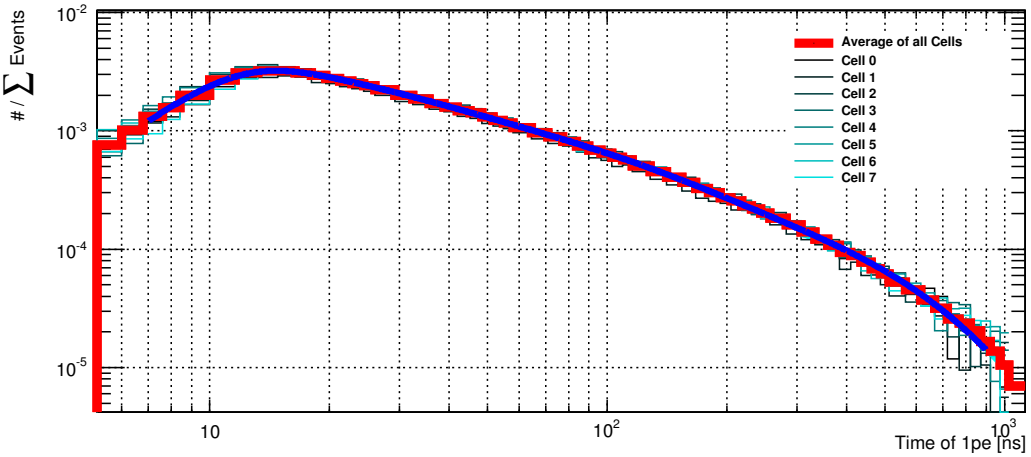

Figure 5.11: Fit of time distribution of the SiPM afterpulsing after averaging over eight T3B cells for the September 2011 test beam phase. The fit can be used as a template for the AP contribution specific to this phase.

within one phase were approximately ±1°C for the runs considered for analysis and primarily caused by the day-night-cycle. For the dedicated laboratory measurements the T3B cells were located in a climate chamber that can keep the temperature with high precision. The temperature was adjusted such that the sensor attached to a T3B cell measures the same temperature as measured on average at the respective test beam phase. Furthermore, the same bias voltage was supplied to the T3B cells. The

oscilloscope settings were set similar to the ones at the test beam (see Section 5.1.1) with the only difference that the oscilloscopes are self triggered on the thermal darkrate of the SiPMs in physics and in intermediate run mode. Three different runs were taken with a trigger threshold of 0.5 p.e., 1.5 p.e. and 2.5 p.e., recording one million events per run. The acquired waveforms were decomposed by the L1 calibration. The event selection requires exactly 1 p.e., 2 p.e. or 3 p.e., respectively, within a tolerance time window of ±2.4 ns around the trigger time to accept a waveform for further analysis (see Figure 5.10). So the exact number of pixels that fired in the triggered signal is defined and quasi every identified pixel firing at a later point in time can be attributed to SiPM afterpulsing. Note that the contribution from random thermal SiPM darkrate was taken into account by a pedestal subtraction which assumes that the occurrence of AP becomes negligible after 1400 ns. With the explained setup, the time distribution of SiPM afterpulsing can be quantified with high precision. An initial 1-pixel signal and its afterpulse originate by definition from the same pixel and its AP behaviour is independent of the other pixels. Therefore, the afterpulsing distribution of a SiPM scales linearly with the number of pixels fired (see Figure 5.10). The overall statistics was increased by averaging over the scaled AP distribution of the three different runs and also by averaging over the thus obtained distribution of eight T3B cells neglecting SiPM-to-SiPM variations within the set of SiPM devices selected for T3B. The resulting distribution originating effectively from 24 million recorded darkrate events quantifies SiPM afterpulsing in a range of $0 - 1000$ ns. The statistical fluctuations are low as shown in Figure 5.11. This distribution is fitted by a function of the following form:

$$f(t) = \frac{Erf(a \cdot t - b) + 1}{2} \times c \cdot (e^{-\frac{t}{\tau_1}} + e^{-\frac{t}{\tau_2}} + e^{-\frac{t}{\tau_3}}), \tag{5.1}$$

where Erf is the error function and a, b, c and τ_1, τ_2, τ_3 are free parameters of the fit. This functional form enables an optimal fit to the data. The fit parameters are extracted and the corresponding fit function can be used as a template. This template is representative for the afterpulsing of a T3B SiPM under the operating conditions of a distinct test beam phase. The procedure is repeated for other test beam phases respecting their individual conditions. The obtained fit templates can be used to evaluate the average afterpulsing contribution at a certain point in time after a SiPM pixel fired. This contribution is subtracted for all pixels that fired e.g. in response to a cell-traversing hadron acquired in a certain test beam period. Details on the application of the afterpulsing correction will be explained in Section 6.3.

Calibration to the MIP Energy Scale

The response of a T3B cell to a tile-traversing minimum ionizing particle (MIP) is characterized by a signal with high amplitude (large number of photon equivalents) detected within a few nanoseconds due to the photons created in the scintillator followed by the delayed signals of few pixels that fire predominantly due to SiPM afterpulsing (see Figure 5.12, left). The transition between those two contributions is smooth.

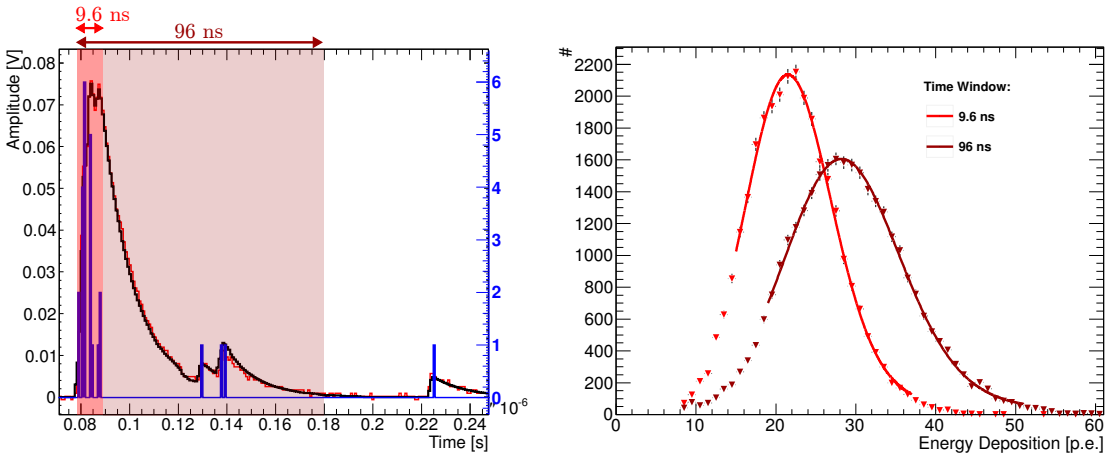

Figure 5.12: Decomposed waveform of the energy deposition of a tile-traversing electron originating from a ^{90}Sr radioactive source (left). The quantification of the deposited energy depends sensitively on the time window over which identified photon equivalents are integrated. This integration time window determines the shape of the measured energy distribution and its most probable value (right).

Therefore, the energy deposition in terms of photon equivalents that can be assigned to a tile-traversing MIP depends sensitively on the time window over which one integrates. Moreover, the photon detection efficiency of a SiPM depends on the ambient temperature and the applied bias voltage. For lower temperatures or higher V_{bias}, a larger number of pixels fire in response to one MIP. The purpose of this L2 calibration step is a quantification of the response of the T3B cells to MIPs in dependence of the time integration window and the operating conditions at the test beam.

A series of dedicated measurements was performed in the laboratory to achieve this goal. A radioactive Strontium-90 source was positioned above one T3B cell under study (see Figure 5.13). A second T3B cell was located underneath. The whole setup was located in a climate chamber to ensure a stable temperature during all measurements. The emitted electrons were collimated by a tungsten casing with an opening of 1 mm in diameter and pointed at the center of the tile under study.

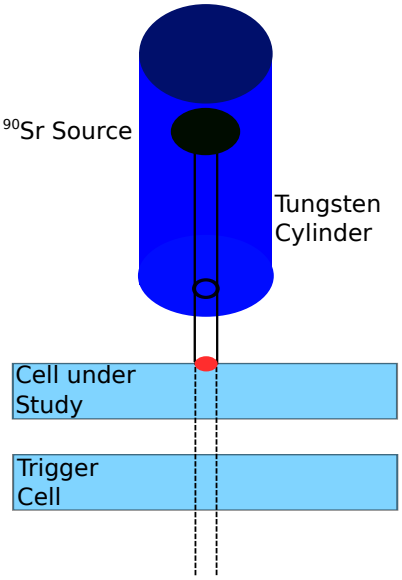

Figure 5.13: Sketch of the trigger coincidence setup.

Strontium-90: Strontium-90 is a radioactive isotope which undergoes two subsequent beta decays. The unstable ^{90}Sr decays with a half life of 28.8 years into Yttrium which is short lived (half life of 64.1 hours) and decays further into the stable Zirconium. Both decays emit a continuous beta spectrum with an end point

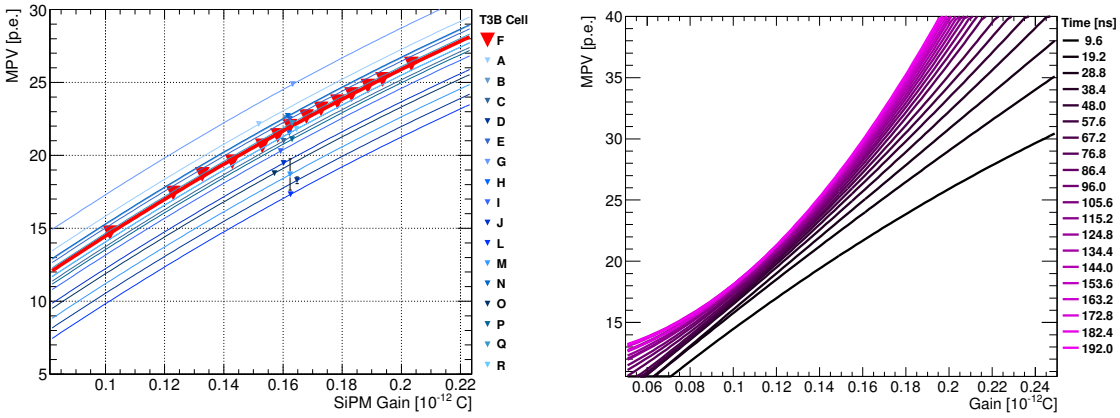

Figure 5.14: Dependence of the most probable energy deposition of ^{90}Sr electrons on the SiPM gain for all T3B cells in a time integration window of 9.6 ns (left). The master cell (denoted as F) was subject to a bias voltage scan for discrete time integration windows (right). The dependence of the master cell is fitted with a polynomial of second order for all time windows.

energy of 0.54 MeV and 2.27 MeV, respectively. The highest energetic electrons can traverse the T3B cell under study and deposit their remaining energy within the trigger cell.

The trigger settings of the T3B DAQ were adjusted such that a signal > 3 p.e. has to be detected for both cells simultaneously. This coincidence requirement ensured the selection of events in which the electron traverses the cell under study completely generating a MIP-like signal. Electrons are not perfect MIPs. The energy deposition of a ^{90}Sr electron is larger than that of a highly energetic muon. But it has a constant relation to the signal of a MIP. We will determine this scale factor in the course of this L2 calibration step. Using the T3B DAQ, the signals of 20.000 electrons were recorded and reconstructed by the L1 calibration procedure. Then, the energy distribution in terms of p.e. was determined for different time integration windows in a range of 9.6 ns up to 192 ns (see Figure 5.12, right). The obtained distributions were fitted by a Langau function which consists of a Landau convoluted with a Gaussian function (see Section 3.3.3 for details). The most probable value (MPV) is very stable against statistical fluctuations. It is extracted from the fit as a key parameter of the corresponding distribution. The procedure was repeated for all 15 T3B cells. Additionally, a bias voltage scan with discrete steps in a range of ± 500 mV around the standard operating voltage was performed for one "master" cell. The extracted MPV values are plotted against the SiPM gain which is known from the L1 calibration (see Figure 5.14, left). For the calibration to the MIP scale we assume that temperature changes and changes in the applied bias voltage influence the gain of a SiPM likewise. Therefore, we study the dependence of the MIP MPV on the SiPM gain in these laboratory measurements. At the test beam, the gain is determined continuously and refreshed every ~ 15 min (at SPS) for each T3B cell individually. This MPV-gain dependence is fitted with a

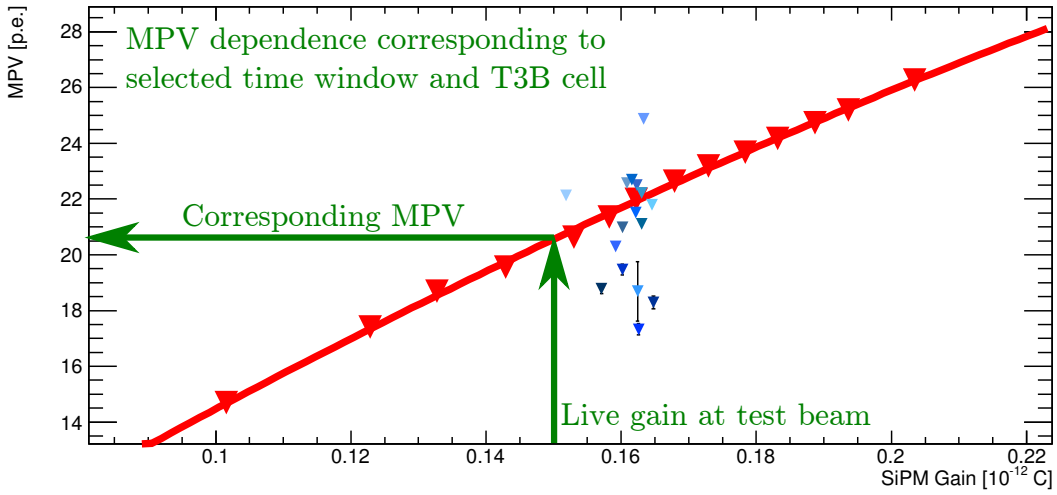

Figure 5.15: Explanation of the procedure of the calibration to the MIP scale on the basis of the MIP MPV-gain dependence for a time integration window of 9.6 ns. After choosing a time window and determining the gain of the inquired T3B cell, the MPV can be evaluated from the corresponding fit function.

polynomial of second order for the master cell and - assuming an identical dependence for different SiPM devices - projected on the MPV values of the other T3B cells. The procedure is repeated for a set of different time integration windows. Figure 5.14 (right) shows the influence of the choice of the time window. While the MIP-gain dependence of a SiPM is linear for short integration times (photon signals are predominant), it becomes quadratic for longer integration times (the afterpulising contribution dominates) and converges for very long integration times. At late times relative to the initial photon signal, the occurrence of afterpulsing decreases and the probability to integrate an additional afterpulse becomes very small. This illustrates the significance of the AP contribution. Thus, a short time integration window of e.g. 9.6 ns is to be preferred for an analysis of the true energy deposition of particles cleaned from detector effects.

We now have most of the information needed for a calibration of energy depositions at the test beam to the MIP scale. For this, we utilize the fits of the MPV-gain dependence. In the first step, we choose an integration time window and look up the gain corresponding to the current test beam event that we intend to calibrate. We select the fit from the ^{90}Sr data with the matching time window and of the matching T3B cell (see Figure 5.15). Then, we evaluate the fit function at the position of the determined gain and obtain the number of pixels that would fire in response to a MIP at that gain value. The energy deposited by a hadron shower at the test beam can now be calibrated to the MIP scale with the following formula:

$$E[MIP](\Delta t_i, j) = \frac{E[p.e.](\Delta t_i, j)}{MIP[p.e.](\Delta t_i, j)} = \frac{E[p.e.](\Delta t_i, j)}{MPV_{e^-}[p.e.](\Delta t_i, j) \cdot C_{e^- \Leftrightarrow \mu^-}}, \tag{5.2}$$

where Δt_i refers to the chosen time integration window, j to the index of the T3B cell

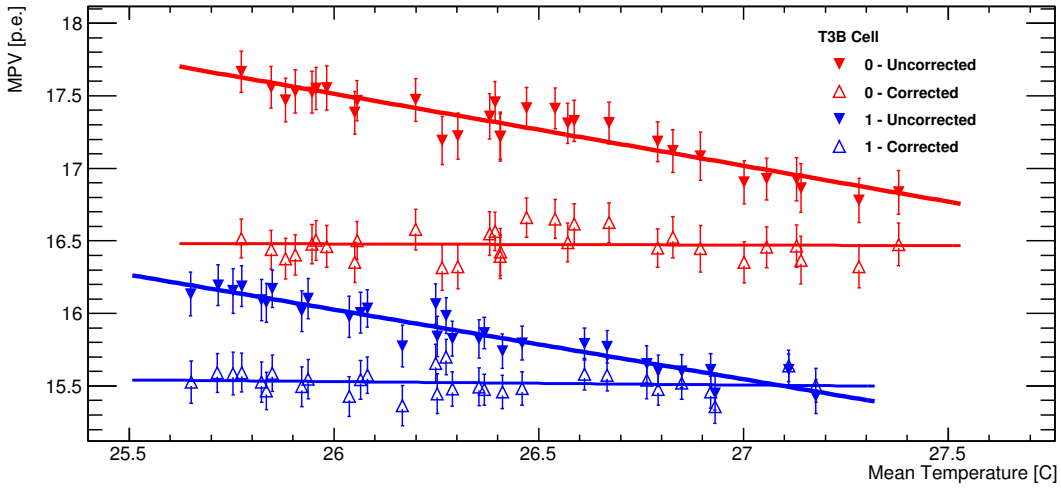

Figure 5.16: Validation of the calibration to the MIP scale with muon data for the central two T3B cells and a time integration window of 9.6 ns. Calibrating to a default value of 20 p.e. eliminates the temperature dependence of the MIP MPV and results in an average MPV of 16.4 p.e. instead of 20 p.e.. The ratio can be identified as the scale factor $C_{e^- \Leftrightarrow \mu^-}$.

and $C_{e^- \Leftrightarrow \mu^-}$ is the scale factor between the energy deposition of muons and electrons. This factor still needs to be determined to finalize the calibration to the MIP scale.

In the following, we will use the muon data from the test beam to validate the success of this calibration. At the beginning of the October 2011 test beam phase, the T3B experiment has recorded a large muon sample of 13.4 million muon events within 40 hours without interruption. The data was split into 30 sets in which the MIP MPV and the mean temperature was identified. The temperature varied in a range of $\sim 2°$C due to the day-night-cycle. This is enough to determine the MPV-temperature dependence which is characterized by an average MPV drop of $-3\,\%$ per Kelvin for the two central T3B tiles (see Figure 5.16). We will concentrate our efforts on these two cells, since the beam was focussed on the center of the calorimeter and they are consequently hit the most often. If the calibration to the MIP scale is working successfully, it should eliminate the MPV-temperature dependence when applied to the muon sample. Following the calibration procedure explained above, we choose a time integration window of 9.6 ns, determine the average gain for each of the 30 muon sets and evaluate MPV_{e^-} from the fit function for the given cell. In the following, we define a calibration scale S_{calib}. It was arbitrarily chosen to a value of $S_{calib} = 20$ p.e.. We divide this calibration scale by the MPV_{e^-} determined for each of the 30 muon sets and obtain an equalization factor C_{Eq}. Multiplying this factor with the uncorrected MPV value extracted from the muon sets ($MPV_{\mu^-}^{uncorr.}$) should eliminate the temperature dependence and result ideally in a corrected MPV value ($MPV_{\mu^-}^{corr.}$) of 20 p.e. for all sets.

$$MPV_{\mu^-}^{corr.}(i) = MPV_{\mu^-}^{uncorr.}(i) \cdot C_{Eq}(i) = MPV_{\mu^-}^{uncorr.}(i) \cdot \frac{S_{calib}}{MPV_{e^-}(i)}, \tag{5.3}$$

where i is the index of the muon data set.
Figure 5.16 shows that the temperature dependence could be eliminated efficiently. Note that this originates from the determination of $MPV_{e^-}(i)$ according to the gain utilizing the calibration data acquired in the laboratory. Nevertheless, the corrected MPV value amounts to 16.4 p.e. instead of 20 p.e.. This is due to the fact that we tried to equalize the muon data with data from ^{90}Sr electrons. The division of these numbers is identified as the ratio between the most probable energy deposition of a minimum ionizing particle and a cell-traversing electron $C_{e^-\Leftrightarrow\mu^-}$:

$$C_{e^-\Leftrightarrow\mu^-} = \frac{16.4\,p.e.}{20\,p.e.} = 0.82 \tag{5.4}$$

With the muon data acquired at the test beam, we could demonstrate that this L2 calibration step works and determine the scale factor between the energy deposition of electrons and muons at the same time. The value of the scale factor $C_{e^-\Leftrightarrow\mu^-}$ of 0.82 is in accordance with simulation studies of the energy distribution of cell-traversing muons and ^{90}Sr electrons (see [81] for details) and was therefore utilized for the calibration of T3B data. The calibration information is now complete and can be loaded in the analysis to calibrate the energy depositions of hadronic showers to the energy scale of minimum ionizing particles.

5.2 T3B Simulation

Every modern particle physics experiment tries to compare and reproduce its results with computer based Monte Carlo (MC) simulations. A highly dedicated MC simulation unifies ideally all the knowledge about the underlying physics of the experiment and comprises all information of the response and characteristics of the used detector technology. If the simulation matches the data in all aspects within the statistical uncertainty one can assume that the physics and the detector is understood with a certain precision. But the interesting case is if significant discrepancies are observed. The observation of such discrepancies can either mean that some detector or operational systematics are not respected or modelled correctly which is likely if the discrepancies can be seen consistently looking at the different data sets from many perspectives. This way a MC simulation helps to improve the understanding of the experiment itself. If the systematics seem under control and the data matches the simulation well for one data set (e.g. hadronic showers in a steel absorber environment) but not for another data set in which one key parameter of the experiment was under study and therefore intentionally altered (e.g. hadronic showers in a tungsten absorber environment) one can learn about new aspects of the underlying physics. In this case the theoretical description is insufficient and known effects have to be treated with higher precision (e.g. neutron interaction processes in hadronic showers) or new physical effects have to be studied for a consistent explanation and a deeper understanding of the observed data. R&D test beam experiments try to support the understanding and improvement

of certain aspects of MC simulations such as the time evolution of hadronic showers in the case of T3B.

As a first step of the T3B simulation, physics events of hadronic showers were generated using a detailed model of the geometry of the CALICE calorimeter and T3B and of the different materials used. The energy depositions and their corresponding hit times were extracted from the simulation. This step was performed by a T3B customized implementation of the simulation framework Geant4 [66]. Then, the intrinsic response of the T3B detector technology on energy depositions is modeled and applied to the events generated by Geant4 in a data driven approach. This step is commonly referred to as digitization. It requires detailed knowledge of the key parameters of the detector. In a data driven approach, one avoids to implement every single detail into the simulation (like the development of a charge avalanche within a SiPM pixel). Instead, one randomizes the simulated data according to determined parameter distributions which represent a folding of many subdetector effects. After the digitization step, one aims to provide simulated data in the same format as test beam data (i.e. an identical waveform shape and appearance) so that it can be passed through the analysis procedure without modification.

5.2.1 Geant4 Production of Simulated Data

GEANT stands for **GE**ometry **AN**d **T**racking. It is a software toolkit designed to simulate particle interactions with matter. To use it, one needs to define the geometry of the experiment and its material type and budget as precisely as possible. During execution, a virtual particle gun fires particles of chosen type and momentum towards the detector. The particle is tracked and subject to a large variety of processes. On its passage, Geant4 simulates all possible interactions of particles within the detector material, including elastic and inelastic scattering, ionization energy loss, particle decay and more. With a certain probability, the particle creates or is converted into a number of secondary particles which are tracked further. A cascade of particles develops in which e.g. the point in time, the amount and the position of the energy deposition of every shower particle can be determined and saved. In Geant4, the cascade ceases when all created particles have either escaped the defined world volume of the simulation or when their range has fallen below a so-called range cut. If the energy of a particle is so low that it cannot travel a distance larger than the defined range cut in the current medium its energy is deposited immediately and it is not tracked further. A small range cut allows for a higher precision, but increases the necessary computing time and disk usage. The choice of the range cut depends on the focus of the experiment and its required precision.

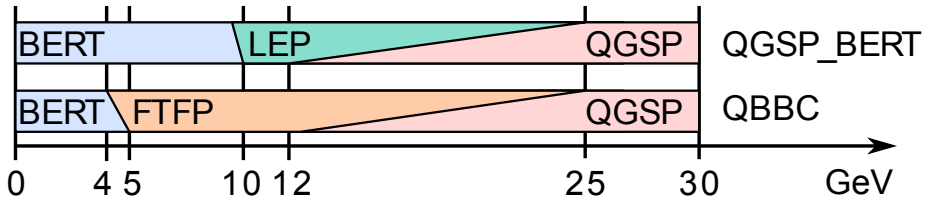

Figure 5.17: Sketch of the model content of the Geant4 physics lists QGSP_BERT and QBBC with respect to the energy range in which the models are valid (all physics lists use the respective models applied at 30 GeV for higher energies as well). Figure from [83].

Geant4 Physics Lists

In the interactions of electromagnetic cascades only electrons, positrons and photons are produced. The processes involved are theoretically well understood can be modeled and described to a high level of precision [82]. The physics of hadron cascades on the other hand is more complex and still not perfectly understood. In hadronic interactions, a large variety of processes can contribute and a large number of different particle species can be created. Unlike e^+, e^- and photons, hadrons are compound objects with a substructure that can become apparent and relevant for the interaction depending on the energy of the interacting particles. For a hadronic projectile impinging on an absorber with a momentum lower than ~ 1 GeV (see Section 3.1.3), only the nucleons of the target nuclei are on the right length scale to contribute to the interactions. At higher momenta, the partonic substructure of the interacting hadrons cannot be neglected anymore. Instead of a hadron interacting with nucleons, processes at high momenta can only be described correctly through the interaction of a quark (or gluon) of the projectile with a quark (or gluon) of one nucleon of the target nucleus. In a simulation of hadronic showers, the contributing hadronic processes (mediated by the strong force) cannot be calculated analytically anymore. Geant4 uses sets of approximations and parametrizations to describe the hadronic interactions of particles with matter. These sets follow different theoretical models and assumptions which are usually only valid in a limited range of particle energies. To obtain a consistent description over the full range of energies, different sets are combined to so-called physics lists with transition areas around sensible energy points at which either the one or the other description can be used (see Figure 5.17). Which physics list is the best one to choose is usually decided by the level of agreement with the experiment. It is therefore essential to compare the data with the simulation using several different physics lists.

A commonly used physics lists is QGSP_BERT. At high energies QGSP_BERT uses the **q**uark-**g**luon **s**tring model to describe inelastic pion-nucleon scattering on a partonic level followed by an external **p**recompound and de-excitation model to handle the fragmentation of the residual nuclei and the corresponding emission of protons, neutrons, light ions, photons and more. At low energies, the list uses the **Bert**ini cascade model to describe hadronic interactions on the nucleon scale. At intermediate energies,

QGSP_BERT uses additionally a **l**ow **e**nergy **p**arametrization (LEP) which originates from experimental data of past high energy experiments. In such a parametrization, no detailed modeling of the underlying physics is performed. QGSP_BERT is one of the standard physics lists used for simulation studies at CLIC [27] and at LHC [67], [84]. In all newer versions of Geant4 a **h**igh **p**recision extension of the list, called QGSP_BERT_HP is available which emphasizes the tracking of low energetic, potentially delayed neutrons and uses realistic cross sections for neutron capturing processes. This list is of major relevance for the T3B experiment, since delayed neutrons created in the hadronic cascade are the main source of late energy depositions in the detector. Due to these arguments, the differences between QGSP_BERT and QGSP_BERT_HP will be studied in the context of the time development of hadronic showers. HP extensions of this sort are currently being developed for a series of other physics lists as well. For the simulation studies of T3B, the physics list QBBC is also considered. In contrast to QGSP_BERT, it uses the Fritriof model at intermediate energies to describe partonic interactions followed by a precompound model for the fragmentation of the residual nuclei. QBBC uses a binary cascade model for protons and neutron-nucleus inelastic interactions at energies below 1.5 GeV (not shown in Figure 5.17) and does also respect the influence of low energetic neutrons, but with a different model for neutron capture than QGSP_BERT_HP [85]. It is therefore well suited for a cross check to the results of QGSP_BERT_HP. A detailed description of the individual cascade and partonic models and the corresponding physics lists can be found in [83].

Monte Carlo Event Generation for the T3B Experiment

For a valid Monte Carlo simulation, the material composition and the geometry of the CALICE steel SDHCAL, of the CALICE tungsten AHCAL and of T3B have to be modeled accurately within Geant4. Furthermore, their relative positioning within the test beam area has to be implemented. The implementation refers to the T3B test beam periods of September and October 2011, because we will focus in the analysis (see Chapter 6) on the data acquired within these phases. All simulations have been performed with Geant4 version 9.4 patch 3 due to issues in the time stamping of energy depositions in version 9.5. patch 1. A range cut of 0.05 mm was applied for all simulations. Figure 5.18 shows the event display of simulated hadron showers in both of the respective calorimeters, while the longitudinal and lateral dimensions of the calorimeters and the material budget of the individual layer components are summarized in Table 5.1. In the October T3B test beam phase, the SDHCAL consisted of 50 steel layers of 2 cm thickness out of which the first 40 were equipped with active RPCs while the last 10 calorimeter layers were left empty (omitting the Micromegas prototype layer). T3B was attached directly to the backside of the last steel absorber plate. In the September test beam period, the WHCAL consisted of 38 layers of tungsten with a thickness of 1 cm and was fully equipped with active scintillator cassettes. The T3B layer was positioned in slot 40 of the HCAL Stack leaving an air gap of 3.45 cm to the last absorber plate. The Tail Catcher and Muon Tracker (TCMT) present during the test beam phase was approximated by a 50 cm long steel block. It was positioned in

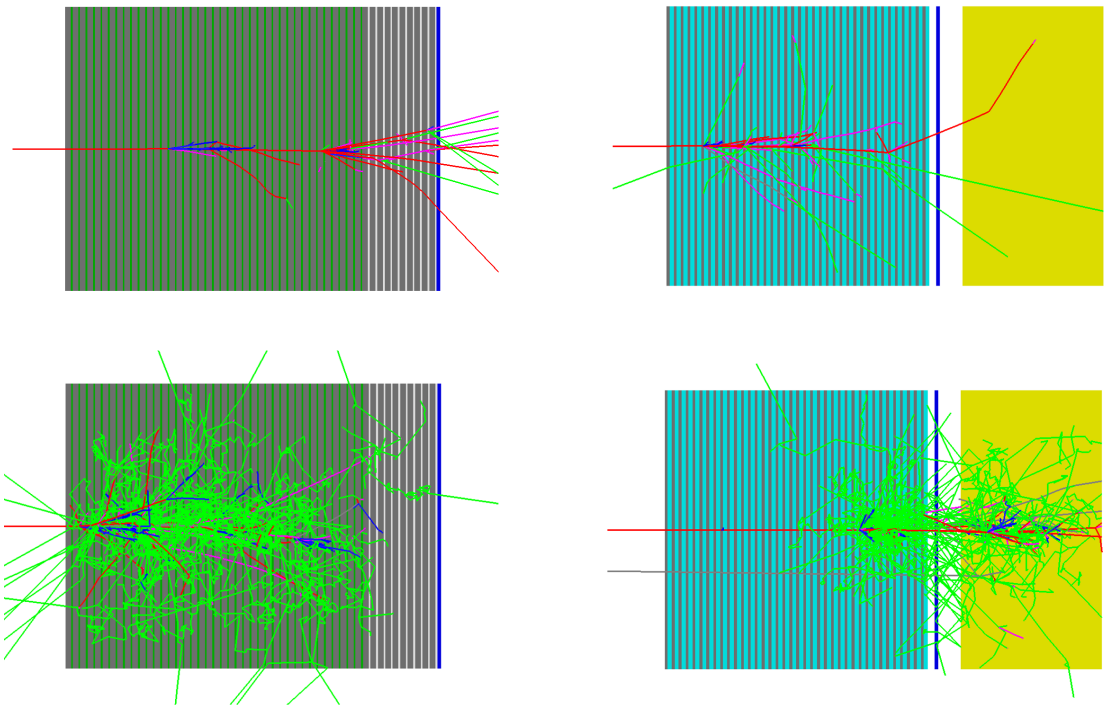

Figure 5.18: Event displays of the T3B Geant4 simulation for the SDHCAL (left) and the WHCAL (right) for π^+ impinging with a momentum of 60 GeV. The color coding of the tracks represents the particle type. The electromagnetic component (e^+, e^- and photons) is shown in blue. Concerning the hadronic component, π^+, π^- and protons are shown in red while neutrons are highlighted in green. Only the tracks of particles with an energy of > 450 MeV (top) or > 50 MeV (bottom) are shown. The T3B detector layer is highlighted in blue.

a distance of 9 cm behind the T3B layer. The T3B layer itself was modelled through two aluminium layers surrounding a layer of PCB material (**P**rinted **C**ircuit **B**oard hosting electronics) and the active scintillator. The scintillating material was modeled as G4_Polystyrene.
Geant4 comprises an implementation of Birks' law for certain materials (among others G4_Polystyrene). Birks' law is of special importance for the energy deposition of low energetic particles and has to be simulated correctly. Note that the late hadron shower evolution originates primarily from low energetic delayed neutrons. Figure 5.18 highlights the contribution of the neutron component to the hadronic shower. While the neutron number count is low for shower particle energies above 450 MeV, the large neutron contribution in the low energetic regime becomes apparent when reducing the visualization cut of shower particle tracks to > 50 MeV.

Birks' Law: Before stopped by the surrounding medium, the specific energy loss per unit length dE/dx of a low energetic charged particle is significantly increased (see Bethe-Bloch equation in Section 3.1.1). Compared to minimum ionization,

SDHCAL	Dimensions [cm]
lateral size	100
SDHCAL long.	130.65
T3B long.	1.3

WHCAL	Dimensions [cm]
lateral size	99
WHCAL long.	93.1
Air long.	3.45
T3B long.	1.3
Air long.	9
Steel Block long.	50

T3B Layer Component	Thickness [mm]
Al Cassette	1
Air	2.3
Scintillator	5
Air	1
PCB	1.7
Al Cassette	2
Total	13

SDHCAL Layer Component	Thickness [mm]
Steel	20
Epoxy	1.6
PCB g10	1.2
Mylar	0.23
Graphite	0.1
Glass	1.8
RPC Gas	1.2
Total	26.13

WHCAL Layer Component	Thickness [mm]
Steel Support	0.5
Tungsten	10
Air	1.25
Steel Cassette	2
Cable Mix	1.5
PCB	1
Scintillator	5
Steel Cassette	2
Air	1.25
Total	24.5

Table 5.1: Dimensions of the calorimeters and material constituents of the layers of the respective calorimeters as implemented in the T3B Geant4 simulation. All components are ordered longitudinally in beam direction.

the dE/dx is e.g. a factor of 4 (or 20) higher for 100 MeV (or 10 MeV) protons [38] leading to a high ionization density in the surrounding medium. In the case of organic scintillators, the fraction of the deposited energy that can be converted into light (scintillator light yield) is significantly reduced due to quenching effects between the excited molecules. In this quenching, the ionized molecules interact and may de-excite radiationless. As a consequence, the scintillator light yield per unit length dL/dx is non-linear for particles with high dE/dx. A widely used, semi-empirical description of this non-linearity was developed by Birks and is expressed by the formula:

$$\frac{dL}{dx} = S \cdot \frac{dE/dx}{1 + k_B \cdot dE/dx}, \tag{5.5}$$

where S is a proportionality constant and k_B the material dependent Birks'

constant which has to be determined for each type of scintillator by experiment.

For the T3B Geant4 simulation, data sets of protons, π^+ and μ^- impinging on the SDHCAL and WHCAL with an energy of 60 GeV, 80 GeV and 180 GeV were generated for the physics lists QGSP_BERT, QGSP_BERT_HP and QBBC. Each set comprises two million events. The simulation saves the key parameters of the T3B experiment in raw form. The amount (in keV), the time (in ns) and the position (in mm) of the energy deposition of each shower particle is recorded. Furthermore, the longitudinal shower starting point is logged for each event (details in Section 5.3 and [77]). As the next step, the generated data was digitized to be comparable to the acquired test beam data.

5.2.2 Digitization of Simulated T3B Events

The hadron shower events generated by the T3B Geant4 simulation are passed through a digitization procedure which introduces the response of the T3B detector into the simulation in a data driven approach. Key parameters from the simulation and from test beam data were determined to support this procedure. The digitization procedure aims to achieve a realistic simulation. Figure 5.19 shows the workflow of the digitization procedure as executed for the simulated data on an event-by-event basis.

As a first step, all energy depositions of an event are categorized in time with a binning of 0.8 ns and assigned to the respective T3B cells according to their spacial occurrence. Then, the deposited energy is rescaled from units of keV to units of photon equivalents for each time bin. Two digitization constants have to be determined to perform this step, namely the conversion factor $C_{keV \leftrightarrow MIP}$ which transforms the energy deposition from keV to MIP - the energy scale of minimum ionizing particles - and the factor $C_{MIP \leftrightarrow p.e.}$ which converts from MIP to p.e.. The constant $C_{keV \leftrightarrow MIP}$ is extracted from the energy deposition distribution in the central T3B cell of muons simulated with an energy of 180 GeV. Fitting the distribution and determining its most probable value leads to a conversion factor of $C_{keV \leftrightarrow MIP} = 805.5\,\text{keV/MIP}$. The constant $C_{MIP \leftrightarrow p.e.}$ is obtained from muon data at 180 GeV acquired at the test beam. As for the simulated muons, the energy distribution of the central T3B cell is fitted, but the native unit of the calibrated test beam data is p.e., so a value of $C_{MIP \leftrightarrow p.e.} = 24\,\text{p.e./MIP}$ can be extracted from the data. Note that at the test beam, this value can vary due to temperature changes (as previously shown in Figure 5.16). The conversion factor was determined as the average value of the whole muon data set. The factor does also depend on the integration time window, but converges for large windows to the value of 24 p.e. (previously shown in Figure 5.14). This conversion value for a maximized time window is the right choice, as we will see below in the photon time distribution step.

In the next digitization step, the energy deposited in each time bin of 0.8 ns is smeared according to a poissonian distribution. The underlying motivation is derived from the photon statistics in the T3B cell entity consisting of the photon sensor and the scintillator tile. A typical photon yield of an organic scintillator is 1 photon per 100 eV

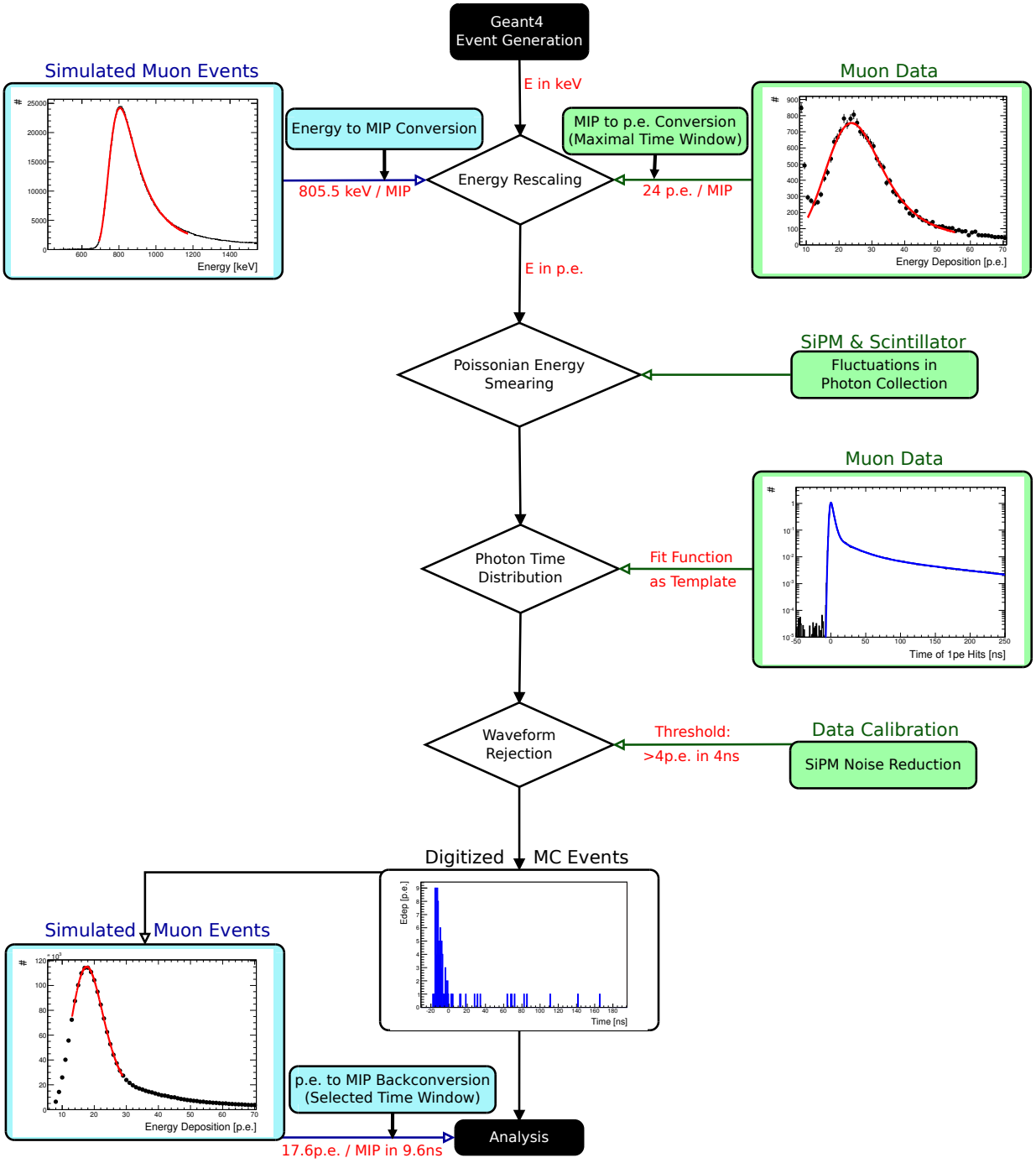

Figure 5.19: Workflow of the T3B digitization procedure executed on an event-by-event basis. For the digitization, several parameters and distributions were determined from test beam data (green, right) and from simulated data (blue, left).

of deposited energy [17]. A minimum ionizing muon which deposits 805.5 keV when traversing the T3B scintillator creates approximately 8000 photons. These photons are emitted in random directions, but the photon sensor is located at one distinct place. The probability of a photon to make it to the photon sensor and to create a signal is described by poissonian statistics. In the poissonian digitization step, the energy deposition in one time bin is randomized according to a poissonian distribution with a mean value identical to the amount of deposited energy (in units of integer photon equivalents). The resulting value of the deposited energy is assigned to the respective bin. The procedure is repeated for all time bins. This approach approximates the influence of the scintillator and the SiPM on the amount of detected energy in one step. Furthermore, all energy depositions of < 0.5 p.e. within 0.8 ns are ignored in the following. Figure 5.20 (left) shows the effect of this digitization step. The direct Geant4 output is randomized by the poissonian energy smearing. A limit of 400 p.e. was chosen for the poissonian mean value which is responsible for the peak at 400 p.e. providing a simple approximation of the saturation cut-off of a SiPM for which at most all 400 pixels can fire.

In Geant4, the energy deposition of a shower particle occurs instantaneously, while in reality, the measured signals comprise not only the timing of the hadronic shower but also the intrinsic timing of the individual detector components. As we are interested in the former and not all contributions that influence the timing can be unfolded in the test beam data, the intrinsic timing behaviour of the T3B detector has to be modeled in the simulation. Muons traversing a T3B scintillator cell represent a quasi-instantaneous energy deposition. For obvious reasons, no physical late energy depositions are present in this test beam data, so the observed timing behaviour originates exclusively from detector effects. A large test beam data sample, consisting of 5.4 million muon events at an energy of 180 GeV, was used to model the intrinsic timing of the T3B detector system. Only muon hits of the central T3B cell were selected. Here, a hit is defined as a waveform in which this cell identifies more than 15 p.e. (or 0.6 MIP) over the full range of the T3B acquisition window of 2.4 μs. This eliminates pure SiPM noise events efficiently. The timing of all photon equivalents identified within the selected set of waveforms is histogrammed and fitted by a custom function of the form of Equation 5.1 (see Figure 5.19). Note that the afterpulsing of the SiPM is also introduced into the simulation during this digitization step. The resulting fit function is used in the following as a template for the timing intrinsic to the T3B detector. At this stage of the digitization, a waveform consists of a number of instantaneous energy depositions of shower particles ordered by their time of occurrence into 0.8 ns bins and quantified in integer units of photon equivalents. Now each photon an energy deposition within the waveform consists of is randomized in time according to the fit function extracted from muon test beam data. The effect of this randomization procedure is shown in Figure 5.20 (right). Note that a global offset correction will account for the time offset introduced into the hit time distribution during this step (see Chapter 6).

Finally, a waveform rejection criterion is defined that is comparable for the test beam and the simulated data. In the calibration procedure of the test beam data, only

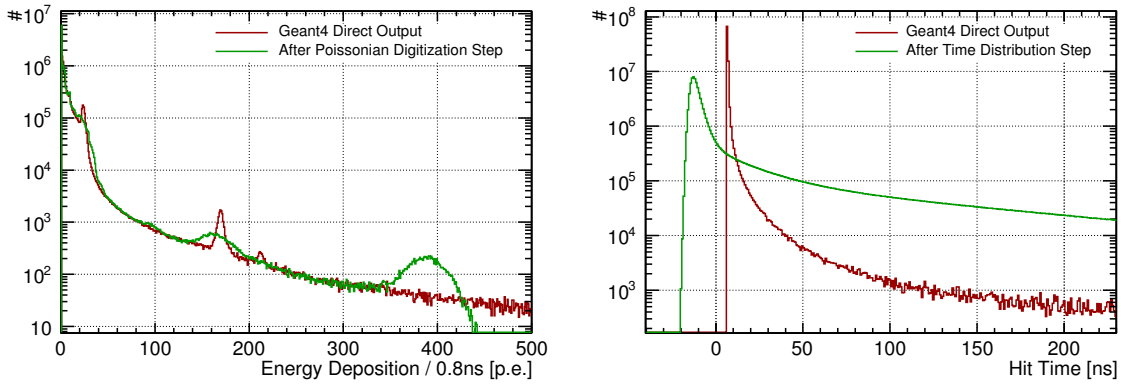

Figure 5.20: Control plots of the poissonian energy smearing step (left) and of the photon time distribution step (right) of the digitization procedure for all energy depositions and their respective hit times segmented into 0.8 ns bins. The data originates from a simulation of 60 GeV π^+ with the physics list QBBC. The direct output of the Geant4 event generation is shown in red, while digitized distributions highlighting the effect of the respective digitization steps are shown in green.

analog waveforms containing at least one sampling point > 12.5 mV (corresponding to a threshold of 2.5 p.e.) are considered for the waveform decomposition. This cut was introduced to avoid the execution of the decomposition procedure for too many pure noise events. A cut comparable to this has to be defined in terms of photon equivalents to make sure that the same range of energy depositions is used in the analysis. Requiring more than 4 p.e. within a time window of 4 ns somewhere within the waveform proved to be a good criterion. This rejection criterion is applied to test beam and simulated data likewise.

In the digitization procedure, we transformed the Geant4 generated energy depositions and their timing into waveforms that are expressed in terms of photon equivalents and that are geometrically categorized according to which T3B cell they belong. In the second level data calibration, a procedure was established to calibrate the energy depositions quantified in terms of photon equivalents within a limited time window (of e.g. 9.6 ns) to the MIP scale (see Section 5.1.2). A similar procedure has to be applied to simulated data. As before, the energy distribution of simulated muons is histogrammed for the central T3B cell, but for fully digitized events the histogram is given in units of p.e.. Fitting this distribution and extracting the most probable value results in a p.e. to MIP backconversion factor of e.g. 17.6 p.e./MIP that is specific for a selected time window of 9.6 ns. The procedure can be repeated for other time windows to obtain a calibration set equivalent to the one for test beam data.

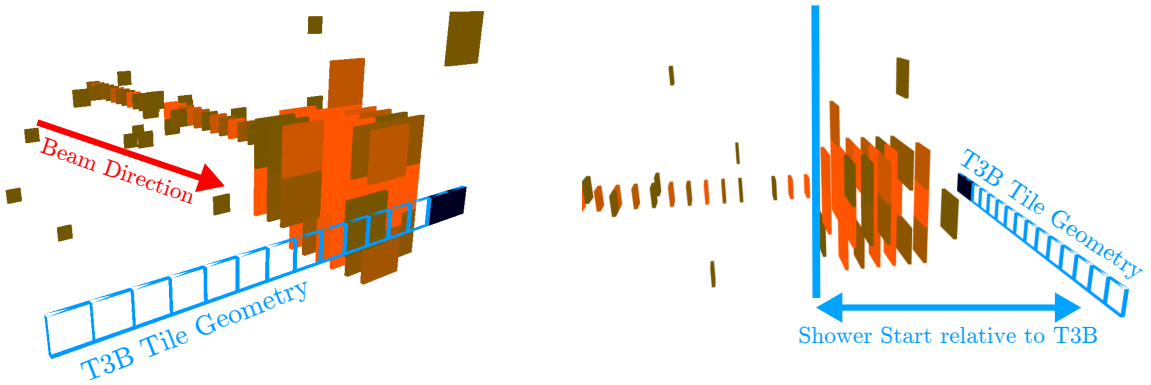

Figure 5.21: Event display of a hadron shower for which the T3B data (blue) and the CALICE tungsten AHCAL data (orange) was successfully synchronized. The longitudinal shower starting point can be identified relative to the position of the T3B cell strip.

5.3 Synchronization of CALICE to T3B Data

During the data taking periods performed together with the CALICE analog tungsten calorimeter, the T3B data acquisition system was triggered externally by the calorimeter (see Section 4.3.2 for details on the CALICE trigger system). Therefore, the physics events recorded by T3B and the CALICE tungsten AHCAL should match and an offline synchronization of the data is possible. If successful, the synchronization allows access to all the information the calorimeter has recorded on an event-by-event basis, such as the amount of energy deposited in each of the ∼8000 calorimeter cells, a particle identification provided by the Cerenkov counters, a trigger line history which records the time at which a device (e.g. a veto scintillator) present at the test beam saw a signal and more. The primary goal of the data synchronization is the identification of the longitudinal position of the shower start within the calorimeter. When categorizing the T3B events relative to this shower start, one can study the time development of hadronic showers also longitudinally.

The shower start is the longitudinal position of the primary inelastic interaction of the incoming particle within the calorimeter. To estimate the calorimeter layer where the primary interaction occurred an algorithm is used which detects the change from a minimum ionizing particle track to multiple secondary particles (see Figure 5.21). It searches longitudinally for an increased energy deposition together with an increased number of calorimeter cell hits over several consecutive layers. It is the default shower start finder developed and used by the CALICE AHCAL group and its parameters were determined empirically through simulation studies of the CALICE AHCAL (find details in [86]). In the T3B simulation the identification of the shower start was performed using the same algorithm. A detailed description on how the synchronization is performed and the shower start can be found is given in [77]. In that thesis, the synchronization of the CALICE tungsten AHCAL and T3B and the longitudinal time development of

hadron showers with T3B is one of the primary topics.

Chapter 6

The T3B Experiment - Analysis and Results

The T3B experiment was part of a rich test beam programme carried out by the CALICE Collaboration in the years 2010/2011 and recorded hadron shower events in a wide particle energy range between 2 GeV and 300 GeV (details in Section 4.3). Several run characteristics concerning the particle beam or the calorimeter have been changed during the test beam campaign to obtain a thorough understanding of the time development of hadronic showers: T3B acquired hadron data within a tungsten (CALICE WAHCAL, see Section 3.4.1) or steel (CALICE SDHCAL, see Section 3.4.2) based calorimetric environment to study the influence of the respective absorbers on shower timing. Different types of particles (muons, pions, protons etc.) were impinging the calorimetric structures. Large muon samples were taken as calibration data. They do not initiate showers (see Section 3.1.1) and their energy depositions can be assumed as quasi-instantaneous. At the same time, the muon data comprises all detector effects. For these reasons, the timing of hadron showers will be investigated relative to the standard signals of muons. In a particle beam with positive polarity, hadron showers are initiated by pions or by protons. The energy of the impinging particles represents another beam characteristic. We will focus on particle energies of 60 GeV, 80 GeV and 180 GeV since T3B recorded large hadron data sets for both absorber types at these energies. Statistical limitations are an important factor when studying rare energy depositions occurring at late times and restrict the achievable precision of the analysis. Finally, the acquired hadron data will be compared to simulated data sets. An extensive GEANT4 based event generation, digitization and event reconstruction has been carried out for the T3B experiment (see Section 5.2). Hadron data sets have been generated to validate or reveal the differences of simulation models that influence shower timing relative to test beam data. The physics lists QGSP_BERT, QGSP_BERT_HP and QBBC were used for that purpose (see Section 5.2.1 for details). Furthermore, differences in the shower evolution for impinging protons or pions will be investigated utilizing simulated data sets.

The influence of these run characteristics on the shower timing will be analyzed and quantified on the basis of several shower properties. The accessible parameters that can be attributed to hadronic energy depositions by the T3B experiment are the following: The geometrical point of occurrence can be given laterally through the subdivision of T3B into 15 scintillator tiles with a width of 3 cm. Longitudinally, the shower depth of an energy deposition (meaning its position relative to the shower start) is known for the T3B data acquired with tungsten absorber due to the successful offline synchronization the WAHCAL and the T3B data. For an extensive investigation of the longitudinal shower evolution, the reader is referred to [77]. The point in time when a scintillation photon gets detected by a SiPM can be specified with an accuracy of 0.8 ns due to the high sampling rate (1.25 GSa/s, see Section 4.2) of the oscilloscopes used for the T3B experiment. The timing when a particle traverses a T3B cell and deposits energy can be given with a precision of approximately 1 ns. Finally, the energy deposited by a cell-traversing particle can be quantified in terms of MIP (the energy scale of minimum ionizing particles) when utilizing the calibration information retrieved from laboratory measurements with a Strontium-90 source (see Section 5.1.2).
The T3B analysis comprises a one dimensional analysis of the time distribution of hadronic energy depositions and a two dimensional analysis of the average shower timing in relation to each of the given parameters. These plots are compared for the various run characteristics explained above.

In this chapter, we will first introduce the analysis framework. It was created and used to process the calibrated test beam data as well as the digitized and reconstructed simulated data. Furthermore, it prepares the data for the final comparison of different run characteristics. This comparison will be carried out in two different approaches: At first, we will analyze the time of the first hit (TofH) of shower particles incident on the T3B cells. This approach allows for a quantification of individual energy depositions. Then, we will analyze the time of hit (ToH) of scintillation photons on the light sensors. In this approach, all energy depositions are taken into account, also small ones occurring delayed after an initial high deposition within the same T3B cell. In this thesis, we focus on a standalone analysis of the T3B data. A thorough analysis using the additional information of the CALICE WAHCAL that is accessible through synchronization can be found in [77].

6.1 Analysis Framework

The analysis framework processes T3B data that belongs to one specific configuration of run characteristics with one of the two analysis approaches. An example of such a configuration is the TofH analysis of hadrons impinging with 60 GeV on the tungsten calorimeter (CALICE WAHCAL). Different run configurations can be analyzed sequentially and compared to each other in the following. Figure 6.1 shows a schematic workflow of the analysis framework.

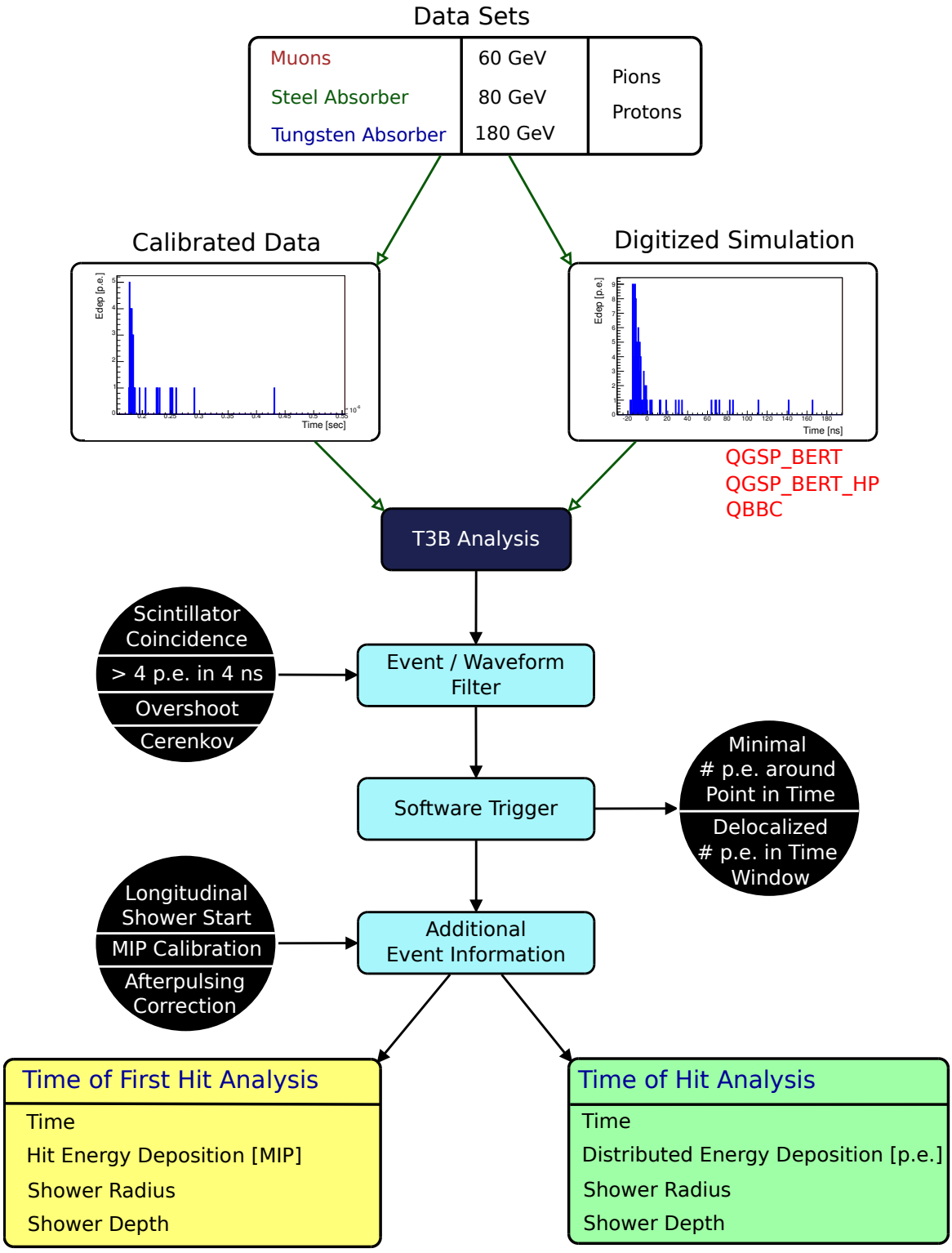

Figure 6.1: Workflow of the T3B analysis framework.

6.1.1 Run Selection

In a first step, all runs with exactly the same configuration of run characteristics are selected and their qualification for further analysis is checked on the basis of certain criteria. For example, test beam runs during which the beam settings were changed, in which hardware problems occurred or during which the accelerator showed irregular operation are categorized as bad and are rejected for the analysis. Furthermore, data quality plots generated by the T3B calibration framework (see Section 5.1.1) were reviewed to verify stable operation and tested for e.g. unphysical jumps in the pedestal values, the SiPM gain or shifts of the acquisition window relative to the hardware trigger time. In the case of tungsten data, we select only runs taken in the September 2011 test beam phase since the majority of 60 GeV, 80 GeV and 180 GeV runs were taken in this phase and because the environmental (e.g. ambient temperature) and calorimetric (e.g. T3B behind 38 HCAL layers and adjoining Tail Catcher positioned behind T3B) conditions within only one test beam phase are most consistent. In the case of steel data, only one test beam phase exists.

6.1.2 Run Processing

Test beam runs that passed the run selection as well as simulated data are analyzed on an event-by-event basis. In either case, the analysis is executed on the time resolved hit distribution of photon equivalents for all 15 T3B cells (decomposed waveforms in the case of test beam data, digitized and reconstructed energy depositions in the case of simulated data).

Software Filter

The analysis framework provides a set of filters, which are relevant for the processing of test beam data. There is the scintillator coincidence filter, which searches the T3B channel that recorded the scintillator coincidence signal of the CALICE trigger system (see Section 4.3.2 for details on the T3B trigger system). Since the trigger time offset is constant, the coincidence signal should always be found at the same point in time. If it is missing, the event was not triggered by an impinging beam particle and is therefore rejected. The same is true if several beam particles hit the calorimeter within e.g. the recorded time window of 2.4 μs. In this case the filter finds multiple coincidence signals. Such multi-particle events are rejected as they could fake delayed energy depositions. Note that the coincidence signal has a width of $\sim$ 50 ns. If a second beam particle traverses the coincidence scintillators within this dead time, the multi-particle event cannot be identified using the coincidence information. At the test beam, the beam intensity was chosen low enough that the probability for such fast multi-particle events is small. If the secondary particles originate from the same beam particle (e.g. if a particle decays or hits an obstacle on its way to the experiment) the veto scintillator information can be used to reject such events. For this to work, one of the secondaries

needs to propagate in a certain distance from the beam axis so that it traverses the veto scintillator.
Another filter requires more than four photon equivalents within a time window of 4 ns somewhere within the decomposed waveform of a cell. If this requirement is not met the signal of this cell is categorized as pure noise and not considered for the analysis of this event. The threshold was chosen to be more restrictive than the noise rejection threshold of the waveform decomposition (remember: only raw waveforms with at least one waveform sample with a value $> 12.5\,\mathrm{mV}$ are decomposed, see Section 5.1.1) and introduced to apply a comparable lower energy cut to test beam as well as simulated data. This cut was already applied for simulated data during the event reconstruction (see Section 5.2.2) and is here executed likewise for test beam data.
If the energy deposition within a single T3B cell is high (i.e. $> 5 - 6\,\mathrm{MIP}$), the probability rises that the recorded waveform exceeds the dynamic voltage range of the oscilloscopes. This represents one of the limitations of the T3B experiment. In this case, the waveform is vertically cut for a certain time period and the waveform decomposition cannot reproduce the correct amount and time distribution of photons. Information on these overshoots is available to the analysis framework, and an overshoot filter can be selected to reject such waveforms.
Finally, a Cerenkov filter is capable of selecting events that originate from a distinct type of beam particles (e.g. pions and protons). It searches the T3B channels that recorded the signal of the two Cerenkov counters. Depending on the used gas mixture and the adjusted pressure, all particles below a certain mass generate a signal. The right combination of the information of the two counters can help to identify particles of a distinct sort (see Section 4.3.1 for details).

Software Trigger

Two different software triggers are available that help to reject SiPM noise and to select energy depositions for the analysis in a consistent way. They are applied in the analysis of test beam and simulated data likewise.
The delocalized energy trigger searches each waveform in an event chronologically for an energy deposition. One needs to define a threshold in terms of photon equivalents and a time window of a certain width. The time window is shifted chronologically through the waveform until it contains a number of p.e. above the predefined threshold. This identified time window characterizes the first hit of a T3B cell. The actual number of found p.e. is assigned to the hit as its energy deposition. The time of the second identified p.e. is assigned as its software trigger time (the time of first hit). Choosing the second fired pixel reduces the probability that random thermal SiPM noise defines the timing of the first hit.
For the localized energy trigger, one defines explicitly the trigger time. A waveform is triggered and passed for further analysis if a minimal energy deposition (in number of photon equivalents) can be found in a certain time window around the predefined trigger time. All p.e. found outside of this window are ignored in the following analysis. This trigger serves as an adjustable lower energy cut in the time of hit analysis. Here,

TofH Analysis	Filter	Trigger	Complementary Info
Data	Scintillator Coincidence	Delocalized Energy: > 8 p.e. in 9.6 ns	MIP Calibration
	> 4 p.e. in 4 ns		(Shower Depth)
Simulation	> 4 p.e. in 4 ns	Delocalized Energy: > 8 p.e. in 9.6 ns	p.e. to MIP Backconversion
			(Shower Depth)

Table 6.1: Steering parameters in the analysis framework for the time of first hit analysis.

the threshold is increased to a value that is very unlikely to be exceeded by random SiPM noise (see Section 6.3).

Complementary Event and Calibration Information

Additional information can be loaded within the analysis framework to be applied on an event-by-event basis. This comprises the level 2 calibration information (see Section 5.1.2), which allows for a calibration of the energy depositions of first cell hits to the MIP scale respecting SiPM device specifications and its current gain. In the case of simulated data we will use the p.e. to MIP backconversion calibration factor for that purpose which was determined during the digitization procedure (see Section 5.2.2). Also an access of the run period specific afterpulsing information is possible. This information is used to minimize the contribution of SiPM afterpulsing to the ToH analysis results. The exact procedure will be explained in Section 6.3. Apart from this, the longitudinal shower start of each event can be accessed in this step of the analysis framework for test beam and simulated data likewise.

6.2 Time of First Hit

For the time of first hit analysis, the analysis framework is executed for all test beam and simulated data sets with a distinct configuration of the software trigger, filters and usage of complementary information. A summary of these steering parameters is shown in Table 6.1. The restriction of the trigger time window to only 9.6 ns makes the analysis of first hits very robust against SiPM afterpulsing. We will investigate the energy depositions of shower particles primarily within an energy range of 0.4 MIP to 5 MIP. While the lower threshold originates from the 8 p.e. requirement of the software trigger, the upper limit is chosen due to the high overshooting probability above 5 MIP. We did not apply the overshoot filter in this analysis since the time of the first hit can

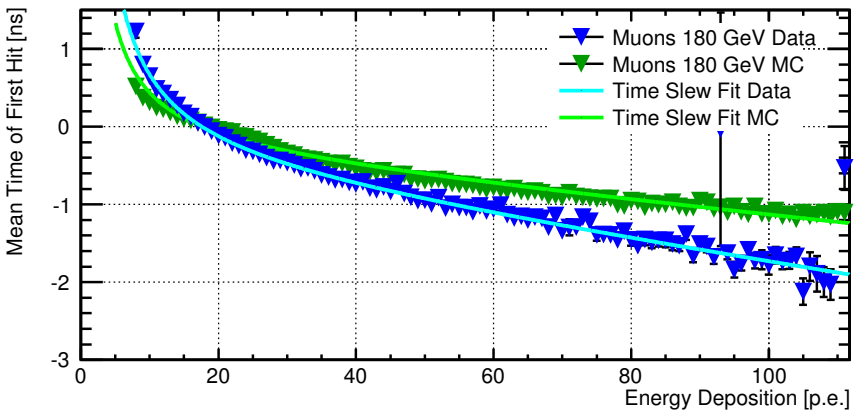

Figure 6.2: Dependence of the mean time of the first hit on the hit energy for muon data acquired at the test beam (blue) and simulated muons (green) for a beam energy of 180 GeV and for the central T3B cell.

be determined for overshoot waveforms as well.
We will furthermore focus predominantly on a time range between -20 ns and $+200$ ns around the typical hardware trigger time. This time range is most relevant for timing calorimetry at CLIC since it is comparable to the length of a bunch train and the time integration window of the CALICE AHCAL electronics. Whenever we refer to the mean time of the first hit, it is the time value averaged within this reduced time window. Nevertheless, timing information was acquired and can in principle be studied to an upper limit of $\sim 2\,\mu$s.

6.2.1 Time of First Hit Specific Calibration Procedures

After the execution of the analysis framework and before we can compare the analysis results of different run characteristics, we have to apply two additional calibration routines which are specific to the time of first hit determination: A time slew correction and a time offset normalisation.

Time Slew Correction

A statistical effect, which we call time slew, is created by the dependence of the time distribution of the detected photons of a cell hit on the hit energy and the functional principle of the delocalized energy trigger. The effect is well known and related to the fixed threshold (the second found photon equivalent) used for the definition of the time of occurrence of an energy deposition. The signal generated by a high energy deposition exhibits a steeper rising edge than the signal from a low energy deposition. So for a high energy deposition, a large number of SiPM pixels fires very quickly after the shower particle(s) traversed a T3B cell and the delocalized energy trigger identifies the

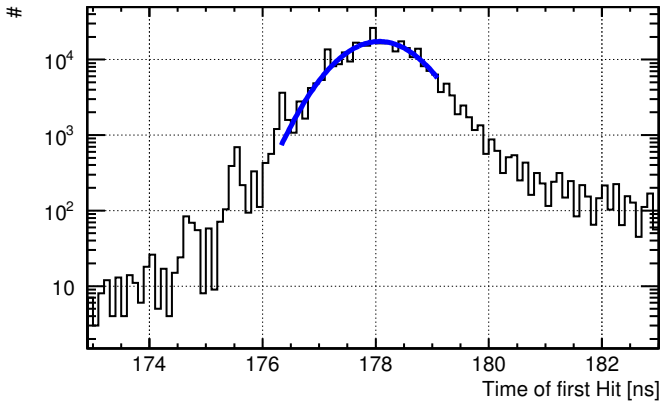

Figure 6.3: Determination of the typical time offset of a data sample by fitting the time of first hit distribution with a Gauss. Shown is the distribution for hadrons impinging with 60 GeV on the tungsten calorimeter. The binning effect originates from the native hardware time resolution of 0.8 ns (see text for details).

time of first hit, on average, with a very small time delay. In the case of a low energy deposition, in which just a small number of pixels fired (the lowest accepted depositions comprise only 8 p.e.), the time of the second identified photon equivalent tends to be found, on average, significantly delayed. Since this effect is related to an imperfect time of first hit determination, we will apply a calibration routine that corrects for it on a hit-by-hit basis. Figure 6.2 shows the dependence of the mean time of the first hit on the hit energy for muons. The time slew effect is less pronounced for simulated muons than for muon data acquired at the test beam. While a steep rise up to a delay of 0.6 ns (MC) or 1.3 ns (Data), respectively, is observed for the lowest energy depositions, the dependence weakens for higher energies and falls off to a value of -1 ns (MC) or -2 ns (Data) at 120 p.e. (~ 6.8 MIP). The distribution was chosen to have a delay time of zero at a value of 17.6 p.e. which corresponds to an energy deposition of 1 MIP in a 9.6 ns time window. The following functional form was found to fit the time slew distribution well:

$$\bar{t}_{TimeSlew} = \frac{a}{E[p.e.]} + b \cdot E[p.e.] + c \tag{6.1}$$

In the TofH analysis, the extracted time slew fit is used as a template. Depending on the energy deposited by a first hit, the identified time is normalized to zero time slew according to this template. Note that after the time slew correction, the time values can be given with a binning finer than 0.8 ns (e.g. in Figure 6.3). Nevertheless, binning effects originating from the native hardware time resolution of 0.8 ns arise which is why we refrain from using a finer binning in the analysis.

Time Offset Normalisation and TofH Time Resolution

Since different hardware trigger configurations have been used in different test beam phases and due to the photon time distribution procedure applied for simulated data

Data Set	Muons	Steel			Tungsten		
	180GeV	60GeV	80GeV	180GeV	60GeV	80GeV	180GeV
Timing Precision	1.07 ns	1.00 ns	1.53 ns	1.31 ns	0.70 ns	1.08 ns	0.69 ns
Events in Analysis	5.40M	1.60M	1.85M	1.20M	4.06M	4.48M	0.74M
# Events with Hits	790k	203k	302k	422k	716k	1037k	170k
# First Hits	854k	312k	492k	782k	1014k	1540k	308k
Multiplicity	1.08	1.54	1.63	1.85	1.42	1.49	1.81

Table 6.2: Time stamping precision achieved and statistics obtained (all T3B cells, all hit energies and all hit times) at the test beam for data sets acquired with different run characteristics. Note that the multiplicity is the number of identified first hits divided by the number of events with first hits. For the hit statistics, the beam energy, the calorimeter type and depth and also the particle beam composition play a role.

(see Section 5.2.2), the hardware trigger time offset varies for data sets with different run characteristics. We have to apply a global method to normalize this time offset for all data sets in a consistent way. Therefore, we generate the one-dimensional time of first hit distribution for the central T3B cell for each data set (see Figure 6.3). The peak of this distribution (and its width in particular) represents the detector response to the quasi instantaneous part of the energy depositions within showers. Its maximum is therefore well defined within the shower evolution and well suited as normalization point for the time offset correction. Thus, we fit a Gauss in a narrow region around the peak.[1]. The time of the maximum extracted from the Gauss fit is used as the global time offset ($t = 0$) for the data set and subtracted in the TofH analysis. The systematic uncertainties of this $t = 0$ determination are estimated to be at the level of 100 ps to 200 ps. Apart from this, it was found that - after the offset determination - the timing of all simulated data sets deviates consistently by 290 ps from the timing of test beam data. The origin of this data to simulation offset is so far unknown, but it is corrected for by subtracting an additional 290 ps from all simulated data sets.
The precision with which the moment of an energy deposition (i.e. the moment of shower particles traversing a T3B cell) can be timestamped depends on the intrinsic time resolution achievable with the T3B cells, the photon reconstruction, the time jitter introduced by the used coincidence scintillators from the beam line and the hardware trigger system. In this sense, the width of the fitted Gauss represents an upper limit of the TofH resolution achievable with T3B cells. Table 6.2 shows the time stamping precision achieved for a number of selected data sets.

6.2.2 Analysis Results

We now have all information at hand which is necessary for a discussion and investigation of the time of first hit analysis results. Figure 6.4 gives an overview over the available

[1] In fact, we follow a two-step approach. We fit a preliminary Gauss in a region of -2.4 ns to $+1.6$ ns around the maximum bin. A second refined Gauss is fitted in a range of $-2.5\,\sigma_{G1} < Max_{G1} < +1.5\,\sigma_{G1}$.

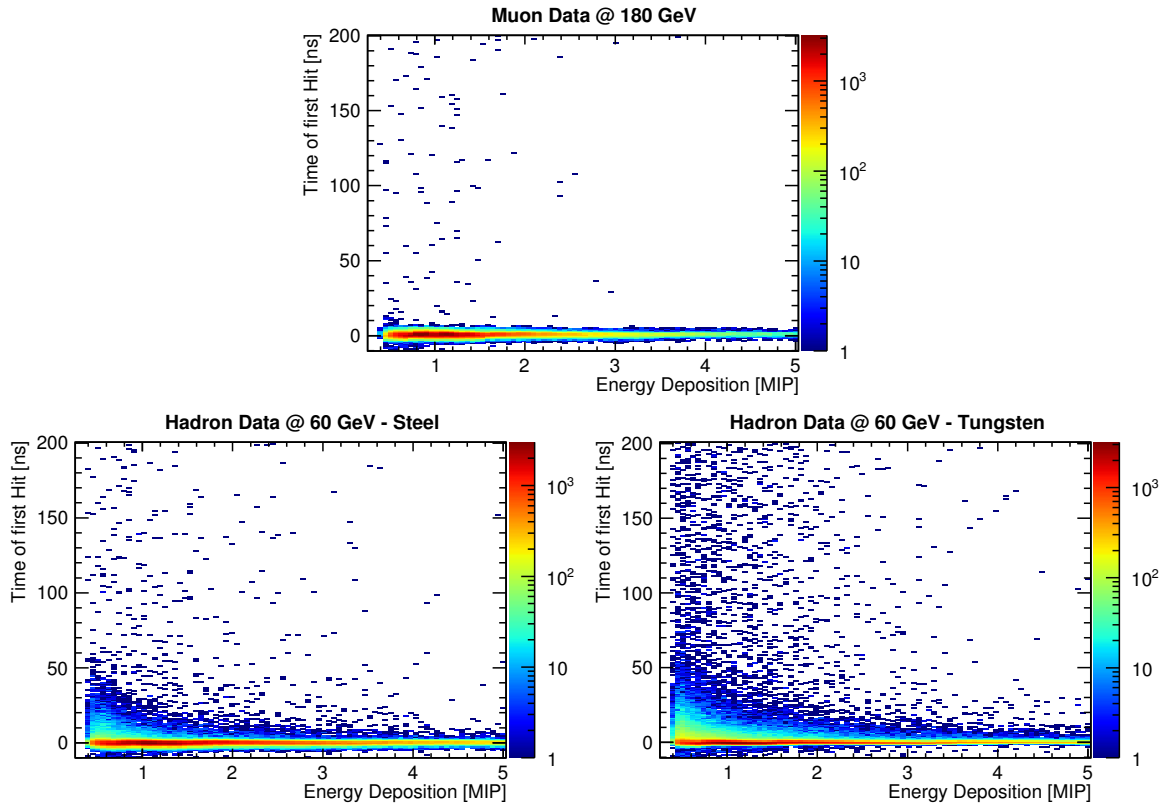

Figure 6.4: Distribution of 203.103 T3B events with identified first hits with respect to their time of occurrence and the energy deposited by them for different run characteristics, namely muon data (top) and hadron data in steel (bottom, left) and tungsten (bottom, right).

TofH information and first insight into the physical properties of hadronic showers with respect to timing. It shows the time of first hit distribution in dependence of the identified hit energy for muon data and hadron showers developing in steel and tungsten with an impinging particle energy of 60 GeV. Here, all T3B cells are combined into one plot. The hadron data consists predominantly of π^+ events, but since no particle identification is performed the data samples include an admixture of protons, kaons and also μ^+. To allow for a direct comparison of the distributions, all three histograms comprise the same number of events in which at least one T3B cell identified a first hit. Since the statistics is the lowest for steel data, it is reduced for muon and tungsten data. For the rest of the TofH analysis we will use the full statistics available (see Table 6.2). Separated by T3B cell number, these plots form the basis of the TofH analysis in which different projections of the histograms will be studied. Note that we do not distinguish showers starting at different depths, i.e. we use the whole T3B standalone data, unless specified otherwise. In each subsection of the analysis, we will first give a short physical motivation for the investigation of the shower characteristic with respect to timing. Then, we compare the data sets and try to quantify the level of agreement or the differences observed by T3B.

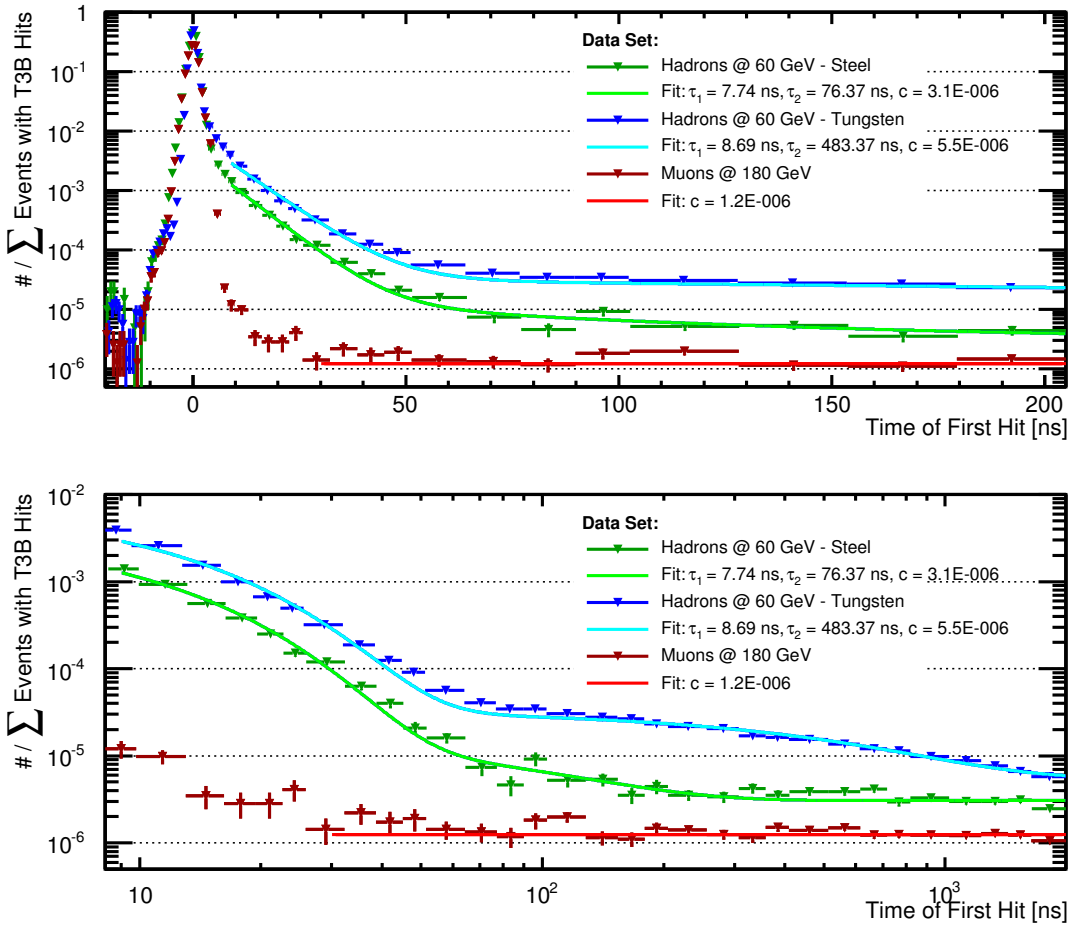

Figure 6.5: Time of first hit distribution of the muon, steel and tungsten data in a time range of −20 ns to 200 ns (top). The histograms are normalized to the number of events in which at least one first hit could be identified. The same distributions are shown in a time range from 9 ns up to 2000 ns on a logarithmic time scale (bottom). Here, the peak of the distributions was excluded for better visibility.

Hadron Shower Timing in Different Absorber Materials

Within a hadronic cascade, absorber materials with high atomic number Z are expected to release an increased number of evaporation neutrons. So in total, a higher fraction of the initial energy of an impinging hadron is eventually deposited through neutrons. Since these neutrons are scattered and captured predominantly at the end of the development of the hadronic cascade with lowest energies and before the final absorption of the shower energy, they are the leading origin of delayed energy depositions. Therefore, one expects that a significantly higher fraction of the shower energy is deposited late for tungsten absorber material ($Z_{\mathrm{W}} = 74$) relative to steel ($Z_{\mathrm{Fe}} = 26$). Muons do not initiate showers and their energy depositions are expected to be quasi instantaneous. Two neutron interaction processes are predominant in the context of delayed energy

depositions. The elastic scattering of evaporation neutrons with the calorimeter material is expected to occur at a timescale of $\mathcal{O}(10\,\text{ns})$, whereas neutron capture processes can occur at very late times with a delay of up to $\mathcal{O}(100 - 1000\,\text{ns})$ (see Section 3.1.3).

These hypotheses are corroborated by the acquired test beam data: Figure 6.4 (top) shows that all energy depositions initiated by impinging muons were detected quickly within a small time window around the hardware trigger time (t=0). The isolated late hits in this Figure are caused by SiPM noise and give a good impression of the quality of the noise rejection criteria applied for the analysis. Only 105 out of 215.000 first hits, which corresponds to less than 0.05 %, were identified at a hit time later than 8 ns. The situation is very different for the hadron data samples. In the case of steel (see Figure 6.4, bottom left), 1.2 % (3329 out of 277000) of the first hits were detected with a delay of more than 8 ns. In the case of tungsten (see Figure 6.4, bottom right) the late shower component was even more emphasized with 3.6 % (8965 out of 251000) of the first hits occurring delayed. While the largest part of a hadron shower (99.92 % of the first hits) has decayed after 50 ns in the case of steel data, the tungsten data exhibits a notable late activity (0.5 % of the first hits) even at late times beyond 50 ns. In general, it is observed that the late shower activity is significantly larger for tungsten relative to steel data at all times. This is shown in Figure 6.5 (top), in which the time distribution of all first hits, normalized to the number of events with T3B hits, is plotted. Similar to the muon time distribution, the hadron data samples exhibit a quasi instantaneous component which contributes (due to the intrinsic time resolution of T3B) only in a range of -8 ns to 8 ns. Additionally, in the case of hadron data there is a fast shower component τ_{fast} contributing at intermediate times which passes smoothly into a slow shower component τ_{slow} (at $t \approx 50\,\text{ns}$). Therefore, for a first evaluation of the involved parameters, the late time development of hadron showers was fitted by a simple model which consists of a sum of two exponential decays and a constant c that takes the random SiPM noise contribution and possible additional contributions with very long time constants that cannot be resolved by T3B due to the limited acquisition window into account:

$$\frac{N_{TofH}}{\sum N_{\text{Events with T3B Hits}}} = A_1 \cdot exp(-\frac{t}{\tau_{fast}}) + A_2 \cdot exp(-\frac{t}{\tau_{slow}}) + c, \tag{6.2}$$

where N_{TofH} is the number of identified first hits and A_1 and A_2 are the amplitudes of the fast and slow component, respectively. From laboratory measurements, investigating the noise and cross talk rate of the 15 SiPMs used within T3B, we expect the order of magnitude of the contribution from SiPM noise to be $\mathcal{O}(10^{-6})$. Variations in the run conditions (such as temperature or voltage variations) influence the occurrence of SiPM noise. Furthermore, the statistics available for the respective data sets determines the accuracy with which rare processes can be resolved, and therefore influences the constant c. For steel data, for example, the number of events with T3B hits is substantially smaller than for muon data (see Table 6.2).
Since the fit is executed over six orders of magnitude, we follow a two step approach. We first fit the slow shower component together with the constant c in a range from 90 ns to 2000 ns and fix the obtained parameters for the subsequent total fit. With the

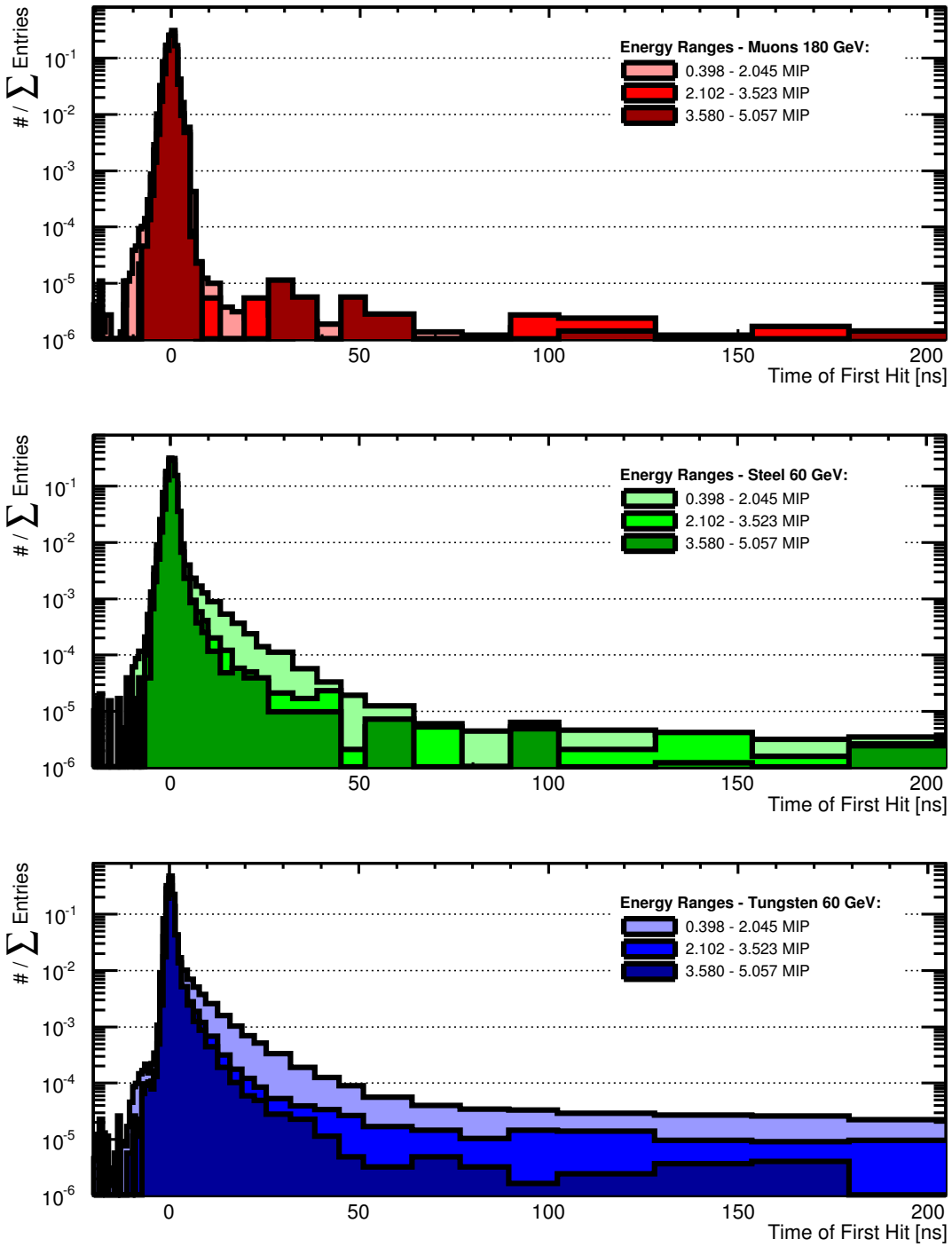

Figure 6.6: Energy dependence of the time of first hit distribution for three different energy ranges for muon (top), steel (center) and tungsten (bottom) data. The time distributions are scaled to the number of entries to allow for a shape comparison of the energy ranges.

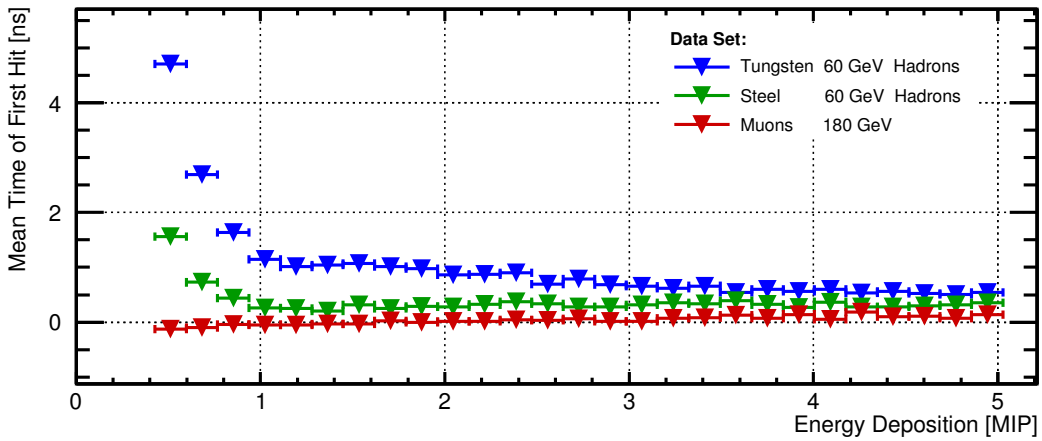

Figure 6.7: Energy dependence of the mean time of first hit for muon (red), steel (green) and tungsten (blue) data.

described procedure we find a fast decay time of about 8 ns for both hadron data samples (7.7 ns for steel, 8.7 ns for tungsten data), whereas the very late shower development differs largely for steel and tungsten data. In the case of steel data, the slow decay occurs with a time constant of about 80 ns and its contribution to the fit becomes less than 10 % for times later than 290 ns where the constant c dominates the distribution. For tungsten data, on the other hand, the slow decay time amounts to about 500 ns and plays an important role (with a contribution of $> 10\,\%$) up to the end of the investigated acquisition time at 2 μs. This is shown in Figure 6.5 (bottom) in which the same distributions are plotted in a larger time range from 9 ns up to 2000 ns on a logarithmic time scale. The highly emphasized late shower component of tungsten relative to steel data can be quantified by the ratio R_i of the respective amplitudes A_i multiplied by the corresponding extracted time constants τ_i:

$$R_i = \frac{A_i^{tungsten} \cdot \tau_i^{tungsten}}{A_i^{steel} \cdot \tau_i^{steel}} \tag{6.3}$$

Note that the product $A_i \cdot \tau_i$ is the definite integral of the exponential component related to τ_i from zero to infinity. Thus, it corresponds to the total number of energy depositions (per event and detectable by T3B) that are caused by the type of processes occurring with the time constant τ_i. Evaluating the ratios R_i, we find that the fast shower component τ_{fast} is emphasized by a factor of $R_{fast} = 2.3$ and the slow component even more by a factor of $R_{slow} = 13.4$ in tungsten with respect to steel.

The energy dependence of the timing of hits is studied in Figure 6.6. It shows the time of first hit distribution for muon, steel and tungsten data split into three different energy ranges from ~ 0.4 MIP to ~ 5 MIP. Since the energy depositions induced by muons are prompt, no energy dependence is observed here. For steel data, the majority of late hits deposits only little energy, predominantly in the lowest range of 0.4 MIP to 2 MIP. In the case of tungsten data, on the other hand, the time distribution exhibits a

significantly delayed contribution not only in the lowest, but also in the intermediate and in the high hit energy range. Comparing the statistics of the three energy ranges, we find that for steel data 61 % of all identified hits deposit energy in the low, 20 % in the intermediate and 8 % in the high energy range (the remaining 11 % deposit energies above 5 MIP). The total fractional contribution of the different energy ranges for tungsten is 63 %, 18 % and 7 %, respectively. For this comparison, the time range between −20 ns and 200 ns was taken into account. But the distributions are largely dominated by the quasi instantaneous shower contribution between −8 ns and 8 ns. We conclude that, concerning prompt hits, the average composition of energy depositions (e.g. of minimum ionizing particles depositing 1 MIP relative to multiple particle hits in one cell which results in a significantly higher energy deposition) is very similar for hadron showers propagating in steel and tungsten.
Figure 6.7 shows the mean time of the first hit in dependence of the hit energy. As expected, no delay is observed at any energy for muon data. For steel, the average hit time is slightly delayed by 1.6 ns at 0.5 MIP, but this delay decreases quickly down to less than 300 ps for energies above 1 MIP. Also in this direct hit energy comparison, the tungsten data exhibits, on average, a significantly delayed shower contribution at all energies. At 0.5 MIP, the average delay is with 4.7 ns about three times larger than for steel. At $\sim$ 1 MIP, the mean TofH does still amount to more than 1.1 ns and decreases down to 500 ps at $\sim$ 5 MIP.

The observed differences and the general trend of the late shower propagation within tungsten compared to steel are in good agreement with the expectations from theory and empirical studies of other high- and low-Z absorber materials performed in the past (see Section 3.1.3 and [38]).

The Lateral Time Distribution of Hadronic Showers

Due to the fact that the π^0s which constitute the electromagnetic fraction of a hadron shower are created within the first few interactions of the shower development and due to the very different lengths scales of the radiation length X_0 and the nuclear interaction length λ_I, the hadronic cascade can be, on average, geometrically subdivided into two different zones. A central shower core, which is dominated by the electromagnetic fraction and a shower halo, which is dominated by the hadronic component of the shower. The shower tails (longitudinally and laterally) comprise a significant contribution from low energetic evaporation neutrons. Therefore, the energy depositions in the shower center are expected to be prompt, whereas a significant delay should be observed with increasing shower radius. This effect should be more pronounced (steeper) in a tungsten absorber environment than for steel, since here, the ratio of λ_I to X_0 is much larger ($\sim$ 27 for tungsten and $\sim$ 10 for iron) and since the abundance of evaporation neutrons is increased for tungsten.

These trends are reflected in accordance with theory by the lateral timing profile shown in Figure 6.8. In both absorbers, late energy deposits are more important in the outer region of the shower. In the next section, we will prove that this timing characteristic

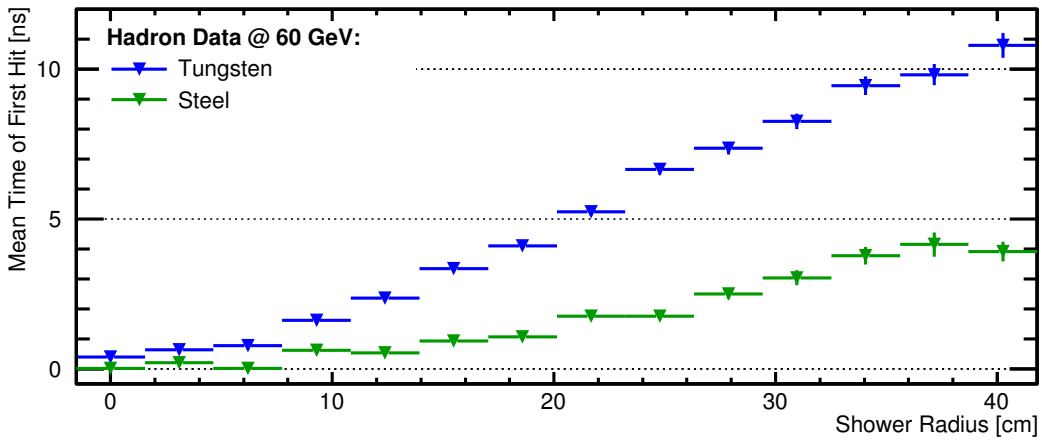

Figure 6.8: Lateral shower timing profile of the mean time of first hit for steel (green) and tungsten data (blue).

can be attributed to delayed shower contributions and is not related to differences in the geometrical and calorimetric depths of the respective calorimeters (the thickness of the SDHCAL and WAHCAL is 130.6 cm and 93.1 cm or 6.5 λ_I and 5.1 λ_I, respectively). While the average hit time is at all radii larger for tungsten data than for steel data, the deviation between the profiles increases with the shower radius. At a radius of $\sim$ 40 cm, the mean TofH is, in the case of tungsten (10.8 ns), 2.8 times larger than for steel (3.9 ns). In the shower center, this relative timing difference amounts to only 370 ps.

The origin of this deviation of the mean TofH can be understood through a shape comparison of the time of first hit distribution for different shower radii (see Figure 6.9). We study the two different effects which contribute.

On the one hand, there is the intrinsic time the prompt component of the hadronic shower (consisting of the electromagnetic fraction, charged pions and protons etc.) needs, on average, to propagate to large radii. Note that this contribution can not be simply attributed to the direct time of flight. This becomes apparent when examining the TofH distributions in a narrow range around the peak (see Figure 6.9, bottom). The maximum of the TofH distribution is shifted to later times for larger radii. At the largest investigated lateral shower range (23.3 – 38.7 cm), the maximum of the distribution is found with a delay of $\sim$ 700 ps in the case of steel, and even more delayed at $\sim$ 1000 ps for tungsten. The average depth of the shower start for all hadron events acquired for the WAHCAL (SDHCAL) at 60 GeV is found at 2.08 λ_I (see Figure 6.11) which corresponds to a geometrical depth of 38 cm (41.6 cm). The direct time of flight of a particle traveling with the speed of light from this calorimeter depth of 2.08 λ_I to the end of the calorimeter at 93.1 cm (130.6 cm) and out to a radius of 38.7 cm amounts to 2.24 ns for the WAHCAL (3.23 ns for the SDHCAL). If the particle would have travelled on a straight line to the central T3B tile, the time of flight would have been 1.84 ns (3.00 ns). The difference of 400 ps (230 ps) is by far smaller than the observed delay times. So the intrinsic prompt development of a hadron shower (without the direct

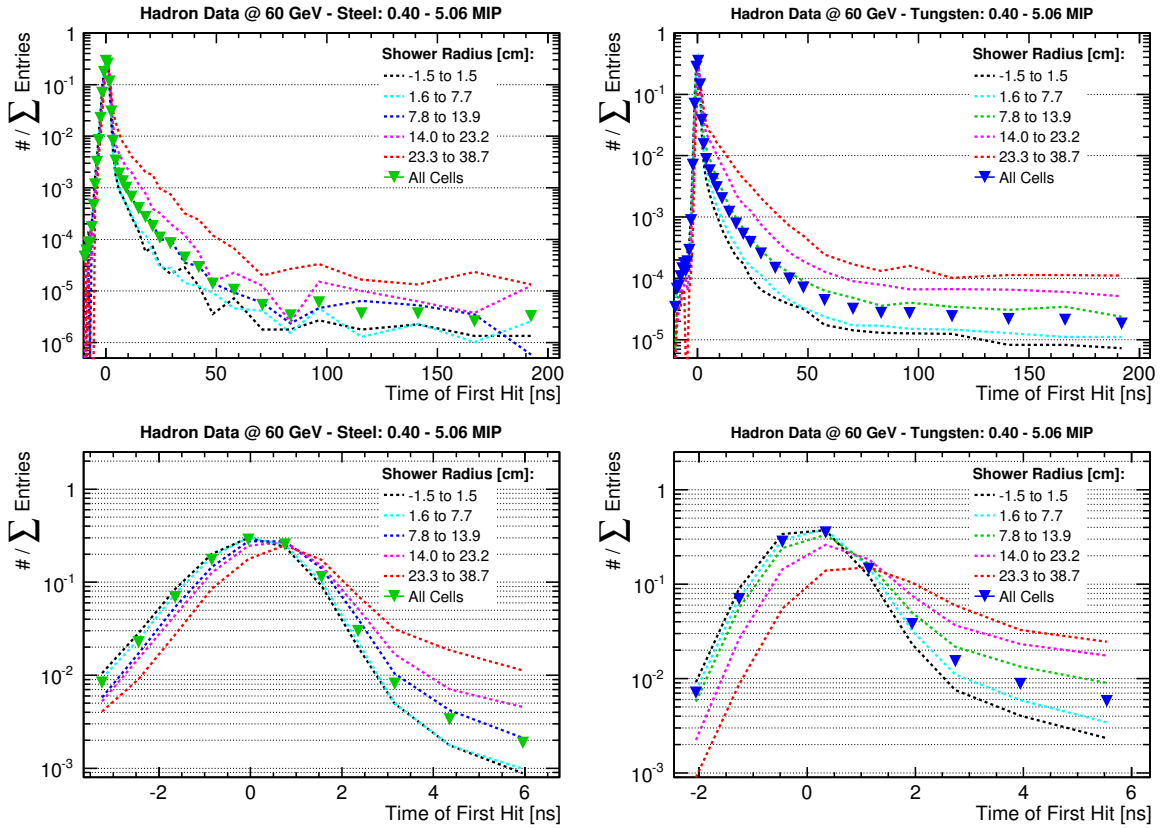

Figure 6.9: Time of first hit distribution for steel (left) and tungsten data (right), split by the shower radius. The distribution is shown in the standard time window ranging from −20 ns to +200 ns (top) and in a zoomed view towards the peak from −3.2 ns to +6 ns (bottom). The distributions are normalized to the number of entries to allow for a line shape comparison.

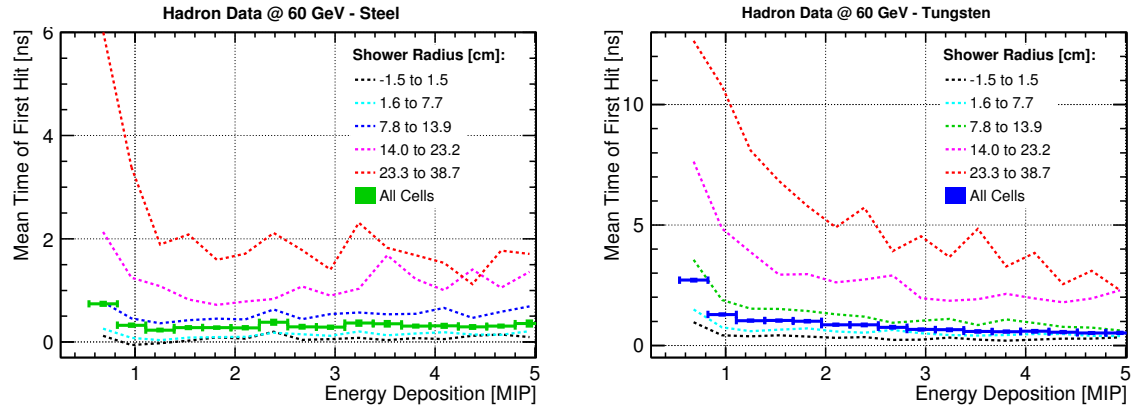

Figure 6.10: Energy dependence of the mean time of first hit, split by the shower radius for steel (left) and tungsten data (right).

time of flight difference discussed above) takes, on average, more than $\sim 600\,\text{ps}$ in the case of tungsten, and $\sim 470\,\text{ps}$ in the case of steel. This intrinsic delay of the prompt shower component is caused by the multitude of interactions of the shower particles on their way through the calorimeter and an effective increase of the average propagation distance of shower particles.
The second effect can be attributed to the fact that the fractional contribution of the delayed part of the shower (interaction processes of evaporation neutrons) is emphasized for larger shower radii. This can be investigated with the same TofH distributions. It manifests in Figure 6.9 (bottom) through a decrease of the maximum of the distribution and is substantially more pronounced for tungsten compared to steel. For tungsten, for example, the fraction of the first hits identified at the time of the maximum is 26 % smaller in the largest shower radius range compared to the shower center. For steel this difference in the height of the maximum amounts to only 6 %. If a smaller fraction of the hits is found in the prompt shower peak, the delayed shower hits contribute a larger part. This is shown in Figure 6.9 (top). Here, the fractional contribution of the delayed shower component (at times $> 10\,\text{ns}$) is about one order of magnitude larger for the outermost lateral range compared to the center for tungsten as well as for steel data. It is also apparent from these TofH distributions, that the delayed component (at times $> 10\,\text{ns}$) contributes about one order of magnitude more for tungsten compared to steel at all radii.
Finally, we can study the dependence of the mean TofH on the hit energy for different distances from the shower center (see Figure 6.10). We find that, for steel, the characteristic functional dependence of the mean TofH, which was discussed in the last section for all T3B cells combined, is primarily caused by energy depositions occurring at radii larger than 7.8 cm. At smaller radii the functional form is flat and prompt at all hit energies. Also for tungsten, the outer shower region contributes largely to the overall shape of all cells combined. Nevertheless, the contribution of delayed energy depositions is more pronounced for tungsten than for steel data at all radii (note the different scale of the Y-axis).

T3B in Different Calorimeter Depths

In a short excursion, we verify the comparability of the steel and tungsten standalone data, acquired in different calorimeter depths of $\sim 6.5\,\lambda_I$ and $\sim 5.1\,\lambda_I$ behind the CALICE SDHCAL and the WAHCAL, respectively. Therefore, we perform a simulation study in which the number of calorimeter layers in front of T3B can be changed. We use the physics list QBBC for this purpose. For both calorimeter types, we simulated sets of 2 million π^+ events with an impinging particle energy of 60 GeV for which the T3B layer was positioned in a calorimeter depth of $\sim 3\,\lambda_I$, $\sim 4\,\lambda_I$ and $\sim 5\,\lambda_I$ and compare them to the data sets simulated with the actual thickness of the calorimeters. The dimensions and relative distances of the WAHCAL and the SDHCAL and the geometrical depth of the T3B experiment are shown in Figure 6.11. The TofH distributions (see Figure 6.12) exhibit only minor differences in the late shower development in dependence of the amount of absorber material in front of T3B for the steel as well as for the tungsten data

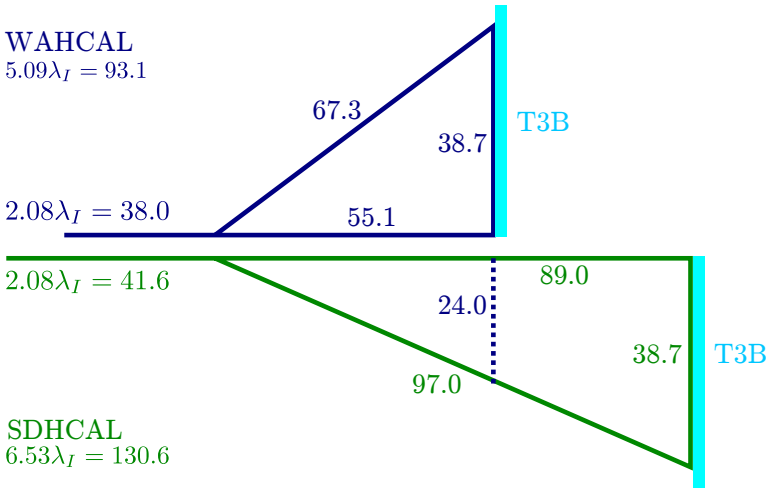

Figure 6.11: Geometrical comparison of the dimensions of the WAHCAL (blue, top) and the SDHCAL (green, bottom). All dimensions are given in centimeter. The average depth of the shower start amounts to $2.08\,\lambda_I$.

set. In particular, no consistent systematic development with the calorimeter thickness can be observed. This is similar for the dependence of the mean TofH on the hit energy (see Figure 6.13). Although a small systematic behaviour can be assumed for very low hit energies, the distributions match for the most part for all calorimeter depths studied for each of the two absorber types within the level of precision achievable with T3B ($\sim 200\,\text{ps}$). Note that absolute time differences that arise due to the increased direct time of flight of shower particles to the T3B experiment when located in greater depth were corrected for by the time offset calibration explained in Section 6.2.1. This offset calibration is performed in accordance with the situation at the test beam, since the time t=0 was always defined through the arrival time of signals on the central T3B cell and not relative to the point in time when a beam particle enters the calorimeter. Therefore, differences can only appear if a systematically different part of the shower development is measured in a different calorimeter depth. On the scale of the deviation in thickness of $1.4\,\lambda_I$ which amounts geometrically to 28.0 cm in the case of the SDHCAL and 25.6 cm in the case of the WAHCAL and with T3B positioned at the end of the calorimeter, such differences are not significant and within statistical and systematic uncertainties of T3B. Remember that no shower start separation was performed here and that the discussed data sets comprise all possible shower depths.
The differences with respect to the calorimeter depth could be also visible when studying the lateral shower timing, i.e. the lateral dependence of the mean time of first hit on the distance from the beam axis. Simply considering time of flight differences, the lateral timing profile would be expected to exhibit a higher delay at large radii when T3B is located in a smaller depth. This is related to the fact that the difference in distance between a straight line from the shower start to the central T3B cell and a straight line from the shower start to a shower radius of 38.7 cm (see Figure 6.11) is larger if T3B is positioned closer to the shower starting point ($\Delta d(\text{WAHCAL}) = 67.3\,\text{cm} - 55.1\,\text{cm} = 12.2\,\text{cm}$ and $\Delta d(\text{SDHCAL}) = 97.0\,\text{cm} - 89.0\,\text{cm} = 8.0\,\text{cm}$). The fact that such an effect

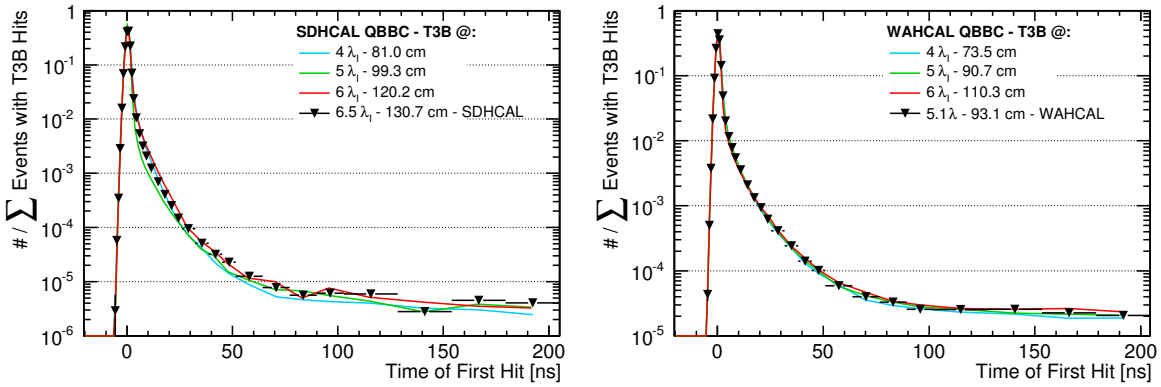

Figure 6.12: Comparison of the time of first hit distribution for simulated 60 GeV π^+ impinging on a SDHCAL (left) or WAHCAL (right) with a variable thickness of $\sim 3\,\lambda_I$, $\sim 4\,\lambda_I$ and $\sim 5\,\lambda_I$ and T3B positioned behind.

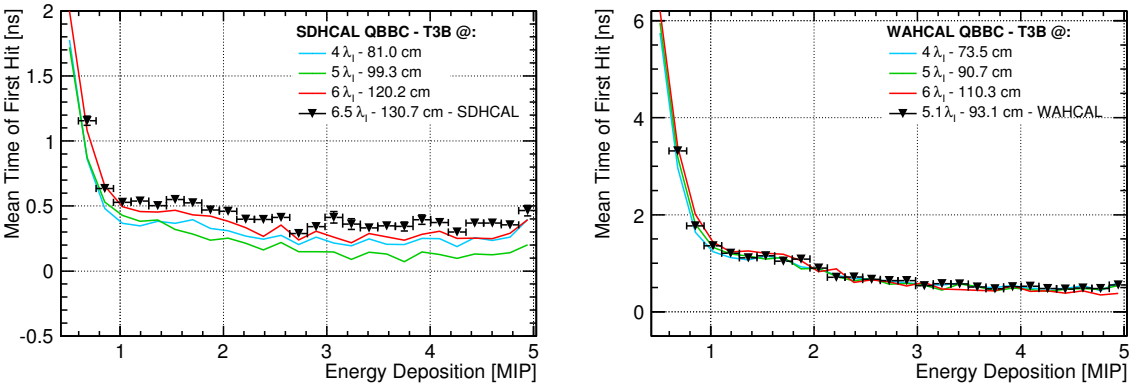

Figure 6.13: Comparison of the energy dependence of the mean TofH for the SDHCAL (left) or WAHCAL (right) with T3B after $\sim 3\,\lambda_I$, $\sim 4\,\lambda_I$ and $\sim 5\,\lambda_I$ (π^+ at 60 GeV).

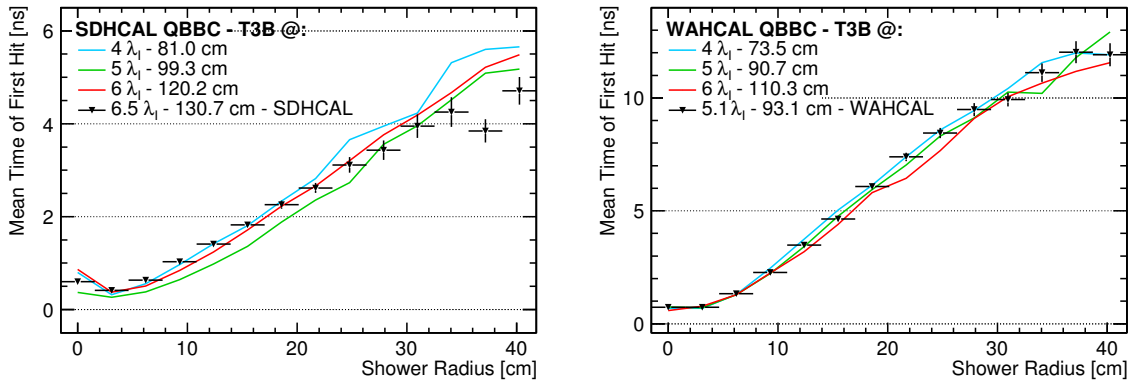

Figure 6.14: Comparison of the lateral shower profile of the mean TofH for the SDHCAL (left) or WAHCAL (right) with T3B after $\sim 3\,\lambda_I$, $\sim 4\,\lambda_I$ and $\sim 5\,\lambda_I$ (π^+ at 60 GeV).

does not cause a systematic difference (exceeding the uncertainties) when comparing the lateral timing in different depths (see Figure 6.14) corroborates the hypothesis that geometrical effects represent only a minor contribution to the lateral line shape and that the mean time of first hit is largely dominated by the delayed shower fraction instead. Altogether, this verifies that the comparison of data acquired with the SDHCAL and the WAHCAL is legitimate, although their calorimetric depth differs by $\sim 1.4\,\lambda_I$.

The Comparison of Data to Monte Carlo Simulations

In this section, we study to which precision simulation models can reproduce the timing properties of hadronic showers. For this purpose, we compare the GEANT4 physics lists QGSP_BERT, QGSP_BERT_HP and QBBC to data. For each physics list and both detector types, we analyze a simulated data set that comprises two million π^+ events impinging with an energy of 60 GeV. We expect the latter two lists to reproduce the shower timing better than QGSP_BERT since they include a special treatment and a high precision tracking of low energetic shower neutrons.

We find that, for steel, the TofH distribution can be reproduced generally well by all physics lists (see Figure 6.15). QGSP_BERT underestimates the number of hits at intermediate times between 20 ns and 50 ns slightly. QBBC, on the other hand, overestimates the number of hits a bit at times in the range $3 - 10$ ns. For tungsten, on the other hand, the distribution is reproduced very well by QBBC and QGSP_BERT_HP, but not by QGSP_BERT. At late times above 50 ns, where the capture of low energetic neutrons becomes most relevant, QGSP_BERT overestimates the number of delayed hits largely by a factor ranging from 1.9 at 58 ns to 2.8 at 192 ns.
Concerning the functional form of the of the mean TofH dependence on the hit energy (see Figure 6.16), QBBC and QGSP_BERT_HP reproduce the data well for both absorber types. Only for steel and at intermediate shower hit energies of $1 - 2$ MIP, QBBC exhibits a slightly too large mean TofH. As above, QGSP_BERT can not deliver a good description of the late shower timing in tungsten. Although the obtained functional form is similar to the one from data, the mean TofH turns out to be between 2 ns and 0.5 ns too large over a wide hit energy range of 0.4 MIP to 3.5 MIP, respectively.
Also a comparison of the lateral shower timing reveals a similar performance of the different simulation models (see Figure 6.17). All physics lists reproduce the steel data satisfactory on the level of precision achievable with T3B. In the case of tungsten, QGSP_BERT overestimates the delayed shower contribution at all radii, but increasingly in further distance from the shower core. While the difference to data in the mean TofH amounts to only 2.0 ns at a radius of 9.2 cm, it increases up to 7.8 ns in the outer shower region at 40.2 cm. For the high precision neutron lists, the lateral timing profile agrees generally well with data. Only at larger radii the mean TofH is slightly too high on the level of $\sim 1 - 2$ ns.

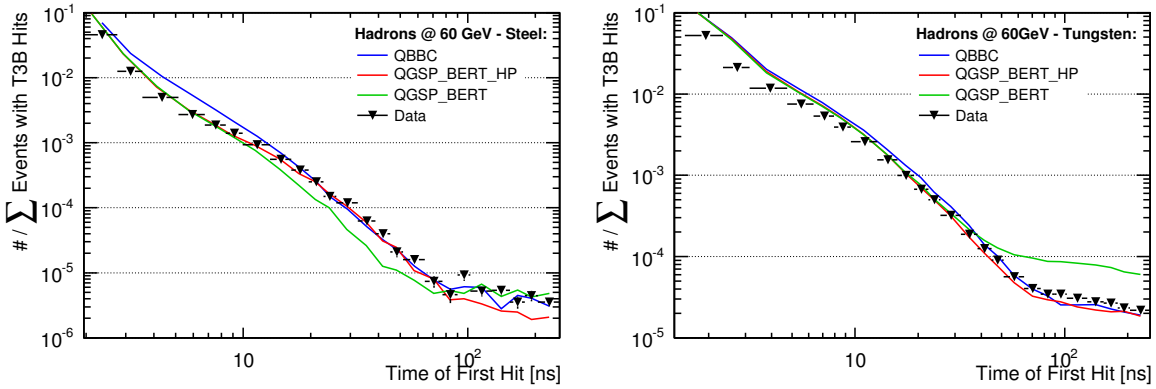

Figure 6.15: Comparison of the time of first hit distribution of Monte Carlo and test beam data for steel (left) and tungsten (right). The time axis is given on a logarithmic scale.

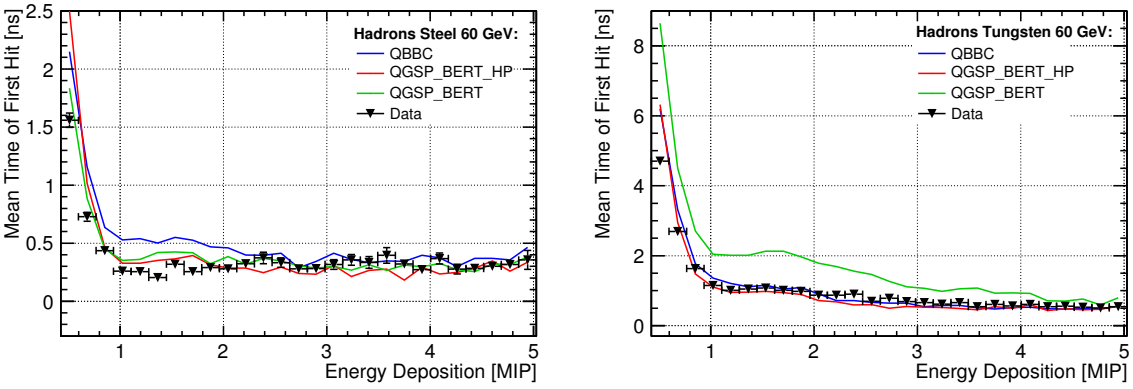

Figure 6.16: Comparison of the energy dependence of the mean time of first hit of Monte Carlo and test beam data for steel (left) and tungsten (right).

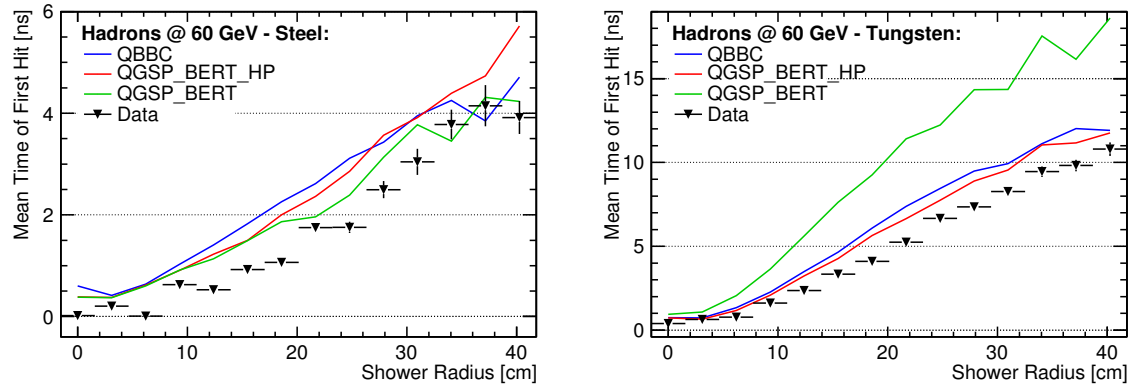

Figure 6.17: Comparison of the lateral shower profile of the mean time of first hit of Monte Carlo and test beam data for steel (left) and tungsten (right).

The Dependence of Hadronic Shower Timing on the Particle Energy

Interactions within the hadronic cascade can occur on a partonic level only in the first few nuclear collisions where the energy carried by the shower particles is high ($> 1\,\mathrm{GeV}$). The π^0s which induce the electromagnetic shower fraction are only generated in such partonic collisions. If more energy is available for the shower development, more collisions above the pion production threshold of $\sim 1\,\mathrm{GeV}$ are possible. Therefore, the electromagnetic fraction of a hadronic shower increases systematically with the energy of an impinging beam particle. Calculations predict that the electromagnetic fraction should increase on a level of $\sim 10\,\%$ when increasing the energy of the impinging particle from $50\,\mathrm{GeV}$ to $200\,\mathrm{GeV}$ (see Section 3.1.3). We assume that, in this aspect, steel and tungsten show a similar behaviour to copper and lead, respectively, for which this value has been determined. Since electromagnetic subshowers deposit their energy promptly, one would expect that the delayed shower component is reduced for higher beam energies.

To study this dependence, we create the same set of plots as above for test beam data acquired at a beam energy of $60\,\mathrm{GeV}$, $80\,\mathrm{GeV}$ and $180\,\mathrm{GeV}$. The functional form of the TofH distribution (see Figure 6.18) exhibits an excellent agreement of the data samples for tungsten and for steel, which seems to be completely independent of the beam energy. The slight systematic increase in the number of hits per T3B event for both absorbers originates from the fact that the hit probability of T3B increases for higher energetic showers. This is corroborated by the fact that the dependence of the mean TofH on the hit energy (see Figure 6.19) and the lateral timing profile (see Figure 6.20) match generally well on the level of precision of T3B for the three investigated energies and both absorbers.
In general, no systematic increase or decrease of delayed shower components could be observed. We conclude that the overall effect of the shower energy on the timing properties of hadronic showers is small in a range of $60 - 180\,\mathrm{GeV}$ and that a $\sim 10\,\%$ change in the electromagnetic shower fraction cannot be resolved within the statistical and systematic uncertainties of the T3B experiment. This means that the mean TofH agrees between the three investigated energies within a few hundred picoseconds for all hit energies and all shower radii. A systematic increase or decrease in the abundance of first hits of delayed relative to fast shower components would have been easily revealed by the investigation of the hit time distribution (see Figure 6.18) if the number of hits per time bin differs by more than approximately $\pm 50\,\%$.

The Difference between Protons and Pions

Hadron showers induced by impinging protons have to obey the law of baryon number conservation. This means that if a nuclear collision happens on a partonic level with an impinging baryon, also the final state after the collision has to contain a baryon. Thus, the fractional energy that is available for the formation of π^0s is reduced and proton induced showers are expected to be more hadronic. In the past, simulation studies

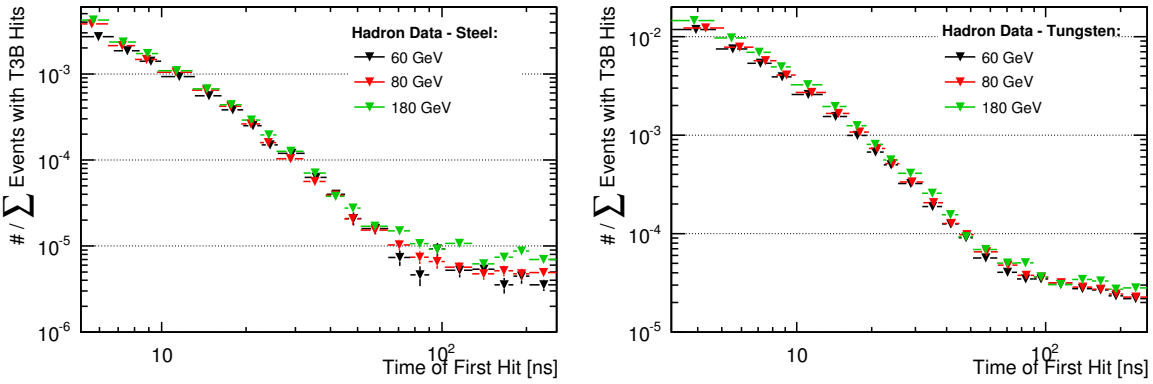

Figure 6.18: Comparison of the time of first hit distribution at different beam energies for steel (left) and tungsten (right) data. The time axis is given on a logarithmic scale.

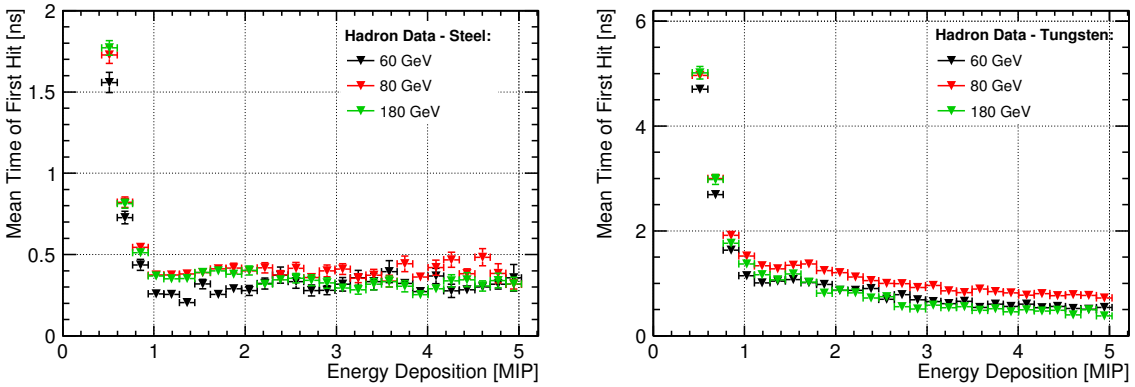

Figure 6.19: Comparison of the energy dependence of the mean time of first hit at different beam energies for steel (left) and tungsten (right) data.

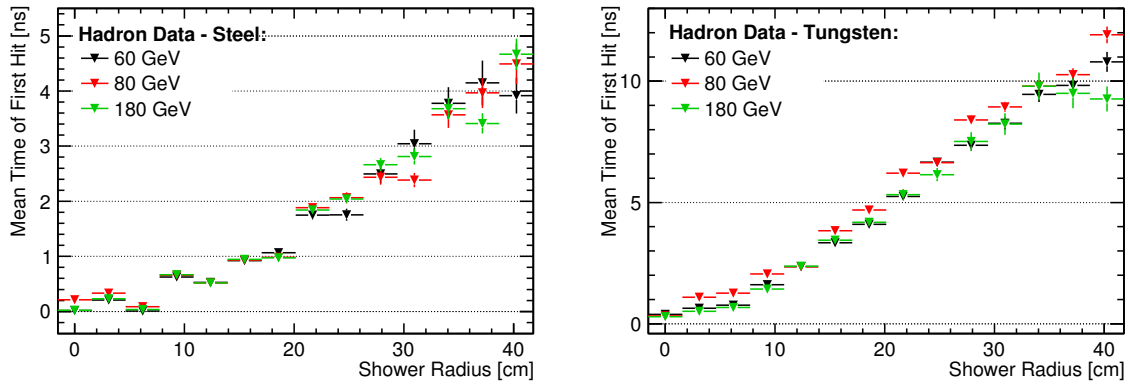

Figure 6.20: Comparison of the lateral shower profile of the mean time of first hit at different beam energies for steel (left) and tungsten (right) data.

showed that the electromagnetic fraction is reduced by $\sim 15\,\%$ due to this effect, in the case of impinging protons compared to pions (independently of their energy, see Section 3.1.3 for details). Therefore, proton induced showers are expected to exhibit a more pronounced late shower component.

This effect was studied through an extensive Monte Carlo simulation. Samples of two million π^+ and proton events have been generated with the high precision physics lists QBBC and QGSP_BERT_HP at an energy of 60 GeV for both absorbers. No significant differences between pion and proton data can be identified through the TofH distribution (see Figure 6.21). Figure 6.22 shows that the mean TofH appears to be slightly larger for proton compared to pion data in range of $0.5 - 2\,\mathrm{MIP}$ for both absorbers. This difference amounts roughly to $\sim 100\,\mathrm{ps}$ in the case of steel and 200 ps in the case of tungsten and is observable for both physics lists. These deviations lie within the range of the systematic uncertainties ($\sim 200\,\mathrm{ps}$) of T3B. On the basis of this simulation, we do not expect T3B to observe significant differences between proton and pion data with respect to the energy dependence of the mean TofH. Also the lateral timing profile of T3B (see Figure 6.23) does not reveal a significant difference in the mean TofH at any shower radius.
Altogether, the Monte Carlo generated T3B data does not exhibit an emphasis of the delayed shower component of protons with respect to pions which is pronounced enough to be observable by T3B. Nevertheless, an investigation of the mean TofH suggests the correct tendency at low hit energies. According to this study, also an increased electromagnetic fraction of $\sim 15\,\%$ does not result in a delay of proton relative to pion induced showers which is significant on a level of $> 200\,\mathrm{ps}$.

Estimation of Necessary Shower Integration Times

In this section, we try to estimate which fraction of the total energy that is, on average, deposited by a hadron shower is measured within a certain shower radius and within a certain integration time. We will compare how this radial and temporal shower fraction differs for a steel and tungsten absorber structure. This property is most relevant for the performance of a calorimetric system at CLIC. The achievable jet energy resolution is better if the measured fraction of a shower is maximized (see Section 2.3.2). If the delayed component of a hadron shower is large for the used absorber material, also the integration time has to be increased in order to detect the same shower fraction as for an absorber material that generates only few delayed particles. On the other hand, if a long integration time is chosen, the hadron shower can be, on average, larger in its geometrical dimensions since it also comprises the delayed hadronic tail. But in the case of larger showers, it is more difficult for particle flow algorithms to distinguish the energy depositions of different jet particles and the confusion factor increases. In this regard, the longitudinal and lateral dimension of the measured shower fraction should be as small as possible. Apart from this, also the pile-up of collider events plays an important role in the case of long integration times. So the aim is to integrate a large shower fraction while keeping the shower integration time and integration radius from

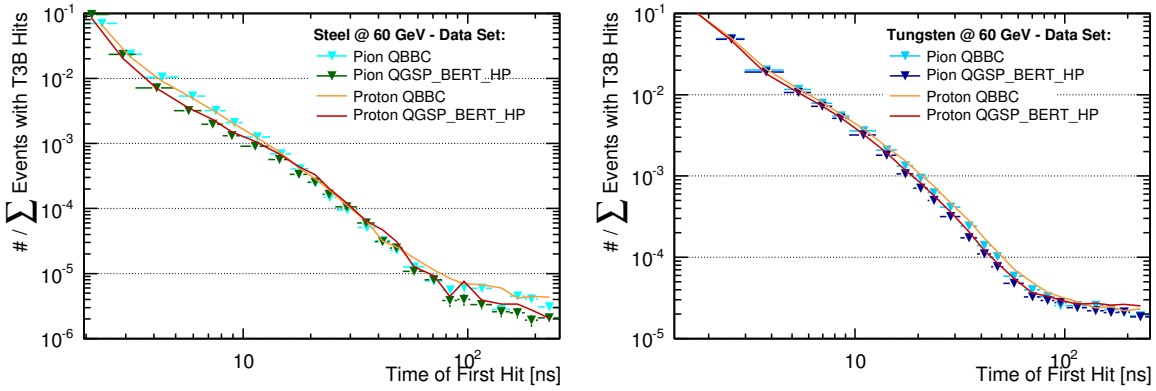

Figure 6.21: Comparison of the time of first hit distribution for impinging protons and pions in the case of Monte Carlo generated steel (left) and tungsten (right) data. The time axis is given on a logarithmic scale.

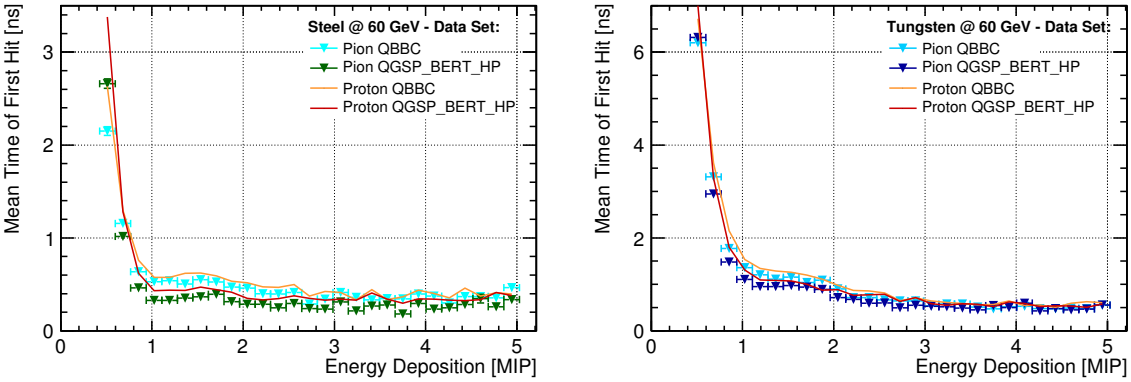

Figure 6.22: Comparison of the energy dependence of the mean time of first hit for impinging protons and pions in the case of MC generated steel (left) and tungsten (right) data.

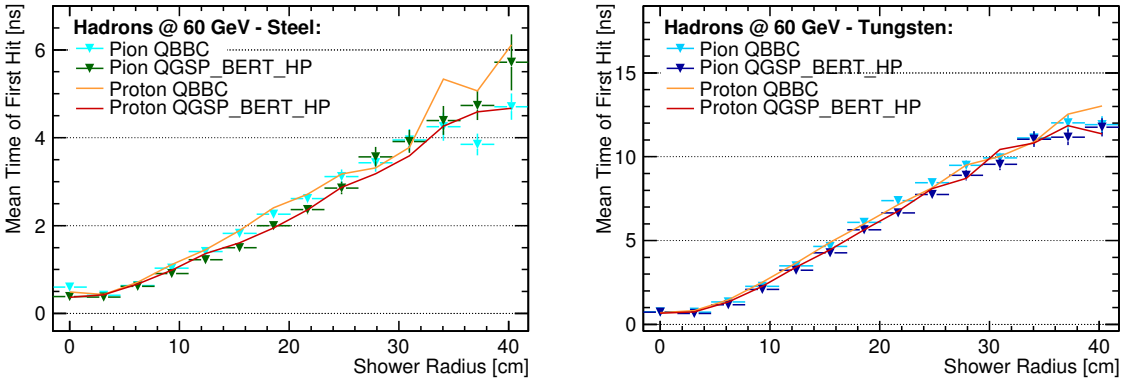

Figure 6.23: Comparison of the lateral shower profile of the mean time of first hit for impinging protons and pions in the case of MC generated steel (left) and tungsten (right) data.

the shower core moderate.

The T3B experiment cannot measure hadron showers on an event by event basis. Nevertheless, the collected data comprises energy depositions at all shower radii and in all shower depths. Note that the contribution of the longitudinal shower tail is emphasized in the acquired data, since the shower start of an event is more likely to occur at the beginning of the calorimeter than at the end where the T3B experiment is located (see [77] for details). In this sense, the shower fractions that we will obtain in this section represent only an indication of the measured delayed component. When we use the term "shower energy" in this section, we mean the fraction of the total shower energy that is detected by T3B which was positioned in a distinct calorimeter depth. For a full timing calorimeter, the contribution of the delayed shower component to the in total detected energy fraction of a shower would be somewhat reduced. Furthermore, we consider only the first hits on the T3B cells in this analysis. A preliminary study investigating multiple hits has shown that only about 3 % of all first hits are followed by a second hit with an amplitude of at least 30 % of that of the original hit within the recording time of the data acquisition. Such secondary hits will be respected in the time of hit analysis (see Section 6.3). Due to these considerations, the analysis of the shower fraction presented here should be understood as an estimation of this shower property. For this analysis, we compare the hadron data acquired at the test beam at a particle energy of 60 GeV for steel and tungsten absorber and muons at 180 GeV. First, we quantify the summed total energy that was deposited by all first hits within all events of a data sample. This total energy is artificially reduced by the limited dynamic range of the T3B oscilloscopes and the related signal overshoots (see Section 5.1.1). Figure 6.24 shows the energy deposition distribution of all first hits. If no overshoot filter is applied within the analysis framework, the distribution exhibits a peak around a hit energy of 6.5 MIP, which comprises all overshoot waveforms. The Figure shows that the distribution remains unaffected from overshoots below a hit energy of $4.5 - 5$ MIP. We assume that the hit energy is approximately Langau distributed and fit a Langau in the range of $0.6 - 4.5$ MIP. We then extrapolate the fit to higher energies and redistribute all first hits with an energy deposition of > 4.5 MIP according to the obtained fit template. The upper range of the redistribution was chosen such that the transition of the overshoot corrected distribution below and above 4.5 MIP is smooth. Thus, one obtains an upper energy cutoff of 10 MIP for muons, 17.5 MIP for steel and 28 MIP for tungsten data. The maximal energy E_{max} that could be detected with a T3B cell in the case of a sufficiently large dynamic oscilloscope range is approximated in this procedure. The hierarchy turns out as expected: For muon data E_{max} is lower than for hadron showers, since it is only one ionizing particle that traverses a T3B cell. If a hadron shower develops, a large number of particles can traverse the same cell and thus, E_{max} is significantly higher. The highest particle density is reached in the electromagnetic core of a hadron shower. For tungsten, electromagnetic subshowers are very dense due to the small radiation length X_0 of 0.35 cm (see Section 3.1 for details). For iron, on the other hand, X_0 is about five times larger. Thus, E_{max} is expected to be larger for tungsten than for steel. Keeping the hit time the same and redistributing the energy deposition of overshoot waveforms, one can correct the 2D histograms which were the

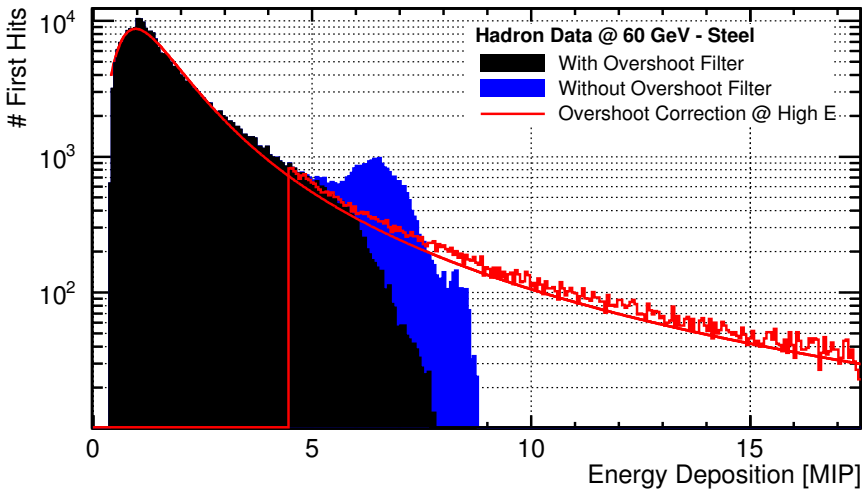

Figure 6.24: Distribution of the hit energy of first hits with (black) and without (blue) the application of an overshoot filter in the analysis framework. The extrapolation of a Langau fit template (red line) towards high hit energies allows for a statistical redistribution of overshoot waveforms (red histogram).

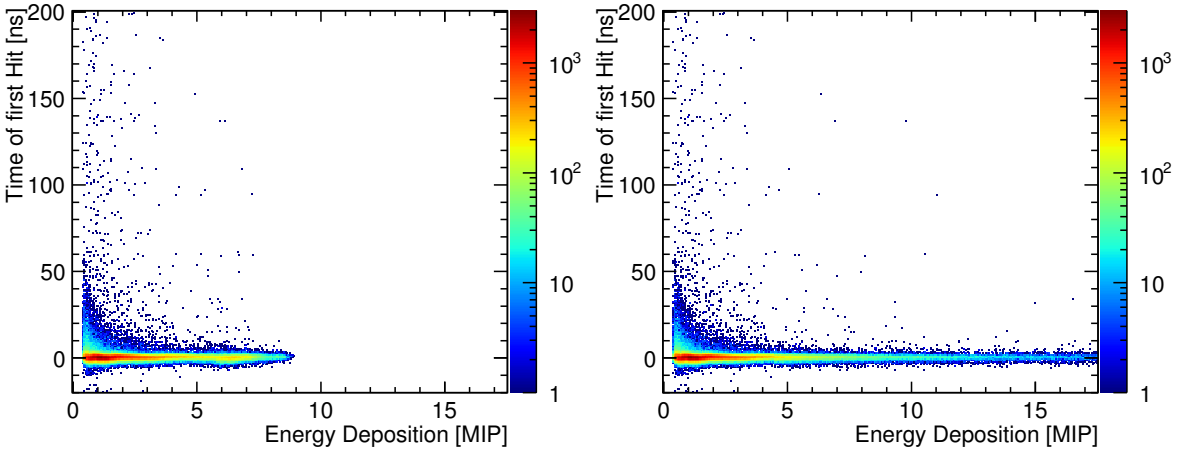

Figure 6.25: Energy dependence of the time of first hit for hadrons impinging with 60 GeV on steel before (left) and after (right) a redistribution of overshoot waveforms is performed. The overshoot correction allows for a determination of the total sum of the deposited energy of the data sample.

basis for most of our studies of the TofH in the high hit energy regime (see Figure 6.25). The correlation of the hit time to the hit energy is lost by the described redistribution procedure, but the previously studied energy dependence of the mean TofH is very weak at high hit energies (see e.g. Figure 6.7).
An additional correction factor originates from the decreasing radial coverage of the 15 cells of the T3B strip. Each T3B cell has the identical dimensions of $3 \times 3\,\mathrm{cm}^2$. But the fraction of the shower area that is covered by a T3B cell of this size decreases with increasing radius (oversimplified view: the circumference of a circle increases as $2\pi r$, but the size of a cell is constant at all radii). So the contribution of energy depositions detected in T3B cells far from the beam axis needs to be scaled up relative to energy depositions measured at the beam center. A scale factor has been determined for each T3B cell and the amplitude of every first hit was rescaled accordingly (a detailed derivation of the necessary scale factors is given in [77]).
Summing the energy deposition of all first hits measured at all shower radii within 200 ns, one can now obtain the total energy E_{tot} from the overshoot corrected hit distribution (see Figure 6.25, right):

$$E_{tot}(r,t) = \sum_{t_{min}}^{t_{max}} \sum_{r_{min}}^{r_{max}} E(r,t) = \sum_{-20\,\mathrm{ns}}^{200\,\mathrm{ns}} \sum_{-1.5\,\mathrm{cm}}^{44.9\,\mathrm{cm}} E(r,t) \tag{6.4}$$

In the following, we use E_{tot} as a normalization constant. With this hit distribution split by the 15 T3B cells, we can now determine isoenergetic lines, meaning lines of a constant fraction of the total deposited energy in dependence of the shower integration time and the radius from the shower core. This is shown in Figure 6.26 for steel and tungsten data. Each point $f^{inv}(r_0, t_0)$ within this plot represents a summation of all energy depositions from t_0 up to 200 ns (t_{max}) and from r_0 to the outer rim of the T3B experiment r_{max}. So the total energy fraction of a shower $F(r_0, t_0)$ that is deposited within a time t_0 and a radius r_0 is:

$$F(r_0,t_0) = 1 - f^{inv}(r_0,t_0) = 1 - \frac{\sum_{t_0}^{t_{max}} \sum_{r_0}^{r_{max}} E(r,t)}{E_{tot}} \tag{6.5}$$

The histograms show the quantitative contribution of the late shower component to the total fraction of the shower energy. The course of the isoenergetic lines shows that $F(r_0, t_0)$ increases only slightly if the integration time is increased to more than several nanoseconds. For tungsten, for example, the fraction of the shower energy contained within a radius of 23.2 cm increases from 78.9 % to 82.0 % ($\Delta F = 3.1\,\%$) if the integration time is increased from 5 ns to 50 ns. For steel, the abundance and the amount of energy deposited by delayed hits is, on average, smaller than for tungsten. Here, F increases by only 0.9 % (from 82.9 % to 83.8 %) for the same temporal increase. Note that this temporal dependence is more pronounced for both absorbers if one integrates over the whole radial size of T3B. With an integration radius of 44.9 cm, ΔF amounts to 6.8 % (2.0 %) for tungsten (steel).
The radial dependence of $F(r_0, t_0)$, on the other hand, is stronger. For tungsten as absorber and an integration time of 10 ns, F increases from 80.9 % to 96.9 % ($\Delta F = 16\,\%$) if all energy depositions within a shower radius of 23.2 cm and 44.9 ns, respectively,

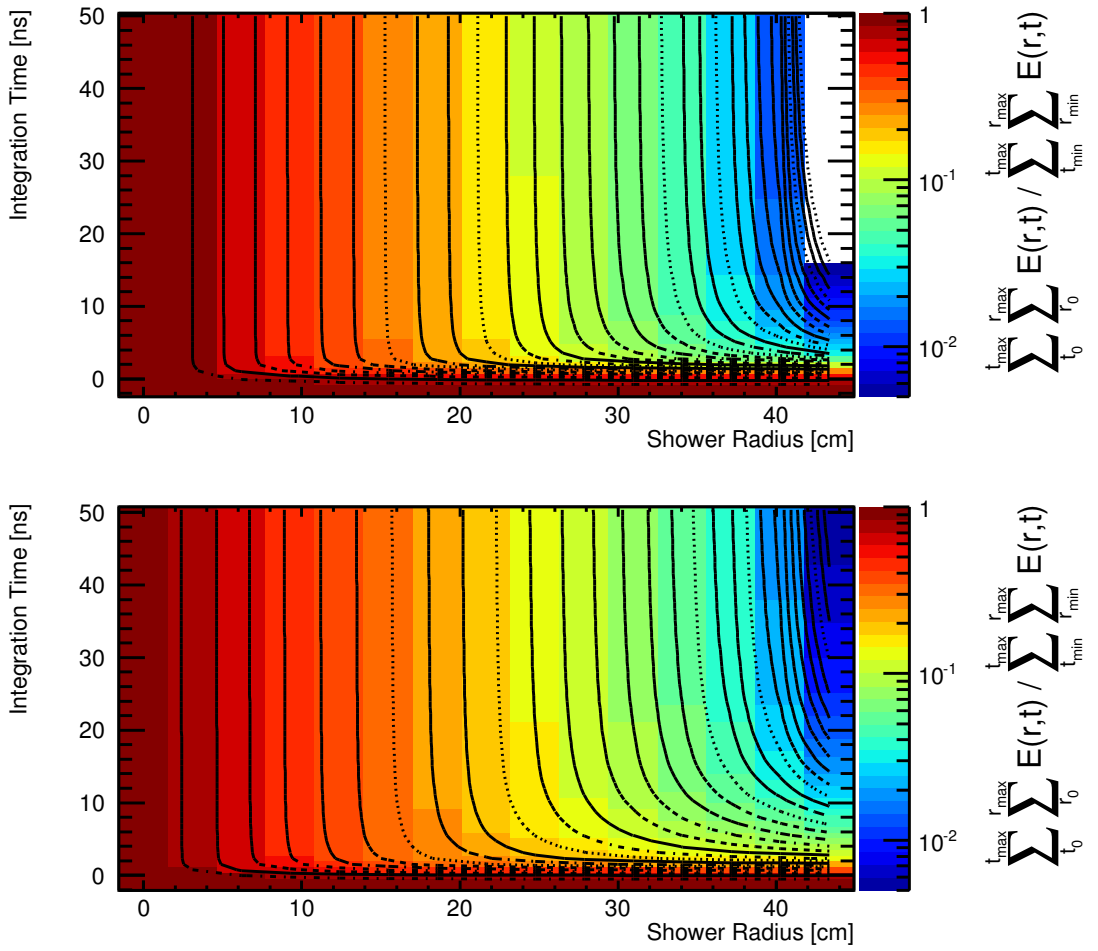

Figure 6.26: Comparison of isoenergetic lines in the case of steel (top) and tungsten data (bottom). One isoenergetic line represents a constant fraction of the total deposited energy in dependence of the shower integration time and the radius from the shower core.

are taken into account. For steel, F increases from 83.4 % to 99.0 % ($\Delta F = 16.6\,\%$, comparable to tungsten) for the same radial increase.
In general, we can state that the quantitatively large energy containment of $> 96\,\%$ within an integration time of $< 10\,\text{ns}$ (and the total covered shower radius of 44.9 cm) for tungsten indicates that the choice of such a time window which was proposed for the calorimetric system of a CLIC detector (see Section 2.4.2) is adequate.

6.3 Time of Hit

In the time of first hit analysis, we were focussing on the time and the energy deposition of the first hit of a T3B cell. This implies, on the one hand, that we neglect all delayed

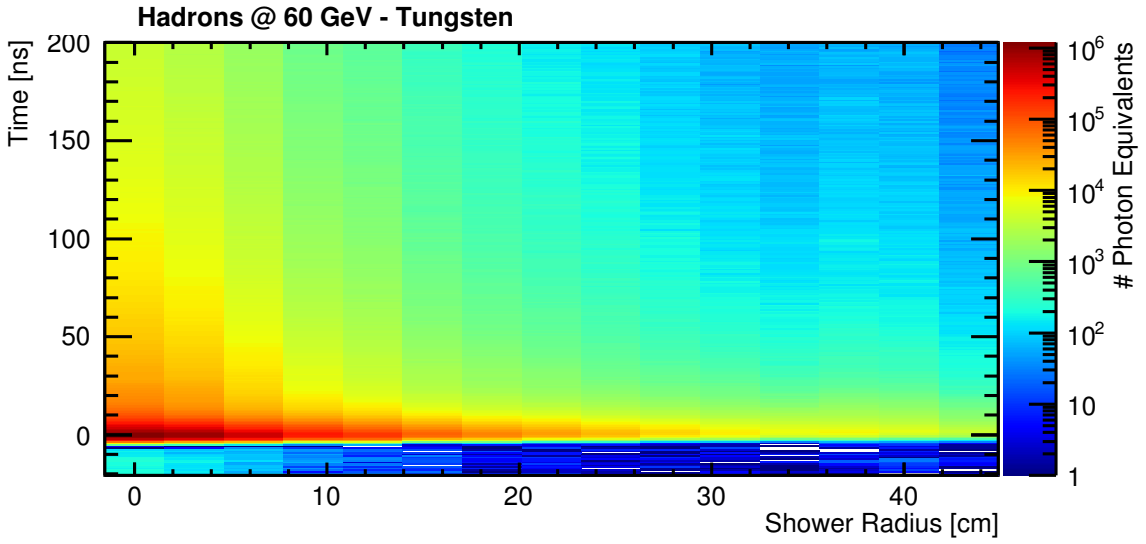

Figure 6.27: Accumulated time distribution of the detected photon equivalents (or fired SiPM pixels) in all events in dependence of the shower radius.

energy depositions that might occur within the same waveform. In a preliminary estimation of this effect (see [77]), we find that the probability of identifying a second hit after the initial one is smaller than 12 %. For this estimation, a hit is identified if more than 8 p.e. are found within 9.6 ns. The total recording time of a waveform is scanned chronologically for a hit. If a first hit is found, the algorithm searches for second hit demanding that the hit condition (8 p.e. within 9.6 ns) is somewhere between the first and second hit not fulfilled. This requirement reduces the probability to identify SiPM afterpulsing wrongly as a second hit. In an alternative approach, we can state that a first hit is in about 3 % of all cases followed by a second hit with an amplitude of > 30 % of that of the original hit within the recording time. In any case, the time of hit analysis incorporates delayed second hits in contrast to the time of first hit analysis. On the other hand, the principle of the TofH analysis implies that the deposited energy is integrated over an extended time window (mostly 9.6 ns) and assigned to the point in time when the energy deposition started. The duration of a such a first hit is primarily dominated by the detection technology, i.e. the time constants of the SiPM and scintillator tile entity a T3B cell consists of. In the TofH analysis, we minimized detector effects to study ideally the pure shower development. The time of hit analysis is complementary to that. Here, we will account for the duration of signals. We will study the properties of hadronic showers when simply integrating all recorded SiPM signals from a fixed reference time (e.g. the event trigger time) and the challenges related to the SiPM and scintillator tile technology used.

The basis for all further analyses of the ToH is a histogram such as the one shown in Figure 6.27 (for hadron data at a particle energy of 60 GeV in tungsten). It represents the time distribution of the detected photon equivalents for all events recorded with the same run characteristics and split by their lateral point of occurrence. In the analysis

ToH Analysis	Filter	Trigger	Complementary Info
Data	Scintillator Coincidence	Localized Energy: > 15 p.e. within −20 ns to 2000 ns	Afterpulsing Correction Template
	> 4 p.e. in 4 ns		(Shower Depth)
	Overshoot		
Simulation	> 4 p.e. in 4 ns	Localized Energy: > 15 p.e. within −20 ns to 2000 ns	Afterpulsing Correction Template
			(Shower Depth)

Table 6.3: Steering parameters in the analysis framework for the time of hit analysis.

(Section 6.3.2) we will compare projections of histograms of this type for different data sets. As for the TofH, we will focus on a time window of −20 ns to 200 ns.
So instead of individual particle hits, the ToH analysis investigates the full distribution of SiPM signals. This comprises a priori fast and delayed energy depositions as well as contributions from thermal SiPM darkrate, SiPM afterpulsing (see Section 3.3.2 for details) and possible long time constants from the scintillator material (or a scintillation of the used mirror foil). Table 6.3 summarizes the steering parameters of the analysis framework used for the ToH analysis. The software trigger has been configured to minimize the contribution from pure SiPM noise waveforms. It demands at least 15 p.e. within the recording time (−20 ns to 2000 ns) which corresponds, in terms of minimum ionizing particles (with a very long integration time window), to ~ 0.6 MIP.

6.3.1 Time of Hit Specific Calibration Procedure

In this section, we give an overview over the time of hit specific calibration routines that address several hardware characteristics and SiPM aspects. First, we will perform a time offset normalization to enable the direct comparison of different data sets. Furthermore, the application of an afterpulsing (AP) correction allows for an investigation of the direct difference between a detector that is largely influenced by afterpulsing and one that is quasi AP free. It enables a study of the dominance of this SiPM effect and how shower properties are obscured by it. A correction of the thermal darkrate contribution will be performed in the same step. Finally, we present a simple handling of signal overshoots.

Time Offset Normalization and ToH Time Resolution

A time offset normalization has been performed analogous to the TofH analysis (see Section 6.2.1). The same fitting algorithm is applied to the one-dimensional time of

Data Set	Muons	Steel			Tungsten		
	180GeV	60GeV	80GeV	180GeV	60GeV	80GeV	180GeV
Timing Precision	1.85 ns	1.89 ns	2.46 ns	2.05 ns	1.59 ns	1.89 ns	1.59 ns
Events in Analysis	5.40M	1.60M	1.85M	1.20M	4.06M	4.48M	0.74M
# Triggered Events	786k	204k	304k	421k	601k	902k	166k

Table 6.4: Time stamping precision achieved and statistics obtained (all T3B cells and all energies) at the test beam for data sets acquired with different run characteristics. For the statistics, the beam energy, the calorimeter type and depth and also the particle beam composition play a role.

hit distribution of the central T3B cell. The extracted time of the maximum of the distribution is used for the normalization of trigger time offsets of different data sets. The precision for the timestamping of instantaneous energy depositions using the ToH is determined simultaneously and shown for different data sets in Table 6.4. Since the ToH analysis incorporates the time distribution of photon equivalents explicitly (in contrast to the TofH analysis), the timing precision of the ToH is a factor of 2 ± 0.4 worse than for the TofH (compare to Table 6.2).

Afterpulsing and Thermal Darkrate Correction

The average afterpulsing characteristics of the SiPMs used within T3B have been measured in the laboratory (see Section 5.1.2). We will now use this information to eliminate the contribution of SiPM afterpulsing to the ToH distribution. For this, we will subtract the average afterpulsing relative to the time of a fired pixel and repeat this for every SiPM that ever fired. Note that this is a statistical approach and that this calibration procedure can not be performed on an event-by-event basis.
First, the test beam phase specific afterpulsing template (discussed in Section 5.1.2) is loaded. This template represents the time distribution of the average AP contribution relative to one SiPM pixel firing at t=0. The afterpulsing correction routine works as follows: It iterates chronologically (bin by bin) through the ToH distribution. First, the afterpulsing template is multiplied by the number of photon equivalents in the first respective bin and subtracted from the ToH distribution relative to the time of this bin. In this step, the ToH distribution was corrected for the AP contribution of this single bin. The resulting distribution represents the basis for the next iteration. The chronologically adjacent bin is selected and now, the template is scaled and subtracted relative to this bin. This iterative AP subtraction is continued to the end of the acquisition time window.
Figure 6.28 shows the impact of this AP correction procedure. It starts taking effect after ~ 10 ns and shows that SiPM afterpulsing is the property which dominates the ToH distribution at later times. The Figure was created for muons at an energy of 180 GeV, which represent quasi-instantaneous energy depositions. The presence of a remainder at times > 10 ns in the distribution hints towards a long time constant of

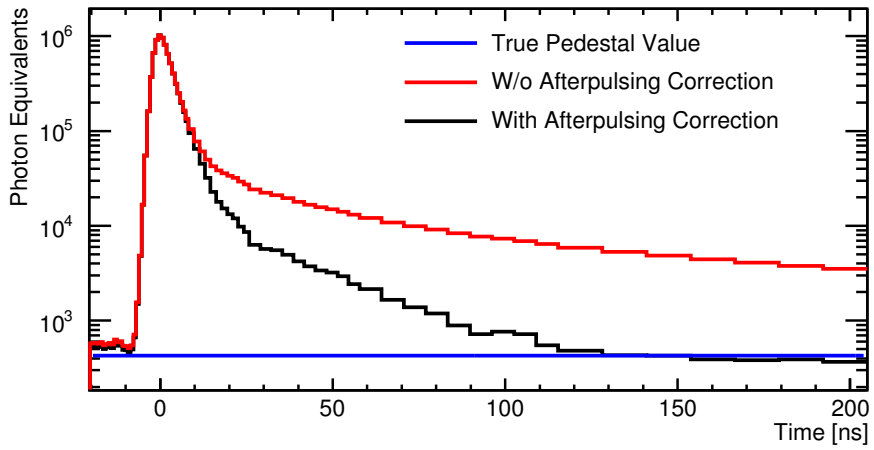

Figure 6.28: Time of hit distribution of the central T3B cell with (black) and without (red) applied afterpulsing correction for muon data at 180 GeV. The afterpulsing corrected pedestal value is shown in blue.

the scintillating material or a slow scintillation of the attached mirror foil which cannot be easily accounted for. Nevertheless, at 50 ns its contribution is nearly one order of magnitude smaller than the contribution from afterpulsing and it almost vanishes for times later than 100 ns.
Random thermal SiPM darkrate is evenly distributed over the recording time. A pedestal subtraction corrects for its contribution. To determine the pedestal value, we first fit a constant to the pretrigger range from -110 ns to -10 ns. But this is not the pedestal of the AP corrected ToH distribution since a photon equivalent detected in this time range might be an afterpulse related to a SiPM pixel that fired at earlier times. To account for this, we fill a histogram exclusively with the value of the extracted fit constant and apply the afterpulsing correction explained above. Eventually (at times $> 1\,\mu$s), the histogram converges to a new value which represents the true afterpulsing corrected contribution of thermal darkrate and will be subtracted from the ToH histogram (see Figure 6.28).
The AP and thermal darkrate correction is applied to test beam and simulated data likewise, since these SiPM effects are introduced implicitly into the simulation during the data driven digitization procedure (photon time distribution according to muon data, see Section 5.2.2).
Note that cell to cell fluctuations in the SiPM afterpulsing are not accounted for as there is only one afterpulsing template per test beam phase. These fluctuations are relatively small for the set of selected SiPMs ($< 12\,\%$) and part of the systematic error in the ToH analysis. As we will see, these fluctuations do not influence the conclusions of the ToH analysis since the investigated trends in the shower development have a substantially larger effect.

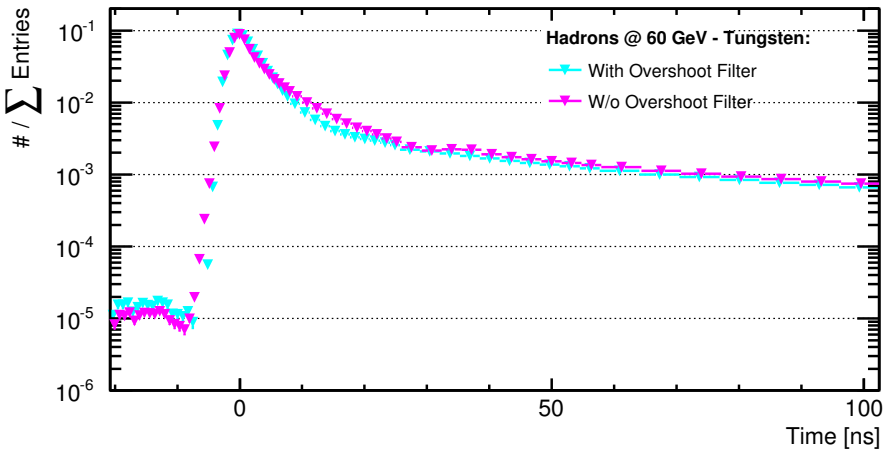

Figure 6.29: Comparison of the ToH distribution for the central T3B cell with and without the application of the overshoot filter. Shown is hadron data at an energy of 60 GeV in tungsten.

Overshoot Filtering

For the time of hit analysis, an advanced overshoot correction proves to be rather complicated. It would require an extrapolation of the raw waveforms in the region where a signal overshoots the dynamic range (in mV) of the oscilloscope (see Section 5.1.1 for details). The optimization of such a fundamental overshoot correction is to be explored in the future, but not available for this thesis. A simple inclusion of overshooting waveforms, on the other hand, would cause a slight distortion of the corresponding ToH distribution. This is shown in Figure 6.29 for the central T3B tile where the occurrence of overshoots is emphasized the most. Including vertically cut waveforms reduces the contribution of the peak of the ToH distribution (at 0 ns) relative to the delayed part (e.g. at 15 ns). To obtain a ToH distribution that is not affected by this hardware limitation, we filter all cut waveforms as a preliminary overshoot treatment and ignore them for the further analysis. This implies that very high (> 5 MIP) energy depositions are excluded from the analysis. The late contribution is consequently somewhat emphasized, particularly for the central cells, since overshoots are more likely to occur when T3B is hit by the electromagnetic shower core. Quantitatively, the overshoot probability amounts to $\sim 6\,\%$ (see Section 5.1.1) at a particle energy of 60 GeV, which is a tolerable systematic bias.

6.3.2 Analysis Results

We now have all information at hand for a analysis of hadron shower properties using the time of hit information. For the ToH, the set of T3B standalone data, which comprises hadron data in steel and tungsten at an energy of 60 GeV, 80 GeV and 180 GeV as well as muon data, was reprocessed (see Table 6.4). In the presented ToH analysis, we will

focus on a particle energy of 60 GeV. The intrinsic properties of the ToH allow a view at the same data from a very different perspective.

Hadron Shower Timing in Different Absorber Materials

Figure 6.30 shows a comparison of the time of hit distribution for muon data at 180 GeV and hadron data at 60 GeV. The data is split laterally into a central shower area ranging from −1.5 cm to 17 cm (central 6 T3B cells combined) and a peripheral shower area ranging from 17.1 cm to 38.7 cm (adjacent 7 T3B cells combined). Note that the muon data comprises in any case only the central T3B cell. All distributions shown in this section were corrected for afterpulsing. The normalization to the number of entries allows for a shape comparison of the different ToH distributions.
The compared data sets show no large differences in the central shower region (see Figure 6.30, left). The only difference of tungsten data relative to muon and steel data at negative times (see Figure 6.30, bottom left) arises from the better time resolution achieved at the tungsten test beam (see Table 6.4). If we investigate the peripheral shower region, on the other hand, we observe the same general trend as in the TofH analysis: The contribution of delayed shower components is most pronounced in tungsten and emphasized in steel relative to muon data. This is shown in Figure 6.30 (bottom right) by the height of the maximum of the distributions. All distributions were normalized to the number of photon equivalents detected in a time window between −20 ns and 200 ns. So a small maximum (such as for tungsten or steel relative to muons) indicates an emphasis of late energy depositions. The time shift of the peak for hadron data (peripheral shower range) relative to muon data (central tile only) towards later times originates from the intrinsic time the prompt part of the hadron shower needs to develop to larger radii. This time shift amounts to about 1000 ps for tungsten and 700 ps for steel data. The differences between the three data sets are most pronounced at intermediate shower times between 10 ns and 40 ns (see Figure 6.30, top right), where the elastic scattering of neutrons is expected to represent the dominant source of delayed energy depositions. The quantitatively small (relative to the instantaneous part), but existing long term influence as expected from neutron capturing processes can be hardly resolved by the ToH distributions.
So with the analysis approach followed by the ToH and the corresponding investigation of time distributed energy depositions, we can reproduce the overall timing properties of hadronic showers in different absorber materials that were identified by the TofH analysis before, although less clear (compare e.g. Figure 6.5).

Using the discussed ToH distributions as a basis, we can investigate the fraction of the shower signal that is detected after a certain integration time by T3B. Note that this is not to be confused with the fraction of the total shower energy but it is the fraction of energy depositions observed by the T3B strip. In particular, no correction with respect to the longitudinal shower depth (i.e. position of T3B relative to the shower start) and no lateral rescaling of the contribution of the energy depositions at different radii was performed (see Section 6.2.2 for details). The time distribution of the

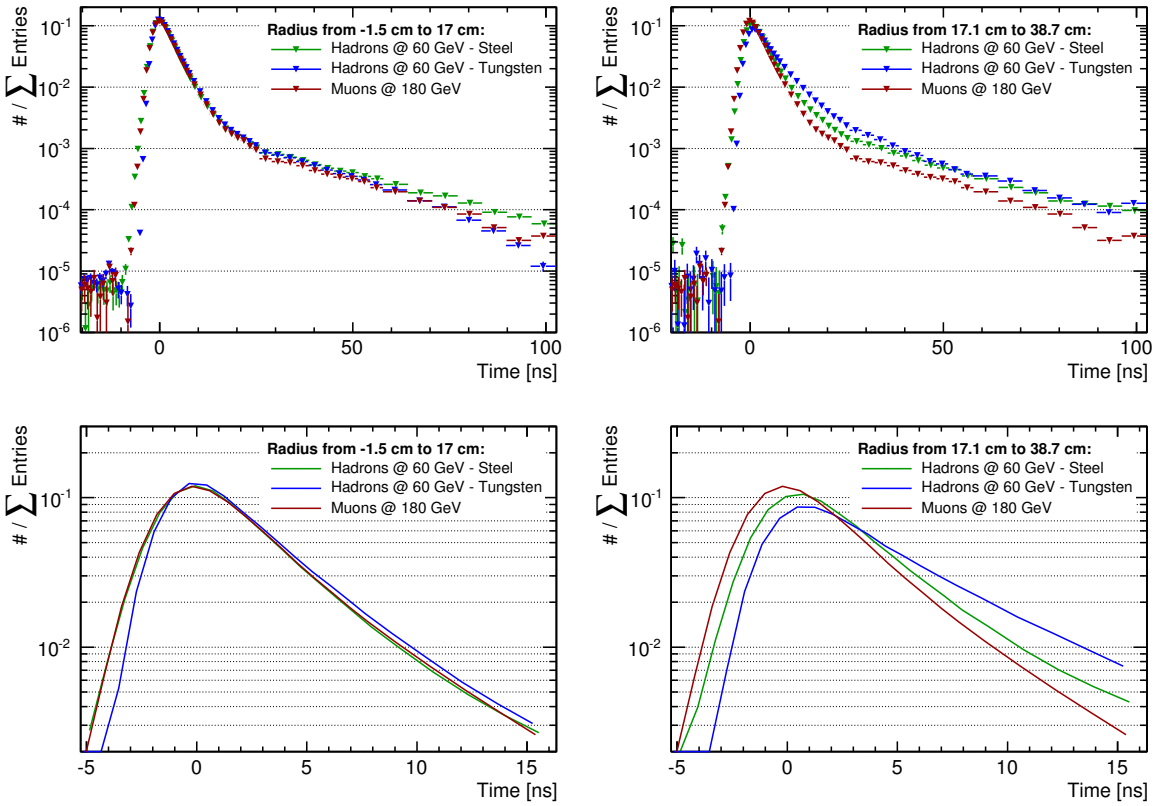

Figure 6.30: Comparison of the time of hit distribution of muons (red) at 180 GeV and hadrons in steel (green) and tungsten (blue) at 60 GeV. The central shower area (left) and the peripheral shower area (right) are each combined into one plot. A view zoomed to the peak of the distribution is shown at the bottom.

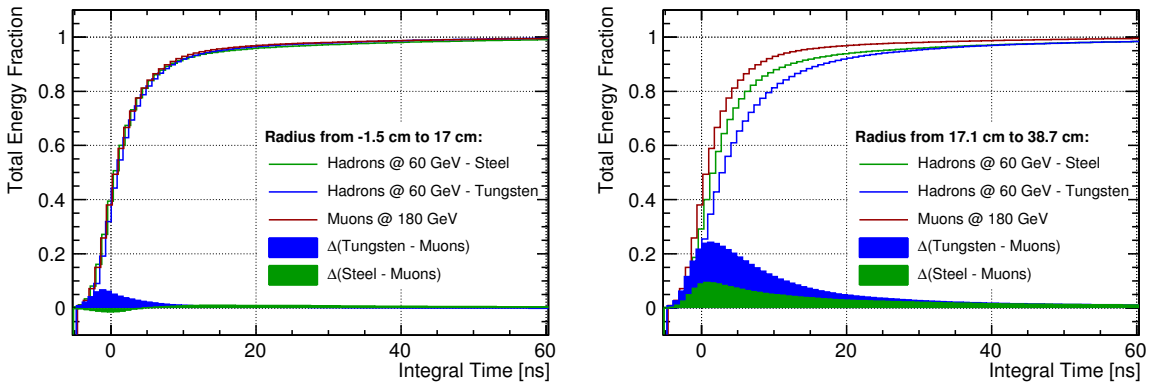

Figure 6.31: Fractional increase of the detected shower signal in dependence of the integration time for the central (left) and peripheral (right) shower area. The difference relative to muon data is shown by filled histograms. The total signal is defined in a time window from −20 ns to 200 ns.

T3B signal fraction is shown in Figure 6.31 for the central and the peripheral shower region. We find that 92 % of the signal in the central shower area is measured within 10 ns independently of the data set, and about 96 % after 20 ns. Since these shower fractions are similar for hadron and muon data, we conclude that they correspond to the time distributed signals recorded for instantaneous energy depositions and that delayed energy depositions do not have a quantitatively large effect on the fractional increase of the detected shower signal in the central region. It can be understood as the default increase due to detector response effects such as the finite time resolution (around t=0) and slow scintillation time constants (at later times).
Focussing exclusively on the peripheral shower area, we find that it takes the longest in tungsten and significantly longer in steel relative to muon data to integrate a certain fraction of the detected shower signal. A fraction of $\sim 90\,\%$, for example, is reached after an integration time of 7.9 ns, 12.2 ns and 16.7 ns for muon, steel and tungsten data, respectively. The Figure does also show the differences relative to muon data. After an integration time of 10 ns, a 11.6 % (4.9 %) smaller fraction is integrated for tungsten (steel) data.
Altogether, the fractional increase of the detected energy with the integration time is much slower for the ToH compared to the values obtained within the TofH analysis (see Section 6.2.2). So in the ToH approach, in which one simply defines an integration time window (200 ns) for the shower starting from a certain event trigger time and includes all energy depositions above a certain threshold (0.6 MIP), the detector effects of the SiPM and scintillator tile technology play an important role and mix with the contribution of delayed energy depositions. Longer integration times seem misleadingly necessary to integrate a certain fraction of the energy depositions of a shower. The situation becomes even more severe, if we do not correct for afterpulsing (see next subsection). In the TofH approach, we use the precise timestamping of individual particle hits and short integration times (of < 10 ns) relative to the timestamps. Here, detector effects are less relevant and a big fraction of the total shower signal can be assigned to a very small time span.

The Lateral Time Distribution of Hadronic Showers

In contrast to the last subsection, in which we split the ToH timing profiles into a central and peripheral region, we will now study the lateral shower timing profile with a finer segmentation and investigate the influence of afterpulsing on the obtained results. Figure 6.32, shows the radial dependence of the mean time of hit (determined within the default time window of -20 ns to 200 ns). Similar to the TofH analysis, we find that the average shower timing appears gradually more delayed in further distance from the shower core (see Figure 6.32, left). The mean ToH is approximately equal for steel and tungsten data in the shower center, where quasi instantaneous energy depositions (e.g. from the electromagnetic shower core) dominate. Due to the temporal extension of energy depositions, the mean ToH is approximately $3 - 4$ ns later than the mean TofH for the central T3B cell (compare Figure 6.8). Towards larger shower radii, the influence of delayed energy depositions increases in tungsten relative to steel. For tungsten, the

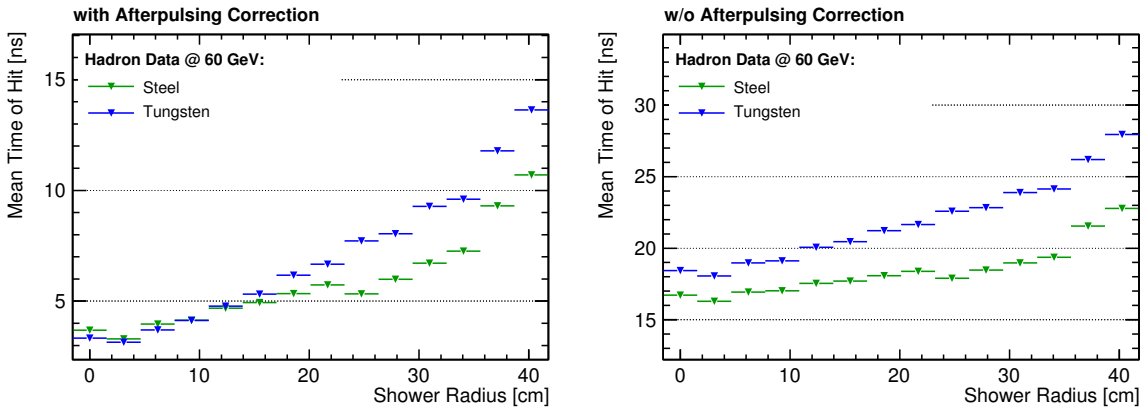

Figure 6.32: Mean time of hit in dependence of the shower radius with (left) and without (right) afterpulsing correction.

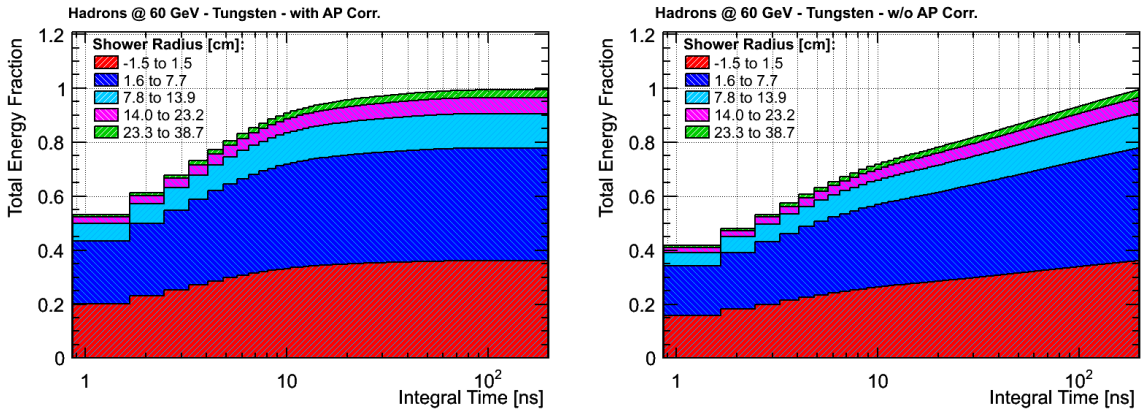

Figure 6.33: Fractional increase of the detected shower signal integrated over all shower radii with (left) and without (right) afterpulsing correction. The relative contribution at different shower radii is shown by the stacking of the individual histograms. Shown is hadron data at an energy of 60 GeV in tungsten.

mean ToH increases by about 10 ns (6 ns) between the center and a shower radius of 40 cm (31 cm). For steel, this increase amounts to only about 7 ns (3 ns). The trend of this increase is comparable to the increase observed in the analysis of the mean TofH for both absorbers (compare Figure 6.8). If we omit the afterpulsing correction (see Figure 6.32, right), the mean ToH increases by an offset of about $12 - 15$ ns at all radii.

Figure 6.33 shows the contribution of individual shower radii to the total signal fraction in tungsten. We find that the largest part of the total shower signal detected in the T3B detector is deposited within a radius of 7.7 cm. With afterpulsing correction (see Figure 6.33, left), 78 % (36 %) of the total shower signal (after the total integration time of 200 ns) is deposited within the central 7.7 cm (1.5 cm). Moreover, the relative increase of the shower fraction between an integration time of 4.5 ns and 200 ns amounts

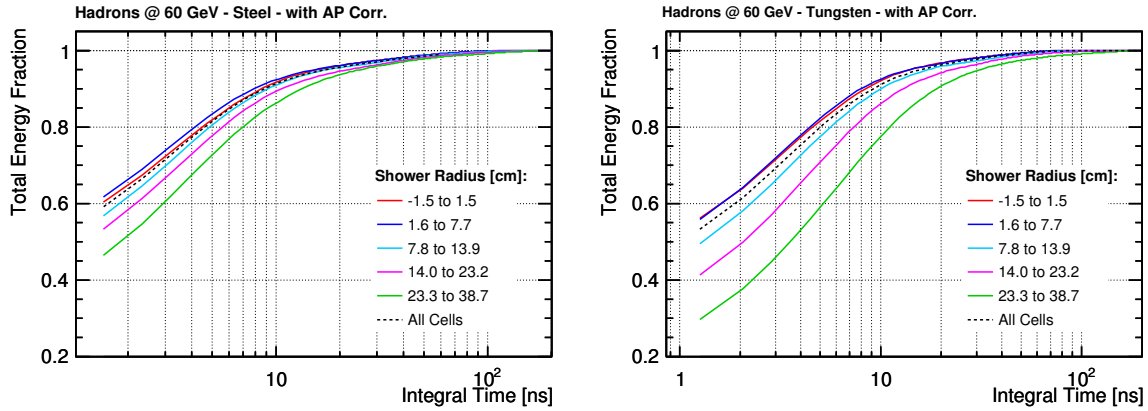

Figure 6.34: Time dependence of the fractional increase of the detected shower signal integrated over the respective lateral shower ranges for steel (left) and tungsten (right) data. Shown is hadron data at an energy of 60 GeV with applied afterpulsing correction.

to only 7.5 % for radii of < 1.5 cm, but 19.1 % for radii of < 13.9 cm, which underlines the influence of delayed contributions at large radii.
The distribution changes drastically, if we omit the afterpulsing correction (see Figure 6.33, right). Comparing the absolute values of the total detected shower signal (not shown in the Figure), we find that it is 28 % larger without an afterpulsing correction. So, in turn, about 22 % of the total signal within 200 ns is only due to afterpulsing. The Figure illustrates the dominance of afterpulsing at late times. After $10 - 11$ ns SiPM afterpulsing obscures the contribution of late energy depositions almost completely and one integrates virtually only afterpulses. So without a dedicated afterpulsing correction, or the usage of advanced SiPMs which are quasi afterpulsing free, there is no profit in integrating energy depositions longer than $10 - 11$ ns.

Finally, we can normalize the shower fractions individually by their respective radial range. So we focus on the time necessary to integrate a certain fraction of the shower signal detected within a certain lateral region. This is shown in Figure 6.34 for steel and tungsten data. All distributions were corrected for afterpulsing. It illustrates clearly the large contribution of delayed signals at large radii, particularly in the case of tungsten data. Expressed in numbers, it takes about 8 ns in the case of steel data to integrate 90 % of the shower signal detected in the central range of < 1.5 cm and ~ 13 ns in the outermost range of $23.3 - 38.7$ cm of the T3B detector (see Figure 6.34, left). In the case of tungsten (see Figure 6.34, right), it takes ~ 8 ns and ~ 19 ns in the same respective ranges of the T3B detector.

The Comparison of Data to Monte Carlo Simulations

As the final step in the ToH analysis, we investigate how the obtained data on hadronic showers compares to Monte Carlo simulations using the physics lists QGSP_BERT, QGSP_BERT_HP and QBBC. All data sets were corrected for afterpulsing.

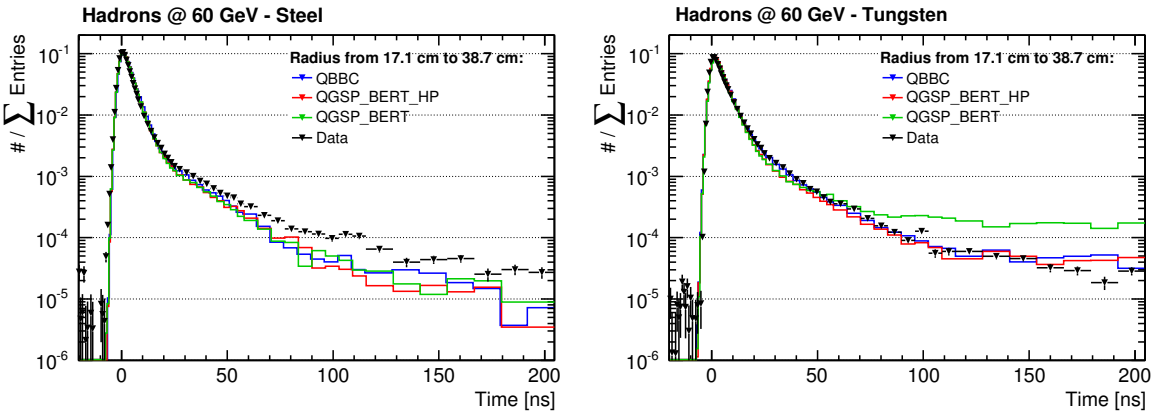

Figure 6.35: Data vs. MC comparison of the time of hit distribution for steel (left) and tungsten (right).

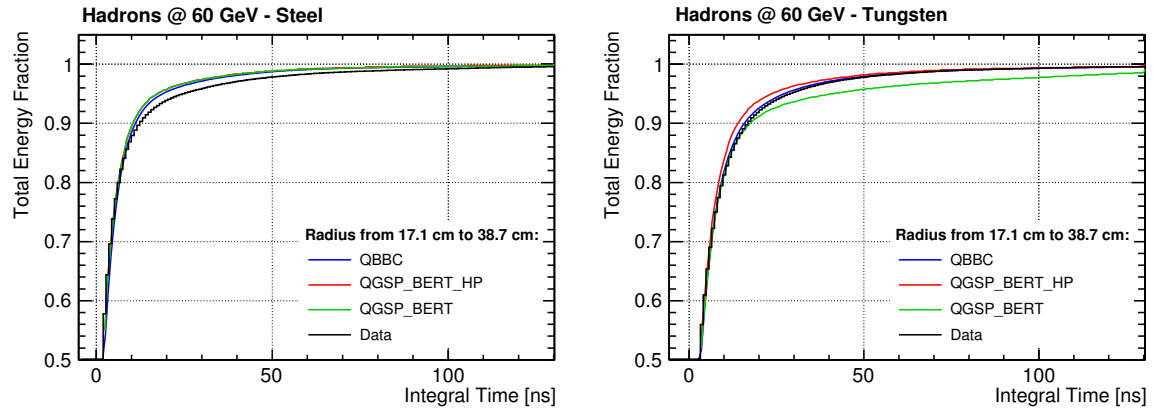

Figure 6.36: Data vs. MC comparison of the fractional increase of the detected shower signal in dependence of the integration time for steel (left) and tungsten (right).

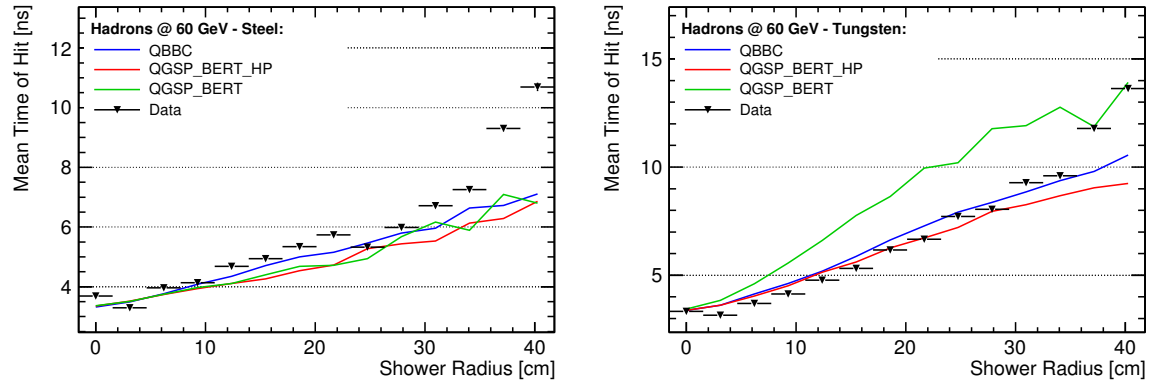

Figure 6.37: Data vs. MC comparison of the lateral profile of the mean ToH for steel (left) and tungsten (right).

Figure 6.35 shows the time of hit distribution for steel and tungsten data in the peripheral shower area. In the case of steel (see Figure 6.35, left), the shape of the distributions of all physics list matches the data roughly. At times > 30 ns a slight systematic increase of the data of unknown origin is present. For tungsten (see Figure 6.35, right), on the other hand, the ToH distribution of QGSP_BERT shows a significant systematic increase of the shower contributions at hit times larger than ~ 80 ns, underlining the overestimation of delayed hits for this physics list. Additionally, a small systematic decrease can be identified for the physics lists QGSP_BERT and QGSP_BERT_HP at intermediate shower times of $20 - 40$ ns. Here, QBBC matches the data best.
Integrating over these distributions, we can study the time dependence of the total signal fraction in the peripheral shower region. The effects discussed above translate into the signal fractions shown in Figure 6.36. In the case of steel (see Figure 6.36, left), the systematic effect causes a slightly faster increase of the total signal fraction for simulation relative to data. For tungsten (see Figure 6.36, right), QGSP_BERT_HP overestimates the increase of the total shower fraction slightly at intermediate hit times ($10 - 40$ ns), while QGSP_BERT suggests a significantly too long integration time to achieve a signal fraction of larger than 91 %. A fraction of 97 %, for example, is reached after ~ 40 ns for data and QBBC whereas it takes an integration time of 76 ns in the case of QGSP_BERT.
Finally, we compare the dependence of the mean ToH on the shower radius in Figure 6.37. Apart from the outermost lateral shower region of > 35.7 cm all physics lists reproduce the data well in the case of steel (see Figure 6.37, left). In the case of tungsten (see Figure 6.37, right), this is only true for the high precision neutron lists QGSP_BERT_HP and QBBC. QGSP_BERT overestimates the contribution of delayed energy depositions and consequently the lateral timing profile of the mean ToH increasingly with the shower radius. While the mean ToH differs at a radius of 9.3 cm by only 1.4 ns from data, the discrepancy increases up to 3.2 ns at a radius of 34.1 cm.
To sum up, the results of the comparison of the ToH shower profiles with simulated data are consistent with the conclusions obtained in the TofH analysis in Section 6.2.2. QGSP_BERT disqualifies for the simulation of hadronic showers when timing is of importance while the high precision lists QGSP_BERT_HP and QBBC reproduce shower timing well and achieve an overall good agreement with data.

Chapter 7

Summary, Conclusions and Outlook

7.1 Summary and Conclusions

This thesis discussed the time evolution of hadronic showers in highly granular calorimeters with tungsten and steel absorbers. The T3B experiment was specifically designed for a measurement of the timing characteristics of showers in the context of this thesis. The performance and the results of the data on hadronic showers acquired with the T3B detector were presented in detail.

The motivation for the T3B experiment is based on the requirements of a full detector system for the future linear e^+e^--collider CLIC. CLIC will feature a high collision energy of up to 3 TeV. The detector system will follow the Particle Flow concept for the event reconstruction. This makes a deep (in terms of nuclear interaction lengths) and at the same time highly compact calorimetric system for the maximal containment of particle jets necessary. Due to its high density, tungsten is a viable option as absorber material. Furthermore, the high collision rate of particle bunches of 2 GHz requires a precise timestamping of energy depositions in all subdetector systems and short signal integration times to avoid the pile up of physics and background events. On the other hand, the time development of hadron showers is not instantaneous which demands an extended signal integration time. To find an optimal compromise, the timing characteristics of hadron showers in tungsten have to be investigated in detail. This was the aim of the T3B experiment.

Based on theoretical and empirical considerations, a set of known processes and shower properties are expected to contribute to the time evolution of hadronic cascades. Hadron showers comprise a certain electromagnetic fraction. Its quantity depends primarily on the energy of the impinging particle, the particle sort and the absorber material used. Electromagnetic subshowers originate from the creation and subsequent decay of π^0s into two photons. This occurs preferentially within the first few nuclear interactions of the hadron shower where the energy of shower particles is above the pion production threshold. Since the radiation length is substantially smaller than the nuclear interaction

length for calorimetric absorber materials such as steel or tungsten, a hadron shower can be, on average, geometrically subdivided into a densely ionizing electromagnetic core and a surrounding halo dominated by the hadronic shower fraction. While the electromagnetic fraction of the shower energy is deposited promptly, the hadronic part can exhibit a significant delay. Nuclear shower interactions are characterized by a fast intranuclear cascade phase in which impinging hadrons traverse an absorber nucleus and transfer a fraction of their energy to the nucleons and release some of them. Additionally, there is a slow evaporation phase in which the excited nucleus releases its surplus energy primarily by the emission of low energetic neutrons. Such neutrons give rise to significantly delayed energy depositions in the active calorimeter material. Absorber materials with high atomic number release a substantially larger amount of evaporation neutrons. Several nuclear properties such as their lower binding energy per nucleon contribute to this effect. In the delayed evaporation phase, the most relevant neutron interaction processes are elastic scattering which is expected to be observed on a timescale of approximately 10 ns, while neutron capture is expected to occur up to several microseconds after the shower start.

The T3B experiment was designed to verify and quantify these shower timing characteristics. The heart of the T3B detector consists of 15 scintillator cells of a size of $3 \times 3 \times 0.5\,\mathrm{cm}^3$ whose light signal is detected by silicon photomultiplier (SiPMs). The 15 T3B cells are arranged in a linear strip and mounted on an aluminium base plate. The signal readout is performed by fast oscilloscopes providing a sampling rate of 1.25 GHz. All components were selected for their fast timing capabilities. A fast scintillator with a pulse width (FWHM) of 1.3 ns and a fast SiPM with a single photon signal width (FWHM) of 10 ns was chosen. The SiPM was integrated into to the scintillator cells. Thus, both components form a SiPM tile entity. No wavelength shifting fiber was used to guide the scintillation light to the sensor as this would introduce an additional time constant into the system.
The T3B experiment was part of the CALICE test beam campaign 2010/2011 carried out at the CERN PS and SPS. The T3B strip was positioned behind two different calorimeter prototypes of the CALICE collaboration, namely the WAHCAL and the SDHCAL, hosting a tungsten and a steel absorber structure, respectively. Data of muons and of hadronic showers was acquired in a wide particle energy range of 2 GeV to 300 GeV. A custom data acquisition software optimized for test beam conditions was developed from scratch for that purpose.

An extensive calibration procedure was developed to account for the characteristics of SiPMs and to strip detector effects from data and extract the intrinsic time evolution of hadronic showers. In the course of this, the single photon response of SiPMs was continuously monitored at the test beam through the acquisition of SiPM darkrate (identical signal shape). The signal response of a SiPM to the energy deposition of a particle traversing the scintillator is a combination of single photon signals occurring at different times. Utilizing the monitored 1-photon signal, the signal response to cell-traversing particles could be decomposed into its components. With this novel data reconstruction procedure, the time of arrival of photons on the light sensor could be

determined with sub-nanosecond precision and the energy deposition of cell-traversing particles could be quantified with high accuracy.
To enable a comparison of the acquired test beam data to Monte Carlo simulations, the geometry of and the materials used within the T3B experiment and the CALICE calorimeter prototypes and their relative arrangement was implemented into a customized T3B simulation framework based on Geant4. Large hadron and muon event samples were generated for three hadronic shower models named QGSP_BERT, QGSP_BERT_HP and QBBC. QGSP_BERT is the default model used in simulations at the LHC experiments and in physics benchmark studies performed for CLIC. QGSP_BERT_HP and QBBC are high precision models which emphasize the tracking and the interaction processes of low energetic neutrons. A digitization procedure was developed and applied to the generated data to account for the response of the T3B detector to particles. The necessary parameters were extracted from muon data acquired at the test beam. After the digitization procedure, simulated energy depositions can be given (analogously to test beam data) in terms of a time distribution of single photons.

After the calibration procedure, the energy depositions of hadronic showers can be quantified and categorized through a set of variables. Searching the acquisition window chronologically for signals, one can define the first hit of a T3B cell with high accuracy. The time of an energy deposition can be given with a precision of $\sim 1\,\text{ns}$. The amount of energy deposited can be quantified in terms of MIPs (the energy scale of minimum ionizing particles traversing a cell). Through the high segmentation of the T3B strip, the radial position of an energy deposition is given with an accuracy of 3 cm. Finally, information on the longitudinal shower depth of the T3B detector is accessible. Through a successful synchronization of the data of T3B to the data of the CALICE tungsten calorimeter prototype (WAHCAL), the position of the T3B strip could be determined relative to the position of the shower start in the direction of the shower propagation. This set of variables represents the basis for the analysis of the shower characteristics explained above. A thorough investigation of the T3B data utilizing the shower depth variable is given in the thesis [77] which is released in parallel to this thesis. Here, we focussed on the other three variables: Time, radius and amount of energy deposition. Note that T3B is a high statistics experiment and that the timing properties of hadron showers were studied on average and not on an event-by-event basis.
The time distribution of first cell hits was investigated comparing tungsten, steel and muon data. A substantial abundance of delayed energy depositions was observed for hadron shower data. Furthermore, the abundance was found to be significantly increased for tungsten relative to steel data. Statistically, two delayed contributions could be clearly distinguished and their time constants could be extracted. For steel and tungsten data a time constant of about 8 ns was identified. This is in accordance with the expected time scale of elastic scattering processes of neutrons released in the evaporation phase of the shower development. Additionally, a long time constant was observed, which differs with a value of about 80 ns and 500 ns significantly for steel and tungsten data, respectively. This is in accordance with the expected time scale of energy depositions initiated by neutron capture processes.
Investigating the timing of energy depositions, we found that the amount of energy

deposited by delayed cell hits is typically small. For steel, it is primarily smaller than 1 MIP. This is also true for tungsten, but here also delayed hits with an energy deposition of up to $3 - 4$ MIP contribute.
The lateral timing profile measured by T3B supports clearly the geometrical distinction into a shower core dominated by the electromagnetic and a shower halo dominated by the hadronic fraction. The increase of the mean time of the first hit for a shower radius of 40 cm relative to the shower center amounts to about 10 ns for tungsten and 4 ns for steel data. This can be attributed primarily to the increased contribution of delayed energy depositions far from the beam axis and also to the finite time development of a shower to large radii which delays the prompt shower part.
Comparing hadron showers in an energy range between 60 GeV and 180 GeV, no significant differences were observed on the level of timing precision achievable with T3B (~ 200 ps). An increase in the electromagnetic shower fraction of the order of 10 % was expected in this case.
In an extensive simulation study, the shower models QGSP_BERT, QGSP_BERT_HP and QBBC were compared to test beam data. We found that QGSP_BERT is not suited for an accurate description of hadronic showers when timing is of relevance and tungsten is used as absorber material. This is particularly true for the late shower evolution (at $t > 10$ ns). In this case, QGSP_BERT overestimates the contribution of delayed energy depositions substantially. The shower models QGSP_BERT_HP and QBBC, on the other hand, reproduce the shower timing characteristics well.

An undesirable feature of the utilized silicon photomultiplier is the generation of afterpulses which occur at a time later than 10 ns after the initial signal of an energy deposition. In an investigation of first hits the contribution of afterpulses was kept to a minimum, but this is also insensitive to late contributions in cells that also saw an early energy deposition in a given event. In an alternative approach, we took the time distribution of photons within energy depositions and of afterpulses explicitly into account. Through an afterpulsing correction, enabled by dedicated laboratory measurements, we could investigate the influence of afterpulsing on the measured shower characteristics when the full SiPM signals are considered. With applied afterpulsing correction, the general shower characteristics extracted in the first hit analysis could be reproduced with this alternative approach (although less accurate). Without such a correction, on the other hand, the dominating effect of afterpulsing disguises the occurrence of delayed energy depositions. For the utilized type of SiPMs (Hamamatsu MPPC-50), on average 22 % of the total shower signal detected within an integration time of 200 ns is only afterpulsing. In particular, after an integration time of about $10 - 11$ ns one integrates primarily SiPM afterpulsing and the contribution of delayed energy depositions becomes negligible. So in the context of a CLIC calorimeter, we can state that without a highly sophisticated afterpulsing correction or the usage of different advanced SiPMs which are quasi afterpulsing free, there is no use in integrating energy depositions within hadronic showers longer than $10 - 11$ ns. On the other hand, a detailed investigation of the total fraction of the shower energy deposited by first hits indicates that the timing properties of hadronic showers do not demand a longer integration time. We find that ≥ 96 % and ≥ 99 % of the total shower energy is, on

average, deposited within 10 ns for a steel and for a tungsten absorber, respectively.

7.2 Outlook

The T3B experiment is the basis for further investigations of the time evolution of hadronic showers performed by the CALICE collaboration. The FastRPC experiment has the identical outline of T3B (1 strip of active cells positioned behind a calorimeter prototype and read out by fast oscilloscopes), but utilizes the technology of gaseous resistive plate chambers as active component instead of SiPMs attached to scintillating plastic. In this sense, the FastRPC experiment can measure the response of a gaseous detector to delayed evaporation neutrons. It can determine the relative contribution of different neutron interaction processes and compare it to the T3B results (further information can be found in [65]).
Apart from this, a 2^{nd} generation calorimeter prototype will continue the investigation of hadronic shower timing started by T3B on a larger scale. Instead of fifteen cells assembled to a strip and positioned in one distinct calorimeter depth, this prototype will consist of a whole cubic meter of detector volume instrumented with altogether $\mathcal{O}(10.000)$ scintillator cells. Thus, the prototype will be able to detect the energy depositions of a hadronic shower event radially and in direction of the shower propagation simultaneously. The energy deposition of each cell will be timestamped with nanosecond precision. Such measurements can be used to validate and reproduce the results on the average shower timing characteristics delivered by T3B. Additionally, such a prototype will open up the possibility to investigate the time structure of hadronic showers on an event-by-event basis and study correlations of energy depositions within a shower event in a time resolved manner.

Bibliography

[1] *CERN - Conseil Europeen pour la Recherche Nucleaire.* URL: http://www.cern.ch/.

[2] Serguei Chatrchyan et al. "Observation of a new boson at a mass of 125 GeV with the CMS experiment at the LHC". In: *Phys.Lett.* B716 (2012), pp. 30–61. DOI: 10.1016/j.physletb.2012.08.021. arXiv:1207.7235 [hep-ex].

[3] Georges Aad et al. "Observation of a new particle in the search for the Standard Model Higgs boson with the ATLAS detector at the LHC". In: *Phys.Lett.* B716 (2012), pp. 1–29. DOI: 10.1016/j.physletb.2012.08.020. arXiv:1207.7214 [hep-ex].

[4] *The CMS Experiment.* URL: http://cms.web.cern.ch/.

[5] *The Atlas Experiment.* URL: http://www.atlas.ch/.

[6] David Griffiths. *Introduction to elementary particles.* Wiley-VCH, 2008.

[7] S.W. Herb et al. "Observation of a Dimuon Resonance at 9.5-GeV in 400-GeV Proton-Nucleus Collisions". In: *Phys.Rev.Lett.* 39 (1977), pp. 252–255. DOI: 10.1103/PhysRevLett.39.252.

[8] F. Abe et al. "Observation of top quark production in $\bar{p}p$ collisions". In: *Phys.Rev.Lett.* 74 (1995), pp. 2626–2631. DOI: 10.1103/PhysRevLett.74.2626. arXiv:hep-ex/9503002 [hep-ex].

[9] S. Abachi et al. "Search for high mass top quark production in $p\bar{p}$ collisions at $\sqrt{s} = 1.8$ TeV". In: *Phys.Rev.Lett.* 74 (1995), pp. 2422–2426. DOI: 10.1103/PhysRevLett.74.2422. arXiv:hep-ex/9411001 [hep-ex].

[10] K. Kodama et al. "Observation of tau neutrino interactions". In: *Phys.Lett.* B504 (2001), pp. 218–224. DOI: 10.1016/S0370-2693(01)00307-0. arXiv:hep-ex/0012035 [hep-ex].

[11] Robert N. Cahn. "The Eighteen arbitrary parameters of the standard model in your everyday life". In: *Rev.Mod.Phys.* 68 (1996), pp. 951–960. DOI: 10.1103/RevModPhys.68.951.

[12] Y. Fukuda et al. "Measurements of the solar neutrino flux from Super-Kamiokande's first 300 days". In: *Phys.Rev.Lett.* 81 (1998), pp. 1158–1162. DOI: 10.1103/PhysRevLett.81.1158. arXiv:hep-ex/9805021 [hep-ex].

[13] B.T. Cleveland et al. "Measurement of the solar electron neutrino flux with the Homestake chlorine detector". In: *Astrophys.J.* 496 (1998), pp. 505–526. DOI: 10.1086/305343.

[14] Christian Soldner. "Scintillator Tile Uniformity Studies for a Highly Granular Hadron Calorimeter". MA thesis. Ludwig Maximilian Universität München, 2009.
[15] C.N. Yang. *Elementary particles: a short history of some discoveries in atomic physics*. Princeton University Press, 1961.
[16] Laurie M. Brown. "The idea of the neutrino". In: *Phys.Today* 31N9 (1978), pp. 23–28. DOI: 10.1063/1.2995181.
[17] J. Beringer et al. "Review of particle physics. Particle Data Group". In: *Phys.Rev.* D86 (2012).
[18] Makoto Kobayashi and Toshihide Maskawa. "CP Violation in the Renormalizable Theory of Weak Interaction". In: *Prog.Theor.Phys.* 49 (1973), pp. 652–657. DOI: 10.1143/PTP.49.652.
[19] W.S.C. Williams. *Nuclear and Particle Physics*. Oxford University Press, 1997.
[20] Peter W. Higgs. "Spontaneous Symmetry Breakdown without Massless Bosons". In: *Phys.Rev.* 145 (1966), pp. 1156–1163. DOI: 10.1103/PhysRev.145.1156.
[21] J. Alcaraz et al. "Precision Electroweak Measurements and Constraints on the Standard Model". In: 2007. arXiv:0712.0929 [hep-ex].
[22] Stephen P. Martin. "A Supersymmetry primer". In: (1997). arXiv:hep-ph/9709356 [hep-ph].
[23] H. Nishino et al. "Search for Proton Decay via $p \to e^+\pi^0$ and $p \to \mu^+\pi^0$ in a Large Water Cherenkov Detector". In: *Phys. Rev. Lett.* 102 (14 Apr. 2009), p. 141801. DOI: 10.1103/PhysRevLett.102.141801. URL: http://link.aps.org/doi/10.1103/PhysRevLett.102.141801.
[24] John R. Ellis et al. "Supersymmetric Relics from the Big Bang". In: *Nucl.Phys.* B238 (1984), pp. 453–476. DOI: 10.1016/0550-3213(84)90461-9.
[25] A.D. Martin et al. "Parton distributions for the LHC". In: *Eur.Phys.J.* C63 (2009), pp. 189–285. DOI: 10.1140/epjc/s10052-009-1072-5. arXiv:0901.0002 [hep-ph].
[26] G. Weiglein et al. "Physics interplay of the LHC and the ILC". In: *Physics Reports* 426.2–6 (2006), pp. 47 –358. ISSN: 0370-1573. DOI: 10.1016/j.physrep.2005.12.003.
[27] Lucie Linssen et al. "Physics and Detectors at CLIC: CLIC Conceptual Design Report". In: (2012). arXiv:1202.5940 [physics.ins-det].
[28] Frank Simon. "Prospects for Precision Higgs Physics at Linear Colliders". In: (2012). arXiv:1211.7242 [hep-ex].
[29] (ed.) Brau James et al. "International Linear Collider reference design report. 1: Executive summary. 2: Physics at the ILC. 3: Accelerator. 4: Detectors". In: (2007).
[30] ILC Global Design Effort. *The International Linear Collider: A Technical Progress Report*. Tech. rep. 2011.
[31] P. Lebrun et al. "The CLIC Programme: Towards a Staged e+e- Linear Collider Exploring the Terascale : CLIC Conceptual Design Report". In: (2012). arXiv:1209.2543 [physics.ins-det].
[32] Toshinori Abe et al. "The International Large Detector: Letter of Intent". In: (2010). arXiv:1006.3396 [hep-ex].

[33] (Ed.) Aihara H. et al. "SiD Letter of Intent". In: (2009). arXiv:0911.0006 [physics.ins-det].

[34] M.A. Thomson. "Particle Flow Calorimetry and the PandoraPFA Algorithm". In: *Nucl.Instrum.Meth.* A611 (2009), pp. 25–40. DOI: 10.1016/j.nima.2009.09.009. arXiv:0907.3577 [physics.ins-det].

[35] I.G. Knowles and G.D. Lafferty. "Hadronization in Z^0 decay". In: *J.Phys.* G23 (1997), pp. 731–789. DOI: 10.1088/0954-3899/23/7/003. arXiv:hep-ph/9705217 [hep-ph].

[36] M. G. Green et al. *Electron - positron physics at the Z*. IoP Publishing, 1997.

[37] J.S. Marshall, A. Munnich, and M.A. Thomson. "Performance of Particle Flow Calorimetry at CLIC". In: (2012). arXiv:1209.4039 [physics.ins-det].

[38] Richard Wigmans. *Calorimetry: Energy Measurement in Particle Physics*. Oxford University Press, 2000, p. 726.

[39] William R. Leo. *Techniques for nuclear and particle physics experiments: A how to approach*. 2nd ed. Springer, 1994, p. 378.

[40] Helmuth Spieler Claus Grupen Boris A. Shwartz. *Particle detectors*. Cambridge University Press, March 2008.

[41] Veronique Bernard, Norbert Kaiser, and Ulf-G. Meissner. "The Pion charge radius from charged pion electroproduction". In: *Phys.Rev.* C62 (2000), p. 028201. DOI: 10.1103/PhysRevC.62.028201. arXiv:nucl-th/0003062 [nucl-th].

[42] Randolf Pohl et al. "The size of the proton". In: *Nature* 466 (2010), pp. 213–216. DOI: 10.1038/nature09250.

[43] T.A. Gabriel et al. "Energy dependence of hadronic activity". In: *Nucl.Instrum.Meth.* A338 (1994), pp. 336–347. DOI: 10.1016/0168-9002(94)91317-X.

[44] G. Audi, A.H. Wapstra, and C. Thibault. "The Ame2003 atomic mass evaluation (II). Tables, graphs and references". In: *Nucl.Phys.* A729 (2002), pp. 337–676. DOI: 10.1016/j.nuclphysa.2003.11.003.

[45] Hanno Bruckmann, Ulf Behrens, and Bernd Anders. "Hadron Sampling Calorimetry: A Puzzle Of Physics". In: *Nucl.Instrum.Meth.* A263 (1988), p. 136. DOI: 10.1016/0168-9002(88)91026-1.

[46] A. Caldwell et al. "Measurement of the time development of particle showers in a uranium scintillator calorimeter". In: *Nucl.Instrum.Meth.* A330 (1993), pp. 389–404. DOI: 10.1016/0168-9002(93)90568-3.

[47] Claude Leroy, Yves Sirois, and Richard Wigmans. "An Experimental Study of the Contribution of Nuclear Fission to the Signal of Uranium Hadron Calorimeters". In: *Nucl.Instrum.Meth.* A252 (1986), p. 4.

[48] G.L. Bayatian et al. "CMS physics: Technical design report". In: (2006).

[49] *ATLAS: Detector and physics performance technical design report. Volume 1*. Tech. rep. 1999.

[50] Adam Nepomuk Otte. "Observation of VHE Gamma-Rays from the Vicinity of magnetized Neutron Stars and Development of new Photon-Detectors for Future Ground based Gamma-Ray Detectors". PhD thesis. Technische Universität Muenchen, 2007.

[51] *MEPhI - Moscow Engineering Physics Institute*. URL: http://www.mephi.ru/eng/.
[52] Kolja Prothmann. "Comparative Measurements of Silicon Photomultipliers for the Readout of a Highly Granular Hadronic Calorimeter". MA thesis. Ludwig Maximilian Universität München, 2008.
[53] S. Uozumi. "Study of MPPC Performance for the GLD Calorimeter Readout". In: *eConf* C0705302 (2007), CAL10.
[54] *MPPC Multi-Pixel Photon Counter Technical Information Pamphlet*. Hamamatsu Photonics. URL: http://sales.hamamatsu.com/.
[55] *Saint-Gobain*. URL: http://www.detectors.saint-gobain.com/.
[56] Marius Groll. "Construction and commissioning of a hadronic test-beam calorimeter to validate the particleflow concept at the ILC". PhD thesis. University of Hamburg, 2007.
[57] *BC-418, BC-420, BC-422 Premium Plastic Scintillators - Data Sheet*. URL: http://www.detectors.saint-gobain.com/Plastic-Scintillator.aspx.
[58] *Fermilab - Fermi National Accelerator Laboratory*. URL: http://www.fnal.gov/.
[59] *DESY - Deutsches Elektronen-Synchrotron*. URL: http://www.desy.de/.
[60] C. Adloff et al. "Construction and Commissioning of the CALICE Analog Hadron Calorimeter Prototype". In: *JINST* 5 (2010), P05004. DOI: 10.1088/1748-0221/5/05/P05004. arXiv:1003.2662 [physics.ins-det].
[61] M. Reinecke. "Integration Prototype of the CALICE Tile Hadron Calorimeter for the International Linear Collider". In: (2008).
[62] Mark Terwort. "Status of the CALICE analog calorimeter technological prototypes". In: *J.Phys.Conf.Ser.* 404 (2012), p. 012066. DOI: 10.1088/1742-6596/404/1/012066. arXiv:1209.2594 [physics.ins-det].
[63] Oskar Hartbrich and Mark Terwort. "Recent Advances of the Engineering Prototype of the CALICE Analog Hadron Calorimeter". In: (2012). arXiv:1201.5264 [physics.ins-det].
[64] C. Adloff et al. "Hadronic energy resolution of a highly granular scintillator-steel hadron calorimeter using software compensation techniques". In: *JINST* 7 (2012), P09017. DOI: 10.1088/1748-0221/7/09/P09017. arXiv:1207.4210 [physics.ins-det].
[65] Marco Szalay. "Study of hadronic showers with the fastRPC analog detector". MA thesis. Technische Universität München, 2013.
[66] *Official GEANT4 homepage*. URL: http://www.geant4.org/geant4/.
[67] A. Dotti et al. "Recent improvements on the description of hadronic interactions in Geant4". In: *J.Phys.Conf.Ser.* 293 (2011), p. 012022. DOI: 10.1088/1742-6596/293/1/012022.
[68] *Radiant Mirror Foil*. URL: http://solutions.3m.com.
[69] *Black Aluminium Foil BKF24*. URL: http://www.thorlabs.com.
[70] *Max-Planck-Institute for Physics*. URL: http://www.mpp.mpg.de/.
[71] F. Simon and C. Soldner. "Uniformity Studies of Scintillator Tiles directly coupled to SiPMs for Imaging Calorimetry". In: *Nucl.Instrum.Meth.* A620 (2010), pp. 196–

201. DOI: 10.1016/j.nima.2010.03.142. arXiv:1001.4665 [physics.ins-det].

[72] Patrick Eckert et al. "Characterisation Studies of Silicon Photomultipliers". In: *Nucl.Instrum.Meth.* A620 (2010), pp. 217–226. DOI: 10.1016/j.nima.2010.03.169. arXiv:1003.6071 [physics.ins-det].

[73] *Official PicoTech homepage*. URL: http://www.picotech.com/.

[74] *Texas Instruments homepage*. URL: http://www.ti.com.

[75] *Agilent Technologies homepage*. URL: http://www.home.agilent.com.

[76] *Qt application framework homepage*. URL: http://qt.nokia.com/products/.

[77] Lars Weuste. "Mass Measurement of Right-Handed Scalar Quarks and Time Measurement of Hadronic Showers for the Compact Linear Collider". PhD thesis. Ludwig Maximilian Universität München, 2013.

[78] *ROOT Data Analysis Framework homepage*. URL: http://root.cern.ch.

[79] D. Dannheim, W. Klempt, and E. van der Kraaij. "Beam tests with the CALICE tungsten analog hadronic calorimeter prototype". In: *LCD-Note-2012-002* (2012).

[80] Simon Pfau. "A Study of Silicon Photomultiplier Properties in the Context of Highly Granular Calorimeters". MA thesis. Technische Universität München, 2012.

[81] Frank Simon. "Studies of Scintillator Tiles with SiPM Readout for Imaging Calorimeters". In: *J.Phys.Conf.Ser.* 293 (2011), p. 012074. DOI: 10.1088/1742-6596/293/1/012074. arXiv:1008.2466 [physics.ins-det].

[82] V.N. Ivanchenko et al. "Geant4 models for simulation of multiple scattering". In: *J.Phys.Conf.Ser.* 219 (2010), p. 032045. DOI: 10.1088/1742-6596/219/3/032045.

[83] Nils Feege. "Low-energetic hadron interactions in a highly granular calorimeter". PhD thesis. Universität Hamburg, 2011.

[84] E. Abat et al. "Study of the response of the ATLAS central calorimeter to pions of energies from 3 to 9 GeV". In: *Nucl.Instrum.Meth.* A607 (2009), pp. 372–386. DOI: 10.1016/j.nima.2009.05.158.

[85] A. Ribon et al. "Status of Geant4 hadronic physics for the simulation of LHC experiments at the start of LHC physics program". In: *CERN-LCGAPP-2010-02* (2010).

[86] C. Adloff et al. "Tests of a particle flow algorithm with CALICE test beam data". In: *JINST* 6 (2011), P07005. DOI: 10.1088/1748-0221/6/07/P07005. arXiv:1105.3417 [physics.ins-det].

List of Figures

List of Tables

Acknowledgments

This thesis would not have been possible without the help and support of many people:

First of all, I want to thank my supervisor **Frank Simon**, who advised me during the last four years of research. He was always available for vibrant discussions and supported me with brilliant ideas and astonishing intuition.

Furthermore, I thank my supervising professor **Christian Kiesling** whose enthusiasm motivated me to do research in the fascinating field of particle physics and the whole BELLE group for all the interesting and funny discussions during tea time.

I also thank my colleague **Lars Weuste** who designed and developed the T3B experiment together with me over the last three years. We spent countless hours in the laboratory, in the experimental test beam halls at CERN, sometimes controlling the SPS beamline on our own during a long night shift, and in front of the analysis PC. Our vivid and sometimes heated discussions made the whole T3B experiment a success. Special thanks to the **CERN LCD** and the **DESY FLC** group who provided invaluable advise and support during the test beam phases.

I also thank **Katja Seidel**, **Michal Tesař** and **Marco Szalay** who enriched my everyday life at the institute.

Finally I thank my family **Christa**, **Karl** and **Jasmin Soldner** who supported me for the last 30 years in every situation of my life and my girlfriend **Nina Nowatius** for always being my muse.